LOW SYMMETRY METALLOPHTHALOCYANINES AND THEIR NANOPARTICLE CONJUGATES FOR PHOTODYNAMIC ANTIMICROBIAL CHEMOTHERAPY

A thesis submitted in fulfilment of the requirements for the degree of

DOCTOR OF PHILOSOPHY

Of

RHODES UNIVERSITY

By

NKOSIPHILE MASILELA

January 2013

DEDICATION

To

My Mother

Gladys Nkosi

My Fiancée

Ntombexolo "Zola" Siyo

My Sisters

Busisiwe, Bongiwe and Zandile

My Brothers

Mthunzi, Bonginkosi and Nhlanhla

ACKNOWLEDGEMENTS

To him; who created man, heaven and earth, the creator of the universe, the true source of light and wisdom. Thanks to God for strengthening me in all things, for me to reach this far is not by intelligence but it's your will.

My deepest gratitude's goes to my supervisor, Professor Tebello Nyokong. Thank you for your supervision and guidance that led to the success of this work. Prof., thank you for giving me the opportunity of going to do part of my research in Canada. I would also like to thank my host supervisor and his research group at the University of Western Ontario. My gratitude's also goes to Dr Edith Antunes for the guidance and support.

To my Fiancée Zola Siyo, a special thank you for your unconditional love, strength and support. To my family, my mother Gogo Nkhosi thank you so much Dlamini for your prayers, "*wena lowacedza lubombo ngekuhlehletela*", and to my sister's thank you for your financial support at all times. To Mthundzi thank you Mnaka for your strength and support. Popo and Nhlanhla thank you bomnaketfu.

Thanks to the Department of Science and Technology (DST) and National Research Foundation (NRF), South Africa through DST/NRF South African Research Chairs Initiative for Professor of Medicinal Chemistry and Nanotechnology and Rhodes University for financial support. I thank DAAD and Henderson for financial support.

I would like to thank my group the S22 research group and the entire Chemistry Department. I also like to thank Gail Cobus and the Electron microscopy unit (EMU)

ACKNOWLEDGEMENTS

for their help. Last but not least I will like to thank the Chemistry Department technical team for their assistance.

Abstract

This thesis reports on the syntheses of novel low symmetrically substituted Zn, Sn, Ge and Ti MPc complexes containing a single carboxylic or cysteinyl group available for attachments to MNPs. The complexes were extensively characterized by various techniques to ensure their purity. Various metallic nanoparticles consisting of silver (AgNPs), gold (AuNPs) as well as quantum dots (QDs) were successfully prepared and conjugated to the low symmetry phthalocyanine complexes. The conjugates were successfully characterized using many techniques. The Q-band maxima of the MPcs were observed at completely different wavelength regions depending on the nature of the substituents and the central metal used. Blue shifting of the Q band in the absorption spectra was observed for the complexes in the presence of AuNPs, while aggregation was observed in the presence of quantum dots. The complexes were successfully electrospun into polymer fibers for the antimicrobial inhibition of bacteria.

The photophysical and photochemical properties of these complexes were extensively investigated. Higher triplet and singlet oxygen quantum yields were achieved for the Ge Pc complexes, with all the complexes giving reasonable singlet oxygen quantum yields. An enhancement in triplet and singlet oxygen quantum yields was observed for all the complexes in the presence of metal nanoparticles. However, the singlet oxygen quantum yields decreased for all the complexes when incorporated into electrospun fibers. The antimicrobial behaviour of the complexes was investigated against *Bacillus Subtilis* and *Staphylococcus Aureus* in solution and in the fiber matrix. High antimicrobial inhibitions were observed for the Ge complexes

followed by the ZnPc derivatives. All the low symmetry ZnPc derivatives were conjugated to AgNPs and their antimicrobial behaviour was compared to their symmetrical counterparts. The best antimicrobial inhibition behaviour was observed for the low symmetry Pcs when compared to their symmetrical counterparts. In the absence and in the presence of AgNPs, axially ligated SiPc also showed better antimicrobial activity when it was compared to the unsubstituted ZnPc complex.

CONTENTS

CONTENTS

CONTENTS

CONTENTS

CHAPTER 3

Results and discussion

CONTENTS

CONTENTS

CONTENTS

List of Abbreviations

A	-	Absorption
Ac	-	Acetate
ADMA	-	Tetrasodium α,α–(anthracene-9,10-diyl)
		dimethyl malonate
DMSO-d$_6$	-	Deuterated dimethylsulfoxide
DMF-d6	-	Deuterated dimethylformamide
D$_2$O	-	Deuterated water
DBU	-	1,8-Diazabicyclo[5.4.0]undec-7-ene
DCM	-	Dichloromethane
DMAc	-	Dimethyl acetamide
DCC	-	Dicyclohexylcarbodiimide
DPBF	-	3-Diphenylisobenzofuran
DMF	-	*N,N*-dimethylformamide
DMSO	-	Dimethylsulfoxide
F	-	Fluorescence
HOMO	-	Highest occupied molecular orbital
LUMO	-	Lowest unoccupied molecular orbital
IR	-	Infrared
IC	-	Internal conversion
ISC	-	Intersystem crossing
I	-	Light intensity
MCP	-	Monochromator photomultiplier

LIST OF ABBREVIATIONS

P	-	Phosphorescence
PDT	-	Photodynamic therapy
PACT	-	Photodynamic antimicrobial chemotherapy
PMT	-	Photomultiplier tube
PS	-	Polystyrene
PVP	-	Polyvinyl pyrrolidone
^{1}H NMR	-	Proton nuclear magnetic resonance spectroscopy
SEM	-	Scanning electron microscopy
TCP	-	Tetracarboxyphenoxy
THF	-	Tetrahydrofuran
TP	-	Tetraphenoxy
MC	-	Monocarboxy
MCs	-	Monocysteinyl
MPC	-	Monophenoxy carboxy
ODE	-	Octadiethyl
TDE	-	Tetradiethyl
TSPc	-	Tetrasulfonated phthalocyanine
TCSPC	-	Time correlated single photon counting
TEM	-	Transmission electron microscopy
^{3}MPc*	-	Triplet state of phthalocyanine
VR	-	Vibrational relaxation
XRD	-	X-ray diffraction
XPS	-	X-ray photoelectron spectroscopy

LIST OF ABBREVIATIONS

STP   -   Sphere to prism transformation

NaC_3 -   Sodium citrate

NP   -   Nanoparticle

GSH   -   Glutathione

TGA   -   Thioglycolic acid

SOC   -   Spin-orbit coupling

UV-vis   -   Ultraviolet visible

List of symbols

Å	-	Angstrom
ΔA_s	-	Changes in the singlet state absorbances
ΔA_T	-	Changes in the triplet state absorbances
$^1O_2(^1\Sigma^-_g)$	-	Singlet oxygen
T_1	-	First excited triplet excited state
Φ_F	-	Fluorescence quantum yield
τ_F	-	Fluorescence lifetime
$h\nu$	-	Light
ε	-	Molar extinction coefficient
T_n	-	nth triplet state
α	-	Non-peripheral position
β	-	Peripheral position
T_2	-	Second excited triplet state
S_1	-	Singlet excited state
S_0	-	Singlet ground state
$^3O_2(^3\Delta_g)$	-	Triplet molecular oxygen
Φ_Δ	-	Singlet oxygen quantum yield
ε_S	-	Singlet state molar extinction
τ_T	-	Triplet lifetime
Φ_T	-	Triplet quantum yield
ε_T	-	Triplet state molar extinction coefficient
r	-	Centre to centre

LIST OF SYMBOLS

R_0	-	Förster distance
$^3O_2$	-	Ground state oxygen
λ_{abs}	-	Wavelength of absorption spectrum maximum
λ_{emi}	-	Wavelength of emission spectrum maximum
λ_{exci}	-	Wavelength of excitation spectrum maximum
I_{abs}	-	Rate of light absorption by the photosensitizer
J	-	Förster overlaps integral
κ_2	-	Dipole orientation factor
S	-	Seconds

List of figures

List of tables

List of schemes

CHAPTER 1

Introduction

1.1 Phthalocyanines

In this thesis phthalocyanines (Pcs) have been studied alone and when conjugated to nanoparticles (NPs). Unsymmetrically substituted Pcs are the subject of this thesis, especially those containing mono-carboxyl groups which enable linking to metal nanoparticles (MNPs) and to quantum dots (QDs). Pcs will also be electrospun into fibers for use in bacterial inactivation.

1.1.1   History and discovery

The name 'phthalocyanine' was coined from its precursor phthalic acid derivative 'phthalo', and 'cyanine' from the Greek word for blue. Phthalocyanines (Pcs) are synthetic analogues of naturally occurring porphyrins and are a versatile class of compounds that have received much attention for application in everyday life. The first phthalocyanine complex was reported in 1907. The complex was discovered accidentally by Braun and Tcherniac as a by-product during the synthesis of *o*-cyanobenzamide from phthalamide [1-3].

This complex was first observed as an unknown insoluble bluish compound which was later identified as a metal-free phthalocyanine. Then in 1927, the first copper phthalocyanine was synthesized by de Diesbach and coworkers when they tried to convert o-dibromobenzene into phthalonitrile but its structure was not correctly formulated [4]. The structural elucidation was later done by Linstead [5]. Iron Pc was also accidentally discovered in 1928, when a blue product was found in a reaction flask where only white product was expected at the Scottish Dyes Ltd [6-8]. At a later (1935) stage its structure was confirmed by X-ray crystallography by Robertson showing that the phthalocyanine molecule is a rather planar molecule with a

chemical formula $C_{32}H_{18}N_8$ corresponding to the unmetallated phthalocyanine [9, 10].

1.1.2   Structure and some applications of phthalocyanines

Phthalocyanines are conjugated, aromatic molecules that consist of 32 carbons, 8 nitrogens, 16 hydrogens at the periphery, and 2 hydrogens in the center of the ring that can be substituted upon addition of a central metal ion [11]. The Pc molecule consists of four isoindole units that are linked by four nitrogen atoms and they assemble a two-dimensional 18π electron conjugated system, in which more than 70 different metals and non-metals can be incorporated into the center Fig. 1.1. The 18π electron system that surrounds the core center of these heterocyclic compounds renders them chemically and thermally stable. This extended conjugation of the π electron system is known to be responsible for their blue-green colour.
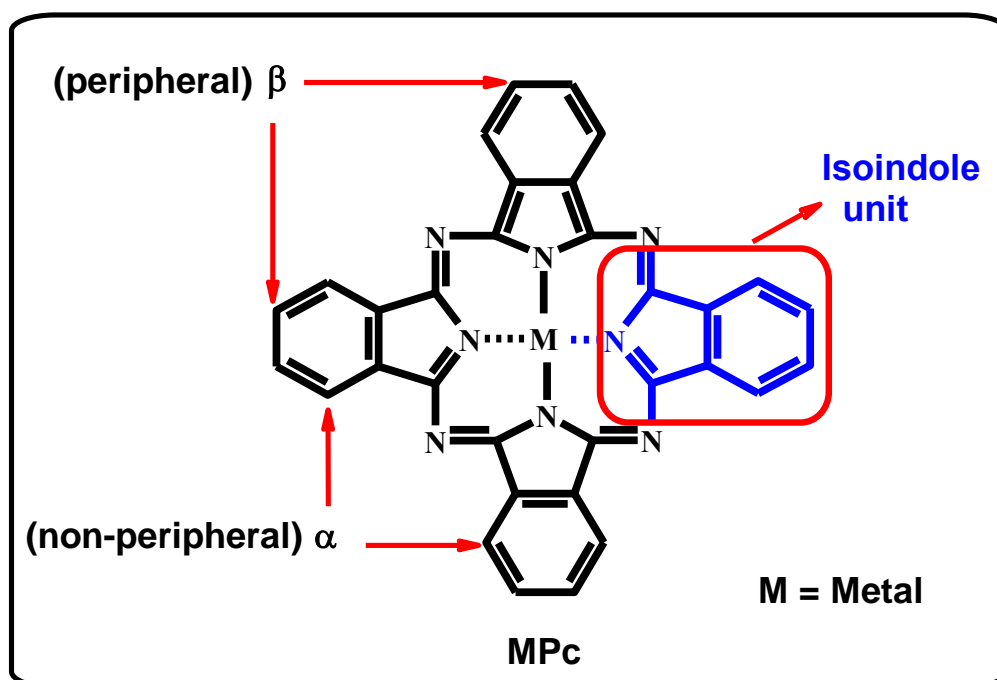
Figure 1.1: The structure of metallophthalocyanine

Because of the flexibility of the structure of phthalocyanine complexes, they can be engineered for many applications since they possess 16 available sites on the ring structure, where many substituents can be introduced to modify the chemical properties for different technological applications. Substitution with different organic ligands either at the peripheral (β) or at the non-peripheral positions (α) enhances the solubility of these complexes [12-16].
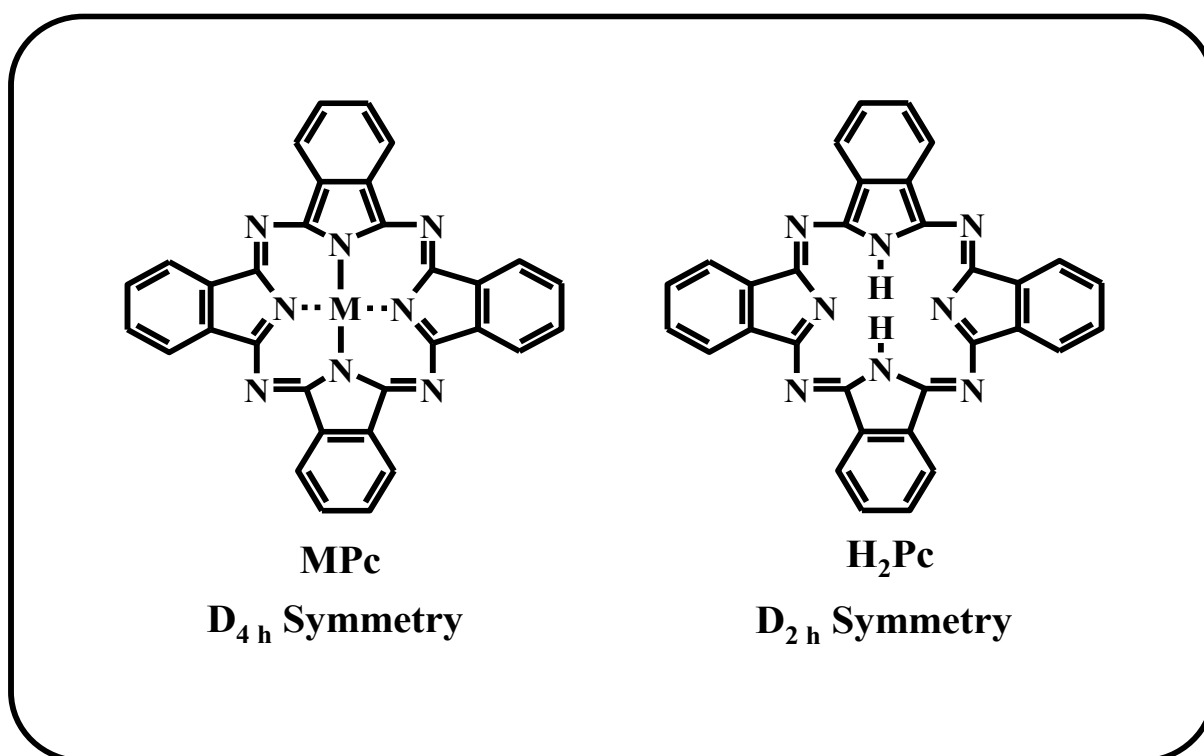
Figure 1.2: The molecular structures of metallated (MPc) and unmetallated (H$_2$Pc) phthalocyanines

Metallated phthalocyanines (MPcs) (Fig. 1.2) possess D$_{4h}$ geometry, while their unmetallated (H$_2$Pc) counterparts exhibit a D$_{2h}$ symmetry. However, some metal ions (such as Ti, Pb, Sb and Ta) do not perfectly fit in the cavity because of their larger ionic size which in some cases leads to loss of symmetry. The size of the Pc cavity or the distance between the two adjacent nitrogen atoms is known to be ~270-290 pm

[17], and large metal ions tend to distort the geometry of the Pcs, leading to a change in planarity to a square pyramidal system, and consequently a reduction in symmetry from D_{2h} to C_{4v} symmetry [18-21].

Since their discovery, phthalocyanines have drawn much attention for a wide variety of applications due to their diverse, excellent structural, electronic, chemical and optical properties [6]. Because of their bright, beautiful blue-green colour and their considerable thermal and photochemical stability, they have been traditionally used as dyes for colouring of clothes (e.g. for dying blue jeans and other clothing), paints for plastics, inks in pens and for contact lenses [6-8, 16, 22]. They are also used in ink jet printing [6], electrophotography and in photocopying machinery [6, 22]. Emerging applications of phthalocyanines include their use in catalysis [23-26], photovoltaic or dye sensitized solar cells (DSSCs) [27-30], fuel cells [31], liquid crystal display devices [32, 33], electrochemical sensors [34-37], electrochromic display devices [38-40], optical computer re-writable discs (CD-RW) [41, 42], molecular electronics [43] and semi-conductor devices [43, 44]. Phthalocyanines are considered second generation photosensitizers for photodynamic therapy (PDT) of cancer because of their intense absorption in the near infrared region [11, 17, 39, 44]. They have been successfully used in many countries for PDT [45-50]. PDT is considered to be a low-cost, non-invasive and a gentle procedure for treatment of various tumours [51]. On the other hand, PDT may be applied with high efficiency in the inactivation of pathogenic microorganisms which are resistant to antibiotics [52]. This type of PDT is called photodynamic antimicrobial chemotherapy (PACT) [52].

1.1.3   Synthesis of low symmetry phthalocyanines

Several approaches have been developed to date to obtain mono-functional low symmetry phthalocyanines. These include statistical condensation employing two different phthalonitriles [53-55] (Scheme 1.1), ring opening of a subphthalocyanine [56-63], or reaction of a polymer-bonded phthalonitrile with differently substituted dicarbonitriles in solution followed by cleavage from the polymer and released of the desired phthalocyanine product [64-68].
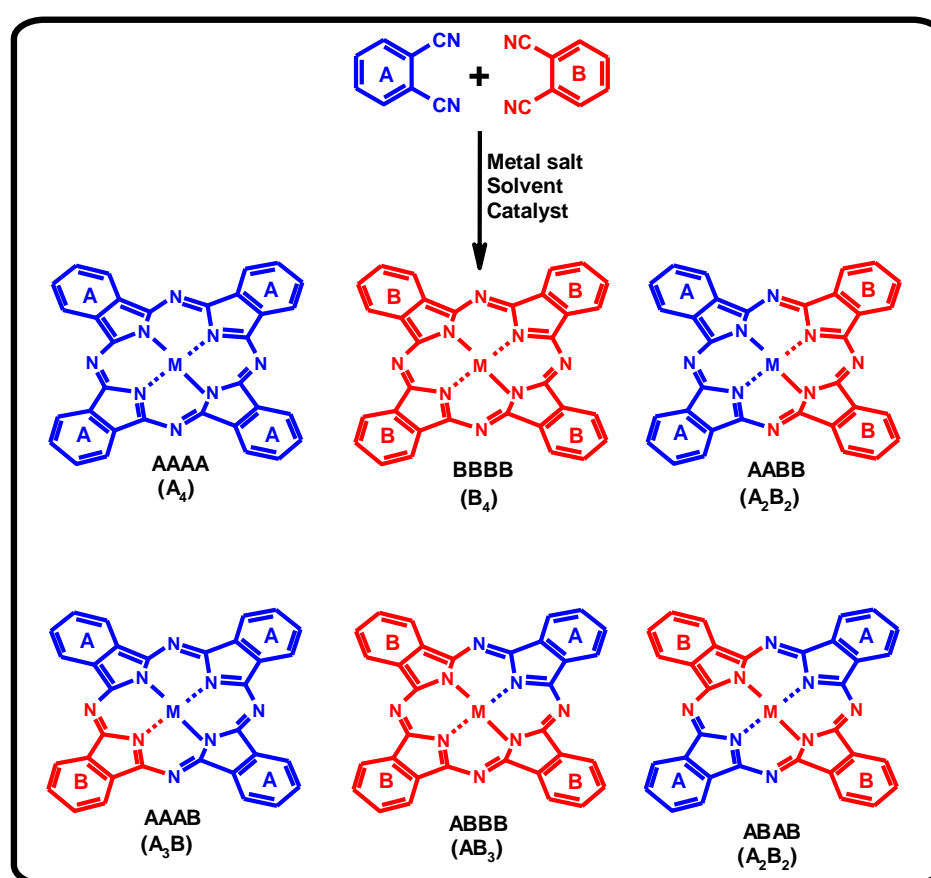
Scheme 1.1:A schematic representation of the synthesis of low symmetry phthalocyanines [53-55]

The most common strategy for the formation of low symmetry Pcs to date is to carry out condensation reactions with two different precursors to form compounds with AAAA, AAAB, AABB, ABAB, ABBB, and BBBB structures (Scheme 1.1) [53-55, 68].

The formation of the ABBB type structures can be achieved in statistical terms by fine-tuning the ratio of the precursors, and its chromatographic separation from the other products is usually relatively straightforward. However the separation of AABB and ABAB structures is challenging, since these isomers have identical molecular weights and usually have similar molecular properties. In this work, the focus is on the synthesis of low symmetry Pcs of the type ABBB product with only one carboxyl group, which may then be selectively coupled to amino functionalized nanoparticles via amide bond formation.

Symmetrically substituted phthalocyanine complexes have been extensively researched [69-72], however, they lack binding selectivity [73]. Asymmetrically substituted phthalocyanines offer the possibility of improving selectivity since groups with different physico-chemical properties may be attached to the ring, allowing for further conjugation with nano-materials [74-80], or other molecules of biological importance such as proteins and peptides [81]. Unsymmetrically substituted Pcs have thus become of increasing interest in fields such as non-linear optics [82], photodynamic therapy (PDT) of cancer [83, 84], in the development of ordered phthalocyanine Langmuir–Blodgett thin films [85] and for dye sensitized solar cells [86]. Of particular importance are derivatives bearing one reactive electrophilic or nucleophilic substituent [87]. For PDT applications, phthalocyanines tend to show poor selectivity for tumours. This may be overcome by incorporating a substituent (functional groups such as carboxyl, thiols, sulfo or amino group) capable of covalently binding the molecule to a suitable carrier, e.g. nanomaterials,

antibodies, lipoproteins and membrane proteins, which then directs the sensitizer to

the tumour without affecting the normal surrounding tissue [88].

1.1.4 Axial ligation in phthalocyanines

MPc complexes containing Si(IV), Ge(IV), Sn(IV), Ga(III) etc., as central metals

capable of binding one or two ligands in the axial position (Scheme 1.2), are of great

interest since axial ligands prevent aggregation through steric hindrance [89-92].

Studies have also shown that zinc [92] and iron [93] phthalocyanine complexes can

axially coordinate cyano and pyridine groups leading to very stable complexes.
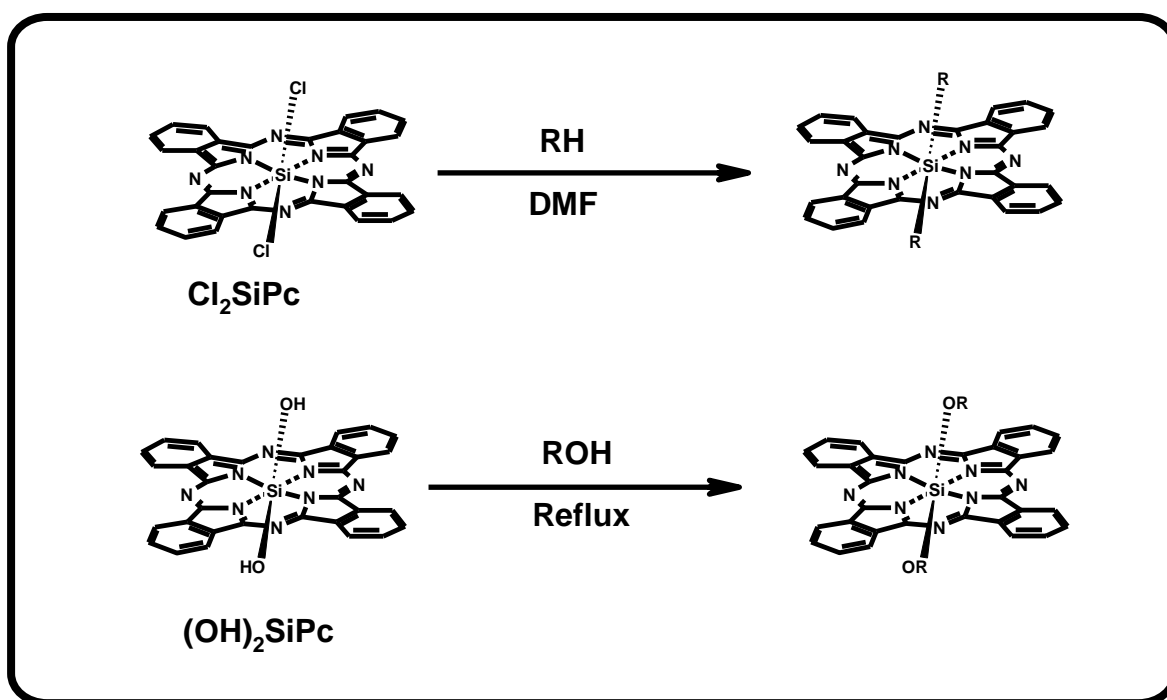
Scheme 1.2: Axial substitution on dichloro (Cl$_2$SiPc) and ((OH)$_2$SiPc) dihydroxy silicon phthalocyanines

SiPc in particular can coordinate a wide variety of ligands through reaction

pathways as illustrated in Scheme 1.2 [94-96]. Most liquid alcohols successfully react

with dihydroxyl silicon phthalocyanine or dichloro silicon phthalocyanine without
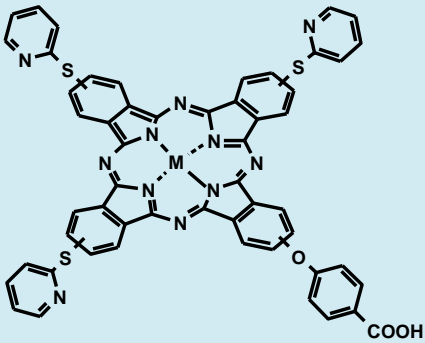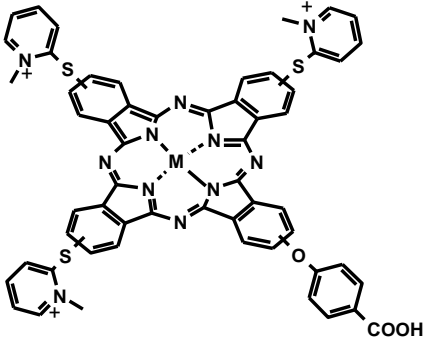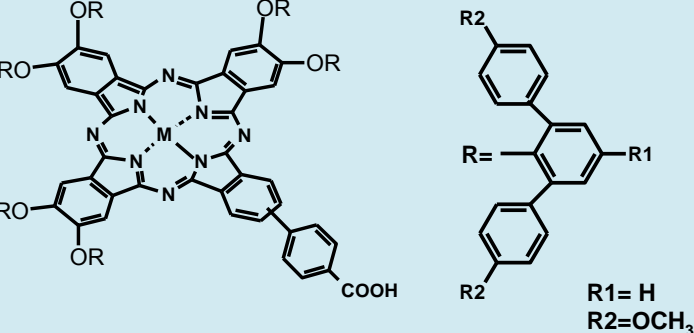
the need for an additional solvent. Solid acids need a solvent but liquid acids will most likely form silylester when reacted with dichloro silicon phthalocyanine. Rafaeloff et al. [95] reported on a simple reaction between glacial acetic acid with dichloro silicon phthalocyanine to produce a silyl ester, showing the ease of introducing acids to SiPc via axial ligation. Kenney and co-workers [97] have reported on a very effective PDT agent commonly referred to as Pc-4 (see Table 1.1). The aim of the thesis is to introduce RSH groups to SiPcs to allow for coordination to Au or Ag NPs. The ease of axial ligation serve as advantage to introduce ligands with RSH groups, compared to peripheral substitution on the ring with RSH groups which is difficult and challenging.
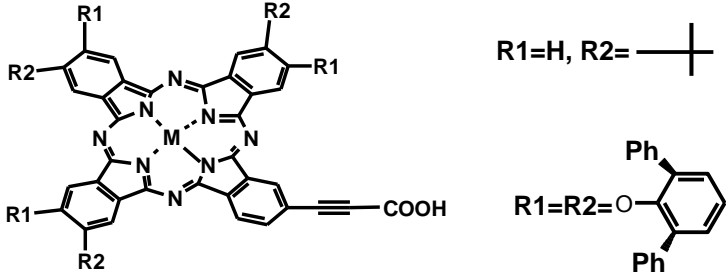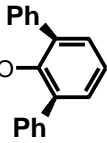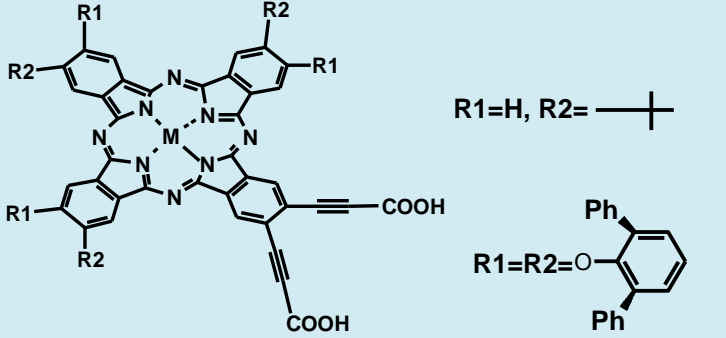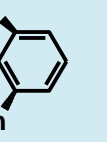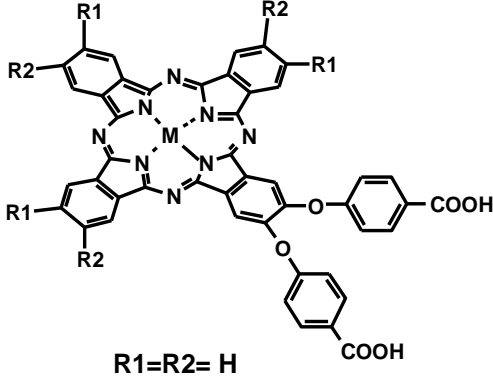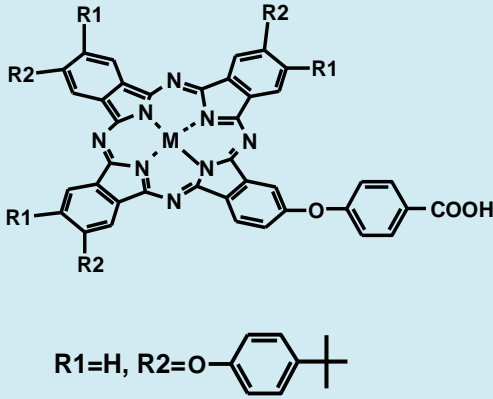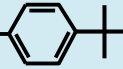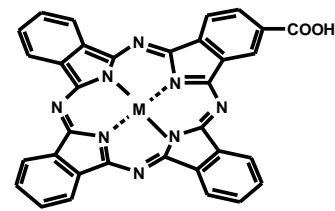
Peripherally alkylthiol-substituted Pcs are more difficult to synthesize and handle due to possible formation of Pc to Pc disulfide bonds. In this thesis, low symmetry phthalocyanines containing both carboxylic acid and amino functionalities and their conjugates to AgNPs are presented for the first time.
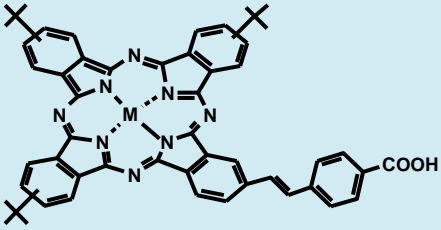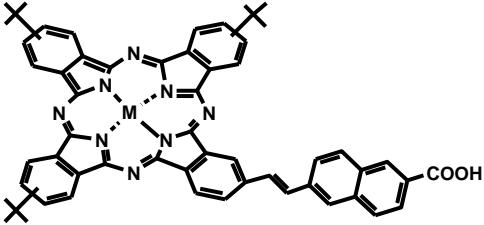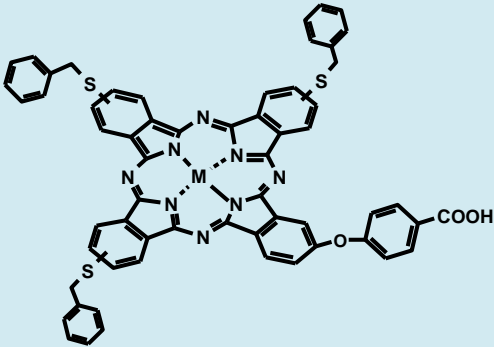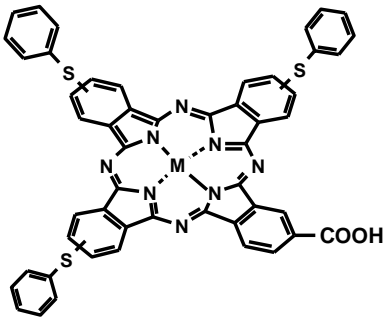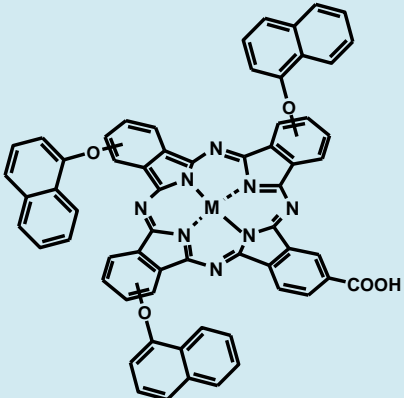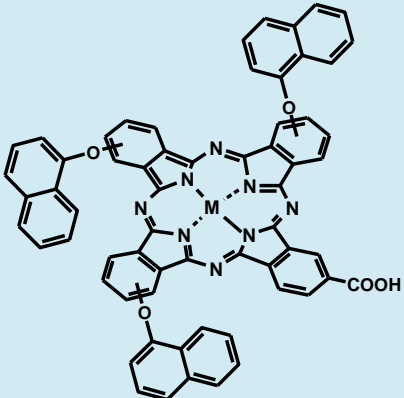
1.1.5 Known examples low symmetry and axial ligated SiPc of interest in this thesis
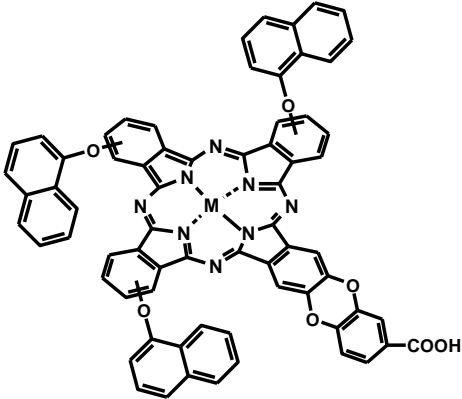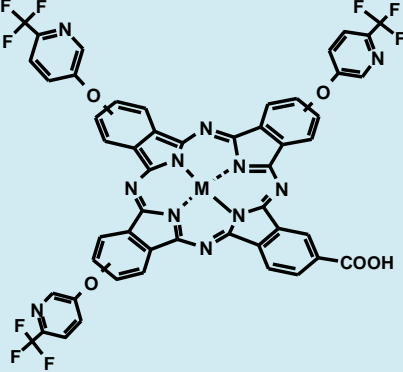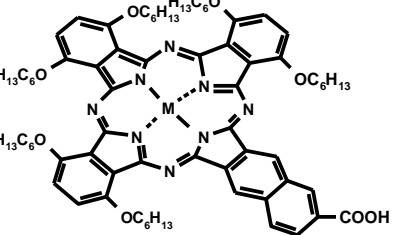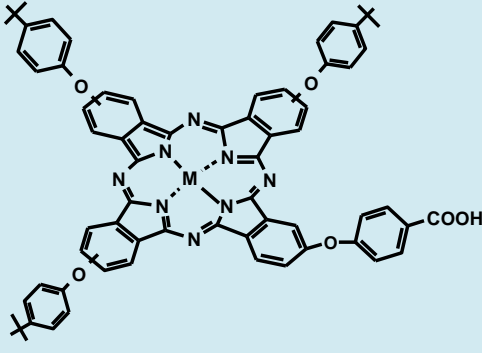
Table 1.1 shows low symmetry phthalocyanines consisting of a carboxylic functional group or an alkylthiol group and a symmetrical silicon Pc axially ligated with alkyl groups.
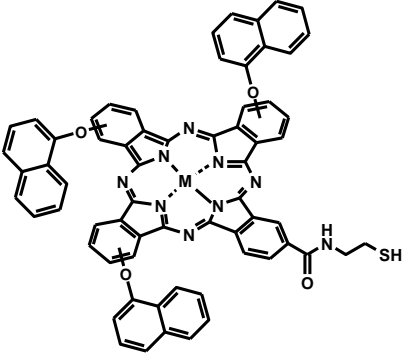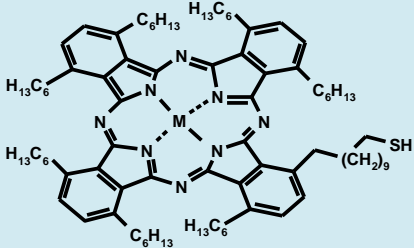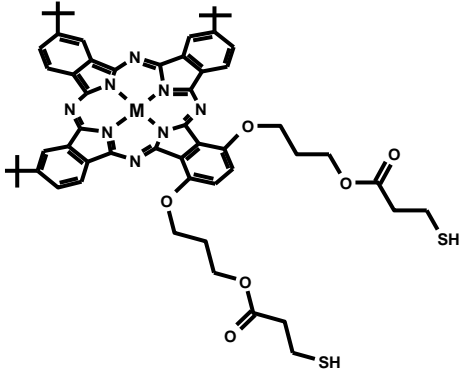
Table 1.1: A selection of known low symmetry phthalocyanines consisting of either a carboxylic or alkylthiol groups and a selection of axially ligated silicon Pc complexes.
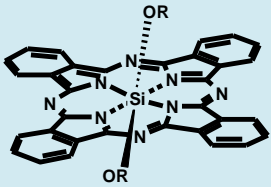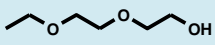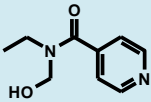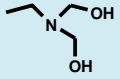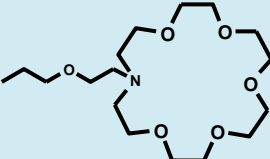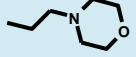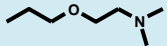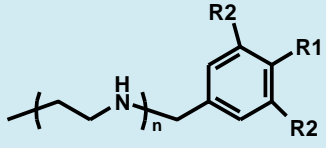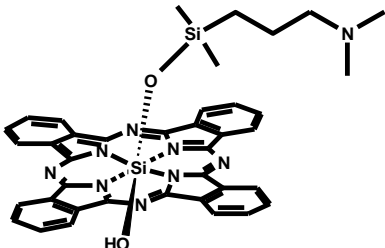
Chemical structure	metal	reference
	Zn (**1**) Mg (**2**), Al (**3**), H_2 (**4**)	[98] [99]
	Mg (**5**), Al (**6**), H_2 (**7**)	[99]
	Zn (**8**)	[100]

Structure		Metal	Ref.
R1=H, R2= (tert-butyl); R1=R2=O (2,6-diphenylphenoxy, Ph/Ph)		Zn (**9**)	[101]
		Zn (**10**)	
R1=H, R2= (tert-butyl); R1=R2=O (2,6-diphenylphenoxy, Ph/Ph)		Zn (**11**)	[101]
		Zn (**12**)	
R1=R2= H		Zn (**13**)	[102]
R1=H, R2=O—C6H4—(tert-butyl)		Zn (**14**)	[102]
		Zn (**15**)	[**103**]

	Zn (**16**)	[104]
	Zn (**17**)	[104]
	Co (**18**)	[105]
	Zn (**19**), H$_2$ (**20**)	[106]
	Zn (**21**), H$_2$ (**22**) Mg (**23**)	[107] [108]

	Zn (**24**), H₂ (**25**)	[107]
	Mg (**26**)	[108]
	Mg (**27**) , Zn (**28**), H₂ (**29**)	[109]
	Zn (**30**)	[110]
	Zn (**32**)	[110, 111]

	Zn (**33**)	[112]
	Zn (**34**)	[113]
SH protected with OCCH₃	H₂ (**35**)	[114]

R =	(36)	[115]
	(37)	
	(38)	
	(39)	
	(40)	[116]
	(41)	[117]
	(42)	[116]
 n = 1, R1 = R2 = H n = 2, R1 = R2 = H n = 2, R1 = Cl, R2 = H n = 2, R1 = OMe, R2 = H n = 2, R1 = R2 = OMe	(43) (44) (45) (46) (47)	[118]
	(48)	[97]

The aim of this thesis was to synthesize low symmetry phthalocyanine complexes with only one carboxylic functional group to be conjugated to amine functionalized metal nanoparticles via amide bond linkages. A number of low symmetrically substituted phthalocyanines with only one carboxylic group have been reported in literature [98-111], Table 1.1. Various substituents at the peripheral position in

conjunction with the monocarboxyl group were incorporated into the phthalocyanine ring to enhance solubility of the ring systems. As Table 1.1 shows, mainly ZnPc derivatives have been reported containing monocarboxyl, while there are no reports on Si, Ti and Ge, thus the synthesis of low symmetry (with monocarboxy) phthalocyanines containing of Sn(IV), Ti(IV) and Ge(IV) is presented in this thesis. The synthesis of low symmetry phthalocyanines consisting of a cysteinyl moiety with both carboxylic and amino groups is reported for the first time in this thesis. The complexes were designed for the dual purpose of using either the carboxy or the amino group on the surface of the nanoparticles to form a conjugate. As Table 1.1 shows, there are very few Pcs containing RSH groups [112-114] due to the difficulties encountered during synthesis, as discussed above. Silanols have probably been the most successful of the silicon phthalocyanines used in photodynamic therapy (PDT) [97]. Many axially ligated silicon phthalocyanine derivatives have been reported but not containing RSH groups [115-118]. This work therefore employs SiPcs axially ligated with RSH groups for attachment to NPs. This complex is reported for the first time, in this thesis.

Phthalocyanines synthesized in this thesis are shown in Table 1.2. The complexes are:

Tris {9 (10), 16 (17), 23 (24)-[(4-phenoxy)-2-(4-cysteinyl)] phthalocyaninato} Zn, Ge(OH)$_2$, TiO and Sn(OH)$_2$ (abbreviated as ZnMCsPc (**49**), (OH)$_2$SnMCsPc (**50**), (OH)$_2$GeMCsPc (**51**), OTiMCsPc (**52**))

Hexakis {9; 10, 16; 17, 23; 24 – [1,2-bis-(diethylaminoethylthiol)]-2-(4-phenoxycarboxy) phthalocyaninato} Zn , Ge(OH)$_2$, TiO, and Sn(OH)$_2$ (abbreviated as ZnMPCPc (**53**), (OH)$_2$SnMPCPc (**54**), (OH)$_2$GeMPCPc (**55**), OTiMPCPc (**56**)).

Tris {9 (10), 16 (17), 23 (24)-[4-(2-diethylaminoethanethiol)-2-(4-carboxy)] phthalocyaninato} Zn, Ge(OH)$_2$, TiO, and Sn(ac)$_2$. [Abbreviated as ZnMCPc (**57**), (ac)$_2$SnMCPc (**58**), (OH)$_2$GeMCPc (**59**), OTiMCPc (**60**) and bis-(1,6-hexane dithiol) SiPc (abbreviated as SiHDTPc (**61**)].

Amino, carboxylic and thiol functional groups are good stabilizers for numerous metal nanoparticles [119-127], hence our interest in this thesis. The remaining substituents are used for increased solubility, their ability to shift the Q band to the red of absorption spectra (required for PDT), and the sulphur and nitrogen atoms which are capable of co-ordination to Au and Ag NPs.

Table 1.2: List of phthalocyanine complexes synthesized and used in this thesis

Chemical structure	metal
	Zn (**49**) (OH)$_2$Sn (**50**) (OH)$_2$Ge (**51**) OTi (**52**)
	Zn (**53**) (OH)$_2$Sn (**54**) (OH)$_2$Ge (**55**) OTi (**56**)
	Zn (**57**) (Ac)$_2$Sn (**58**) (OH)$_2$Ge (**59**) OTi (**60**)

| | Si (**61**) |
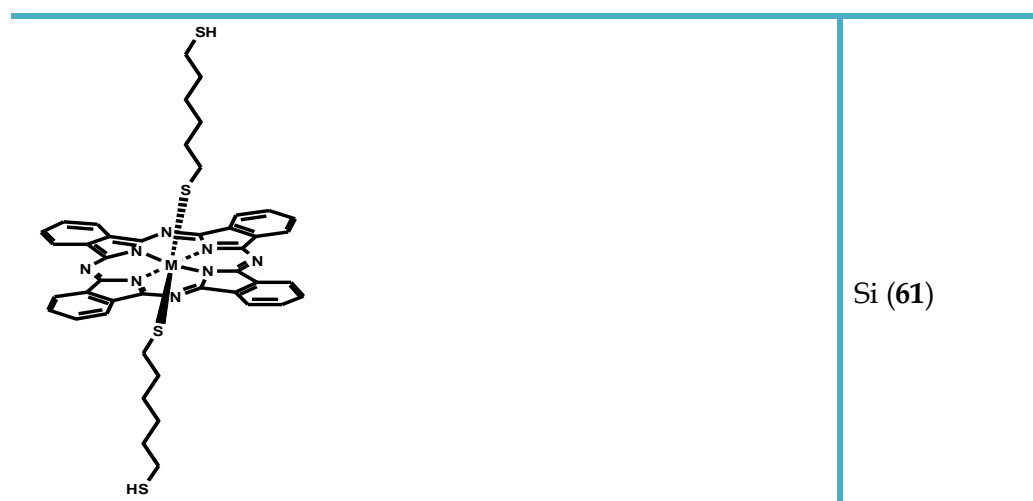
1.1.6   Electronic absorption spectra of phthalocyanines

Phthalocyanines are known to have high molar extinction coefficients, in the order 10^5 M^{-1}.cm^{-1} [17]. Their spectra are characterized by two main distinct absorption bands that arise as a result of π-π* transitions within the delocalized 18π electron system of the ring Fig. 1.3.
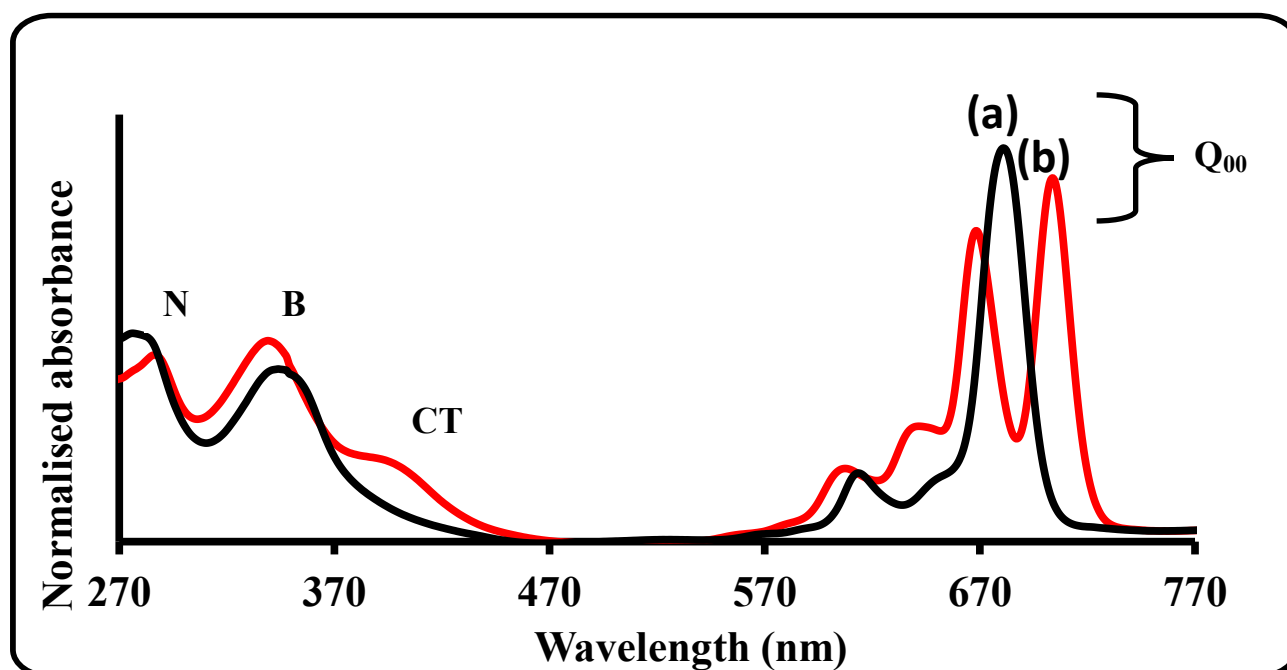
Figure 1.3: Ground state absorption spectra of metallated ((a) black) and unmetallated ((b) red) Pc

Fig. 1.3 shows a significant difference between the absorption spectra of metallated (**a**) and unmetallated (**b**) Pcs. There is a split in the Q-band in the absorption spectrum of the unmetallated phthalocyanine due to its D_{2h} symmetry, as a result of the presence of the two protons at the core of the ring. The lowest unoccupied molecular orbital (LUMO) is non-degenerate (Fig 1.4) for H_2Pc giving rise to two allowed electronic transitions of different energy levels. The metallated Pc show an unsplit Q-band since there is only one allowed transition, due to the inherent D_{4h} symmetry, and the degenerate nature of the LUMO.
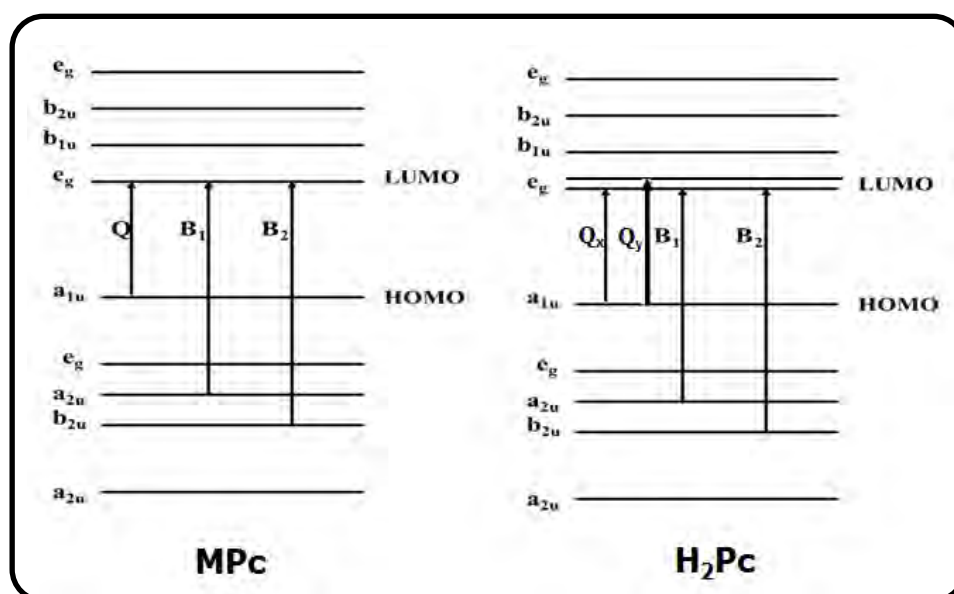
Figure 1.4: Electronic transitions in phthalocyanine complexes that results in Q and B bands

The highly intense band that is observed towards the near infrared region of the spectrum is known as the Q-band (Q_{00}) and it is due to transitions taking place from the a_{1u} of the highest occupied molecular orbital (HOMO) to the e_g of the LUMO, Fig.1.4. The second band, of lower intensity, observed in the region between 300 to 400 nm is known as the B-band (or Soret band) and it is a superimposition of B_1 and B_2 bands [16, 17, 128]. There are also three bands that are normally observed towards

the UV region, the **N**, **L** and **C** bands, which are mainly observed when using transparent solvents. The charge transfer (**CT**) absorption bands Fig.1.3 are not commonly found in all phthalocyanine complexes, and these are only observed when the metal d-orbitals lie within the HOMO-LUMO gap Fig. 1.4 [129,130]. They can be assigned either to the metal to ligand (MLCT) or ligand to metal charge (LMCT) transfers.
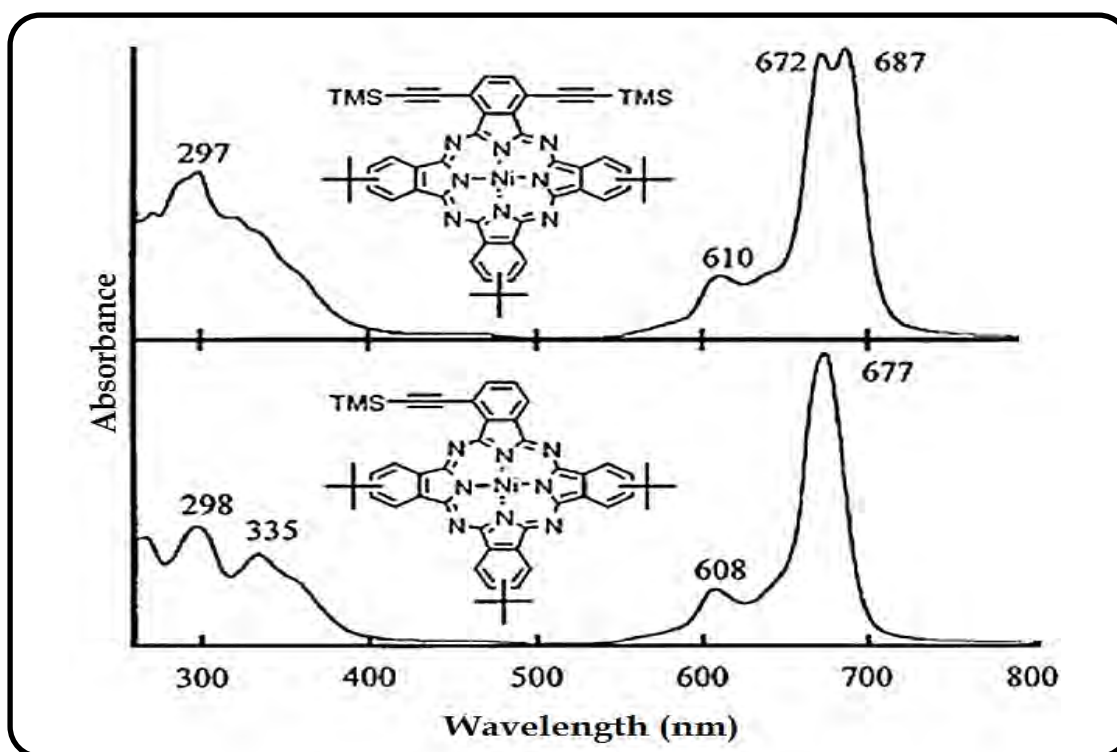
Figure 1.5: UV-vis absorption spectra of Ni(II)2α-trimethylsilylethynylPc and Ni(II)1α-trimethylsilylethynylPc complexes [68, 131].

With low symmetry phthalocyanines, splitting and broadening of the Q-band is observed in numerous cases (Fig. 1.5). Kobayashi and co-workers have explained this behaviour in terms of differences in the electron donating or electron withdrawing behaviour of the substituents at the periphery [68, 131]. The splitting of the Q-band strongly depends on the position of substitution, whether it is β or α

substituted. To date, the optical properties of low symmetry phthalocyanine have not been fully exploited and hence there is no clear trend in terms of the splitting observed in the Q-band.

1.1.7   Aggregation of phthalocyanines
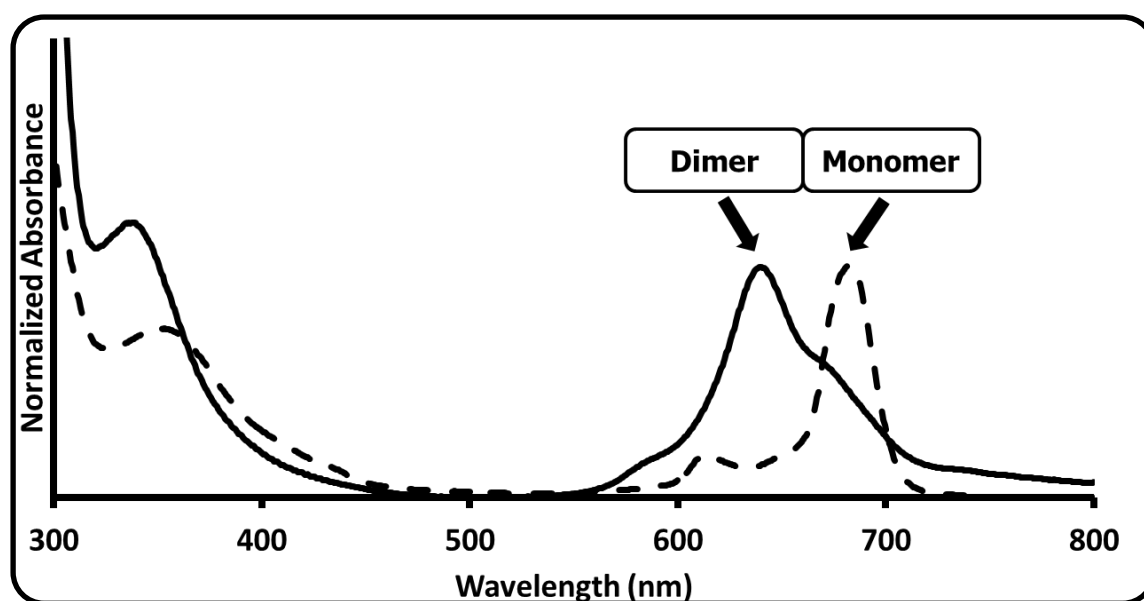
Figure 1.6: Absorption spectra of a typical aggregated phthalocyanine; before (solid line) and after addition of a surfactant (dotted line)

Aggregation in phthalocyanines generally occurs as a result of the co-planar association of phthalocyanine rings progressing from a monomer (lower energy) to a dimer (near 630 nm) and higher order aggregates (at high energy) [132-135]. This may be due to highly concentrated MPc solutions, which brings the neighbouring MPc rings into close proximity. Fig.1.6 shows absorption spectra of an aggregated phthalocyanine in water (solid line) and in the presence of a surfactant (dotted line). It is observed that in the presence of a surfactant there is almost a complete collapse in the band due to aggregates (dimer), while the band due to the monomer is more pronounced.
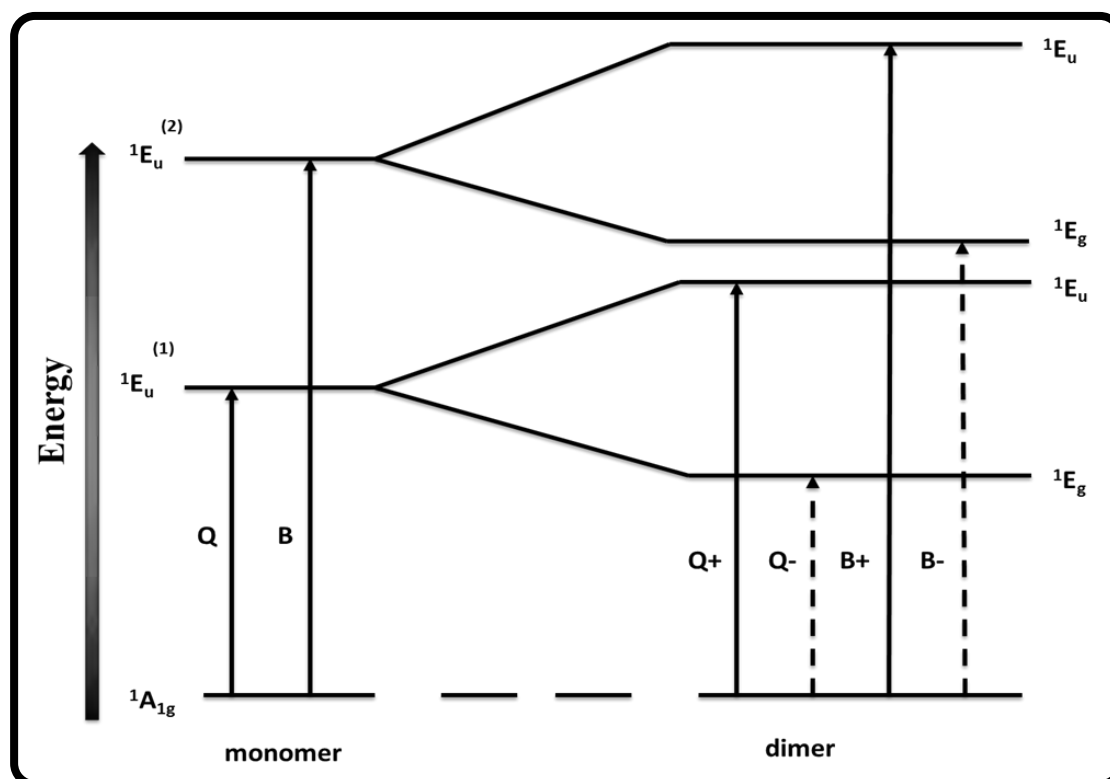
Figure 1.7: Energy diagram showing the split in energy levels of the LUMO upon aggregation

Aggregation in Pcs can also be due to the formation of metal bridges using a ligand [136-139]. According to the exciton coupling theory [138, 139], Fig. 1.7, when two adjacent MPc complexes interact there is an appearance of four degenerate states leading to broadening of spectra showing that aggregates have been formed. The four degenerate states arise from the splitting of ^1E_u excited states, resulting in a pair of symmetry allowed transitions (solid arrows) and a pair of symmetry forbidden transitions (dotted arrows). The transitions that are symmetry forbidden will still occur to a small extent, resulting in the spectral behaviour shown in Fig. 1.6, which is either broadening of the spectra, or complete splitting of the Q-band and finally shift in the Q-band to higher energies. The nature of a solvent also plays a huge role in aggregation of Pc complexes. Aggregation is more highly pronounced in polar

solvents than in non-polar solvents. When polar solvents are used there are stronger

interactions that occur between the Pc rings.

1.2 Photophysical and photochemical parameters

1.2.1 Photophysical parameters
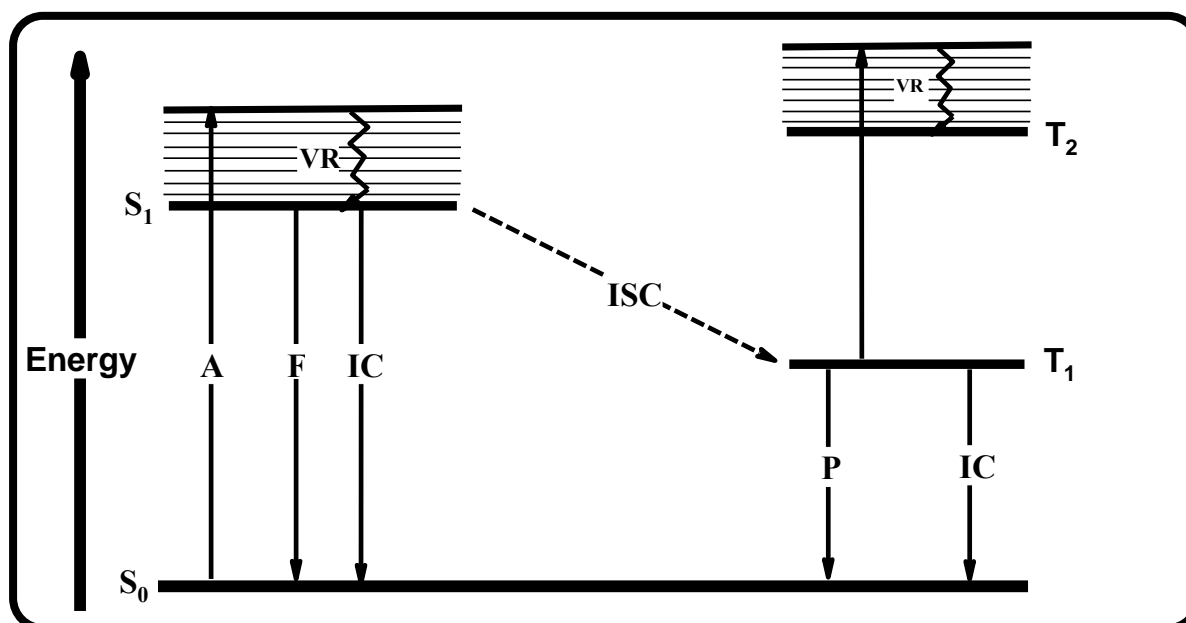
Figure 1.8: The Jablonski diagram displaying transitions of a molecule from its lower energy ground state to its higher energy excited state following irradiation with light; A = absorption, VR = vibrational relaxation, ISC = intersystem crossing, F = fluorescence, IC = internal conversion, P = phosphorescence, S_0 = singlet ground state, S_1 = singlet excited state and T_1 = 1st excited triplet excited state, T_2 = second excited triplet state.

The photophysical and photochemical behaviour of phthalocyanines can be simply

explained by the Jablonski diagram Fig. 1.8 [140].

When a molecule absorbs light (**A**) its electrons are excited causing the overall

excitation of the molecule from its lower energy singlet ground state (**S_0**) to a higher

vibronic energy level of the first singlet excited state (S_1). The molecule will then lose energy from the higher vibronic level through some vibrational relaxation processes (**VR**) to a lower vibronic energy level. From the lowest vibronic level of (S_1), the molecule can undergo (i) fluorescence (**F**) to the ground state (S_0), (ii) give off energy by non-radiative release of heat to its surroundings through internal conversion (**IC**) or, (iii) undergo intersystem crossing (**ISC**) to the 1st excited triplet state energy level (T_1). The change in multiplicity taking place in **ISC** is spin-forbidden according to the selection rules, though it still occurs to some extent as a result of the spin-orbit coupling (SOC). Paramagnetic compounds or atoms with high nuclear charge (heavy atoms) such as indium [141, 142] enhance **ISC** in phthalocyanines. From the triplet state the molecules will still lose energy via **IC** or emit light through the process of phosphorescence (**P**). When the ground state molecular oxygen is present in the system, the Pc molecule can transfer its energy to ground state molecular oxygen to produce singlet oxygen through photosensitization.

1.2.1.1 Fluorescence quantum yields and lifetimes

Fig. 1.9 displays the typical absorption, fluorescence emission and excitation spectra obtained for an MPc complex. The fluorescence of MPcs is observed at longer wavelengths compared to the absorption spectrum and is a mirror image of the absorption spectrum for non-aggregated complexes. The fluorescence excitation is identical to the absorption spectrum for non-aggregated Pcs [143]. For aggregated complexes the absorbance is observed as non-mirror image to the fluorescence emission spectra because dimers are known to be non-photoactive [144].
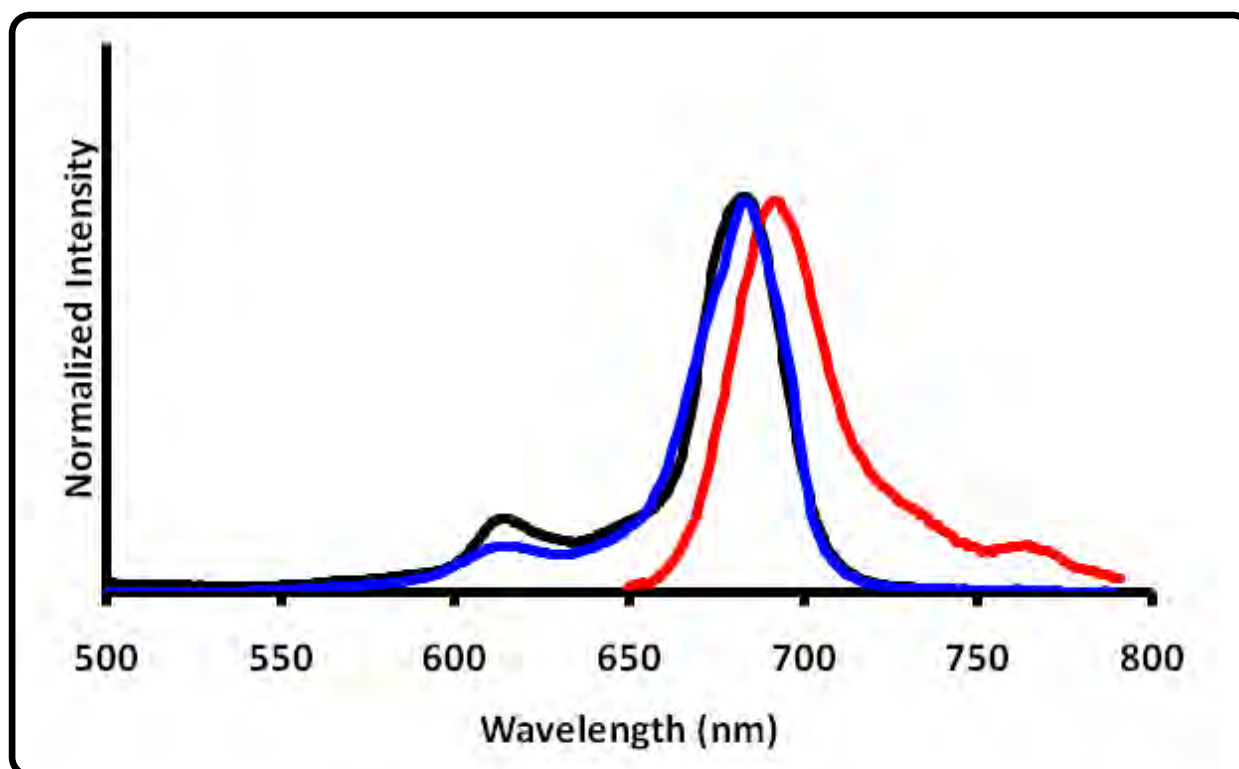
Figure 1.9: The typical ground state electronic absorption (black line), fluorescence excitation (blue line) and emission (red line) of an MPc

Stoke's shifts in MPc complexes are estimated by calculating the distance between the Q-band absorption spectrum and the fluorescence spectrum maxima, provided the molecule has exactly the same absorbance maxima to the excitation spectrum. Stoke's shifts of less than 10 nm are generally observed for Pc complexes, however this value can be affected significantly by the rigidity of the environment, solvent polarity or viscosity and temperature.

Fluorescence quantum yields and lifetimes are photophysical properties that determine and quantify the efficiency of light emission by a molecule. For phthalocyanine complexes the fluorescence quantum yields and lifetimes can vary

greatly depending on the nature of substituents, central metal, refractive indices of the solvents, pH used and temperature [145].

The fluorescence quantum yield (Φ_F) can be generally defined as the number of photons emitted relative to the number of photons absorbed and this is illustrated in Equation 1.1.

$$\Phi_F = \frac{\textit{No. of emitted photons}}{\textit{No. of absorbed photons}} \qquad 1.1$$

Fluorescence quantum yields (Φ_F) may be determined by comparative methods [146, 147] using the fluorescence quantum yield of a known Pc as a standard. In this work ZnPc in DMSO has been used (Φ_F) = 0.20 [148]. The quantum yield of fluorescence is then calculated according to Equation 1.2.

$$\Phi_F = \Phi_F^{std}\, \frac{F.A_{std}.n^2}{F_{std}.A.n_{std}^2} \qquad 1.2$$

where F and F_{Std} are the areas under the fluorescence curves of the MPc derivatives and the standard used. A and A_{Std} are the absorbances of the sample and reference at the excitation wavelength, and n and n_{Std} are the refractive indices of solvents used for the sample and standard, respectively.

Fluorescence lifetimes are usually performed in either the frequency [149-151] or time domains [152, 153], although other techniques involving multi-pulse measurements have also been demonstrated [154]. Time domain measurements are more commonly used. The equipment used for time-domain measurements is based

on gating the fluorescence signal using either time-correlated single-photon counting (TCSPC) techniques [151, 155] (Fig. 1.10) or gated image intensifiers [152]. Fluorescence lifetime determinations can also be made using the absorbance and emission spectra of MPcs [156-158] which is based on application of the Strickler-Berg equation [159].

In this thesis, the time–correlated single photon counting technique (TCSPC) is used [151, 155].
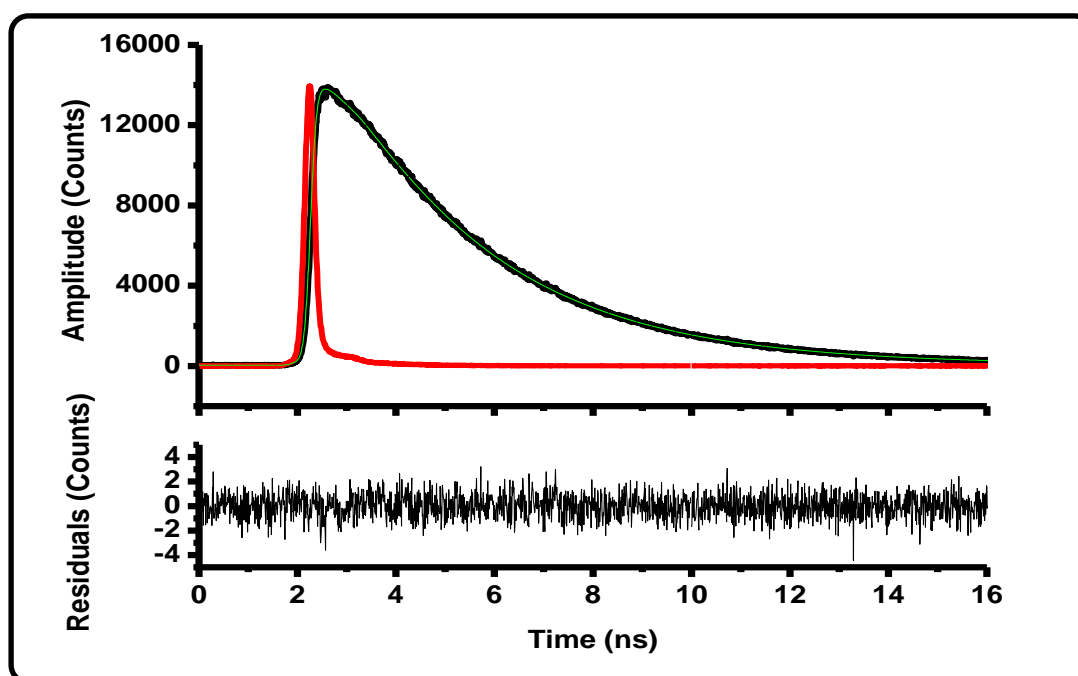
Figure 1.10: Photoluminescence decay curve of a typical MPc in solution

Fluorescence lifetimes for MPc complexes are short, with a typical time scale of the order of picoseconds (ps, 10^{-12}) to nanoseconds (ns, 10^{-9}) [145, 160].

1.2.1.2 Triplet state quantum yields and lifetimes

The triplet quantum yields can be defined as the ability of a photosensitizer to populate the first excited triplet state (T_1). The excited state of a photosensitizer can be studied using a technique known as laser flash photolysis. This technique provides information on the molecules that are undergoing intersystem crossing (ISC) to the triplet state. The triplet-triplet absorption from T_1 to a higher energy state T_n, Fig. 1.8, is monitored [161]. A triplet decay curve from the laser flash photolysis experiment is obtained as a plot of change in absorbance (ΔA) versus time in seconds, Fig. 1.11. From the triplet decay curve in Fig. 1.11, lifetimes of the triplet state may be obtained. For most Pcs the triplet-triplet absorption is observed in the region of approximately 500 nm.
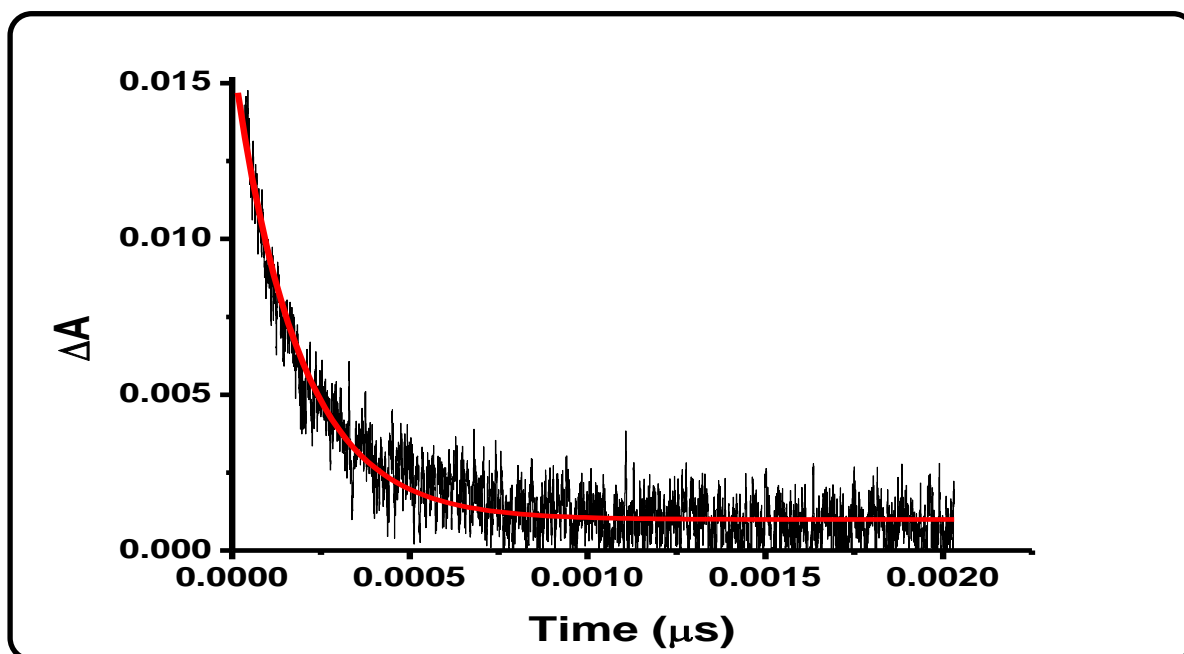
Figure 1.11: A typical triplet decay curve of an MPc following laser flash photolysis

The triplet lifetimes (τ_T) of the transients are conveniently determined by using a software program such as Origin Pro 8 to the triplet decay curve (red line shows fitting), as shown in Fig. 1.11.

The triplet quantum yield (Φ_T) can be determined using comparative methods [162], which involves the use of a known triplet yield (Φ_T) of a standard. Triplet yields are then calculated using Equation 1.3

$$\Phi_T = \Phi_T^{std} \frac{\Delta A_T . \varepsilon_T^{std}}{\Delta A_T^{std} . \varepsilon_T}$$

1.3

where ΔA_T and ΔA_T^{std} are the changes in triplet state absorbance of a Pc molecule and the standard respectively. ε_T and ε_T^{std} are the triplet state molar extinction coefficients for the Pc molecule and the standard, respectively. Φ_T^{std} is the triplet quantum yield of the standard. The values of ε_T and ε_T^{std} are normally determined by use of the singlet depletion method [163], using Equations 1.4 and 1.5.

$$\varepsilon_T = \varepsilon_S \frac{\Delta A_T}{\Delta A_S}$$

1.4

$$\varepsilon_T^{Std} = \varepsilon_S^{Std} \frac{\Delta A_T^{Std}}{\Delta A_S^{Std}}$$

1.5

this involves the use of the change in absorbance of the ground singlet states of both the sample (ΔA_S) and the standard (ΔA_S^{Std}), the changes in the triplet state absorptions of the sample (ΔA_T) and the standard (ΔA_T^{Std}) and the molar extinction

coefficients of their singlet ground state for both the sample (ε_S)and the standard (ε_S^{Std}).

Assuming no energy loss by internal conversion, the triplet state yield and fluorescence are two complementary photophysical processes and they should sum up to one. It is expected that high triplet state quantum yield (Φ_T) values are accompanied by low fluorescence yields (Φ_F) and vice versa.

1.2.2 Singlet oxygen quantum yields

The ability of a photosensitizer to absorb light and produce cytotoxic singlet oxygen serves as a selective tool for photodynamic therapeutic applications.
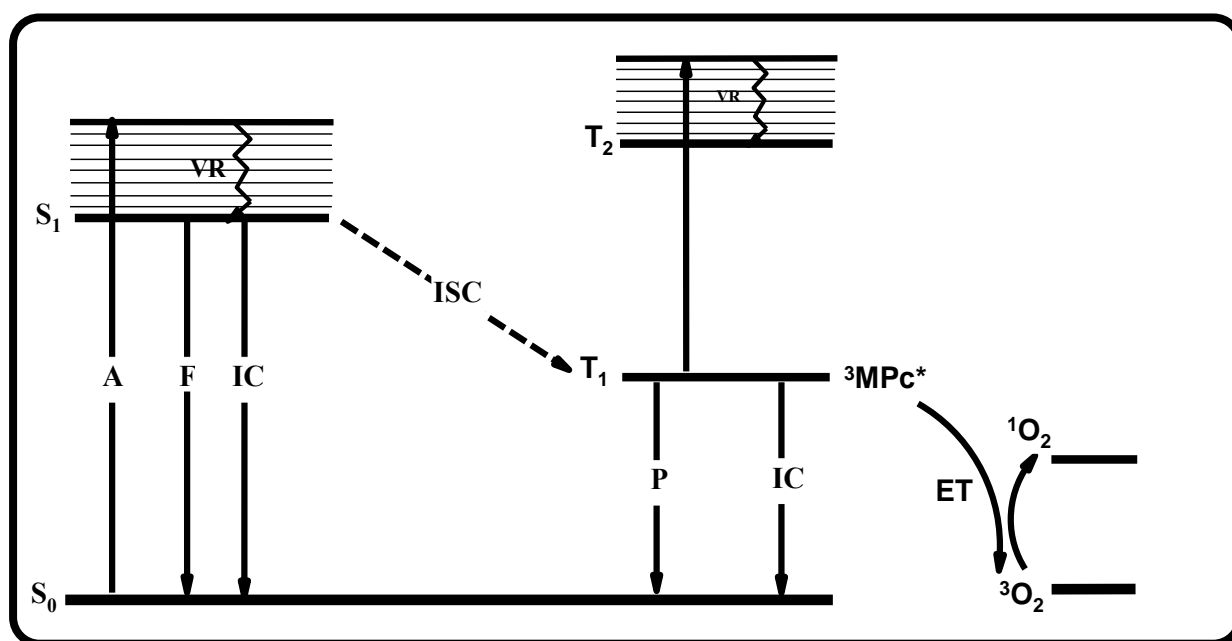
Figure 1.12: **The Jablonski diagram displaying energy transfer (ET) from an excited photosensitizer (^{3}MPc*) to ground state molecular oxygen (^{3}O$_2$) leading to the production of singlet oxygen (^{1}O$_2$)**

The process of photosensitization is shown in Fig. 1.12. The excited triplet state molecule (^{3}**MPc***) transfers its energy to ground state triplet molecular oxygen (^{3}**O$_2$**),

since the energy of the triplet state molecule (^{3}**MPc***) is higher (~110 – 126 kJ mol^{-1}) than the energy required (~94 kJ mol^{-1}) for the excitation of ground state molecular oxygen [164, 165] to form excited singlet oxygen (^{1}**O$_2$**).

$$\text{MPc (ground state)} \xrightarrow{h\nu} \; ^1\text{MPc* (singlet excited sate)} \longrightarrow \; ^3\text{MPc* (triplet excited state)}$$

$$^3\text{MPc* (triplet excited state)} + \; ^3\text{O}_2\,(^3\Sigma_g) \longrightarrow \text{MPc (ground state)} + \; ^1\text{O}_2\,(^1\Delta_g)$$

$$^1\text{O}_2\,(^1\Delta_g) + \text{Substrate} \longrightarrow \text{Substrate}_{(ox)}$$
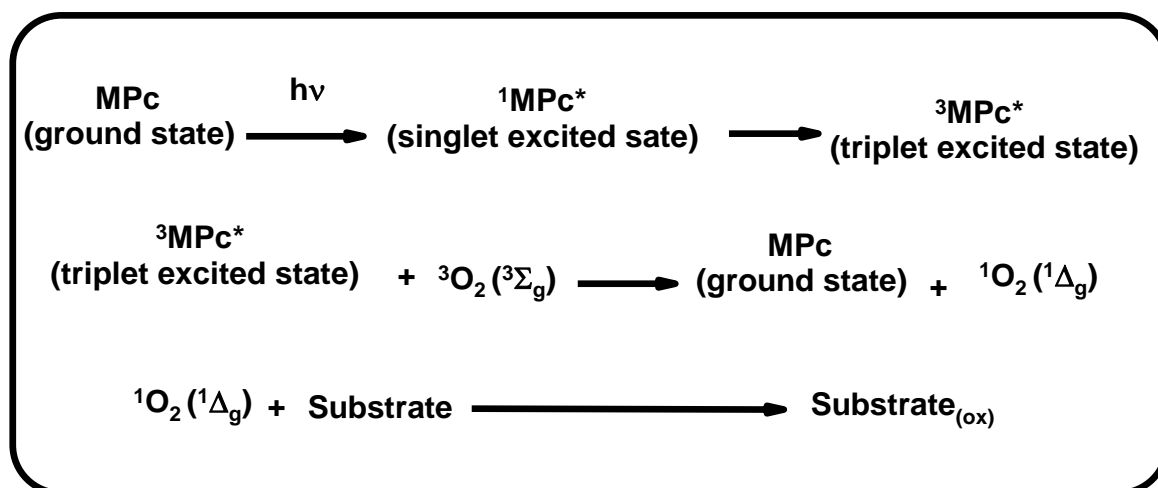
Scheme 1.3: Type II mechanism for the photoreaction of MPc leading to the production singlet oxygen

The mechanisms involved in the singlet oxygen generation process includes the Type II mechanism, Scheme 1.3 [166]. There are other mechanisms through which the photosensitization process could occur, these may be either via the Type I or Type III processes. Type I mechanisms involve free radicals [167], while in Type III, electron transfer from the substrate to the excited state sensitizer may occur [168]. The involvement of the Type II mechanism is widespread in oxygen-rich and air saturated environments where the oxygen concentration is very high. It is believed that the Type II mechanism is a dominant singlet oxygen production pathway in photosensitization reactions.

Experimentally, singlet oxygen quantum yields of phthalocyanines can be determined using optical or chemical methods [169]. The chemical method requires a suitable singlet oxygen sensitive compound (quencher) that can react quickly with

the singlet oxygen in a 1:1 ratio without any side reactions. It is expected that the decomposition product of the quencher should neither react with the singlet oxygen nor interfere with the monitoring process. The chemical method does not require extensive and expensive instrumentation, thus it is used in this thesis. The experiment is usually carried out by irradiating a sample solution containing the phthalocyanine, oxygen and the quencher. The degradation of the quencher is usually monitored spectrocoscopically [170, 171]. The most common chemical quencher in organic solvents is 1,3-diphenylisobenzofuran (DPBF). However, other furans as well as derivatives of anthracene, guanine and bilirubin have been used [170, 172, 173]. In water, the commonly used chemical quencher is anthracene-9,10-bis-methylmalonate (ADMA).

The singlet oxygen quantum yields (Φ_Δ) of the phthalocyanines can then be calculated using a comparative method based on Equation 1.6

$$\Phi_\Delta = \Phi_\Delta^{Std} \cdot \frac{R I_{abs}^{Std}}{R^{Std} I_{abs}} \qquad\qquad 1.6$$

where Φ_Δ^{Std} is the singlet oxygen quantum yield of a known standard, R and R^{Std} are the singlet oxygen quencher photobleaching rates in the presence of the respective MPcs under investigation and of the standard respectively. I_{abs} and I_{abs}^{Std} are the rates of light absorption by the MPcs and the standard, respectively.

Alternatively, absolute methods based on Equation 1.7 can be used.

$$\Phi_{quencher} = \frac{(C_0 - C_t)V_R}{I_{abs}.t}$$

1.7

where C_0 and C_t are the concentrations of the chemical quencher prior to and after irradiation, respectively; V_R is the solution volume; t is the irradiation time per cycle and I_{abs} is defined by Equation 1.8:

$$I_{abs} = \frac{\alpha.A.I}{N_A}$$

1.8

where $\alpha = 1 - 10^{-A(\lambda)}$, $A(\lambda)$ is the absorbance of the sensitizer at the irradiation wavelength, A is the irradiated area, I is the intensity of light expressed as photons cm^{-2} s^{-1}) and N_A is Avogadro's constant. The singlet oxygen quantum yields Φ_Δ can then be calculated using equation 1.9 [174].

$$\frac{1}{\Phi_{quencher}} = \frac{1}{\Phi_\Delta} + \frac{1}{\Phi_\Delta}.\frac{k_d}{k_a}.\frac{1}{[quencher]}$$

1.9

where k_d is the decay constant of singlet oxygen in respective solvent and k_a is the rate constant of the reaction of the quencher with $O_2(^1\Delta_g)$. The intercept obtained from the plot of $1/\Phi_{quencher}$ versus $1/[quencher]$ gives $1/\Phi_\Delta$.

Photophysical and photochemical data on low symmetry phthalocyanine complexes are scarce, as shown in Table 1.3 [99, 98, 103, 107-109, 117, 118, 175-177].

Table 1.3: Some photophysical and photochemical properties of phthalocyanines of interest in this thesis

Compound	Solvent	ϕ_T	ϕ_Δ	ϕ_F	τ_F	τ_T	reference
(2)	DMSO	0.35	-	0.23	4.95	140	[99]
(3)	DMSO	0.40	-	0.11	4.70	110	
(4)	DMSO	0.37	-	0.10	3.57	110	
(5)	H_2O	0.29	-	0.01	2.22	50	
	H_2O Triton X	0.31	-	0.07	4.16	70	
(1)	DMF	0.68	0.63	0.25	-	8	[98]
	DMSO	0.82	0.64	0.16	-	230	
	Chloroform	-	0.49	-	-	5	
	THF	-	0.62	-	-	5	
(34)	Ethanol	-	0.45	-	2.1;1.11	-	[175]
(35)	Toluene	-	-	-	4.99	-	[176]
(22)	THF	0.63	0.55	0.16	2.4	320	[107]
(21)	THF	0.71	0.60	0.10	2.3	360	[108]
(23)	THF	0.56	0.45	0.23	5.1	260	
(25)	THF	0.66	0.56	0.05	2.5	320	
(24)	THF	0.75	0.62	0.12	2.5	450	
(26)	THF	0.65	0.58	0.21	5.2	360	
(29)	DMSO	0.62	-	0.09	2.8;1.2	150	[109]
(28)	DMSO	0.74	-	0.20	2.7	240	
	Methanol	-	-	0.01	2.9	-	
(27)	DMSO	0.49	-	0.52	5.1	275	
	Methanol	-	-	0.55	5.3	20	
(15)	DMSO	-	0.73	0.17	2.7	-	[103]
(41)	DMF	-	0.04	0.03	2.54	-	[117]
(48)	Methanol	-	0.366	-	-	-	[177]
(43)	DMF	-	0.06	0.04	-	-	[118]
	+HCl	-	0.34	0.30	-	-	
(44)	DMF	-	0.03	0.01	-	-	
	+HCl	-	0.38	0.28	-	-	
(45)	DMF	-	0.07	0.01	-	-	
	+HCl	-	0.65	0.30	-	-	
(46)	DMF	-	0.04	0.01	-	-	
	+HCl	-	0.36	0.29	-	-	
(47)	DMF	-	0.06	0.02	-	-	
	+HCl	-	0.47	0.26	-	-	

It has been reported that reducing the symmetry on the phthalocyanine macrocycle can improve their photophysical and photochemical behaviour [178], thus our interest in these type of complexes in this thesis, in addition to their co-ordination to NPs.

1.3   Nanoparticles

At the dawn of the 21st century, the area of nanoscience and nanotechnology became a versatile platform for modern research at the interface of chemistry, physics, materials and the biomedical sciences [179, 180].

1.3.1 Metal nanoparticles (MNPs)

Particles with sizes in the range of 1–100 nm are called nanoparticles (NPs). They are intermediate in size between individual atoms and bulk material.

NPs are divided into metallic, non-metallic, semiconductor and organic NPs. They have unique characteristics mostly due to their high surface-to-volume ratio. Metallic NPs are good representatives of NPs, possessing unique optical, electronic, chemical and magnetic properties that are extraordinarily different from those of the individual atoms and their bulk counterparts [181, 182].

Metal nanoparticles have been of great interest for decades due to the novel properties associated with their reduced dimensions and have found wide range of applications in areas such as catalysis [183, 184], electronics [185, 186], photonics [187], optoelectronics [188], information technology [189], sensing [190–192], and medicine [193–195].

1.3.1.1 Properties and applications of gold (AuNPs) and silver (AgNPs) nanoparticles

Solutions of liquid gold were first mentioned in Africa and Asia, by Egyptian and Chinese authors around the 5th century BC. In fact Ancients believed in their metaphysical and healing powers [196].

Colloidal gold and silver have been used since Ancient Roman times to colour glasses with intense shades of yellow, red and orange, depending on the concentration of the two metals. The famous Lycurgus Cup in the British Museum, dated 4th century AD [197], was made of gold colloids. In the middle ages, gold colloids were used in medicine [196], with many other ancient civilizations developing gold NPs for various applications [198-201].

Gold and silver NPs are at the forefront of the nanotechnology research because of their wide range of applications in areas such as catalysis [202], nano-electronics [203], medical diagnostics and biological imaging [204]. Ease of chemical synthesis and minimal toxicity as compared to some other nanomaterials is an attractive advantage of the Au and Ag NPs [205].

Gold nanoparticles have had a profound impact on a variety of scientific disciplines such as catalysis [206], drug activity enhancement [207], DNA detection and disease diagnosis [208], surface-enhanced plasmon sensing [209], and for the construction of nano devices such as light emitting diodes and solar cells [210].
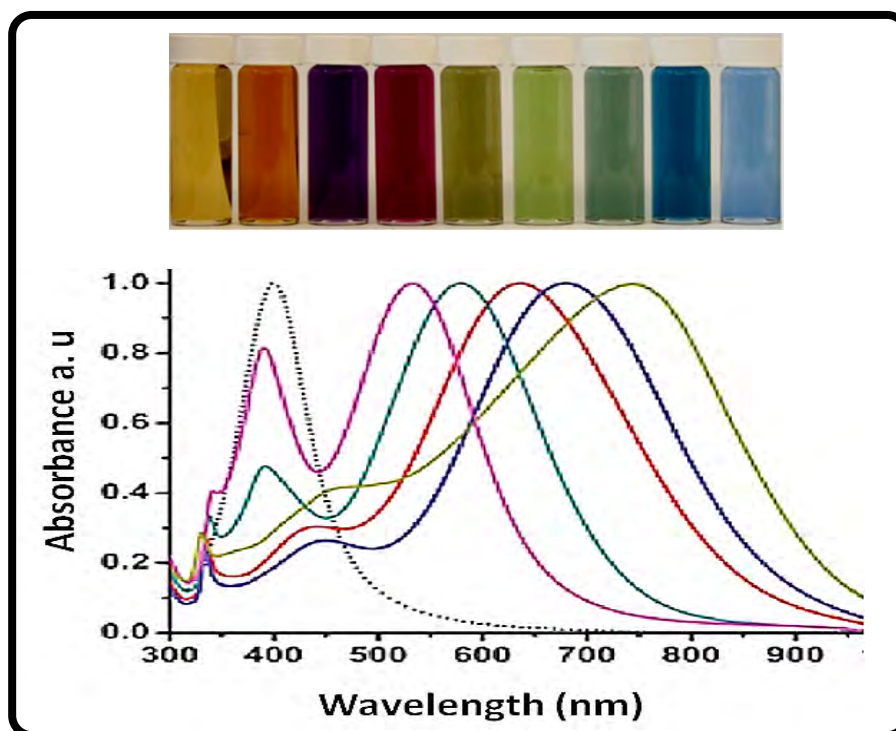
Figure 1.13: UV-vis absorption spectra of various sizes of AgNPs prepared using various conditions [213]. Insert different colours for the AgNPs solution.

The optical properties of silver and gold nanoparticles are tuneable throughout the visible and near-infrared region of the electromagnetic spectrum as a function of nanoparticle size, shape, aggregation states and local environment [119-127, 211-214]. The absorption bands result when the incident photon frequency is resonant with the collective oscillations free electrons of the conduction band, and this is known as the localized surface plasmon resonance (SPR) [215, 216].
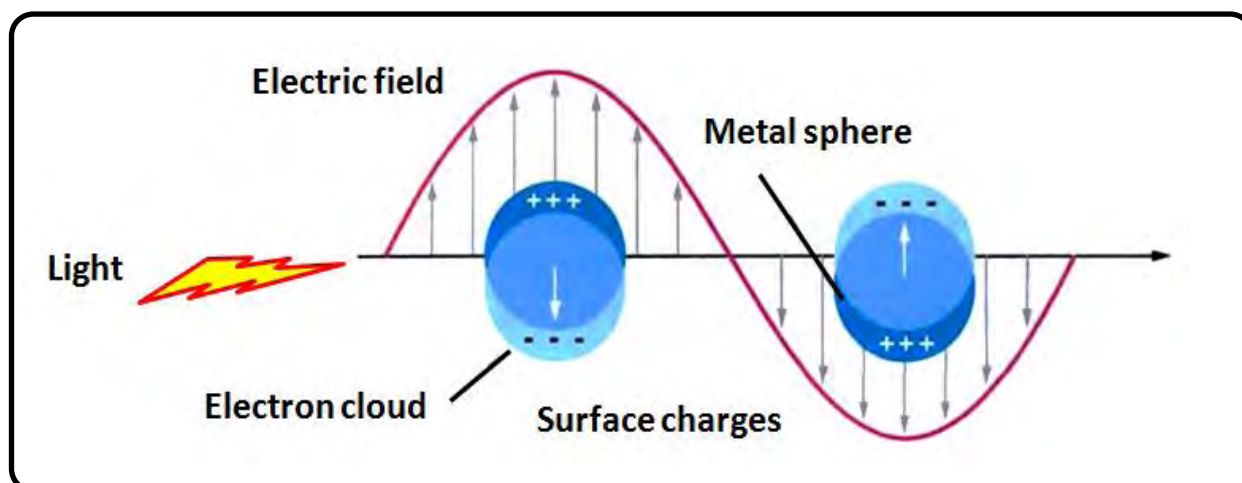
Figure 1.14: Surface-plasmon resonance (SPR) of spherical metal nanoparticle [215, 216]. A dipole is induced and oscillates in phase with the electric field of the incoming light.

Fig. 1.14 shows surface-plasmon oscillation [215, 216] for metallic NPs. The electric field of an incoming light wave induces polarization of the free electrons with respect to the much heavier ionic core of a spherical NP. The positive charges in the NP are assumed to be immobile and the negative charges move under the influence of external fields. Displacement of the negative charges from the positive occurs when the metallic NP is placed in an electric field. This results in a net charge difference at the NP boundaries, giving rise to a linear force to restore the system. As a consequence, a dipolar oscillation of the electrons is created and is known as the surface-plasmon oscillation. The collective oscillation of the electrons is also sometimes denoted as the dipole-particle plasmon resonance to differentiate between the plasmon excitations that occur in bulk-metal surfaces. SPR is the coherent excitation of all the free electrons within the conduction band, leading to an in-phase oscillation [216].

1.3.1.2 Synthesis of gold and silver nanoparticles

Massive efforts have been directed at the methodologies employed in the synthesis of metal nanoparticles with well controlled sizes, shapes (Fig. 1.15), compositions, and surface chemistries, and tailored properties [119-127, 213]. Among these parameters, shape control represents one of the most powerful means to tune the properties of the nanoparticles over a broad range, leading to improvement in their performance in a number of applications.

A variety of instrumental techniques have been employed in the characterization of gold and silver nanoparticles. Due to different geometric structures and surface morphology, scanning electron microscopy (SEM) and transmission electron microscopy (TEM) has been extensively used to characterise these nanoparticles. Beautiful gold and silver NPs with different structural geometries have been synthesized and reported in literature [213, 217, 218]. The TEM and SEM images of some of the geometric structures obtained for AuNPs and AgNPs are presented in Fig. 1.15.
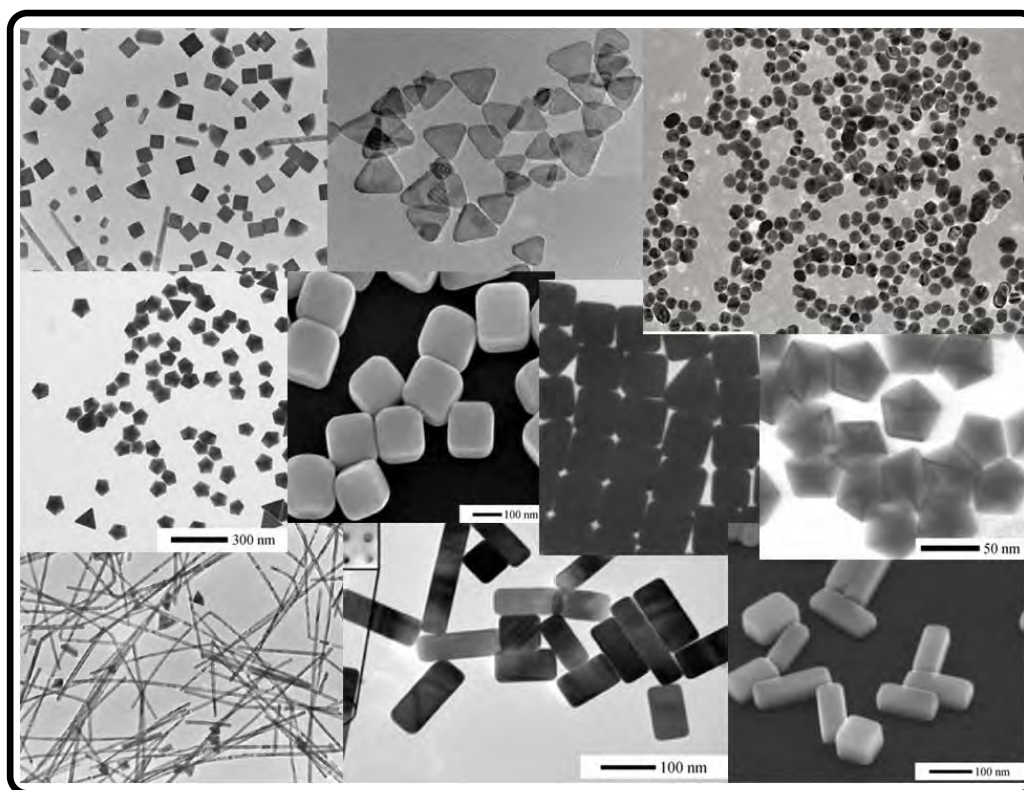
Figure 1.15: TEM and SEM images of various shapes of gold and silver nanoparticles [213, 217]

The different shapes of silver in particular have been believed to behave differently in antimicrobial inhibition of various bacterial growths [218]. Hence one of our interests in this thesis is to use the developed procedures to synthesize AgNPs with different shapes and investigate their antimicrobial activities in the presence of low symmetry phthalocyanines. Synthetic methodology has been much simplified by the pioneering work of Turkevich [219, 220] and Frens [221]. Many papers have been published on controlling the size and shape of nanoparticles in both organic and aqueous media [222]. Functionalization of gold nanoparticles with organic molecules has been carried out via phase transfer catalysis. SH, COOH and NH_2 functional groups of organic molecules are well known to bind to the surface of Au and Ag nanoparticles [213, 217, 223,], hence our interest in Pcs containing these functionalities in this thesis.
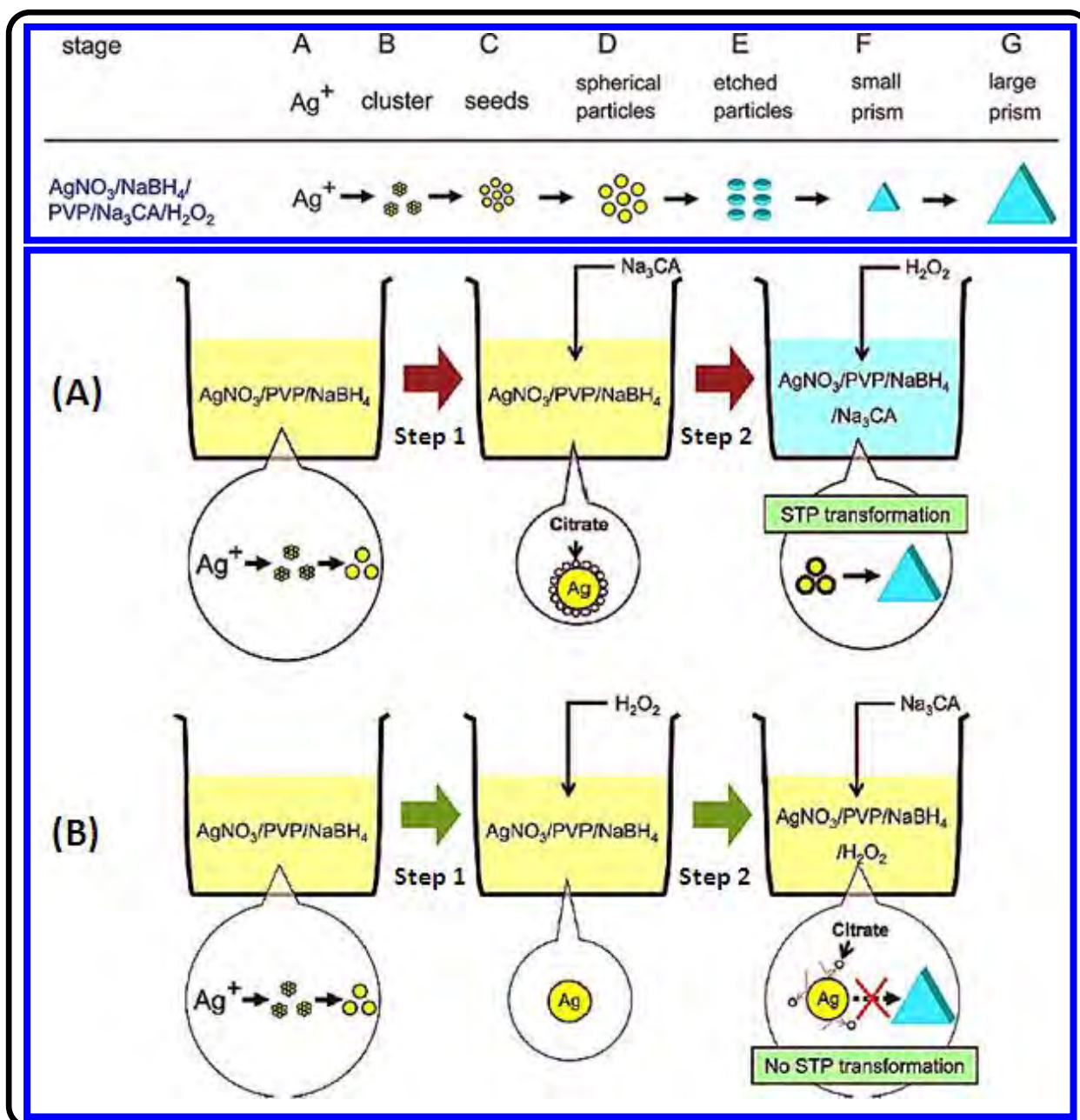
Figure 1.16: Mechanistic formation of various shapes of nanoparticles [217]. PVP = Polyvinylpyrrolidone, STP = Sphere to Prism Transformation

A useful way to make gold and silver nanocubes and nanoprisms of controllable aspect ratio, is through employing the seed-mediated growth method (Fig. 1.16). This method includes few a steps: growth of "seed" particles and growth of such seeds into prisms. When changing some crucial growth parameters in the seed-mediated growth, nanoparticles of shapes other than spheres can be easily achieved. This indicates that this method is a possible option for the synthesis of gold and

silver nanoparticles of other shapes. Polymers such as polyvinylpyrrolidone (PVP) are useful in dispersing the seed solution and allowing them to grow to large spherical nanoparticles, step 1 (Fig. 1.16 A), thus preventing aggregation into clusters. Prism shaped nanoparticles are then obtained by the selective oxidative etching with hydrogen peroxide (H_2O_2) of spherically shaped nanoparticles in the presence of sodium citrate (Na_3CA). This is referred to as sphere to prism transformation (STP), step 2 (Fig.1.16 A). The order in which the sodium citrate is introduced into the solution is very important. The introduction sodium citrate after etching with hydrogen peroxide will not result in the successful transformation of spherical NPs to prisms (STP), step 2 (Fig.1.16 B). This makes the sodium citrate and hydrogen peroxide important for STP transformation. Cubic nanoparticles, on the other hand, can be obtained by reflux at higher temperatures in the presence of a high boiling point solvent such as ethylene glycol (EG) [218].

1.3.1.3 Gold and silver nanoparticle phthalocyanine conjugates

Through covalent bonding, depending on the functionality of the capping material, therapeutic drugs can be chemically linked to the nanoparticles [224-226]. The advantage of using nanoparticles for targeting infectious cells is that they are known to enhance cell membrane permeability because of their size [227-230]. Cook and co-workers were the first to report on a direct linkage of zinc phthalocyanines via a peripheral thiol groups [175, 231] to AuNPs and they investigated the intracellular photodynamic therapy of these chromophores.

Table 1.4: Some AuNP-phthalocyanines conjugates reported in literature

Compound	metal	nanoparticle	reference
(**34**)	Zn	AuNPs	[175]
(**35**)	H2	AuNPs	[176]
1,4-MPyTiPc	Ti	AuNPs	[232]
2,3-MPyTiPc	Ti	AuNPs	[232]
2,3-MPyTaPc	Ta	AuNPs	[232]
α -OTPTaPc	Ta	AuNPs	[233]
α -OTOTaPc	Ta	AuNPs	[233]
Q-TDEMgPc Q-TDEAlPc	Mg Al	AuNPs	[234]
ZnPc(SPh)$_4$	Zn	AuNPs	[235]
THDTZnPc	Zn	AuNPs	[236]
ZnTBMPc	Zn	AuNPs	[237]
ZnTSPc + Polylysine	Zn	AuNPs and AgNPs	[238]
(**28**) + Polylysine	Zn	AuNPs and AgNPs	[238]
(**48**)	Si	AuNPs	[239]
C11Pc	Zn	AuNPs	[240]
THDTZnPc	Zn	AuNPs	[241]
(**33**)	Zn	AuNPs	[112]
CoTAPc	Co	AuNPs and AgNPs	[242]

1,4-MPyTiPc =1,(4)-(2-Mercaptopyridine)phthalocyaninato titanium (IV),2,3-MPyTiPc =oxide, 2,(3)-(2-Mercaptopyridine)phthalocyaninato titanium (IV) oxide, 2,3-MPyTiPc =2,(3)-(2-Mercaptopyridine)phthalocyaninato tantalum (V)Hydroxide, α -OTPTaPc = α-Octa-pentylthioTaPc, α -OTOTaPc = α-Octa-octylthioTaPc, Q-TDEMgPc= Quaternized 2,(3)-tetra[2-(dimethylamino) ethanethio Mg(II)Pc, Q-TDEAlPc= Quaternized 2,(3)-tetra[2-(dimethylamino) ethanethio Al(III)Pc, ZnPc(SPh)$_4$= Tetraphenyl thio ZnPc, TBMPc= tetra-benzylmercapto phthalocyanine, TSPc= Tetrasulfonated phthalocyanine,C11Pc = tetradecakisdecyl-25,25-(11,11dithiodiundecyl) diphthalocyanine, THDTZnPc =[2,9,17,23-Tris-(1,6-hexanedithiol)phthalocyaninato]zinc(II), TAPc = Teraamino phthalocyanine

Table 1.4 shows some phthalocyanine AuNPs conjugates studied in literature [112, 175, 176, 232-242]. There are only a few reports on low symmetry Pc-AuNP conjugates, and to the best of our knowledge, only two reports exist on Pc-AgNP conjugates using symmetrically substituted Pcs. As Table 1.4 shows, the central metal is mainly Zn with a handful of reports on Ti, Ta and Si substituted Pcs. This thesis expands the number of central metals (incorporated into the Pcs) and introduces different ring substituents containing both S and N groups making the Pcs available for binding to Au or AgNPs.

1.3.2 Quantum dots (QDs)

1.3.2.1 Properties and applications

Quantum dots (QDs) have been widely studied as fluorescence tags in biological imaging and labelling due to their highly luminescent properties [243-248] and considerable progress has been made in this regard [243-249]. However, the development of non-toxic QDs for biological applications still needs attention, thus our interest is in the synthesis of less harmful QDs in this thesis. QDs are zero-dimensional nanostructured materials [250]. These colloidal nanocrystalline semiconductors, comprising elements from the periodic groups 12-16 are roughly spherical and with sizes typically in the range of 1–10 nm in diameter.
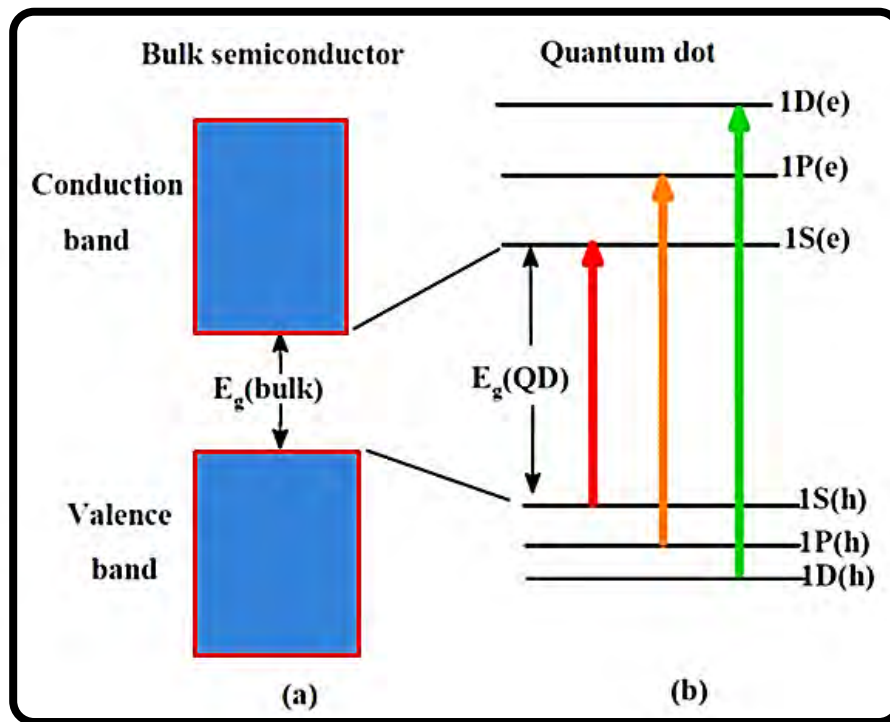
Figure 1.17: Band gap in bulk crystals and QDs showing (a) continuous conduction and valence energy bands separated by a "fixed" energy gap, Eg(bulk) (b) QD characterized by discrete atomic-like states with energies that are determined by the QD radius [251].

In bulk semiconductors, the band gap width is a fixed parameter (Fig. 1.17), determined by the material's identity and sometimes on temperature and pressure of the environment. Electrons normally occupy all states up to the edge of the valence band, whereas states in the conduction band are empty. However, the situation changes in the case of nanoscale semiconductors. At these small dimensions, the regime of quantum confinement is centered where the spatial extent of the electronic wave function is comparable with the dot size [251]. As a result, the electronic structure is altered from the continuous electronic bands to discrete atomic-like states with energies that are determined by the QD radius. These states are well-separated and can be labelled with atomic-like notations (1S, 1P and 1D) as shown in

Fig.1.17 [251, 252]. At such reduced sizes, these nanoparticles behave differently from bulk solids due to quantum confinement effects [253, 254]. Furthermore the valence and conduction bands break into quantized energy levels [255].
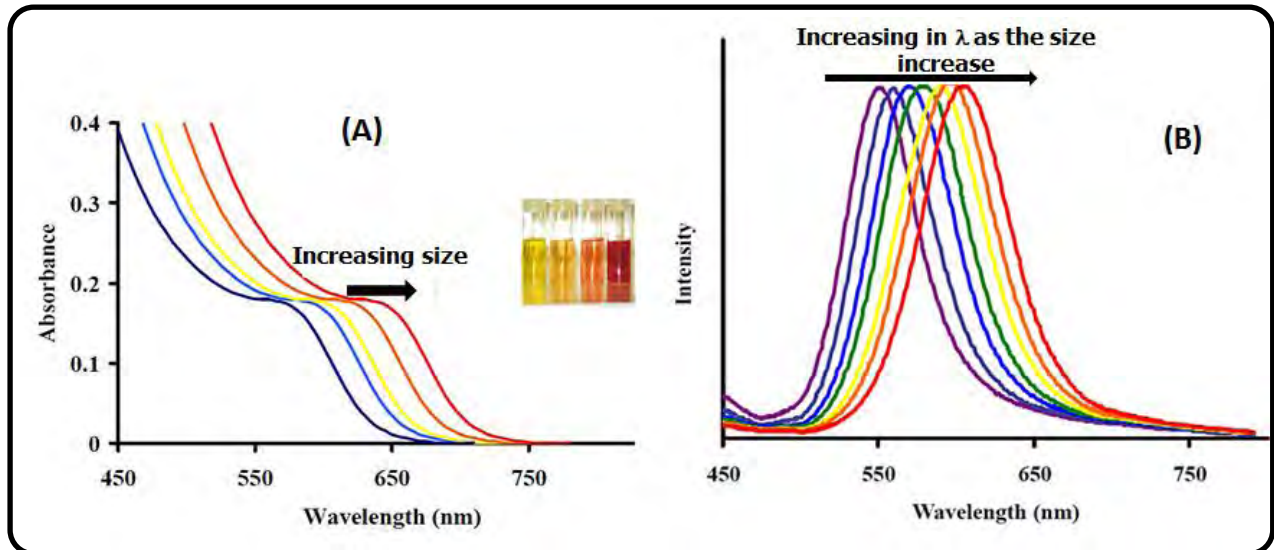
Figure 1.18: Typical absorption (A) and photoluminescence emission spectra of QDs in different stages of growth.

The absorption and emission spectra shift to lower energies with an increase in size (Fig. 1.18 [256]. The emission spectrum of QDs is a symmetrical, sharp peak as shown in Fig.1.18 (B). Fluorescence emission spectra can show high Stokes shifts, depending on the relative energies of the trap states compared to the valence and conduction band edges. Quantum confinements are responsible for the remarkable, attractive optoelectronic properties exhibited by QDs, including their high emission quantum yields, size tuneable emission profiles and narrow spectral bands [251-256]. QDs are studied in a variety of fields including biology, biomedical, electronics and optoelectronics [257, 258]. For these applications, various types of QDs have been synthesized, such as InP, InAs, GaAs, and GaN, as well as porous Si and Si/Ge dots.

In addition, the family of Group 12-16 compounds with heavier atoms such as CdTe, HgSe or PbSe have been studied due to their optical properties which extend into the near-infrared region as shown in Table 1.5 [73-75, 259-270]. There is no data on QD core-shell phthalocyanine conjugates reported to date; hence this thesis reports on CdTe@ZnS coreshells QDs and their conjugation to low symmetry phthalocyanines for the first time. The ZnS shell helps to reduce the toxicity of the CdTe core to some extent by the complete covering of the surface of the core, preventing exposure of the CdTe surface to the surroundings.

Table 1.5: Examples of known MPc-QDs conjugates reported in literature.

Compound	Quantum dots	reference
TmTPyZnPc	CdTe-QD mixed (MPA) CdTe-QD mixed (TGA)	[259]
TmTMPyZnPc	CdTe-QD mixed (TGA)	[259]
TMPAZnPc	CdTe MPA QD mixed	[260]
TmTMPy(Cl)Ga Pc TmTMPy(Cl)In Pc	CdTe-QD mixed (MPA)	[261]
TmMTAAZnPc OmMTAAZnPc	CdTe-QD linked (MPA)	[262]
ZnAPPc ZnMAPc	CdTe-QD linked (MPA)	[74, 75]
ZnAPPc	CdTe MPA TGA L-cysteine mixed and linked	[74, 75]
NiTAPc	CdTe-QD linked (TGA)	[263]
AlTSPc	CdTe MPA CdTe TGA CdTe L-cysteine	[264]

SiOCPc GeOCPc AlOCPc ZnOCPc	CdTe L-cysteine mixed	[265]
ZnTAPc	CdTe MPA	[73]
ZnttbIPc	CdTe MPA Mixed and linked	[266]
(**48**) SiPc158	CdSe TOPO CdTe TBPO	[267, 269]
αTZnPc βTZnPc βOZnPc	CdTe MPA and TGA	[270]
$(OH)2GePcS_4$ $(OH)2SiPcS_4$ $ZnPcS_4$ $(OH)AlPcS_4$	CdTe MPA and TGA	[270]

TmTMPy= tetramethyl-2,(3)-[tetra-(2-mercaptopyridinephthalocyaninato)]zinc(II), TmTMPy= tetramethyl-2,(3)-[tetra-(2-pyridyloxyphthalocyaninato)zinc(II), TMPAZnPc= 2,(3)-[Tetra-(mercaptopropanoic acid phthalocyaninato)zinc(II), TmMTAAZnPc = [2,3-[tetra-(2-mercapto-4-methyl-5-thiazoleaceticacid phthalocyaninato)]zinc(II), OmMTAAZnPc= [2,3-[octa-(2-mercapto-4-methyl-5-thiazoleaceticacid phthalocyaninato)]zinc(II)], ZnAPPc = Zinc aminophenoxy Pc, ZnMAPc = Zinc monoamino Pc, NiTAPc = Nickel tetraamino Pc, AlTSPc = Aluminium tetrasulfonated Pc, OCPc= Octacarboxy Pc, ZnttbIPc=tris[9 (10),16 (17),23 (24)-tert-butyl]imidophthalocyaninato] zinc (II), SiPc158 =[(dimethyl-silylpropylamine)-hydroxy]SiPc , αTZnPc= non peripheral-tetra (2-diethylmethylaminoethylsulfanyl) ZnPc, βTZnPc= peripheral-tetra (2-diethylmethylaminoethylsulfanyl) ZnPc,βOZnPc= peripheral-octa (2- diethylmethylaminoethylsulfanyl) ZnPc, MPA = Mercaptopropionic acid, TGA = Thioglycolic acid, PcS_4 = Tetrasulfonated phthalocyanine, TOPO = Trioctylphosphine oxide, TBPO = Tributylphosphine oxide

1.3.2.2 Synthesis of quantum dots

QDs can be grown directly in aqueous solutions through arrested precipitation [271-274] which is the most popular method and it is employed in this work. This method

has been used to synthesize a wide range of QDs, including CdS, CdSe, CdTe, and HgTe. The possibility of controlling the surface charge and other surface properties of thiol capped QDs can be achieved through the choice of the stabilizing mercapto-compounds appropriately functionalized. The leaching of Cd from the surface of QDs to the surrounding cell environment is the main problem associated with CdTe QDs due to its toxicity. Numerous efforts in reducing the toxicity of CdTe QDs by capping with biological molecules or coating with non-toxic shells have been reported in literature [243-249]. In this thesis, we therefore adopted some of the strategies used in literature to synthesize CdTe QDs with a ZnS shell and an additional penta-peptide to enhance its solubility and to minimize the possibility of Cd leaching.

1.3.2.3 Föster resonance energy transfer (FRET)

FRET is a photophysical process through which an electronically excited fluorescent donor molecule transfers its excitation energy to an acceptor molecule (as depicted in Fig.1.19) [161,275-277] non-radiatively such that the excited state lifetime of the donor decreases and the acceptor is raised to a higher energy state.

The acceptor may or may not be fluorescent and the donor and acceptor fluorophores may be separated or attached. Initially, the acronym FRET referred specifically to situations where the donor and acceptor pairs were both fluorophores but various experiments have shown the same fundamental principles to be obeyed, even when there is no fluorescence. Therefore, the acronym FRET has been suggested to apply to both specific (fluorescence) and general (Förster) resonance energy transfers [278].
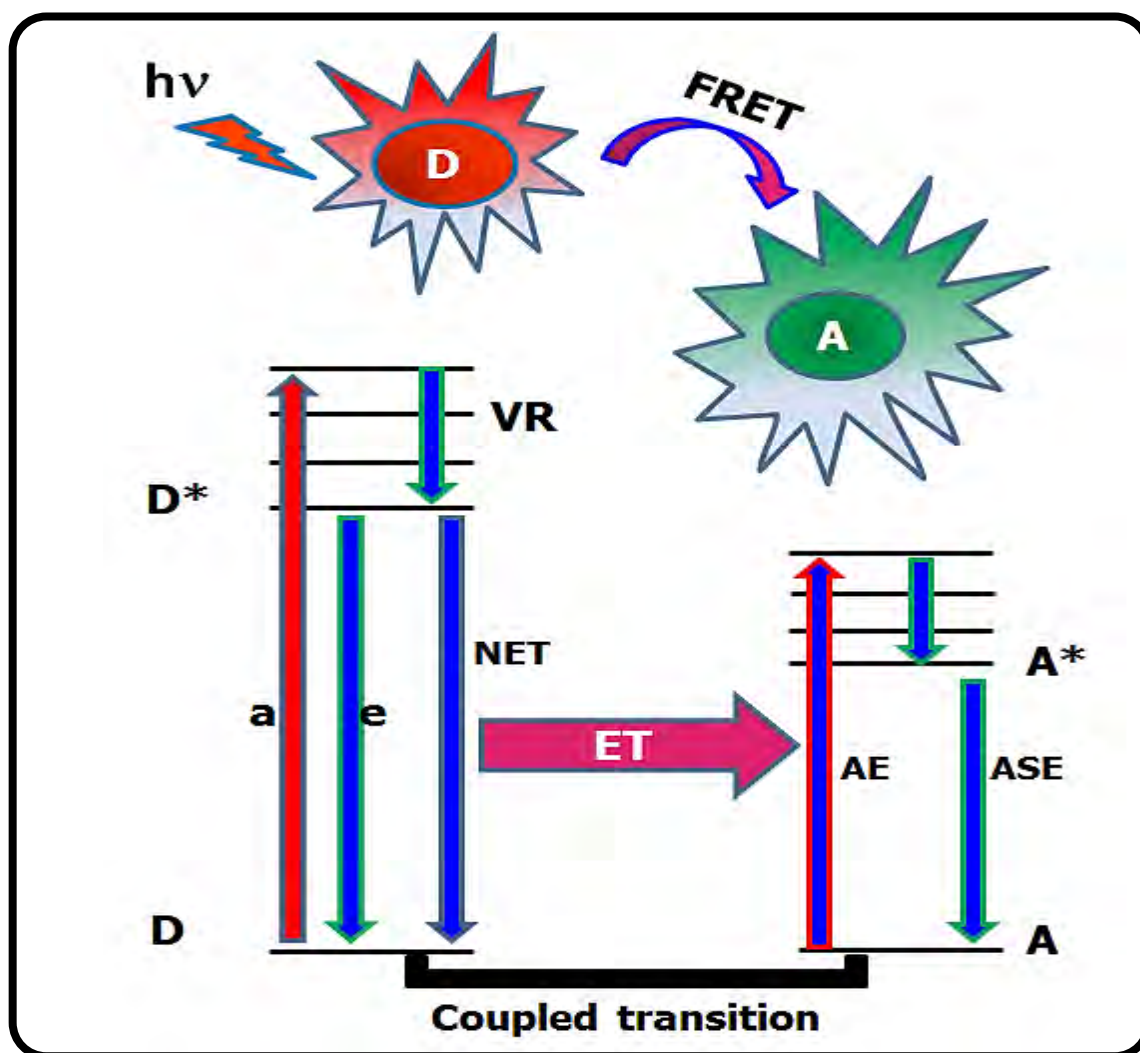
Figure 1.19: Förster resonance energy transfer Jablonski diagram illustrating coupled transitions between donor emission and acceptor absorbance in FRET. D = donor, A = acceptor, a = absorption, e = emission, VR = vibrational relaxation, NET = non-radiative donor energy transfer, AE = non-radiative acceptor excitation and ASE = acceptor sensitized emission [161]. Pictorial representation of FRET.

FRET requires the fluorescence emission spectrum of the donor molecule to overlap with the absorption spectrum of the acceptor and both the donor-acceptor molecules must be within the minimal spatial range, for the donor to transfer its excitation

energy through space to the acceptor. It is also dependent on the relative orientation of the donor and acceptor transition dipoles and on the fluorescence quantum yield of the donor [275, 279]. The lifetime of the excited donor plays important role, as the probability of energy transfer is proportional to this lifetime. The Förster treatment is semi-classical and employs the point-dipole approximation.

Practically, the quenching in the donor photoemission is consequential, and a sensitized acceptor's fluorescence is observed when FRET has occurred.

FRET efficiency (Eff) is determined experimentally from the fluorescence quantum yields of the donor in the absence ($\Phi_{F(QD)}$) and presence ($\Phi_{F(QD)}^{Mix}$) of the acceptor using Eq. (1.10) [280, 279, 281]:

$$\text{Eff} = 1 - \frac{(\Phi_{F(QD)}^{Mix})}{(\Phi_{F(QD)})} \qquad 1.10$$

FRET efficiency (Eff) is related to r (Å) by Eq. (1.11) [282]:

$$\text{Eff} = \frac{(R_0^6)}{(R_0^6 + r^6)} \qquad 1.11$$

where r is the centre-to-centre separation distance (in Å) between the donor and acceptor, R_0 (the Förster distance, Å) is the critical distance between the donor and the acceptor molecules at which the efficiency of energy transfer is 50% and depends on the quantum yield of the donor Eq. (1.12)[280]:

$$R_0^6 = 8.8 \times 10^{23} \kappa^2 n^{-4} \Phi_{F(QD)} J \qquad 1.12$$

where κ^2 is the dipole orientation factor, n is the refractive index of the medium, $\Phi_{F(QD)}$ the fluorescence quantum yield of the donor in the absence of the acceptor, and J is the Förster overlap integral, defined by Eq. (1.13):

$$J = f_{QD}(\lambda)\varepsilon_{MPc}(\lambda)\lambda^4 \, \delta\lambda \qquad\qquad 1.13$$

where f_{QD} is the normalised QD emission spectrum and ε_{MPc} is the molar extinction coefficient of MPc under investigation, λ is the wavelength of the acceptor at the Q-band. It is assumed that κ^2 is 2/3 for mixed QDs with MPc complexes. Such assumptions are often made for donor–acceptor pairs in a liquid media, since their dipole moments are considered to be isotropically oriented during the excited state lifetimes. The $\kappa^2 = 2/3$ was also employed in this work for the linked QDs–MPcs. FRET parameters were computed using the program PHOTOCHEMCAD [283].

1.4 Electrospinning

Pcs in this work were electrospun into fibers for PACT applications, thus electrospinning is discussed.

Electrospinning is the process of generating fibers through an electrically charged jet of polymer solution. The fundamental working principle of electrospinning is similar to that of electrospraying. Electrospinning is a simple, convenient, reproducible process and a generally versatile technique for generating fibers with diameters that range from several micrometers to tens of nanometers [284, 285]. The electrospinning process is highly flexible since various parameters such as solution concentration and molecular weight of the polymer [286] can be fine-tuned to obtain fibers of different diameters to meet the requirements for various applications.

The principal variables that govern the quality of polymer fibers, or determine whether electrospinning will occur at all, are the average molecular weight of the polymer, the nature of the solvent and the magnitude of the electric field used to induce the electrospinning process. Usually, for the process to be feasible, a polymer of adequate average molecular weight should be dissolved in a solvent that has suitable conductivity, surface tension and vapour pressure. The concentration of the polymer solution should be moderately high to facilitate its flow during the electrospinning process.
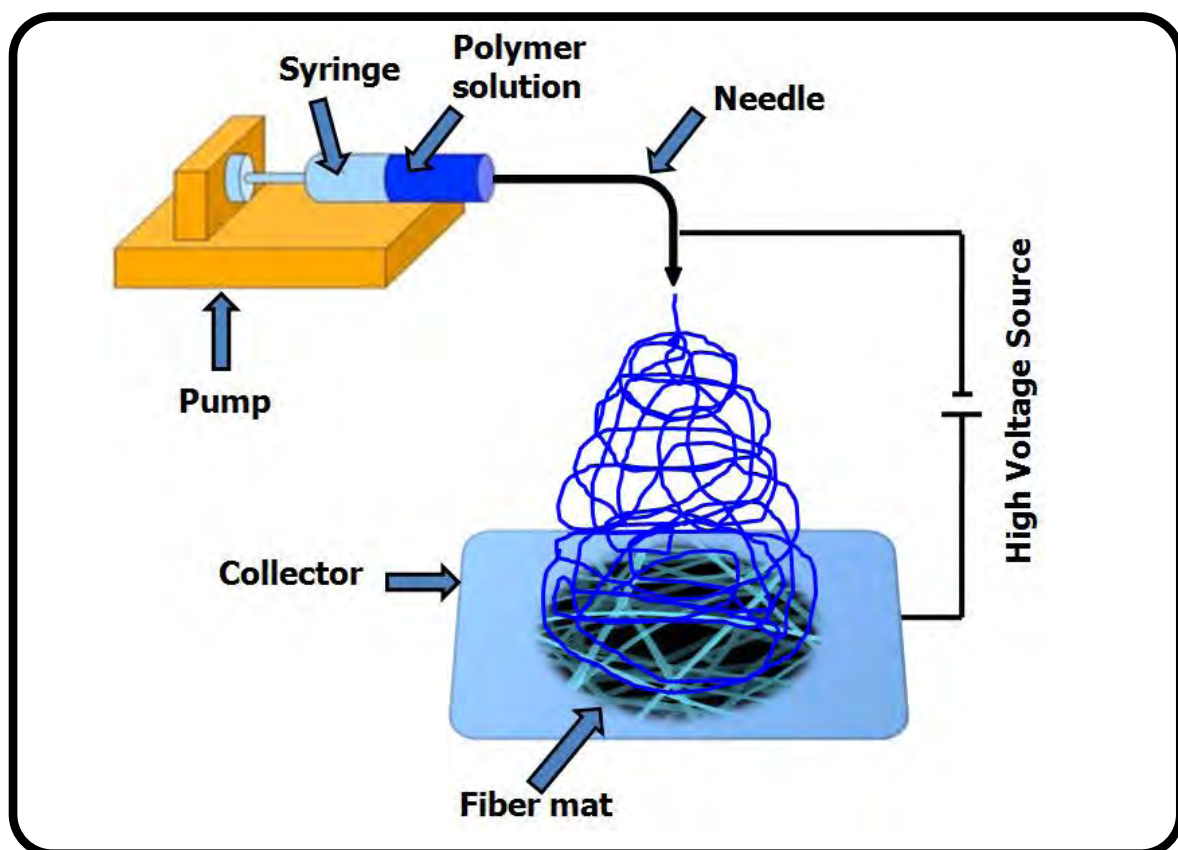
Figure 1.20: Typical diagrammatic set-up of an electrospinning apparatus [287].

The electrospinning set up consists of three basic components (Fig. 1.20) [287]: A container, usually a syringe for the polymer solution, a high voltage source and a conductive collector plate where the fiber mat is deposited.

Practically, during the electrospinning process a polymer solution of known concentration and volume is steadily pumped out of the syringe to form a drop of solution at the tip of the needle. The drop is charged by applying a high voltage to the needle. When the applied voltage is gradually increased, Coulombic forces counteract the surface tension that tends to hold the drop in a spherical shape to distort it into the so-called Taylor cone. When the electric field exceeds a certain threshold value, a charged fluid jet is ejected from the tip of the Taylor cone in the form of fiber towards the collector plate and this is collected as an unwoven fiber mat as shown in Fig. 1.20.

Due to their fine-tuneable properties and flexibility, electrospun nanofibers have received remarkable attention recently for potential use in many applications, including filtration [288-290], composites [291, 292], scaffolds [293] and medical applications [294-296]. The main advantages of electrospun fibers, besides their small fiber diameter, are their high porosity [297], small pore sizes and high specific surface areas [298]. In this thesis, the main interest in using nanofibers, compared to the use of other supports, is their ability to host a variety of molecules which in turn can improve their properties for a specific application.
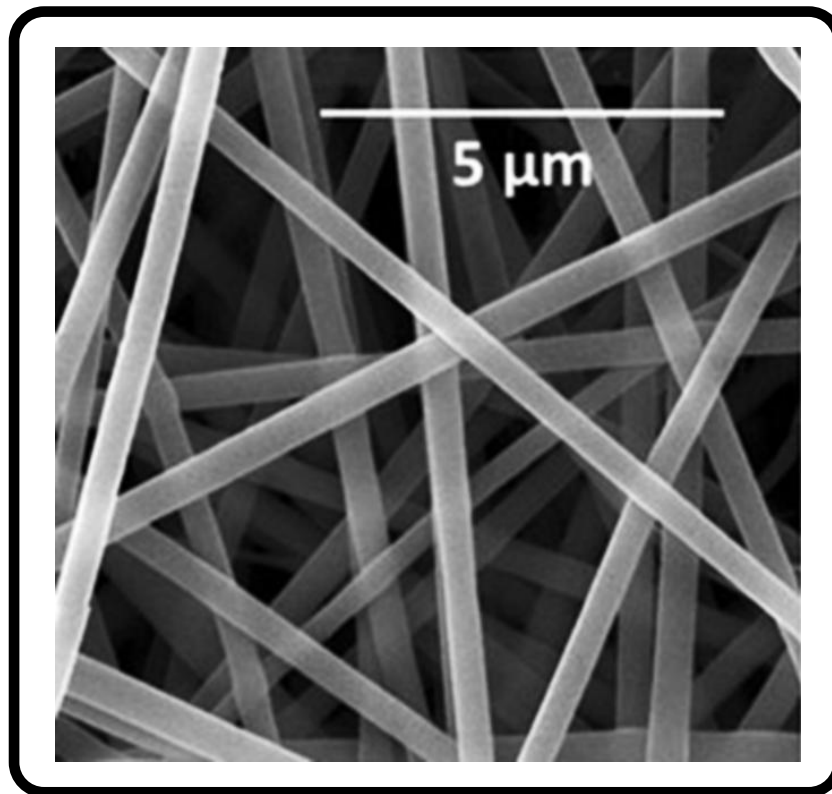
Figure 1.21: Typical scanning electrode microscope (SEM) image of a polyamide electrospun nanofiber [299]

Functionalization of electrospun fibers through the integration of functional molecules into the polymer fiber core, is often desirable in fields such as biosensor technology, tissue engineering, drug delivery, heterogeneous catalysis and nanoelectronics. Our aim in this thesis is to functionalize fibers with phthalocyanines for photodynamic inhibition of bacterial growth. It is the pore size distribution and its three-dimensional geometry that determines the key properties of fiber mats such as filtration or dye loading capacity and its permeability to gases. Fig.1.21 shows a typical scanning electron microscope image of a polyamide electrospun fiber [299].

Table 1.6 shows some typical applications of phthalocyanine functionalized electrospun fibers.

Table 1.6: Examples of known electrospun nanofibers functionalized with phthalocyanines and their applications.

Compound	Polymer support	Application	reference
ZnTmPyPc	polysulfone polymer fiber	photosensitized conversion of methyl orange	[300]
LuTPPc LuTPyPc	polystyrene polymer	photoconversion of 4-nitrophenol	[301]
LuTPPc	polystyrene polymer fiber polyurethane polymer	Photooxidation of 4-chlorophenol	[302, 303]
ZnTPyPc LuTPyPc ZnTAPc LuTAPc	Polystyrene Polymer Fibers Polysulfone Polymer Fibers. Polyurethane Polymer Polyacrylic Acid	4-chlorophenol, 4-nitrophenol, and methyl orange	[304]
LuTAPc ZnTAPc ZnPc	Polyacrylic Acid	NO_2 Gas sensing	[305]
CoTAPc	Poly(ethylene oxide)	for optoelectronic devices (expected)	[306]
ZnPc	Polyurethane	Antibacterial activity, photooxidation of iodide	[307]
CoTAPc	Cellulose fiber	Photoconversion of Reactive Red X-3B	[308]
FeTNPc	TiO_2/Polyvinylpyrolidone	Photoconversion of methyl orange	[309]

HOAlPc(SO$_3$H)$_4$ ZnPc(OC$_2$H$_4$N$^+$CH$_3$)$_4$	Polyurethane	Gram-positive bacteria	**[310]**
HOAlPc(SO$_3$H)$_4$ ZnPc(OC$_2$H$_4$N$^+$CH$_3$)$_4$	Polyurethane	Gram-positive bacteria	**[311]**

TmPyPc = Tetramercaptopyridine phthalocyanine, TPPc = tetraphenoxy phthalocyanine, TPyPc = Tetrapyridyloxy phthalocyanine, TAPc = tetaamino phthalocyanine, TNPc = Tetranitro phthalocyanine

Incorporation of phthalocyanines into electrospun polymer fibers has been reported where the properties of the phthalocyanine is still maintained in the fiber matrix [300-311]. Only two reports exist on electrospun fibers coated with phthalocyanines for bacterial inhibition, with no reports on metal nanoparticles (MNPs)-Pc conjugates. The thesis therefore reports on MNPs-Pc conjugates electrospun into fibers for bacterial inactivation. The presence of NPs enhances the photophysics, thus improving the bacterial growth inhibition.

1.5 Photodynamic antimicrobial chemotherapy

The use of antibiotics to selectively destroy microorganisms represents one of the most ground-breaking progresses made in medicine, resulting in the treatment and suppression of many incurable diseases [311, 312]. At the beginning of the 21st century, microbe-related diseases were reduced to a level that they no longer had a serious impact on human health because of availability of antibiotics. However, bacteria have developed resistance mechanisms against antimicrobial drugs which

were previously highly effective [311, 313]. Methicillin-resistant *Staphylococcus aureus* and vancomycin-resistant *enterococci* are species that are causing much concern at present [314] and there is an urgent need for the development of novel, convenient, non-resistant and low-cost measures to fight microbial diseases [311, 315, 316]. Photodynamic antimicrobial chemotherapy (PACT) represents a potential, alternative, methodology to inactivate microbial cells and has already shown to be effective *in vitro* against bacteria, fungi, viruses and protozoa [311-319].

1.5.1 Background and working principle

The phenomenom of PACT was first described by Oscar Raab in 1890 [317], when he noted the toxicity of acridine orange, which was dependent on light, against *Paramecium caudatum*. However, studies of this phenomenon and its practical use did not appear until the second half of the 20th century. PACT was first proposed for use in the area of tumour therapy and later, its use in antimicrobial therapy, was also studied [315-319]. During the photoinactivation of microbes or tumour cells, target cells are damaged by the interaction of a light activated photosensitive substance in the presence of oxygen [320]. The understanding of the scientific basis of photodynamic antimicrobial chemotherapy (PACT) is still in its infancy, but is accepted to follow similar principles to that of PDT. PACT is based on the concept that a non-toxic photosensitiser, localized in certain cells can be activated by low doses of visible light of appropriate wavelength as shown in Fig. 1.22, to generate singlet oxygen that is cytotoxic to target cells via the Type II mechanism.

The photodynamic activity damages the cytoplasmatic membrane and DNA mainly [321]. Cytoplasmatic membrane damage can involve leakage of cellular contents or inactivation of the membrane transport systems and enzymes [322].
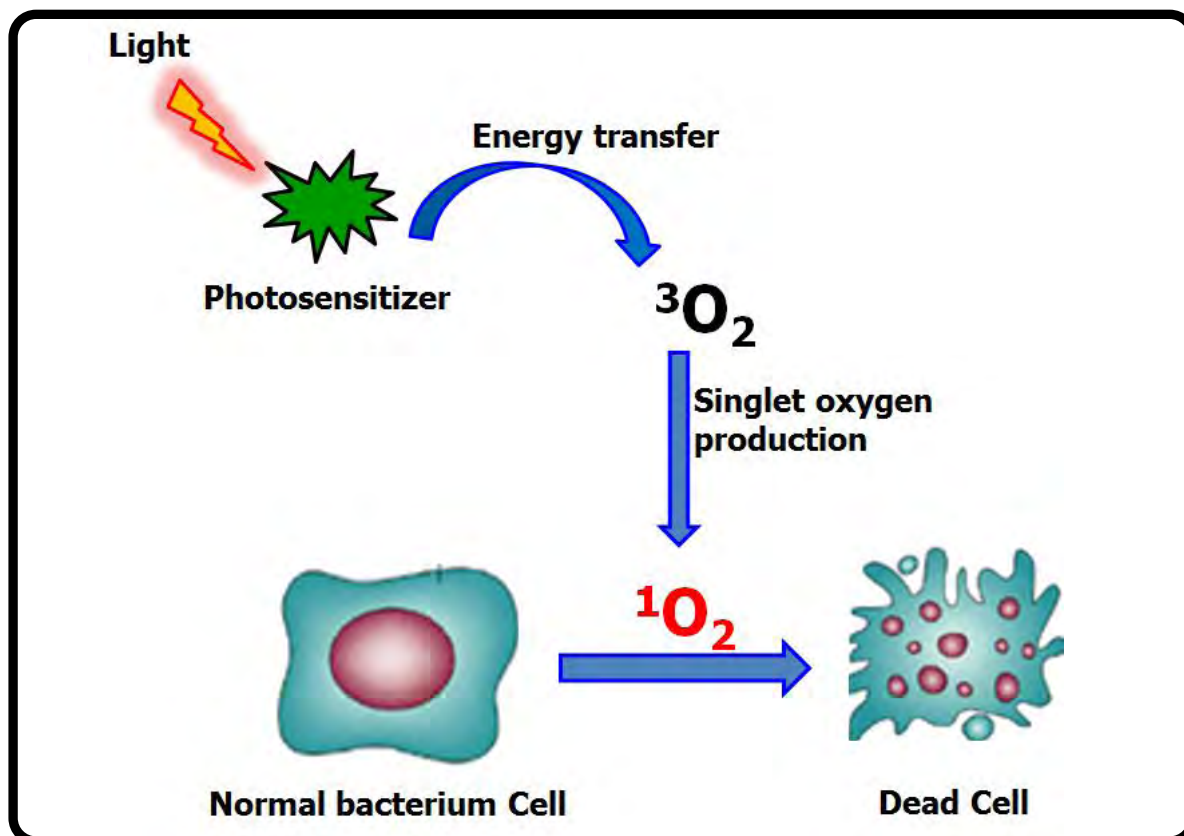
Figure 1.22: Schematic diagram showing cell death after PACT.

PACT has been used effectively particularly in the treatment of localized infections, such as gingivitis and periodontitis [323], cutaneous leishmaniasis [324] as well as root canal biofilm infection [325]. Searching for new photosensitizers with improved photo-bactericidal properties is one of the current directions in PACT development. This thesis therefore aims to introduce low symmetry phthalocyanines combined with nanoparticles as a new direction in the field of PACT.

1.5.2 Phthalocyanines used for photodynamic antimicrobial chemotherapy

Various synthetic dyes, including natural occurring compounds, have been developed for antimicrobial photodynamic therapy [326]. The first published results, more than a century ago, described acridine hydrochloride for the photoinactivation of microorganisms [327, 328]. The phenothiazine dyes such as methylene blue and toluidine blue showed promising results with bacteria and fungi [329]. Several cyanine dyes like pyrvinium and stilbazium, and merocyanines were studied for the photoinactivation of microbes in plasma and serum [330]. Highly conjugated photosensitizers such as porphyrins and phthalocyanines show improved optical properties. Phthalocyanines, which are characterized by their strong, near infrared wavelength absorption approximately >670 nm, long triplet lifetimes (of the order of µs-ms), and high singlet oxygen quantum yields (>0.2) have been studied for application as drugs in microbial photodynamic inactivation [238, 331-338] (Table 1.7). There is only one report where a Pc is studied in the presence of AgNPs, hence the aim of this thesis.

Table 1.7: Examples of phthalocyanine complexes used in PACT

Compound	Bacteria	reference
ZnTPyPc ZnTmPyPc	*Escherichia coli*	[331]
ZnCHmPPc ZnHmPPc	*Candida albicans*	[332]
ZnPc-PL	*Porphyromonas gingivalis*	[333]
ZnTSPc ZnTDEPc ZnTPPc	*Escherichia coli* *Pseudomonas aeruginosa,* *Enterococcus seriolicida,*	[334, 335]
MPyGePc MPySiPc	*Candida albicans*	[336]
GaOMPyPc ZnTMPyPc	*Fungi in biofilms*	[337]
ZnTMPyPc ZnTSPPc	*Staphylococcus aureus* *Pseudomonas aeruginosa* *Candida albicans*	[338]
ZnTSPc + Polylysine (**28**) + Polylysine	*Staphylococcus aureus*	[238]

TPyPc = tetrapyridiloxy phthalocyanine, TmPyPc = tetramethylpyridiloxy phthalocyanine, ZnCHmPPc= zinc 2-chloro-3-[4-(hydroxymethyl)- phenoxy]phthalocyanine zinc, ZnHmPPc= 1-[4 (hydroxymethyl)phenoxy] phthalocyanine Zinc, ZnPc-PL = Zinc monocarboxy – polylysine, TSPc = tetrasulfonated phthalocyanine,TDEPc = tetradiethyl phthalocyanine, TPPc = tetraphenoxy phthalocyanine, MPyGePc = 2(3),9(10),16(17),23(24)-tetrakis-[3-(N-methyl)pyridyloxy]-phthalocyaninato dihydroxygermanium (IV) tetraiodide, MPySiPc= 2(3),9(10),16(17),23(24)-tetrakis-[3-(N-methyl) pyridyloxy]-phthalocyaninato dihydroxy-silicon (IV) tetraiodide, OMPyPc = Octamethyl pyridyloxy phthalocyanine, TMPyPc = Tetramethyl pyridyloxy, TMPyPc= tetrakis-(3-methylpyridyloxy) phthalocyanine, TSPPc = tetrakis-(4-sulfophenoxy)-phthalocyanine , TSPc = tetrasulfonated phthalocyanine

Attaching phthalocyanines onto polymer materials and electrospinning them into cotton like nanofibers offers the possibility of recycling the complexes after use for a

wide variety of possible applications [300-311]. To the best of our knowledge, there are only two reports on the use of the phthalocyanine based nanofibers for photodynamic antimicrobial chemotherapy [310, 311]. Electrospun nanofibers consisting of low symmetry phthalocyanines are studied here for the first time. A comparison of low symmetry and symmetrical phthalocyanines in the presence of AgNPs, electrospun into a polymer composite and their antimicrobial properties are presented here for the first time. AgNPs are used because of their inherent antimicrobial properties [339-358] and a dual combination of Pcs with AgNPs is expected to enhance the antimicrobial growth inhibition.

1.6 Summary of Aims for this thesis

The aims of this thesis can be summarized as follows:

i.   Synthesis and characterization of novel low symmetrically substituted complexes with monocarboxylic and mono-cysteinyl functional group for covalent linkage to amino groups of nanoparticles

ii. Carry out detailed spectroscopic studies (ground state electronic absorption and fluorescence emission and excitation) of the synthesized low symmetrically substituted complexes.

iii. Study the photophysical (fluorescence quantum yields, triplet quantum yields and lifetimes) and photochemical (singlet oxygen quantum yields) behaviour of the low symmetrically substituted complexes alone or in the presence of nanoparticles.

iv. Synthesize and characterize spherical AuNPs and AgNPs, triangular and cubic shaped AgNPs, and CdTe@ZnS coreshell quantum dots.

v.   To conjugate (*via* adsorption or covalent bond formation) AgNPs, AuNPs and QDs to low symmetrically substituted Pcs and investigate their spectroscopic properties

vi. To anchor these complexes onto electrospun polymer fibers through physisorption and characterize these functional fibers using infrared spectroscopy (FT-IR) and scanning electron microscopy (SEM) techniques; to investigate the photochemical properties of the complexes on the fiber.

vii. To investigate the antimicrobial activities of the complexes in solution alone and in the presence of Ag and AuNPs.

viii.   To investigate the antimicrobial activities of the complexes when electrospun into fibers either alone or in the presence of nanoparticles

ix.   To compare the antimicrobial activities of some low symmetry phthalocyanines to their corresponding symmetrical counterparts in solution and in the fiber matrix.

x.   To synthesize novel alkyl dithiol axially ligated SiPcs and to investigate their interaction with Au and Ag NPs for application in antimicrobial inhibition of bacteria. To bind SiPc complex to a metallothionein protein for drug delivery purposes.

The MPcs under investigation in this thesis are (Table 1.2):

Tris {9 (10), 16 (17), 23 (24)-[(4-phenoxy)-2-(4-cysteinyl)] phthalocyaninato} Zn, Ge(OH)$_2$, TiO and Sn(OH)$_2$ (abbreviated as ZnMCsPc (**49**), (OH)$_2$SnMCsPc (**50**), (OH)$_2$GeMCsPc (**51**), OTiMCsPc (**52**))

Hexakis {9; 10, 16; 17, 23; 24 – [1,2-bis-(diethylaminoethylthiol)]-2-(4-phenoxycarboxy) phthalocyaninato} Zn , Ge(OH)$_2$, TiO, and Sn(OH)$_2$ (abbreviated as ZnMPCPc (**53**), (OH)$_2$SnMPCPc (**54**), (OH)$_2$GeMPCPc (**55**), OTiMPCPc (**56**)).

Tris {9 (10), 16 (17), 23 (24)-[4-(2-diethylaminoethanethiol)-2-(4-carboxy)] phthalocyaninato} Zn, Ge(OH)$_2$, TiO, and Sn(ac)$_2$. [Abbreviated as ZnMCPc (**57**), (ac)$_2$SnMCPc (**58**), (OH)$_2$GeMCPc (**59**), OTiMCPc (**60**) and bis-(1,6-hexane dithiol) SiPc (abbreviated as SiHDTPc (**61**)].

Table 1.2: List of phthalocyanine complexes synthesized and used in this thesis

Chemical structure	metal
	Zn (**49**) (OH)$_2$Sn (**50**) (OH)$_2$Ge (**51**) OTi (**52**)
	Zn (**53**) (OH)$_2$Sn (**54**) (OH)$_2$Ge (**55**) OTi (**56**)
	Zn (**57**) (Ac)$_2$Sn (**58**) (OH)$_2$Ge (**59**) OTi (**60**)
	Si (**61**)

CHAPTER 2
Experimental

2.1 Materials

2.1.1 Solvents

Chloroform, dichloromethane (DCM), diethyl ether, *N,N* dimethylformamide (DMF), acetone, dimethylsulfoxide (DMSO), ethanol (EtOH), n-hexane, methanol (MeOH), tetrahydrofuran (THF), 1-pentanol, toluene, nitric acid (55 %), sulfuric acid (98 %) and thionyl chloride were purchased from SAARCHEM. Ammonia (25 %), hydrogen peroxide (30 %), deuterated chloroform ($CDCl_3$), dimethylacetamide (DMAc), deuterated DMSO (DMSO-d_6) and deuterated DMF (DMF-d_6) were purchased from Sigma-Aldrich. All solvents were purified according to the methods described by Perrin and Armarego [359].

Ultra-pure water was obtained from (Milli-Q water system, Millipore Corp., Bedford, MA, USA).

2.1.2 Reagents for the synthesis of phthalocyanines

Dichloro silicon phthalocyanine (($Cl)_2SiPc$), 1,3-diphenylisobenzofuran (DPBF), 1,6-hexanedithiol, sodium iodide, phenol, 4-hydroxy benzoic acid 1,8-diazabicyclo{5.4.0}-undec-7-ene (DBU), 2-(diethylaminoethanethiol) hydrochloride, zinc phthalocyanine (ZnPc), dicyclohexylcarbodiimide (DCC), trimellitic anhydride, L-cysteine, potassium carbonate, germanium (IV) chloride, zinc (II) acetate, titanium (IV) butoxide, tin (IV) acetate, aluminium oxide (WN-3: neutral) and silica gel 60PF$_{254}$ for column chromatography were purchased from Sigma–Aldrich.

2.1.3 Reagents for the synthesis of nanoparticles

Gold (III) chloride trihydrate (99.9%), 4-mercaptopyridine, tetraoctylammonium bromide (TOABr) (98%), silver nitrate (> 99.8%), sodium borohydride (≥99.0%), sodium citrate (>99.0%), ethylene glycol (EG), α-cyano-4-hydroxycinnamic acid, tellurium powder (200 mesh), thioglycolic acid (TGA), glutathione (98%), NaOH (99.5%) and polyvinyl pyrrolidone (PVP) (MW=10000) were purchased from Sigma-Aldrich. CALNN (C = cysteine, A = Alanine, L = lysine and N = arginine) pentapeptide was purchased from Peptide Protein Research (PPR) (Ltd). C_{20} Phenomenex reverse phase column and Sephadex G25 column stationary materials were purchased from sigma-Aldrich and were employed for chromatographic separations. The rest of the reagents were obtained from commercial suppliers and used as received.

2.1.4 Reagents for bacterial work

Agar bacteriological BBL Mueller Hinton broth and nutrient agar were purchased from Merck. *Staphylococcus aureus* (ATCC 25923) and *Bacillus subtilis* (ATCC6633) were purchased from Microbiologics. Polystyrene (PS) (average molecular weight Mw = 192,000 g/mol) was obtained from Sigma-Aldrich

2.2 Instrumentation

i.   Ground state electronic absorption spectra were recorded on either a Cary 500 UV/Vis/ NIR or Shimadzu UV-2550 UV/Vis spectrophotometer. Quartz cells with 1 cm path-lengths were employed. The absorbances of the phthalocyanines on the fibers were measured by placing the modified fiber directly on a glass plate.

ii.   Elemental analyses for CHNS were done using a Vario-Elementar Microcube ELIII Series.

iii.   Infrared (IR) spectra (KBr pellets)were recorded using either Perkin-Elmer Fourier transform–IR (100 FT-IR) or Perkin-Elmer (ATR) Fourier transform-IR (2000 FT-IR) spectrophotometer.

iv. ^{1}H-nuclear magnetic resonance spectra (^{1}H-NMR) were recorded in deuterated solvents (DMSO-d_6 or DMF-d_6) using either a Bruker AMX400 MHz NMR spectrometer or a Bruker AVANCE II 600 MHz spectrometer.

v.   Mass spectral data for the characterization of phthalocyanines were collected with a Bruker AutoFLEX III Smart beam TOF/TOF mass spectrometer. The instrument was operated in both the positive and negative ion mode. The voltage of the ion sources were set at 19 and 16.7 kV for ion sources 1 and 2 respectively, while the lens was set at 8.50 kV. The reflector 1 and 2 voltages were set at 21 and 9.7 kV respectively. The spectra were acquired using α-cyano-4-hydroxycinnamic acid as the MALDI matrix and a 355 nm Nd:YAG laser as ionizing source.

vi. Scanning electron microscope (SEM) images of electrospun polymer fibers were

obtained using a JOEL JSM 840 scanning electron microscope and the average

diameters obtained using Cell^D software from Olympus.

vii.   Transmission electron microscope (TEM) images were obtained using a Carl

Zeiss Libra transmission electron microscope at 100 kV accelerating voltage

viii.   X-ray powder diffraction patterns were recorded on a Bruker D8 Discover

equipped with a Lynx Eye Detector, using Cu-K$_\alpha$ radiation (λ = 1.5405 Å, nickel

filter). Data were collected at various 2θ ranges, scanning at 1° min^{-1} with a filter

time-constant of 2.5 s per step and a slit width of 6.0 mm. Samples were placed

on a zero background silicon wafer slide. The X-ray diffraction (XRD) data were

treated using Eva (evaluation curve fitting) software. Baseline correction was

performed on each diffraction pattern by subtracting a spline fitted to the curved

background and the full-width at half-maximum values used in this study were

obtained from the fitted curves.

ix.   Fluorescence emission and excitation spectra were obtained on a Varian Eclipse

spectrofluorimeter.

x.   Fluorescence lifetimes were measured using a time correlated single photon

counting setup (TCSPC), Fig. 2.1, (Fluo Time 200, Picoquant GMbH) with a diode

laser as excitation source (LDH-P-670 driven by PDL 800-B, 670 nm, 20 MHz

repetition rate, Picoquant GmbH for Pcs and a LDH-P-C-485 with 10 MHz

repetition rate, 88 ps pulse width, for quantum dots). Fluorescence was detected

under the magic angle with a peltier cooled photomultiplier tube (PMT) (PMA-C

192-N-M, Picoquant GmbH) and integrated electronics (PicoHarp 300E,

Picoquant GmbH). A monochromator with a spectral width of about 4 nm was

used to select the required measured emission wavelength. The response function of the system, which was with a scattering Ludox solution (DuPont), had a full width at half-maximum (FWHM) of about 300 ns. The ratio of stop to start pulses was kept low (below 0.05) to ensure good statistics. All luminescence decay curves were measured at the maximum of emission peak. The data were analysed with the program FluoFit (Picoquant GmbH). The support plane approach [280] was used to estimate the errors of the decay times.
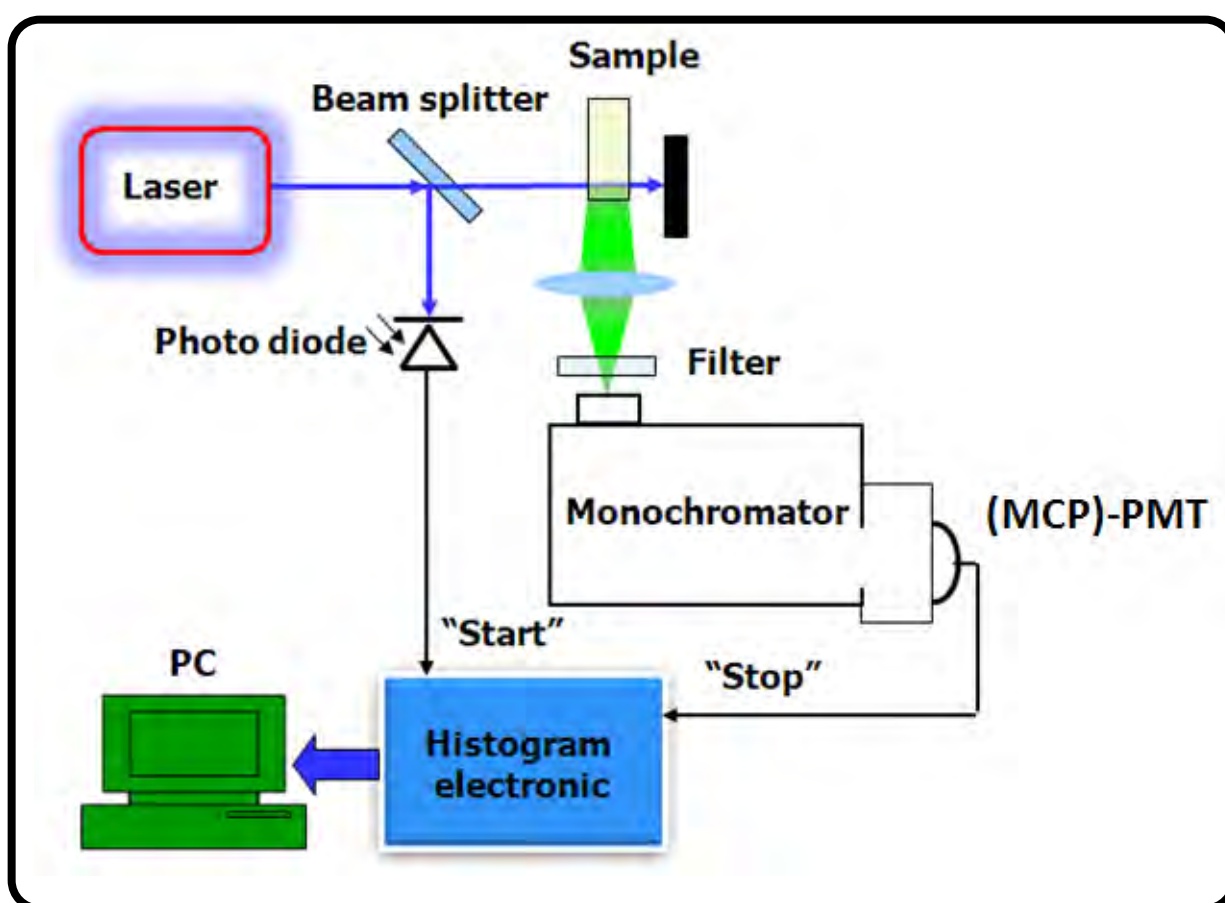
Figure 2.1: Schematic diagram of time-correlated single photon counting (TCSPC) setup. (MCP)-PMT = (Multi channel plate detector)-Photomultiplier tube, PC = Personal computer.

xi.   Laserflash photolysis experiments, Fig. 2.2, were performed with light pulses produced by a Quanta-Ray Nd:YAG laser providing 400 mJ, 9 ns pulses of laser light at 10 Hz, pumping a Lambda-Physik FL3002 dye laser (Pyridin 1 dye in methanol). Single pulse energy ranged from 2 to 7 mJ. The analysing beam source was from a Thermo Oriel Xenon arc lamp, and photomultiplier tube (a Kratos Lis Projekte MLIS-X3) was used as a detector. Signals were recorded with a two-channel 300 MHz digital real time oscilloscope (Tektronix TDS 3032C); the kinetic curves were averaged over 256 laser pulses.
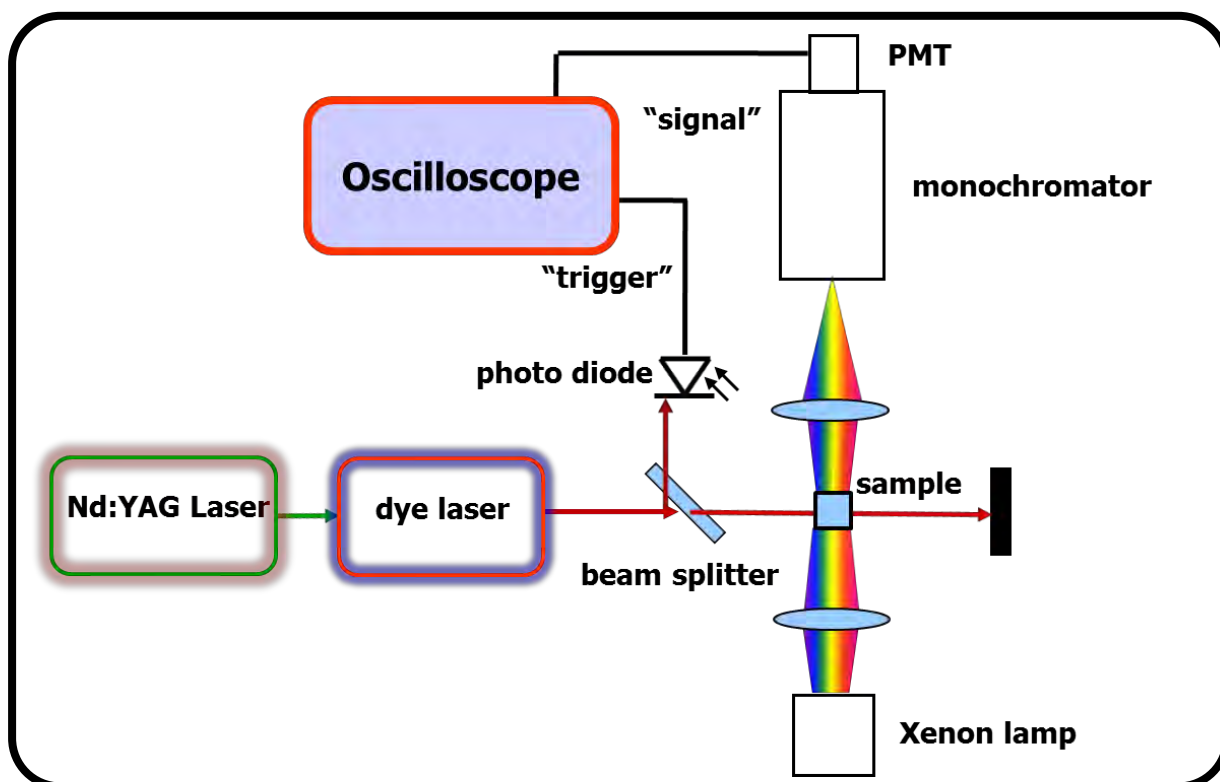
Figure 2.2: Schematic diagram for a laser flash photolysis setup.

PMT = Photomultiplier tube

xii.   Determination of singlet oxygen quantum yields as well as irridiation of bacterial plates was done using General Electric Quartz lamp (300 W) as irradiation

source, Fig. 2.3. A 600 nm glass (Schott) and water filters were used to filter off ultra-violet and far infrared radiations respectively. An interference filter 670 nm with band of 40 nm was placed in the light path just before the cell containing the sample. The intensity of the light reaching the reaction vessel, was measured with a power meter (POWER MAX 5100, Molectron Detector Inc).
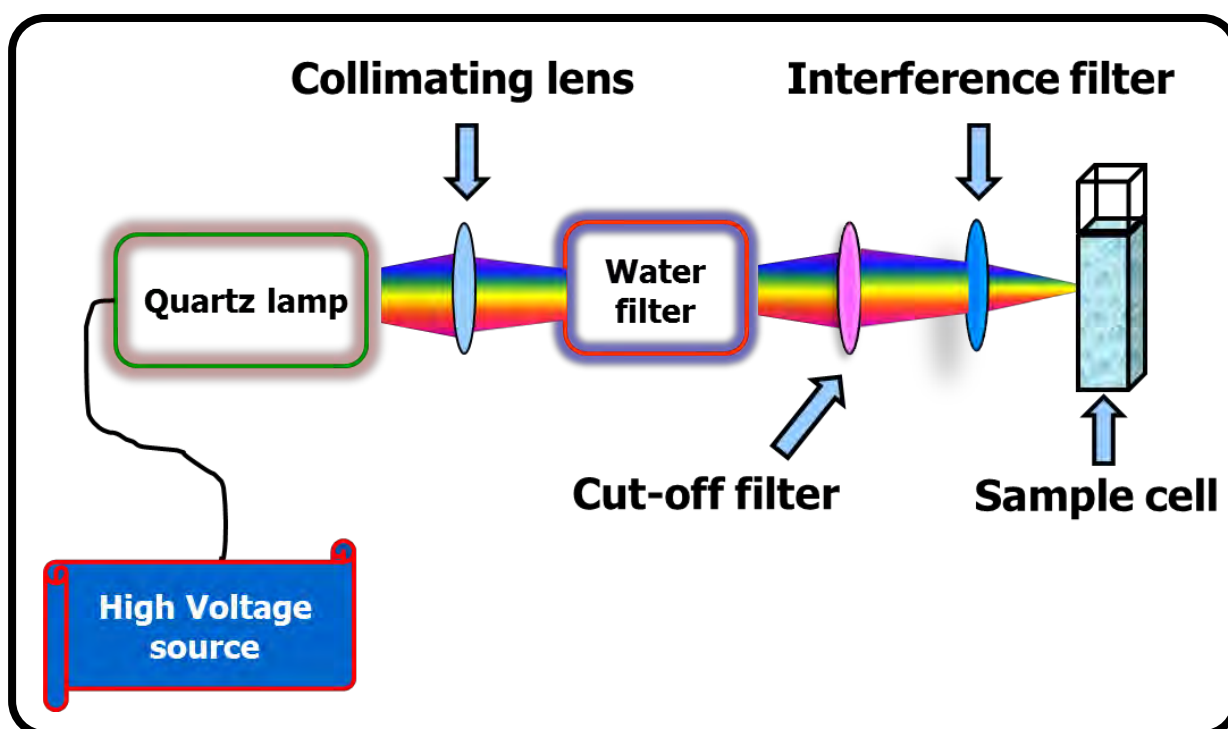
Figure 2.3: Schematic diagram of photo-irridiation setup.

xiii.   Electrospun polymer fibers were obtained from a set up, Fig. 2.4, consisting of a high voltage source (Glassman High Voltage. Inc., EL series, 0-40 kV), a pump (Kδ Scientific, KDS-100-CE), a glass syringe (Am Bildacker 3-7, D-97877 Wertheim, Poulten & Grat GmBh) connected to a steel needle of internal diameter of 0.584 mm and aluminum foil as collector.
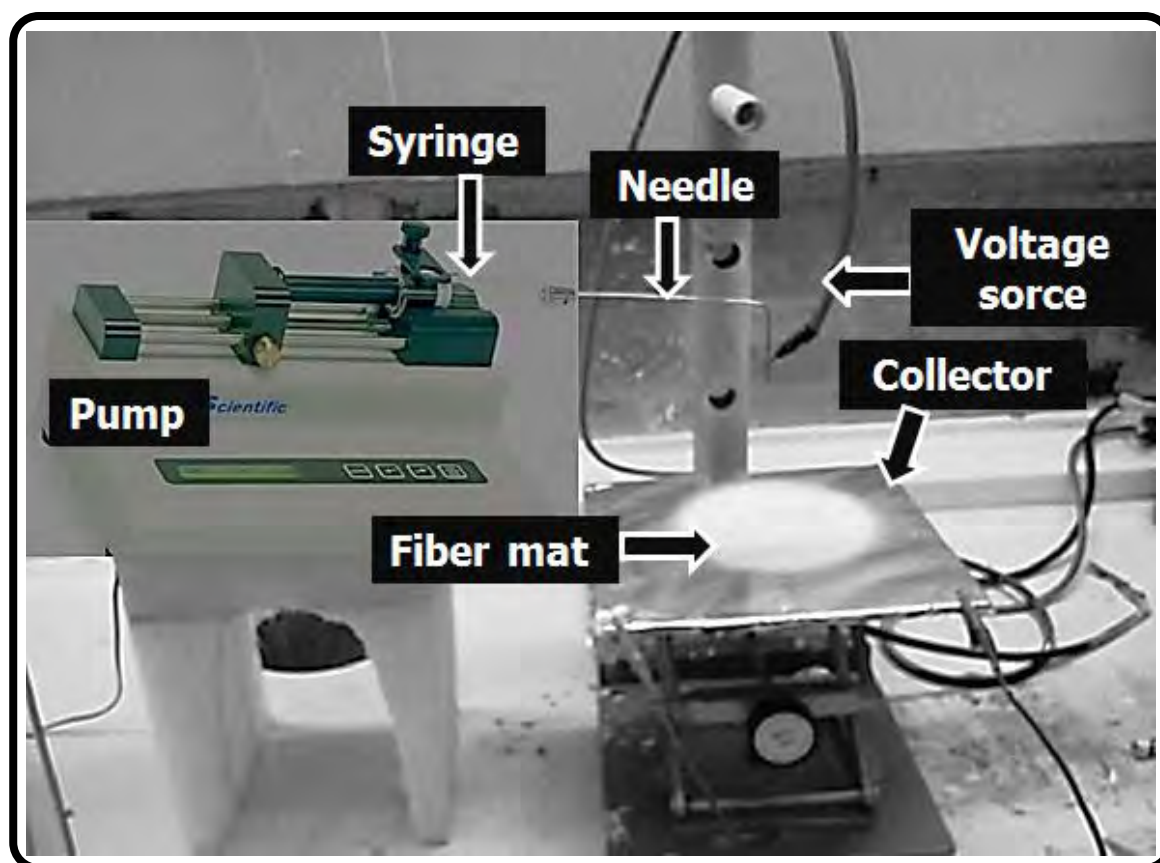
Figure 2.4: Typical electrospinning setup

xiv. X-ray photoelectron spectroscopy (XPS) measurements were performed with a Kratos Ultra Axis X-ray Photoelectron Spectrometer equipped with a monochromated Al source. The base pressure was below 3×10^{-9} Torr. XPS experiments were recorded using a hybrid-slot spectral acquisition mode at 5 mA emission and 15 kV HT. A charge neutralizer was used due to the insulating surface used to prepare the sample. XPS data analyses was performed with Kratos version 2 program.

2.3 Methods

2.3.1 Fluorescence quantum yields (Φ_F)

Fluorescence quantum yields (Φ_F) of the MPcs and MPc-MNPs were determined by a comparative method in either DMF or DMSO using, Equation 1.2. The same solvent was used in each case for samples and standard. Unsubstituted ZnPc (Φ_F^{Std} = 0.20) [148] in DMSO) was employed as the standard. Both the samples and standard were excited at the same wavelength. The absorbances of the solutions at the excitation wavelength were about 0.05 to avoid any inner filter effects.

2.3.2   Triplet quantum yields (Φ_T) and lifetimes (τ_T)

The triplet decay kinetics of the triplet absorption of phthalocyanines were recorded using laser flash photolysis setup, Fig. 2.2. The absorbance of sample solutions and that of the standard were adjusted to be approximately 1.5 at their Q-band maxima. After introducing the solution to a 1 cm quartz cell, argon was bubbled through the solution to remove dissolved oxygen before taking readings. The triplet quantum yields of the sample phthalocyanines were determined using Equation 1.3. Unsubstituted ZnPc Φ_T^{std} = 0.68 [360] in DMF and Φ_T^{std}= 0.65 [361] in DMSO was employed as the standard. Triplet lifetimes were determined from the kinetic data obtained, using ORIGIN Pro 8 software.

2.3.3   Singlet oxygen (Φ_Δ)quantum yields

A chemical method was employed in this work for Φ_Δ determination, using the experimental set-up shown in Fig. 2.3.

The Φ_Δ values were determined by monitoring the change in absorbance (decay of the quencher) at 416 nm for DPBF with time and used for the calculation of Φ_Δ according to Equation 1.6, employing ZnPc in DMF, $\Phi_\Delta^{std} = 0.56$ [362] as a standard. An air-saturated solution of the MPcs (2.0 mL) with the respective singlet oxygen quencher (DPBF or ADMA) (absorbance of MPc ~ 0.2 at the irradiation wavelength in the final solution) was placed in a 1 cm pathlength spectrophotometric quartz cell fitted with a stopper and photolysed at the Q-band region using a 300 W General electric quartz lamp as described above (Fig 2.3). The solutions were prepared in the dark. The wavelength of the interference filter was chosen such that it was close to the Q band absorption of the MPc. The concentration of DPBF or ADMA was kept at ~ 3 x 10^{-5}M to avoid chain reactions. The initial quencher concentrations (corresponding to an absorbance of ~ 1.0) were kept the same for both the standard and the MPcs.

For singlet oxygen quantum yield determinations in water, using phthalocyanines electrospun into fiber matrices, ADMA was used as a singlet oxygen quencher since the fabric materials are intended for use in biological aqueous media. In each case 10 mg of the modified fibers was suspended in an aqueous solution of ADMA and similarly irradiated using the photolysis set-up, Fig. 2.3. The quantum yields (Φ_{ADMA}) were estimated using Equation 1.7 and the extinction coefficient of AMDA in water log (ε) = 4.1 [144]. Equation 1.9 (the absolute method) was employed for

Φ_{Δ}values. The Φ_{Δ} values are estimates due to light scattering and the intensity of light was the one reaching the spectrophotometric cell but not the fibers.

2.3.4   Antimicrobial experiments in solution and in the fiber matrix

2.3.4.1 Antimicrobial activities in solution

The antimicrobial activity of the MPcs alone or MPc-MNP conjugates was studied in solution. *Staphylococcus aureus* (*S. aureus*) or *Bacillus subtilis* (*B. subtilis)* were grown on a nutrient agar plate prepared according to the manufacturer's specifications. The plates were incubated overnight at 37 °C before being used. Firstly, a single colony of *S. aureus* (or *B. subtilis*) from the agar plate was inoculated into 10 mL of Mueller Hinton nutrient broth and allowed to grow at 37 °C for 2 to 6 h until an appropriate optical density (0.6 - 0.8 at 600 nm) was obtained. Separately, solutions of the MPcs, and the MPc-MNP conjugates (100 µL with concentrations ranging from ~0.16 to 25 µM in DMF) were added to the 96 well micro-plates containing 100 µL Mueller Hinton nutrient broth. Then, 5 µL of a solution of *S. aureus* (or *B. subtilis*) prepared in the first step was pipetted into each of the 96 well plates containing the MPcs. The total amount of DMF in each well was at 50 %. The bacteria studied in this work are known to be resistant to DMF [97].

A pair of 96 well plates containing the MPc molecules conjugated to the MNPs (or MPc alone) were then irradiated with visible light for 120 min, while a second set was kept in the dark. The irradiated and non-irradiated plates were incubated overnight in an incubator shaker (~200 rpm) in the dark at 37 °C. The viable microorganisms were corrected using controls containing no Pc or Pc-MNP

conjugates. The optical density of the bacterial viability was determined at 600 nm and expressed as a percentage bacterial growth. The experiments were done in triplicate and the error was estimated to be less than 2%.

2.3.4.2 Antimicrobial behaviour in fiber matrices

Antimicrobial experiments were also tested for MPcs alone or MPc-MNPs conjugate supported in a fiber matrix. Nanofiber samples modified with phthalocyanines were placed on the Baird Parker agar base plates which were pre-inoculated with 100 ml of liquid broth containing a suspension of *S. aureus (*or *B. subtilis)* (~10^7 to10^8 CFU/mL (colony forming unit/mL))**.** One pair of agar plates was kept wet in the dark and the other pair was kept wet under illumination with visible light for 120 min. All the samples were incubated for 16 h at 37 °C and evaluated. A pair of agar plates containing the polymer material without bacteria was used as a control, both in the dark and under illumination. This was aimed at confirming that the changes observed are due to bacterial inactivation and not due to the phthalocyanine leaching, even though the latter is not expected because of solubility issues in water.

2.4 Synthesis

2.4.1   Synthesis of nanoparticles

Nanoparticles synthesized in this thesis include quantum dots (QDs), gold nanoparticles (AuNPs) and silver nanoparticles (AgNPs)

2.4.1.1 Synthesis of quantum dots

The synthesis of the thiol stabilized CdTe QDs has been reported before [264, 274, 363], and the synthesis of CdTe/ZnS core–shell nanoparticles was also achieved using literature method [364]. Modification of these QDs was accomplished as follows: Briefly, a sample of the as-prepared CdTe QDs (40 mg) was added to a 50 ml solution (pH = 10) containing 1 mM $ZnCl_2$ and 4 mM CALNN. The solution was heated to 100 ˚C under argon and then refluxed for up to 5 h in order to control the size of core–shell QDs. Aliquots of the reaction solution were removed at regular intervals to conduct UV-vis absorption and fluorescence experiments. Samples were precipitated by absolute ethanol and dried under vacuum for characterization.

The particle size was determined by powder XRD which uses the Debye–Scherrer equation (Equation 2.1) [365]

$$d(\overset{o}{\text{A}}) = \frac{k\lambda}{\beta Cos\theta}$$
2.1

Where k is an empirical constant equal to 0.9, λ is the wavelength of the X-ray source, (1.5405A˚), β is the full width at half maximum of the diffraction peak, and θ is the angular position of the peak.

2.4.1.2 Synthesis of spherical gold nanoparticles

TOABr stabilized gold nanoparticles were synthesized according to a reported procedure [119]. The purple organic phase which contains the nanoparticles was separated and washed with water.

Glutathione (GSH) stabilized AuNPs [366] were obtained by dissolving GSH in ethanol: water (1:1) to make a 50 mM solution, which was then flushed with argon for 45 min before use. The GSH solution was then added to an equal volume ratio of TOABr stabilized AuNPs in toluene. The mixture was stirred vigorously under argon for 12 h to enable the ligand exchange to take place. After the reaction was complete, the water soluble GSH capped nanoparticles were separated in a funnel, followed by centrifugation. And a 90 % product yield was achieved.

4-Mercaptopyridine capped AuNPs were also obtained following ligand exchange. Briefly a 1 mL of a solution of 4-mercaptopyridine (40 mM) in DMF was added to 10 ml of TOABr stabilized AgNPs under argon atmosphere. The mixture was allowed to react under stirring for 3 h, after this time the solution changed colour from lightly coloured solution to a dark purple indicating formation 4-mercaptopyridine capped AuNPs. The use of 4-mercaptopyridine as a capping agent does not only provide stability for the nanoparticles, but it also allows for axial coordination of the NPs to ZnPc, which was the aim of using the pyridine derivative as a capping agent.

2.4.1.3   Synthesis of silver nanoparticles

2.4.1.3.1   Spherical AgNPs

The procedure followed for the synthesis AgNPs was as reported elsewhere [218] with slight modification. Briefly, a 20 mL DMF solution of $AgNO_3$ (1 mM) was reduced with a sodium borohydride solution (36 mM, 10 mL), which was added dropwise at room temperature under vigorous stirring, to give a light yellow solution. This represents the uncapped AgNPs used for linking SiHDTPc (**61**). To

synthesize mercaptopyridine capped AgNPs, 1 mL of a solution of 4-mercaptopyridine (40 mM) was added to 10 mL of the uncapped AgNPs and allowed to react for 30 min to give the 4-mercaptopyridine stabilized AgNPs. Similarly, 4-mercaptopyridine stabilized AuNPs were synthesized and this allowed for further coordination of the NPs to ZnPc derivatives via axial ligation.

Spherically shaped citrate capped AgNPs of larger size were prepared separately to be used as precursors in the synthesis of triangular shaped AgNPs following literature procedures [218]. Briefly, a 20 mL DMF solution of $AgNO_3$ (1 mM) was reduced with sodium citrate (2 mL of 40 mM aqueous solution) at room temperature. Citrate ions act as both reducing and capping agents. Then, 0.5 mL of 100 mM aqueous sodium borohydride solution was added dropwise under vigorous stirring leading to a light yellow colour. After that, 0.5 mL aqueous solution of polyvinyl pyrrolidone (PVP) (40 mM) was added and the solution changed to a darker yellow colour after the reaction had proceeded for 30 min, indicating formation of spherical AgNPs. The use of PVP as a capping agent not only prevents the agglomeration but also allows controlled growth of Ag nanoparticles in different shapes [367].

2.4.1.3.2 Triangular shaped citrate capped AgNPs

For the synthesis of AgNP triangles, the spherical AgNPs prepared in previous stage were immediately etched with a 30% hydrogen peroxide solution following a reported procedure [217]. The H_2O_2 (0.5 mL) solution was added dropwise with vigorous stirring for 5 min and the reaction left to stir 6 h. After this period the

yellowish spherical AgNPs turned purple, indicating formation of citrate capped silver triangular nanostructures.

2.4.1.3.3 Cubic AgNPs (stabilized with PVP)

Cubic AgNPs were synthesized as reported in literature [218]. Briefly, 5 mL of ethylene glycol (EG) were introduced into a three-neck flask and heated (under stirring) using an oil bath at 150 °C for 1 h. Then, 3 mL of $AgNO_3$ (0.25 M in EG) and 3 mL PVP (0.375 M in EG) were simultaneously slowly injected into the primary EG mixture over a period of 10 min. The reaction mixture was kept at 150 °C for another 45 min. The sample was then centrifuged (at 4500 rpm for 5 min) and washed firstly with acetone and then twice with water to remove the excess amounts of EG and PVP.

2.4.2   Synthesis of phthalocyanines

The following were known phthalonitrile precursors and phthalocyanine complexes used in this thesis:

4-Nitrophthalonitrile (**62**) Scheme 3.1 [368-370], 4-phenoxy phthalonitrile (**63**) Scheme 3.1 [14,371], 1,2-Bis-(diethylaminoethylthiol)-4,5-dicyanobenzene (**64**) Scheme 3.2 [372, 373], 4-(3,4-dicyanophenoxy)-benzoic acid (**65**) Scheme 3.2 [98], 4-carboxyphthalonitrile (**66**) Scheme 3.3 [109,374], and 4-(2-diethylaminoethanethiol)-4-phthalonitrile (**67**) Scheme 3.3 [372, 373] were synthesized according to reported procedures.

2(3)-Tetra-(2-diethylaminoethylthio)-phthalocyaninato zinc(II) (**ZnTDEPc** (**68**)) and octa (2-diethylaminoethylthio) phthalocyaninato zinc (II) (**ZnODEPc** (**69**)) were synthesized as reported before [373, 375], 2(3)-tetra-(phenoxy)-phthalocyaninato zinc(II) (**ZnTPPc** (**70**)) [14, 136] and 2(3)-tetra-(4-phenoxycarboxilic acid)-phthalocyaninato zinc(II) (**ZnTPCPc** (**71**)) [376] were achieved using the methods reported in literature.

2.4.2.1   Synthesis of 4-cysteinyl phthalonitrile (72) (Scheme 3.1)

Compound (**72**) was synthesized as follows: to dry DMF (30 ml) under argon, 3.5 g (25 mmol) of K_2CO_3 was added, followed by L-cysteine (2.07 g, 17.1 mmol) and 4-nitrophthalonitrile (2.0 g, 11.5 mmol). After 4 and then at 24 h, additional K_2CO_3 (3.5 g, 25 mmol) was added to the mixture. The mixture was stirred at room temperature for 72 h, after this time the formed product was dissolved in water: methanol (1:1), and the pH of the solution adjusted to 2 by addition of HCl to give a light reddish brown precipitate. The product was further purified using a size-exclusion column using (5:1) methanol: acetone as eluent (Bio-Beads S-X1 from Bio-Rad).

Yield: (0.96 g, 50%). IR [(KBr)-max/cm^{-1}]: 3428 (OH), 3327 (N-H), 3102 (C–H), 2234 (C≡N), 1628 (N-H bending), 1610 (C=O), 1586, 1427, 1234, 862 (C–H), 742 (C-S-C). ^1H NMR (400 MHz, DMSO-d_6)/ppm: 12.11 (1H, broad s, –COOH), 8.13 (2H, broad, NH_2), 7.24 (1H, d, aromatic C-H), 7.56 (2H, dd, aromatic C-H), 3.89 (1H, d, C-H), 3.46 (2H, dd, S-CH_2). Calc. for $C_{11}N_3H_9S_1O_2$: C 53.46, H 3.64, N 17.00, S 12.97 Found: C 53.32, H 3.58, N 16.97, S 12.66

2.4.2.2   Tris {9 (10), 16 (17), 23 (24)-[(4-phenoxy)-2-(4-cysteinyl)] phthalocyaninato} Zn (49), Sn (OH)₂ (50), Ge (OH)₂(51) and TiO (52) (Scheme 3.1).

A mixture of 4-cysteinyl phthalonitrile (**72**) (0.64 g, 2.6 mmol) and 4-phenoxy phthalonitrile (**63**) (1.72 g, 7.8 mmol) was firstly finely ground, homogenised and placed in a round bottom flask that contained pre-heated dimethyl acetamide (DMAc) (15 mL). The mixture was then stirred under reflux at 130 °C for 7 h in an argon atmosphere in the presence of excess (13.0 mmol) metal salt (zinc acetate for complex (**49**), tin (IV) chloride for complex (**50**), germanium (IV) chloride for complex (**51**) and titanium (IV) butoxide for complex (**52**)) and DBU (0.25 mL) as a catalyst. Thereafter, the mixture was cooled to room temperature and dropped in a (1:1) water: acetone mixture. The green solid product which precipitated was collected by centrifugation, washed with n-hexane and dried in air. Purification was achieved using column chromatography with silica gel as the column material and MeOH:THF (2:10) as eluent followed by the addition of (2:1) THF:DMF to elute the second fraction which was the desired product. The product was dried in air and first washed with water/methanol, then NaOH/methanol and finally washed with ethanol, acetone, n-hexane and diethyl ether.

ZnMCsPc (49):

Yield: (0.14 g, 13 %). IR (KBr, cm⁻¹): 3452(O-H), 3330 (N-H) 3128(C-H), 2977 (carboxylic acid OH), 1629 (N-H), 1598 (C=O), 1534(C=C), 1447, 1348, 1300, 1235 (C-O-C) 878, 712 (C-S-C), 701,620, 553. ¹HNMR (DMSO-d₆): δ, ppm 9.01-9.18 (12H, m,

Pc-H), 8.12-8.44 (2H, broad, NH$_2$), 7.27-7.88 (12H, m, aromatic-H), 7.10-7.21 (3H, dd, aromatic-H), 6.41-6.48 (2H, m, S-CH$_2$), 4.53-4.59 (1H, br, OH) 3.62-3.71 (1H, br, C-H). UV/Vis (DMF) λ_{max} nm (log ε): 346 (3.67) 678 (5.09).Calc. for C$_{53}$ H$_{33}$ N$_9$ S$_1$ O$_5$ Zn: C 65.45, H 3.39, N 12.96, S 3.29 Found: C 64.98, H3.41, N13.01, S 3.13 MALDI TOF MS Mw: Calcd: 973.36 Da, Found: [M-H]$^-$972.82 Da.

(OH)$_2$SnMCsPc (50):

Yield: (15%) (0.34 g). IR (KBr, cm^{-1}): 3447(O-H), 3319 (N-H) 3121(C-H), 2980 (carboxylic acid OH), 1620 (N-H), 1616 (C=O), 1540(C=C), 1468, 1358, 1335, 1234 (C-O-C) 1099, 885, 717 (C-S-C), 694, 624, 563 (Sn-O). ^{1}HNMR (DMSO-d$_6$): δ, ppm 9.37-9.25 (12H, m, Pc-H), 8.67-8.52 (12H, m, aromatic-H), 8.31-8.53 (2H, broad, NH$_2$) 7.72-7.64 (3H, dd, aromatic-H), 6.37-6.25 (2H, d, S-CH$_2$), 4.44-4.37 (1H, br, OH) 3.51-3.43 (1H, br, C-H). UV/Vis (DMF) λ_{max} nm (log ε): 366 (3.97) 671 (4.84). Calc. for C$_{53}$H$_{35}$N$_9$SO$_7$Sn + H$_2$O: C 59.01, H 3.43, N 11.69, S 2.97 Found: C 58.97, H 3.10, N 12.01, S 3.15 MALDI TOF MS Mw: Calcd: 1060.67 Da, Found: [M+2H] 1062.70 Da.

(OH)$_2$GeMCsPc (51):

Yield: (9%) (0.22 g). IR (KBr, cm^{-1}): 3441(O-H), 3332 (N-H), 3125(C-H), 2986 (carboxylic acid OH), 1630 (N-H), 1621 (C=O), 1525(C=C), 1433, 1339, 1317, 1237 (C-O-C) 978, 858, 716 (C-S-C), 701 (Ge-O), 637, 547. ^{1}HNMR (DMSO-d$_6$): δ, ppm 9.35-9.21 (12H, m, Pc-H), 8.46-8.32 (12H, m, aromatic-H), 8.07-8.24 (2H, broad, NH$_2$), 7.67-7.51 (3H, dd, aromatic-H), 6.26-6.21 (2H, m, S-CH$_2$), 4.37-4.32 (1H, br, OH) 3.57-3.43

(1H, br, C-H). UV/Vis (DMF) λ_{max} nm (log ε): 351 (4.11) 691 (5.04). Calc. for

$C_{53}H_{35}N_9SO_7Ge$ + H_2O: C 61.64, H 3.58, N 12.21, S 3.11 Found: C 61.93, H 3.67, N

12.01, S 2.96 MALDI TOF MS Mw: Calcd: 1014.61 Da, Found: $[M+H]^+$1015.62 Da.

OTiMCsPc (52):

Yield: (11%) (0.26 g). IR (KBr, cm^{-1}): 3444(O-H),3324 (N-H), 3136(C-H), 2972

(carboxylic acid OH),1629 (N-H), 1607 (C=O), 1543(C=C), 1519, 1469, 1385, 1332, 1238

(C-O-C) 1077, 988 (Ti=O), 864, 717 (C-S-C), 704, 633, 569. NMR (DMSO-d$_6$): δ, ppm

9.67-9.61 (12H, m, Pc-H), 8.75-8.65 (12H, m, aromatic-H), 7.98-8.24 (2H, broad, NH_2),

7.46-7.39 (3H, dd, aromatic-H), 6.33-6.28 (2H, m, S-CH_2), 4.51-4.47 (1H, br, OH) 3.78-

3.70 (1H, br, C-H). UV/Vis (DMF) λ_{max} nm (log ε): 336 (3.74) 680 (4.98). Calc. for

$C_{53}H_{33}N_9SO_6Ti$: C 65.49, H 3.39, N 12.97, S 3.29 Found: C 65.52, H 3.42, N 13.12, S

3.44 MALDI TOF MS Mw: Calcd: 971.85 Da, Found: $[M-H]^-$970.86 Da.

2.4.2.3 Hexakis {9; 10, 16; 17, 23; 24 – [1,2-bis-(diethylaminoethylthio)]-2-(4 phenoxycarboxy) phthalocyaninato} Zn (53), Sn (OH)₂ (54), Ge (OH)₂ (55) and TiO (56) (Scheme 3.2).

Synthesis for **53**, **54,** **55** and **56** was as outlined for **49-52** except that 4-(3,4-

dicyanophenoxy)benzoic acid (**65**) [98] (0.68 g, 2.6 mmol) and 1,2-bis-

(diethylaminoethanethio)-4, 5-dicyanobenzene (**64**) [372, 373] (3.04 g, 7.8 mmol) was

employed instead of **72** and **63**. Purification was achieved using column

chromatography with neutral alumina as the column material and DCM:MeOH:THF

(10:5:5) as the eluent, followed by drying. The desired product was first washed with water/methanol, then NaOH/methanol and finally washed with ethanol, acetone, n-hexane and diethylether.

ZnMPCPc (53):

Yield: (0.26 g, 15 %). IR (KBr, cm^{-1}): 3438(O-H), 3134(C-H), 2969 (carboxylic acid OH), 1610 (C=O) 1548(C=C), 1345, 1337, 1131, 854, 748 (C-S-C), 620, 553. ^{1}H-NMR (DMSO-d$_6$): δ, ppm 10.01-10.09 (6H, m, Pc-H), 9.36-9.49 (3H, br, Pc-H), 7.35-7.23 (4H, m, aromatic), 4.63-4.71 (1H, br, OH), 3.25-3.30 (12H, m, S-CH$_2$), 2.98-3.01 (12H, m, N-CH$_2$), 2.56-2.71 (24H, m, CH$_2$-methyl) 1.73-1.79 (36H, q, CH$_3$). UV/Vis (DMF) λ$_{max}$ nm (log ε): 384 (3.95) 695 (5.12).Calc. for C$_{75}$ H$_{98}$ N$_{14}$ S$_6$ O$_3$ Zn + H$_2$O: C 59.31, H 6.45, N 12.91, S 12.67 Found: C 59.48, H 5.70, N 13.17, S 12.74. MALDI TOF MS Mw: Calcd: 1500.5 Da, Found: [M+2H] = 1502.6 Da.

(OH)$_2$SnMPCPc (54):

Yield: (11%) (0.40 g). IR (KBr, cm^{-1}): 3420 (O-H), 3130(C-H), 2969 (carboxylic acid OH), 1614 (C=O) 1553(C=C), 1513, 1422, 1316, 1094, 997, 759 (C-S-C), 631, 614,560, (Sn-O), 543. ^{1}H-NMR (DMSO-d$_6$): δ, ppm 10.13-10.02 (6H, m, Pc-H), 9.42-9.34 (3H, br, Pc-H), 7.57-7.46 (4H, m, aromatic), 4.55-4.47 (1H, br, OH), 3.63-3.58 (12H, m, S-CH$_2$), 3.39-2.31 (12H, m, N-CH$_2$), 2.26-2.17 (24H, m, CH$_2$-methyl) 2.01-1.96(36H, q, CH$_3$). UV/Vis (DMF) λ$_{max}$ nm (log ε):   362 (3.71) 726 (4.90). Calc. for

$C_{75}H_{100}N_{14}S_6O_5Sn$: C 59.73, H 6.29, N 12.35, S 12.12 Found: C 57.03, H 5.99, N 12.18, S 12.42. MALDI TOF MS Mw: Calcd: 1587.81 Da, Found: [M+3H] 1590.80 Da.

$(OH)_2GeMPCPc$ (55):

Yield: (16%) (0.61 g). IR (KBr, cm^{-1}): 3410(O-H), 3131(C-H), 2970 (carboxylic acid OH), 1612 (C=O) 1550(C=C), 1435, 1328, 1116, 947, 750 (C-S-C), 700 (ge-O) 634, 544. ^{1}H-NMR (DMSO-d$_6$): δ, ppm 10.33-10.26 (6H, m, Pc-H), 9.47-9.40 (3H, br, Pc-H), 7.62-7.56 (4H, m, aromatic), 4.48-4.41 (1H, br, OH), 3.52-3.43 (12H, m, S-CH$_2$), 3.10-2.89 (12H, m, N-CH$_2$), 2.51-2.38 (24H, m, CH$_2$-methyl) 1.97-1.81 (36H, q, CH$_3$). UV/Vis (DMF) λ_{max} nm (log ε): 345 (3.64) 614 (5.00).Calc. for $C_{75}H_{100}N_{14}S_6O_5Ge$: C 68.15, H 6.49, N 12.72, S 12.48 Found: C 67.85, H 6.55, N 12.61, S 12.72. MALDI TOF MS Mw: Calcd: 1541.75 Da, Found: [M+] 1541.74 Da.

OTiMPCPc (56):

Yield: (15%) (0.54 g). IR (KBr, cm^{-1}): 3415 (O-H), 3128(C-H), 2973 (carboxylic acid OH), 1617 (C=O) 1549(C=C), 1500, 1428, 1342, 1120, 1038,985 (Ti=O), 754 (C-S-C), 621, 565. ^{1}H-NMR (DMSO-d$_6$): δ, ppm 10.30-10.25 (6H, m, Pc-H), 9.50-9.43(3H, br, Pc-H), 7.61-7.56 (4H, m, aromatic), 4.44-4.37 (1H, br, OH), 3.58-3.49 (12H, m, S-CH$_2$), 3.21-2.43 (12H, m, N-CH$_2$), 2.28-2.16 (24H, m, CH$_2$-methyl) 1.95-1.77(36H, q, CH$_3$). UV/Vis (DMF) λ_{max} nm (log ε): 360 (4.22) 727 (4.93).Calc. for $C_{75}H_{98}N_{14}S_6O_4Ti$: C

60.09, H 6.54, N 13.08, S 12.84 Found: C 59.66, H 5.82, N 12.85, S 12.53. MALDI TOF

MS Mw: Calcd: 1498.99 Da, Found: [M+2H] 1500.98 Da.

2.4.2.4 Tris [9 (10), 16 (17), 23 (24)-4-(2-diethylaminoethanethiol)-2-(4-carboxyphthalonitrile) phthalocyaninato] Zn (57), (ac)₂Sn (58), (OH)₂Ge (59) and OTi (60), Scheme 3.3

A mixture of 4-carboxyphthalonitrile (**66**) (0.22 g, 1.3 mmol) and 4-(2-diethylaminoethanethiol) phthalonitrile (**67**) (0.99 g, 3.9 mmol) was firstly finely ground and homogenised and placed in a round bottom flask that contained pre-heated pentanol. The mixture was then stirred under reflux at 160 ˚C for 26 h under an argon atmosphere in the presence of excess (6.0 mmol) zinc (II) acetate (or Sn (IV) acetate, or Ge (IV) chloride, or Ti (IV) butoxide) as a metal salt and DBU (0.25 mL) as a catalyst. Thereafter, the mixture was cooled to room temperature and dropped in n-hexane to precipitate. The green solid product was precipitated, collected by centrifugation and washed with n-hexane and dried in air. Purification was achieved using column chromatography with neutral alumina as column material and DCM:MeOH:THF (10:3:3) as eluent, followed by drying. The desired product was first washed with water/methanol, then NaOH/methanol and finally washed with ethanol, acetone, n-hexane and diethylether in a Soxhlet extraction apparatus.

ZnMCPc (57):

Yield: (11 %) (0.12 g). IR (KBr, cm⁻¹): 3435(OH), 3214(C-H), 2850-2985(carboxylic acid OH), 1724 (C=O), 1489(C=C), 1346, 1233, 989(Ti=O), 952, 746 (C-S-C),643, 572. ¹H-

NMR (DMSO-d$_6$): δ, ppm 8.89-8.78 (9H, m, Pc-H), 8.64-8.57 (3H, d, Pc-H), 3.62-3.55 (12H, m, S-CH$_2$), 2.99-2.90 (12H, m, N-CH$_2$), 2.13-2.01 (18H, dd, CH$_3$). UV/Vis (DMF) λ$_{max}$ nm (log ε): 342 (3.52) 688 (4.96).Calc. for C$_{51}$N$_{11}$H$_{55}$O$_2$S$_3$Zn: C 60.03, H 5.42, N 15.18, S 9.48 Found: C 59.75, H 5.31, N 14.96, S 9.51. MALDI TOF MS Mw: Calcd: 1015.22 Da, Found: [M-2H] 1013.30 Da.

(ac)$_2$SnMCPc (58):

Yield: (8 %). IR (KBr, cm^{-1}): 3439(O-H), 3213(C-H), 2824-2897 (carboxylic acid OH), 1715 (C=O), 1587(C=C), 1326, 1335 (C-O), 1265, 829, 758 (C-S-C), 673, 559 (Sn-O). ^{1}H-NMR (DMSO-d$_6$): δ, ppm 9.10-9.19 (9H, m, Pc-H), 8.64-8.67 (3H, br, Pc-H), 4.15-4.22 (6H, m, ac-CH$_3$) 3.81-3.88 (12H, m, S-CH2), 3.14-3.20 (12H, q, N-CH$_2$), 2.10-2.16 (18H, dd, CH$_3$). UV/Vis (DMF) λ$_{max}$ nm (log ε): 330 (3.47), 720 (4.90). Calc. for C$_{51}$N$_{11}$H$_{55}$O$_2$S$_3$Sn: C 57.52, N 14.43, H 5.51, S 9.01; Found: C 57.74, N 13.55.H 6.39, S 8.52MALDI TOF MS Mw: Calcd: 1185.71 Da, Found: [M-H]$^+$ 1184.80 Da.

(OH)$_2$GeMCPc (59):

Yield: (10%). IR (KBr, cm^{-1}): 3447(O-H), 3123(C-H), 2854-2969 (carboxylic acid OH), 1731 (C=O), 1559(C=C), 1447, 1348, 1128, 843, 748 (C-S-C), 701(Ge-O), 610, 543. ^{1}H-NMR (DMSO-d$_6$): δ, ppm 9.17-9.19 (9H, m, Pc-H), 8.27-8.29 (3H, br, Pc-H), 4.73-4.78 (2H, br, OH) 3.37 (12H, m, S-CH$_2$), 2.13-2.24 (12H, q, N-CH$_2$), 1.67-1.74 (18H, dd, CH$_3$). UV/Vis (DMF) λ$_{max}$ nm (log ε): 350 (3.26), 695 (4.87). Calc. for C$_{51}$

$N_{11}H_{57}O_4S_3Ge$: C 57.98, N 14.59, H 5.39, S 9.11; Found: C 56.32, N 13.17.H 5.39, S

10.47. MALDITOFMS Mw: Calcd: 1055.59 Da, Found: $[M-3H]^+$1053.18 Da.

OTiMCPc (60):

Yield: (8 %). IR (KBr, cm^{-1}): 3439(O-H), 3213(C-H), 2850-3000 (carboxylic acid OH),

1719 (C=O), 1491(C=C), 1353, 1238, 987(Ti=O), 962, 742 (C-S-C), 572. ^{1}H-NMR

(DMSO-d$_6$): δ, ppm 8.91-8.99 (9H, m, Pc-H), 8.57-8.62 (3H, br, Pc-H), 3.58-3.60 (12H,

m, S-CH2), 2.96-3.01 (12H, m, N-CH$_2$), 1.98-2.01 (18H, dd, CH$_3$). UV/Vis (DMF) λ_{max}

nm (log ε): 340 (3.31), 734 (4.91).Calc. for $C_{51}N_{11}H_{55}O_3S_3Ti + H_2O$: C 59.32, N 15.20,

H 5.52, S 9.32; Found: C 58.69, N 14.43, H 4.29, S 8.73. MALDITOFMS Mw: Calcd:

1012.88 Da. Found: $[M+H]^+$ 1013.58 Da.

2.4.2.5 Synthesis of bis-(1,6-hexanedithiol)SiPc [SiHDTPc (61)] complex, (Scheme 3.4)

The formation of bis-(1,6-hexanedithiol)SiPc complex was accomplished by heating

$((Cl)_2SiPc)$ (2.0 g , 3.27 mmol) in DMF in the presence of 1,6-hexanedithiol (1.0 g, 6.6

mmol) under an argon atmosphere, and under reflux at 120°C for 5 h. The dark blue

crude product was precipitated out with 1:2 ratio of methanol and water and

washed with methanol, ethanol, ethyl acetate, acetone and diethyl ether under

Soxhlet extraction.

Yield: (65 %). IR (KBr, cm^{-1}): 3432(O-H), 3123(C-H), 1557(C=C), 1500, 2593(S-H),

1474, 1350 (CH$_2$), 1235 (C-S), 1092(C-S), 843, 748. ^{1}H-NMR (DMSO-d$_6$): δ, ppm 8.67-

8.96 (8H, m, Pc-H), 9.25-9.38 (8H, m, Pc-H), -1.43 to -1.76 (4H, dd, axial ligand), -2.17 to -2.35 (8H, m, axial ligand-H), -2.39 to -2.87 (4H, dd, axial ligand), -3.14 to -3.87 (8H, m, axial ligand-H). UV/Vis (DMF) λ_{max} nm (log ε): 340, (3.76), 676 (5.02). Calc. for $C_{44}H_{42}N_8S_4Si$: C 62.96, H 5.01, N 13.36, S 15.32; Found: C 62.51, H 4.43 N 12.97, S 15.61. MALDI-TOF-MS Mw Calc: 838.02 Da; Found (M + 2H): 840.1 Da.

2.4.3   Preparation of MPc-MNPs conjugates

2.4.3.1 Synthesis of MPc-GSH capped AuNP conjugates (Scheme 3.5)

Complexes **58**, **59** and **60** were employed in the synthesis of these conjugates, as examples. Each of the monocarboxy Pc (10 mg) was firstly dissolved in DMF (10 mL), then 30 mg DCC was added to convert the carboxylic group (–COOH) of the Pc into an active carbodiimide ester group. The mixtures were left to stir at room temperature under a nitrogen atmosphere for 48 h. After this time, 20 mL GSH-AuNPs in (1:1) water:DMF solvent mixture was added to the activated Pc and the mixture stirred for 48 h to allow for conjugation of the Pc to the GSH-AuNP to take place. After 48 h, the conjugates were separated from un-conjugated nanoparticles using an alumina chromatographic column, first using (1:1) 0.1M NaOH:methanol to elute the nanoparticles followed by (5:1) DMF:methanol mixture to elute the conjugate. In order to ensure that the conjugate were free of unreacted Pcs and AuNPs, the solution of the conjugates were run through a size-exclusion column (Bio-Beads S-X1 from Bio-Rad) using THF: methanol (2:1) as an eluent. And 69% for **58**, 71% for **59** and 70 % for **60** product yields for the were obtained respectively.

2.4.3.2 Synthesis of MPc-AgNPs conjugates (Scheme 3.6)

Complexes **49**, **50**, **51** and **52** were employed in the synthesis of the conjugates with the spherically, triangular and cubic structured AgNPs. Amino groups and carboxylic groups are known to adsorb stronger onto the surface of AgNPs than in AuNPs. Briefly, a solution consisting of 80 µM (5 ml) of various MPc complexes was mixed with 15 ml (~1.0 absorbance SPR) of each of the differently shaped AgNPs in DMF and allowed to react with stirring in the dark for 72 h to allow for adsorption of the Pcs onto the surface of the nanoparticle. The conjugates were then characterized with various techniques as discussed later in chapter three.

2.4.3.3 Formation of SiHDTPc or ZnPc– AgNPs or AuNPs conjugates (Scheme 3.7)

Unsubstituted ZnPc and SiHDTPc (**61**) were employed for this particular type of NP-Pc conjugates, formed via axial coordination. In the synthesis of SiHDTPc-AgNP conjugates**,** a solution of SiHDTPc (10 ml of 100 µM) was mixed with 15 ml of uncapped AgNPs in DMF (absorbance ~0.8 surface plasmon resonance, SPR band) and allowed to react whilst stirring in the dark under an argon atmosphere for 48 h (at room temperature). After this time, the SiHDTPc stabilized AgNPs were obtained and characterized. With the synthesis of SiHDTPc-AuNPs**,** the procedure, conditions and amounts of reagents were the same as for SiHDTPc-AgNP conjugates, except that TOABr stabilized AuNPs were employed instead of uncapped AgNPs.

Similarly the ZnPc – AgNP or AuNP conjugates were also synthesized as for the SiHDTPc-MNPs conjugates except that 4-mercaptopyridine stabilized MNPs (M = Au or Ag) were employed instead of uncapped AgNPs or TOABr capped AuNPs.

The amounts of reagents and the procedures were kept the same except that the reactions were carried out at 80 °C for 48 h instead of at room temperature. 4-Mercaptopyridine capped spherical AgNPs were similarly conjugated to ZnPc derivatives (**49, 53, 57, 68-70**). The conjugates were characterized using transmission electron microscopy (TEM), powder X-ray diffraction (XRD), UV-Vis and FTIR spectroscopies, all discussed later in this thesis.

2.4.3.4 Synthesis of quantum dots - phthalocyanine conjugates (Scheme 3.8)

Complexes **49, 53, 58, 59** and **60** were employed (as examples) for all the Pc ring system type. The quantum dot - phthalocyanine conjugates were synthesized and purified as follows: Each of the monocarboxy Pcs (10 mg, ~1.0×10^{-5} mol) was first dissolved in DMSO (10 mL), then 30 mg DCC added to convert the carboxylic group (–COOH) of the MPcs into an active carbodiimide ester group. The mixture was left to stir at room temperature under a nitrogen atmosphere for 48 h. After this time, 5 mL of the CdTe@ZnS-CALNN QDs in a water:DMSO (2: 8 ratio) solvent mixture was added to the activated Pc and the mixture stirred for 48 h to allow the conjugation of the Pc to the QDs to take place. This solvent mixture was employed to allow for both MPc complexes and CdTe@ZnS-CALNN to dissolve. The linked QD–MPc conjugates were purified by washing firstly with water to remove excess DCC and unlinked QDs (as the linked conjugates are not soluble in water). The sample was then run through a size-exclusion column (Bio-Beads S-X1 from Bio-Rad) using DMSO: methanol (2:1) as an eluent to separate any residual impurities (such as unlinked MPcs) from the linked conjugate, which eluted first, whilst the remaining bands are discarded. The concentration of quantum dot solution was estimated from

the size dependent molar extinction coefficient according to literature [377]; their

molar extinction coefficients were found to be 36600 cm^{-1} M^{-1} for CdTe-TGA QDs1

and 41902 cm^{-1} M^{-1} for CdTe-TGA QDs2. These values were also used for the

CdTe@ZnS, hence they are an estimation for the coreshell QD. A molar ratio of 1.5:1

(MPcs: QD) for the mixed solutions was employed for FRET studies where the MPc

was mixed with QDs without formation of a chemical bond. This is the same ratio

employed in the synthesis of the linked complex, but since the actual amounts of

QDs in the linked complexes is not known precisely, the linked and mixed MPc:QDs

may involve different ratios, hence for the comparison, in discussing the results, this

has to be considered.

2.4.4   Preparation of Pc and Pc-AgNPs modified electrospun nanofibers

The phthalocyanines which were employed for these studies were unsubstituted

ZnPc and complexes **49, 53, 58**, **59**, **60,** and **71** which were electrospun into

polystyrene polymer fibers and their antimicrobial activities compared. In another

set of experiments, the unsymmetrically substituted zinc complexes (**49, 53**, and **57**),

together with their symmetrical counterparts (**70, 69** and **68**), were electrospun alone

and in the presence of AgNPs for growth inhibition bacterial studies.

The polystyrene polymer was employed to enable electrostatic and π–π interaction

between the styrene aromatic systems and the Pcs, and this should prevent leaching

of the Pcs from the polymer fibers during application. The fibers were prepared by

mixing the Pc (or Pc-AgNPs) with the polymer solution and the mixture electrospun

into fibers. The same molar amounts of the particular Pc was added into each

polymer solution for comparison. Briefly, the following conditions were used: a solution containing 2.5 g (1.3 x 10^{-5} moles of polystyrene (PS)) and the mass equivalent (in mg 1.2 x 10^{-6} moles) of the phthalocyanine in 10 mL DMF/THF (4:1) was stirred for 24 h to produce a homogeneous solution. A solvent mixture of DMF/THF was employed to allow both the PS and MPc to dissolve. The solution was then placed in a cylindrical glass tube fitted with a capillary needle. A potential difference of 20 kV (-5 to 15 kV) was applied to provide charge for the electrospinning process.

The distance between the cathode (static fiber collection point) and anode (tip of capillary needle) was 15 cm and the syringe set at a pump rate of 0.5 mL/h for the electrospun polystyrene polymer fibers without the phthalocyanine molecules. All experimental conditions were maintained except that the flow rate was increased to 1 mL/h with the polystyrene/phthalocyanine composite to avoid clogging of the needl

Results and discussion

Chapter 3:

3.1 Synthesis and characterization of phthalocyanines

3.2 Synthesis and characterization of nanoparticles and their phthalocyanine conjugates

3.3 Preparation and characterization of MPc supported polymer fibers

Chapter 4:

Photophysical and photochemical properties

Chapter 5:

Photodynamic antimicrobial chemotherapeutic properties

Chapter 6:

Attempts to bind SiPc to metallothionein protein

Chapter 7:

Conclusions and future prospects

Publications

The results presented in the next section have been published as articles or submitted to peer-reviewed journals. The details of these publications are listed below and are not referred to in this thesis.

1. **Nkosiphile Masilela** and Tebello Nyokong

    The synthesis and fluorescence behavior of new unsymmetrically mono-functionalized carboxy Ge, Ti and Sn phthalocyanines

    Dyes & Pigments 91 (2011) 164-169

2. **Nkosiphile Masilela** and Tebello Nyokong

    Conjugates of low-symmetry carboxy Ge, Sn and Ti phthalocyanines with glutathione caped gold nanoparticles: An investigation of photophysical behavior.

    J. Photochem. Photobiol. A: Chem. **223 (2011) 124-131**

3. **Nkosiphile Masilela** and Tebello Nyokong

    The photophysical and energy transfer behavior of low symmetry phthalocyanine complexes conjugated to coreshell quantum dots; an energy transfer study

    J. Photochem. Photobiol. A: Chem. **247 (2012) 82-92**

4. **Nkosiphile Masilela** and Tebello Nyokong

    Synthesis and physicochemical behavior of new low symmetry Ge, Ti and Sn phthalocyanines: effect of central metal

    Synthetic metals, 162 (2012) 1839-1845

5.   **Nkosiphile Masilela**, Phumelele Kleyi, Zenixole Tshentu, Georgios

Priniotakis, Phillipe Westbroek and Tebello Nyokong

Photodynamic antimicrobial inactivation of *Staphylococcus aureus* using low

symmetrically substituted phthalocyanines supported on a polystyrene

polymer fiber

Dyes & Pigments, 96 (2013) 500-508

6.   **Nkosiphile Masilela** and Tebello Nyokong, The interaction of silver

nanoparticles with low symmetry cysteinyl phthalocyanines and their

antimicrobial effect.

J. Photochem. Photobiol. A: Chem. **255 (2013) 1– 9**

7.   **Nkosiphile Masilela,** Edith Antunes and Tebello Nyokong

Axial coordination of zinc and silicon phthalocyanines to silver and gold

nanoparticles: an investigation of their photophysicochemical and

antimicrobial behaviour.

Jornal of Pophyrins and Phthalocyanines. **Article in press**

Side publications:

8.   Zafar Iqbal, **NkosiphileMasilela**, Tebello Nyokong, Alexey Lyubimtsev,

Michael Hanack, Thomas Ziegler

Spectral, photophysical and photochemical properties of tetra- and

octaglycosylated zinc phthalocyanines

Photochem. Photobiol. Scie. 11 (4) (2012) 679 – 686

9.   Nomasonto Rapulenyane, Edith Antunes, **Nkosiphile Masilela**, Tebello

        Nyokong

        Synthesis and photophysicochemical properties of novel zinc phthalocyanines

        mono substituted with carboxyl containing functional groups,

        J. Photochemistry and Photobiology A: Chemistry 250 (2012) 18–24

CHAPTER 3

3.1 Synthesis and characterization of phthalocyanines

3.1.1 Synthesis
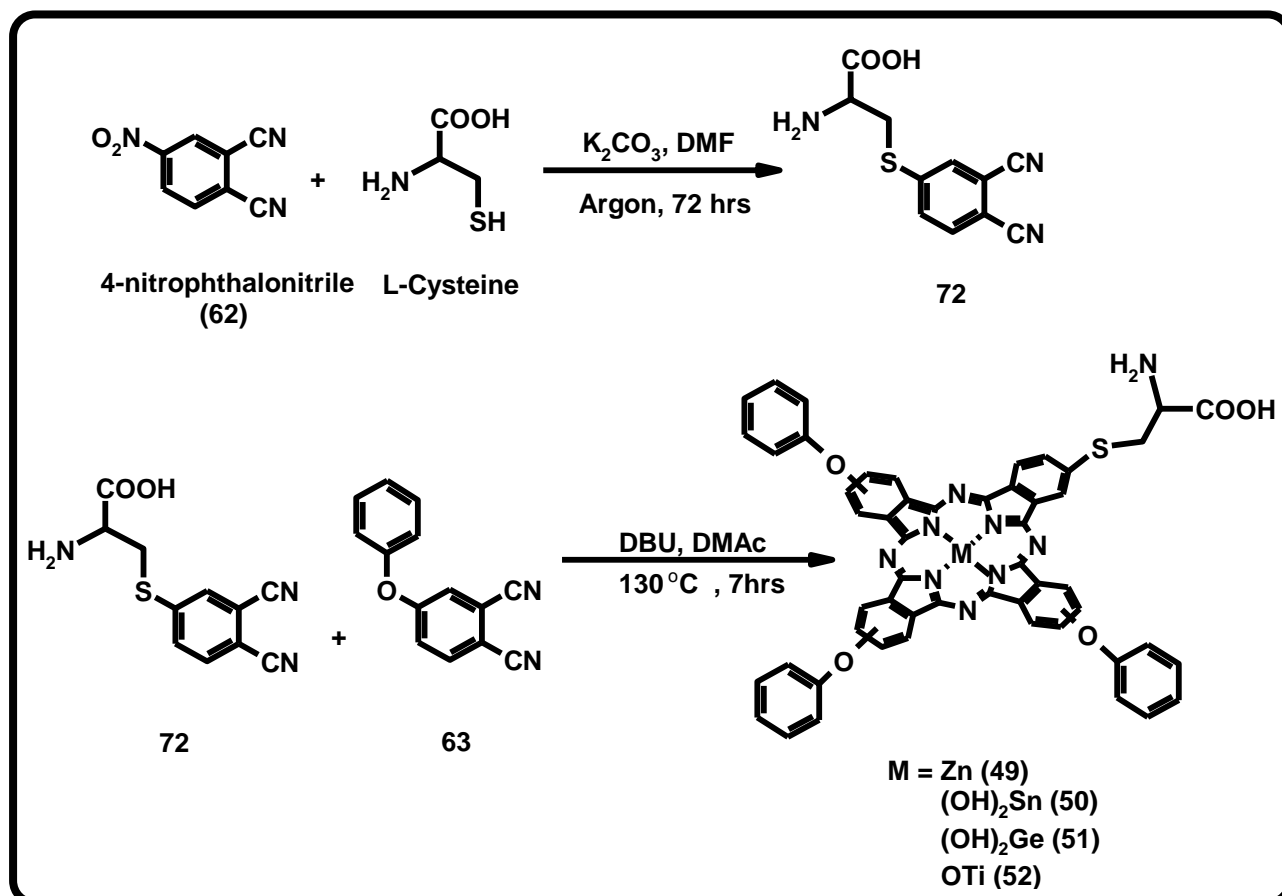
Scheme 3.1: Synthesis of 4-cysteinyl phthalonitrile (72) and the corresponding tetra substituted monocysteinyl ZnMCsPc (49), (OH)₂SnMCsPc (50), (OH)₂GeMCsPc (51), and OTiMCsPc (52) phthalocyanine complexes.

The synthesis of the phthalonitrile consisting of a cysteinyl moiety (**72**) was achieved via the route shown in Scheme 3.1, and gave satisfactory characterization results corresponding to the predicted structure.
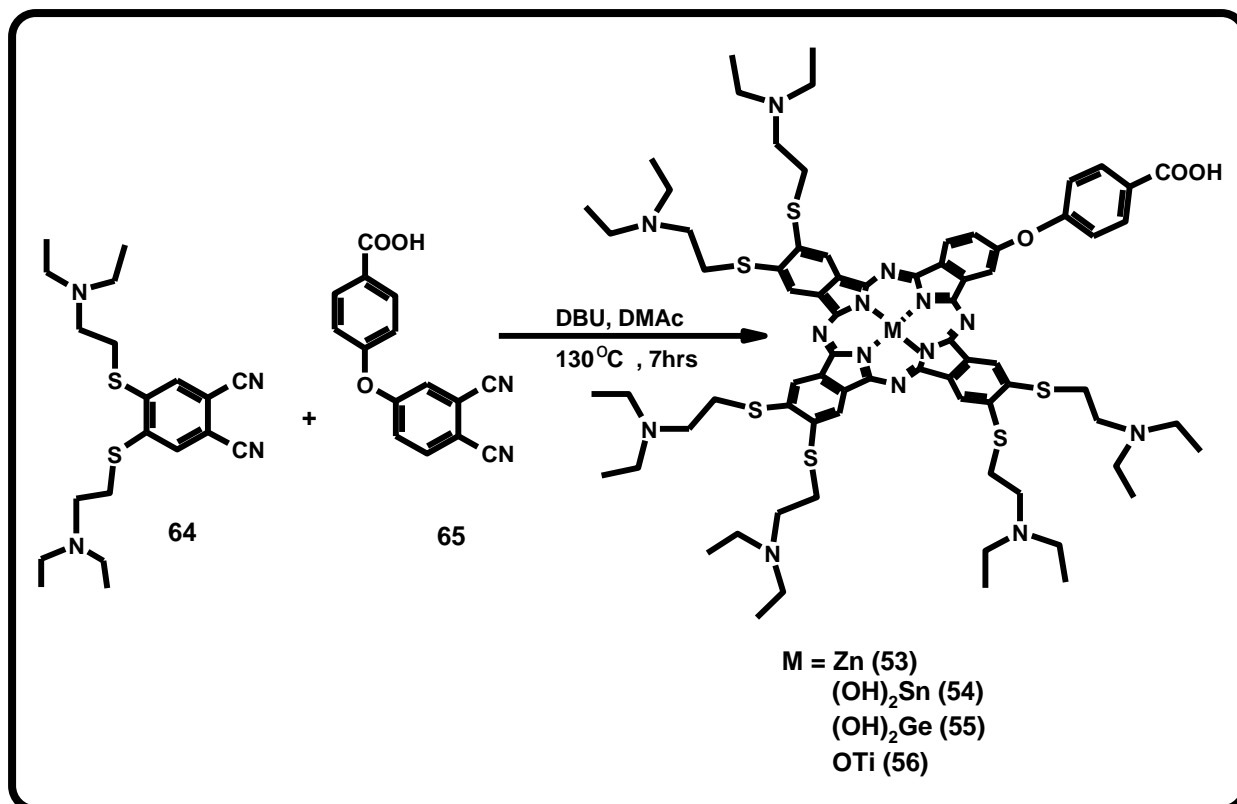
Scheme 3.2: Synthesis of low symmetry monophenoxy-carboxy ZnMPCPc (53), (OH)₂SnMPCPc (54), (OH)₂GeMPCPc (55), OTiMPCPc (56) phthalocyanine complexes

Schemes 3.1 and 3.2 show the routes used in the synthesis of complexes (**49, 50, 51 and 52)** and **(53**, **54**, **55** and **56)**, respectively.

The synthesis of these low symmetry MPc complexes involved the statistical mixed condensation method. This method involves two differently substituted phthalonitrile precursors (in a 3:1 mol ratio), **63 (B)** and **72 (A)** for synthesis of complexes **49, 50, 51** and **52**   (Scheme 3.1) which theoretically lead to mixtures (**AAAA, AAAB, AABB, ABAB, ABBB**, and **BBBB**) of differently substituted phthalocyanine products as previously reported elsewhere [53-55]. The products were separated by extensive chromatography techniques employing various solvent

mixtures and ratios. A similar synthetic route was employed in the synthesis of complexes of **53, 54, 55** and **56** (Scheme 3.2).

In all cases, after precipitation the crude products were washed with a water: methanol (ratio of 9:1) mixture, and centrifuged to remove the AAAA isomer which is water soluble, followed by washing with 2 % NaOH: methanol (8:2) solution to remove the cis and trans isomers (AABB and ABAB) which are soluble in basic aqueous media. The remaining products which were not water soluble were separated as described in the experimental section to get the desired (ABBB) product. The separation of the desired (ABBB) mono-functionalized Pcs complexes from the various compounds formed during synthesis, was a challenging and a crucial step, and this results in the relatively low yields obtained for the desired products ranging from ~9% to 16%.

The structural analyses of all the newly synthesized complexes (**49-52**, **53-56**) were satisfactory and consistent with the predicted structures as shown in the experimental section. The complexes were successfully characterized using a variety of spectroscopic techniques such as the UV-vis, Maldi-TOF MS, IR, ^{1}H NMR and elemental analyses. The phthalonitrile C≡N vibration in the 2200-2250 cm^{-1} region disappeared upon formation of the low symmetry Pcs (**49-52**, **53-56**), and serves as evidence for the formation of phthalocyanines. The infrared data showed aromatic signals at lower wavenumbers which are the fingerprint regions of phthalocyanine complexes. For complexes **49-52,** a characteristic of N-H stretching mode for primary amino groups [378] was observed in the region 3325-3385 cm^{-1}, which is typical for a cysteine NH$_2$ group. This was supported by a corresponding N-H bending mode in

the 1620-1650 cm^{-1} region. The C-H stretching modes were also observed in the 3100-3200 cm^{-1} region. Phthalocyanine aggregation at the concentrations used for the ^{1}H-NMR measurements leads to broadening and overlap of the aromatic signals [379]. The ^{1}H-NMR spectra of all complexes showed the correct integration characteristics for the aromatic Pc ring protons between 8 and 10 ppm. All the other ^{1}HNMR signals integrated correctly for each complex (**49-52**, **53-56**), giving the expected total number of protons and confirming the relative purity and the predicted structures of the complexes.

Mass spectral data obtained were consistent with the structures presented. MPc complexes have been observed to degrade with a variety of molecular weight peaks [M], [M+nH] or [M-nH] (n = 1–3) [380] being present, thus the observed mass spectral data obtained with the molecular weights containing additional 1 to 3 protons is not surprising. The elemental composition of the various products gave satisfactory results corresponding to all predicted structures and confirming the degree of purity of the compounds.

Scheme 3.3 shows the synthetic route employed for the mono-functionalized carboxy (**57-60**) phthalocyanines. A statistical condensation of phthalonitrile **66**(B) and **67**(A) in a 3:1 mole ratio was employed.
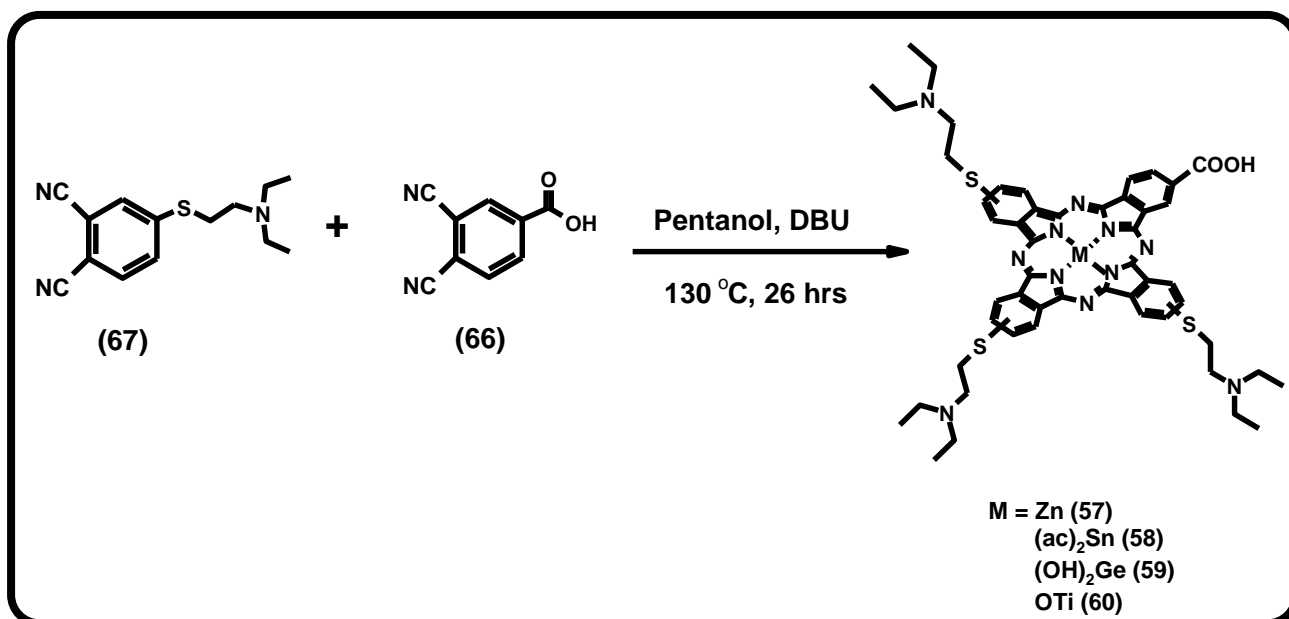
Scheme 3.3: Schematic representation of the statistical synthetic route used for the synthesis of low symmetry monocarboxy ZnMCPc (57), (ac)₂SnMCPc (58) (OH)₂GeMCPc (59), and OTiMCPc (60) phthalocyanine complexes

Phthalonitrile **67** was substituted with bulky groups to enhance the solubility of the low symmetry phthalocyanine, thereby also improving the separation of the various compounds formed. However the separation of the different structures formed was still extremely challenging since it required different solvent ratios with various polarities to elute each compound. Chromatographic separation of the desired product from the other products was undertaken successfully as described in the experimental section. The desired mono functionalized carboxy complexes were obtained in relatively low yields, with complex **57** being obtained with a slightly higher yield of 11 % compared to 8 %, 10% and 8% for complexes **58, 59** and **60** respectively. The structural analyses of all the novel compounds (complex **57-60**) were consistent with the predicted structures. All the ¹HNMR spectral data contained peaks which integrated correctly to give the expected total number of protons for each complex (**57-60**). This then confirmed the relative purity of the

107

complexes as shown in the experimental section. The IR spectra of the complexes showed broad peaks around ~3400-3500 cm^{-1} due to the O–H stretch of the carboxylic acid functional groups, while peaks at ~3000-3200 cm^{-1} are due to C–H stretches, and sharp intense peaks near ~1600 cm^{-1} could be assigned to the C=O groups of the carboxylic acid could also be assigned. The peaks found at 730-750 cm^{-1} are due to C-S-C bond of the substituents. The mass spectra were acquired using α-cyano-4-hydroxycinnamic acid. The matrix employed in this work is known [380] to intensify the fragmentation process, however the observed mass spectral data gave molecular ion peak signals corresponding to the predicted structures as shown in the experimental section. All the other characterization techniques confirmed the structures for each compound as presented in the experimental section in chapter two.
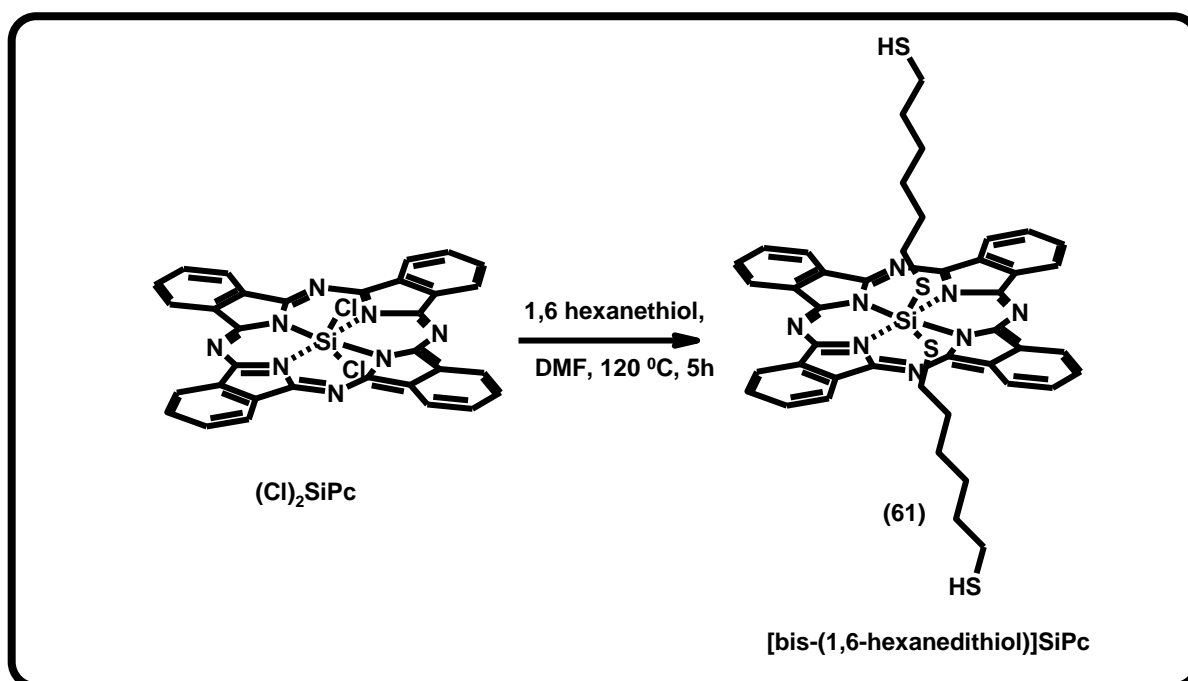
Scheme 3.4. Synthesis of bis-(1,6-hexanedithiol)SiPc (SiHDTPc (61)) complex

SiPc can coordinate a variety of organic ligands via axial ligation [94-96]. The synthesis of the axially ligated alkyldithiol SiPc complex **61** is presented for the first time. The SiHDTPc (**61**) complex was obtained by substitution of the dichloride axial ligands of the SiPc with 1,6-hexanedithiol in the presence of DMF as a solvent. The appearance of S-H (at ~2593 cm^{-1}) signals were observed in the IR spectra of the complex (**61**) suggesting successful substitution. High yields of about 65% were obtained for the complex, and its purity was further confirmed using various characterisation techniques such as UV-Vis, mass spectra, FTIR, ^{1}H NMR and elemental analyses. All techniques gave satisfactory results corresponding to the predicted structure of the complex.

3.1.2 UV-vis spectral characterization
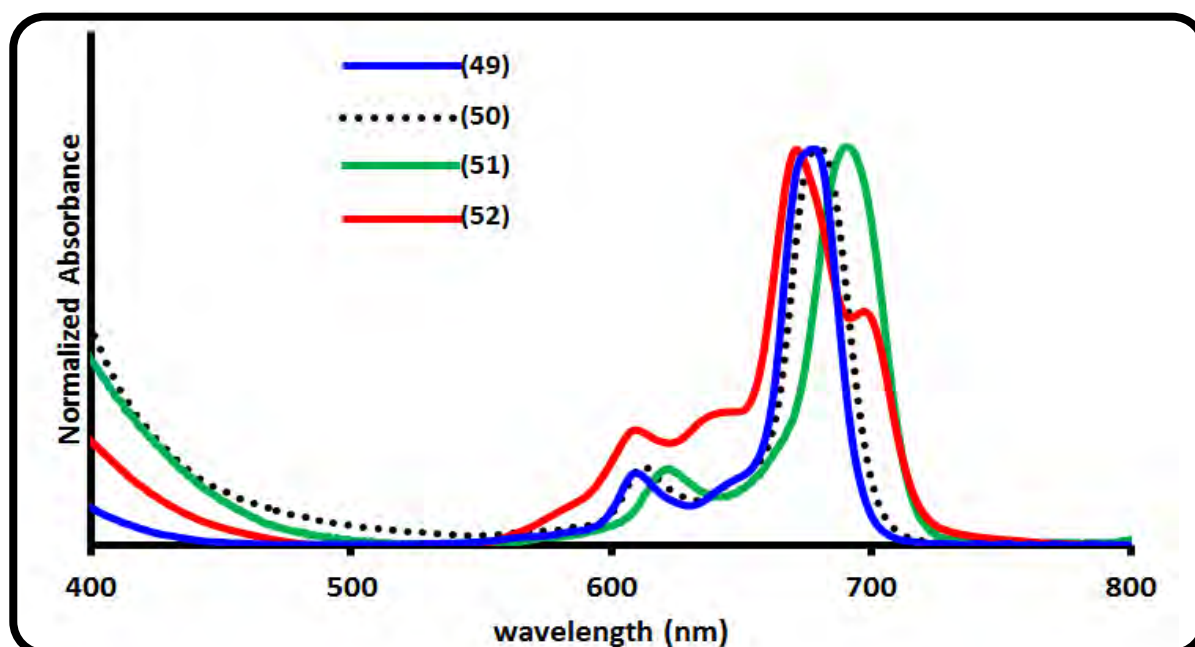
Figure 3.1: Ground state electronic absorption spectra of monocysteinyl ZnMCsPc (49), (OH)₂SnMCsPc (50), (OH)₂GeMCsPc (51), and OTiMCsPc (52) MPc complexes in DMF, conc = 8 × 10⁻⁶ mol.L⁻¹.

The ground state electronic absorption spectra of complexes **49-52**, are presented in Fig. 3.1. A clear split in the Q-band absorption was observed for the titanium phthalocyanine derivative (**52**) in DMF. Broadening and splitting of absorption spectra is known to be due to loss of symmetry [68]. The splitting of spectra is due to the lifting of the degeneracy of the lowest unoccupied molecular orbital (LUMO) to some extent. Interaction between the Pc and the axial ligands has been reported to result in the splitting of the Q-band in TiPc [381], this may explain the split in the Q band for **52**, in addition to loss of symmetry due to unsymmetrical substitution. The OTi (**52**) complex was blue shifted compared to the other complexes. The Q-band absorption (Fig. 3.1) of the germanium phthalocyanine derivative (**51**) was red shifted compared to complex **49**, **50** and **52**, Table 3.1. Metal-dependent shifts in the Q-band for phthalocyanines has been reported where there is considerable deviation from planarity in the macrocycle [382]. A red shift in the Q-band has also been reported with an increase in the covalent radii of the central metal [383]; this is observed in Fig. 3.1. The Q-band absorption spectra of the zinc (**49**) and tin (**50**) derivatives were narrow and they were observed at similar wavelengths, Table 3.1.
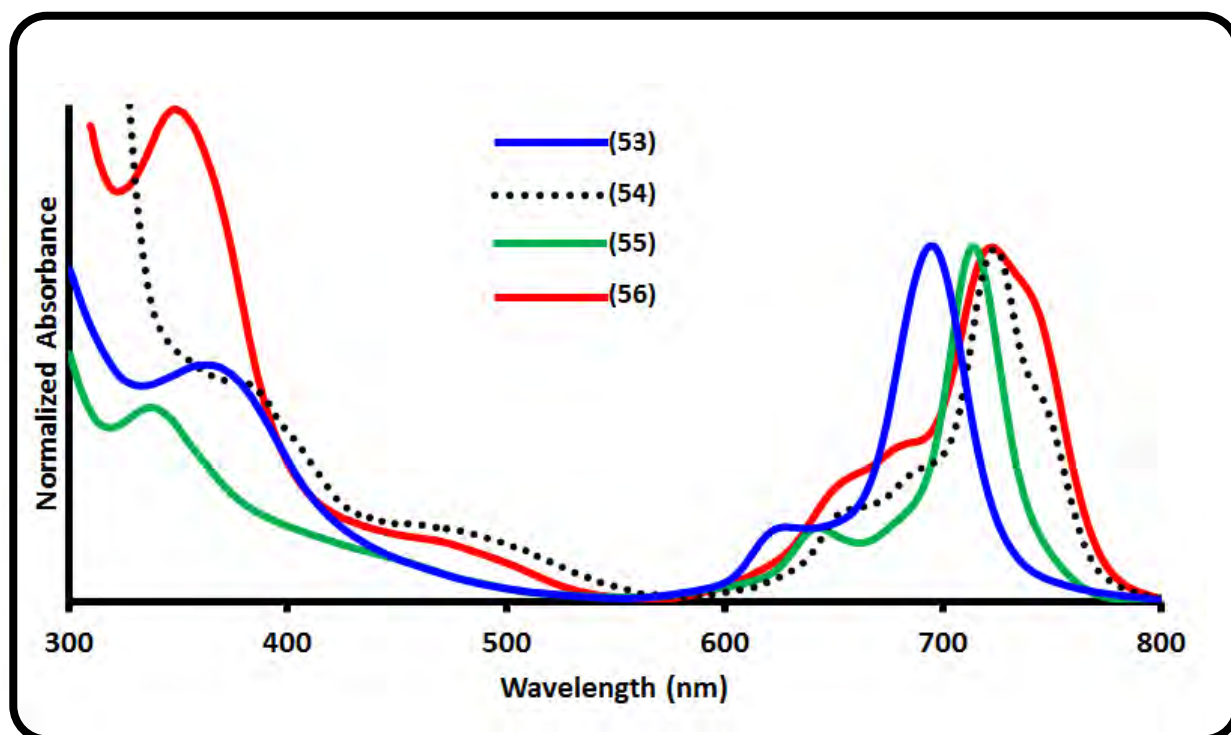
Figure 3.2: Ground state UV-vis spectra of low symmetry monophenoxy-carboxy ZnMPCPc (53), (OH)$_2$SnMPCPc (54), (OH)$_2$GeMPCPc (55), OTiMPCPc (56) phthalocyanine complexes in DMF. conc = 8 × 10^{-6} mol.L^{-1}.

Fig. 3.2 shows the absorption spectra of the low symmetry monophenoxy carboxy complexes (**53-56**) in DMF. A significant split and broadening of the Q band in absorption spectra was observed for the (OH)$_2$Sn (**54**) and OTi (**56**) derivatives in DMF. The broadening of the Q-band in symmetrical Pcs is usually associated with aggregation [133-139], however for unsymmetrically substituted phthalocyanines, lack of symmetry will also result in broadening or splitting of spectra. The corresponding Zn (**53**) and (OH)$_2$Ge (**55**) complexes showed monomeric behaviour and did not show a splitting of the Q-band.

The Q-band absorption spectra of complexes **53-56** were red shifted compared to the **49-56** complexes Table 3.1, due to the high number of electron donating (sulfur) groups present on the periphery. The red shifting observed in the spectra may also

be associated with the conformational distortion caused by the steric hindrance induced by the number of bulky substituents at the periphery of the complexes [384].

Table 3.1.UV-Vis and fluorescence spectral properties of various MPc complexes in DMF.

Compound	Q-abs (nm)	Q-exci (nm)	Q-emi (nm)	Δstokes (nm)	Log ε
ZnMCsPc (49)	678	677	697	20	5.09
(OH)$_2$SnMCsPc (50)	680	681	693	12	4.84
(OH)$_2$GeMCsPc (51)	691	691	698	7	5.04
OTiMCsPc (52)	696,671	693, 672	703	10	4.98
ZnMPCPc (53)	695	700	710	10	5.12
(OH)$_2$SnMPCPc (54)	727, 737	725	738	13	4.90
(OH)$_2$GeMPCPc (55)	714	713	723	10	5.00
OTiMPCPc (56)	726,742	735	747	12	4.93
ZnMCPc (57)	688	688	710	22	4.96
(ac)$_2$SnMCPc (58)	720	712,725	748	23	4.90
(OH)$_2$GeMCPc (59)	695	696	700	4	4.87
OTiMCPc (60)	734	755	765	10	4.91
SiHDTPc (61)	676	676	683	7	5.02

The ground state absorption spectra for complexes **57-60** are shown in Fig. 3.3. A clear broadening of the Q band was observed for the SnPc derivative (**58**). The TiPc derivative (**60**) did not show splitting but the Q band was broadened. The broadening could be due to a lack of symmetry and/or aggregation.
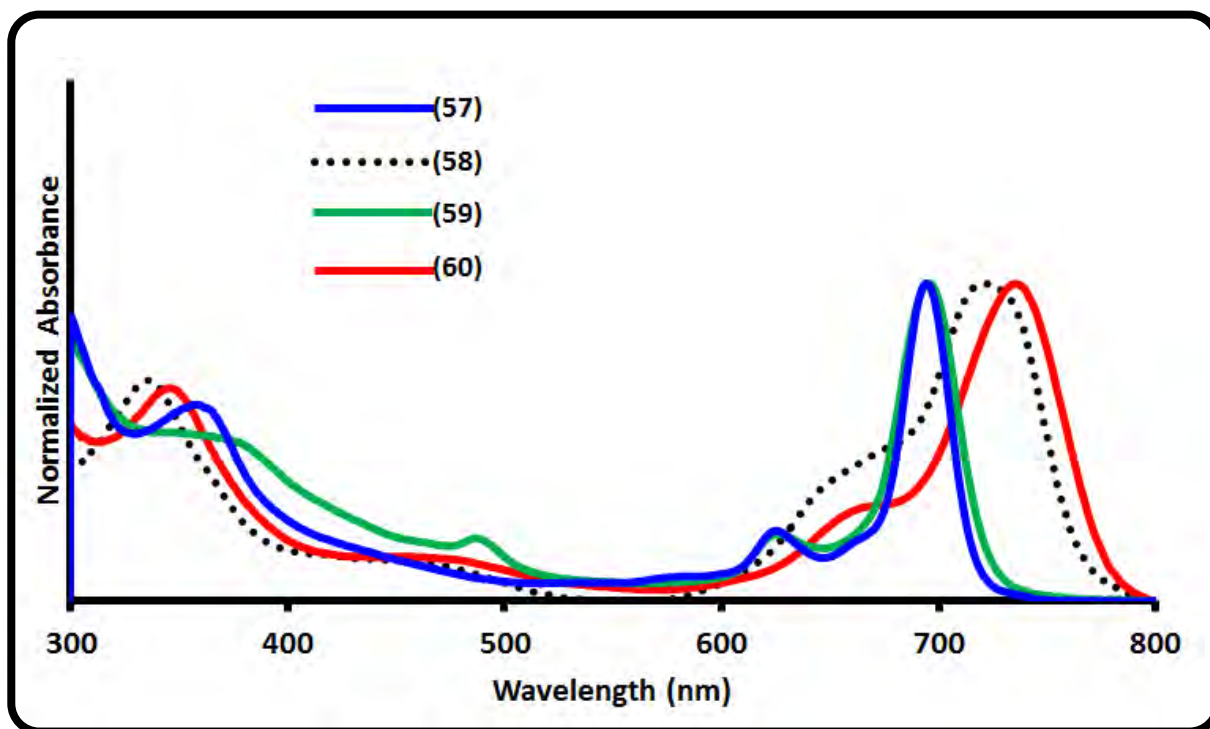
Figure 3.3: Ground state electronic UV-vis spectra of low symmetry monocarboxy ZnMCPc (57), (ac)₂SnMCPc (58), (OH)₂GeMCPc (59), and OTiMCPc (60) phthalocyanine complexes in DMF. conc = 8 × 10⁻⁶ mol.L⁻¹.

Less broadening was observed for the ZnPc and GePc derivative (**57** and **59**). The Q-band absorption maxima in DMF (Fig.3.3) for the various mono-carboxy Pc's were observed at completely different wavelengths (Table 3.1). As shown in Table 3.1, the $(OH)_2Sn$ (**54**), $(Ac)_2Sn$ (**58**) and OTi (**56** and **60**) complexes were red shifted relative to all the other complexes under investigation in this thesis, probably due to the distortion discussed above [384]. This red shifting has also been attributed to the coordination of certain ligands to the Pc ring leading to enlargement of the π-system

113

of the Pc [385, 386]. However certain central metals such as Ti and Sn are known to result in a red shift of the Q band [382].

Charge transfer bands were observed (Fig. 3.3) for complexes **58-60** in the region of 400 to 500 nm, with complex (**59**) showing the most prominent charge transfer band.
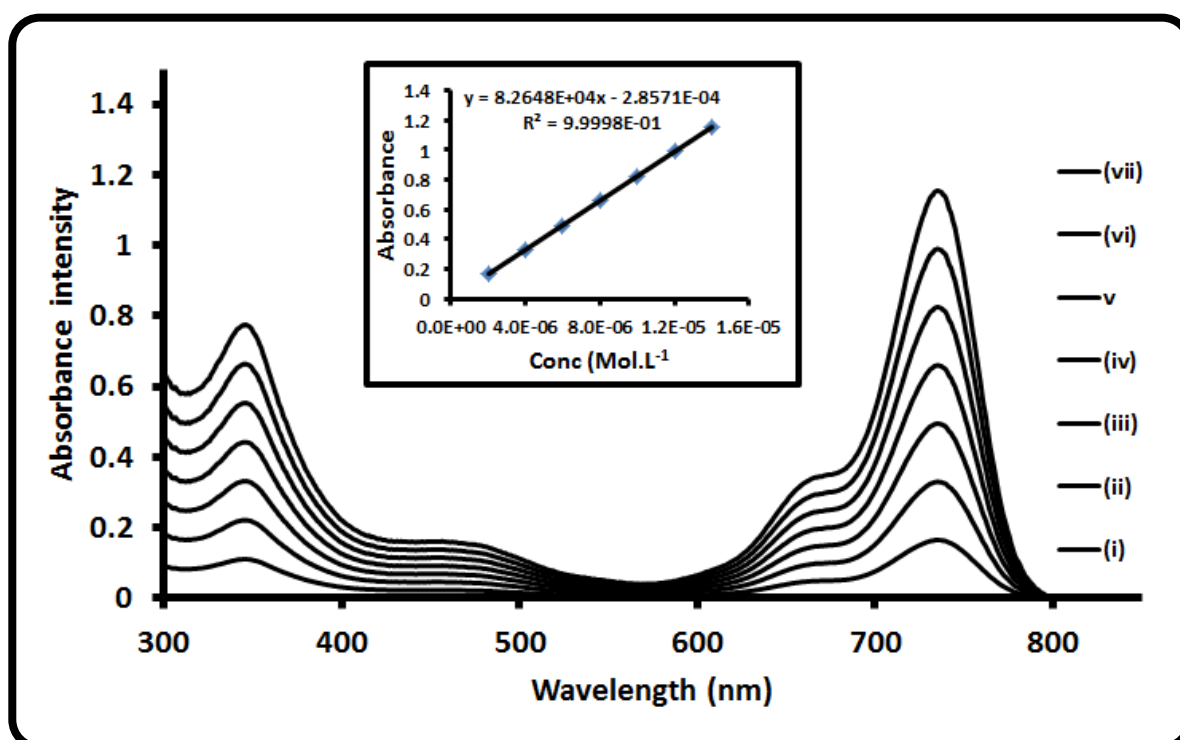
Figure 3.4: Ground state electronic absorption spectra of OTiMCPc (60) at various concentrations: (i) 2 x 10^{-6} (ii) 4 x 10^{-6}, (iii) 6 x 10^{-6}, (iv) 8 x 10^{-6}, (v) 10 x 10^{-6}, (vi) 12 x 10^{-6} and 14 x 10^{-6} mol dm^{-3} in DMF.

Fig. 3.4 shows that as the concentration of complex (**60**) was increased, the intensity of the Q-band absorption maxima also increased, with no new blue shifted bands appearing normally associated to aggregated species. The same trend was also observed with the complexes (**49-59**) which also did not show aggregation in DMF. The Beer–Lambert Law was obeyed for all of these complexes in concentrations

ranging from 2×10^{-6} to 14×10^{-6} mol dm^{-3}. These studies confirm that the broadness in the absorption spectra is not due to aggregation, but most likely due to the low symmetry of the complexes, especially with complexes **58** and **60** as well as **54** and **56**. OTiPc complexes (in general) are known to have a slightly square pyramidal structure [385]. Sn is a large metal therefore it also does not fit into the Pc ring. This may explain why both OTiPc (**52, 56** and **60**) and SnPc (**50, 54** and **58**) derivatives show increased broadening in the spectra, due to the effects caused by both the central metal and the unsymmetrical nature of the substituents. In this work, the red shifting of the Q band for complex **53-60** was strongly influenced by the electron donating nature of the diethylaminoethanethiol substituents.
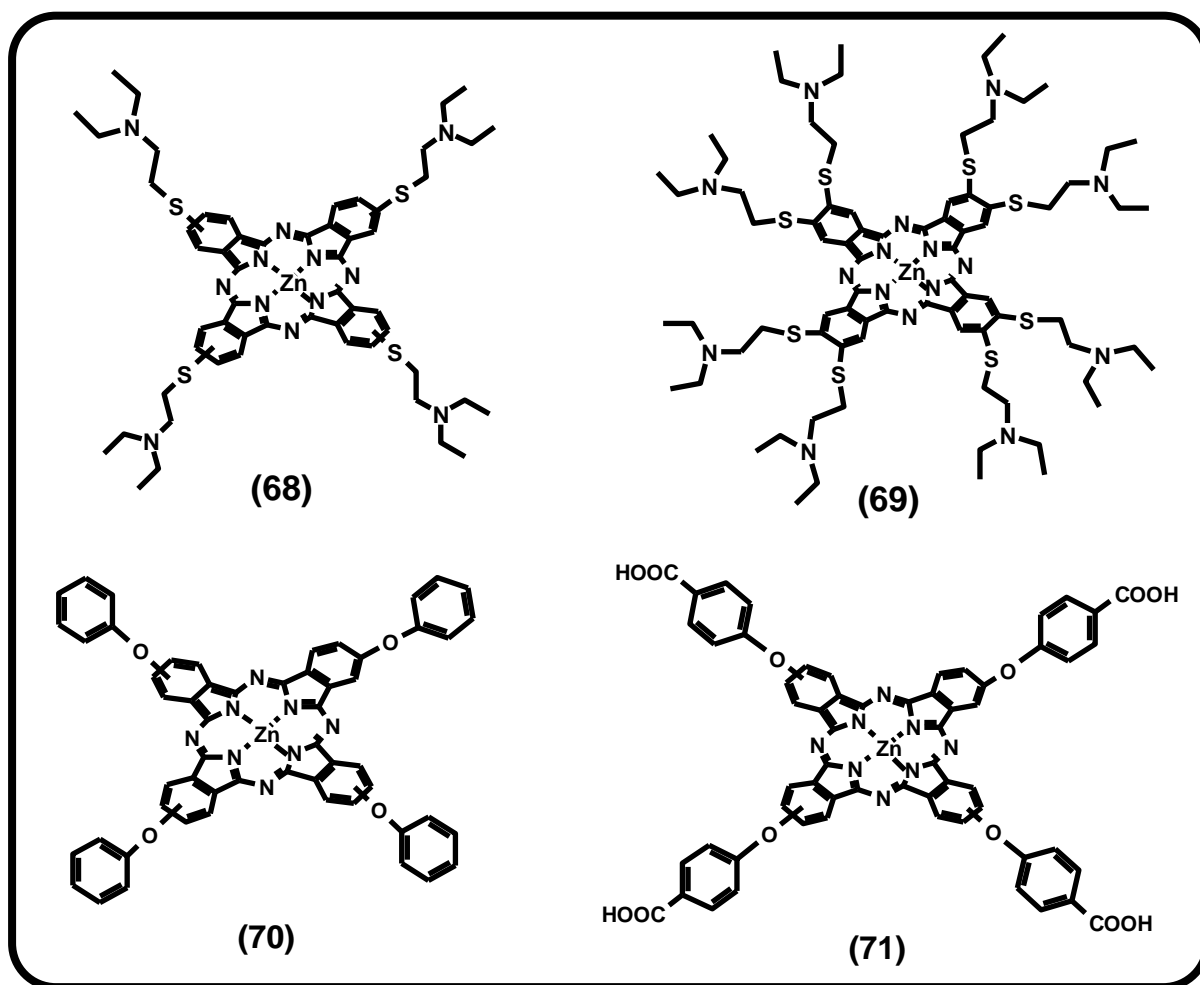
Figure 3.5: Chemical structures of the symmetrically substituted phthalocyanines

These ZnPc derivatives (**68-71**) (Fig.3.5) have been reported before [14, 136, 373, 375, 376]. Their spectral properties are studied in this thesis and compared to their corresponding asymmetrical counterparts. The ZnPc derivatives were selected since these complexes have been widely synthesized and have been used extensively in phthalocyanine chemistry and their chemistry is fully understood. This will therefore assist in the explanation of the effect of symmetry on the physicochemical behaviour of the complexes. The spectra of the complexes together with their symmetrical derivatives are presented in Fig. 3.6.
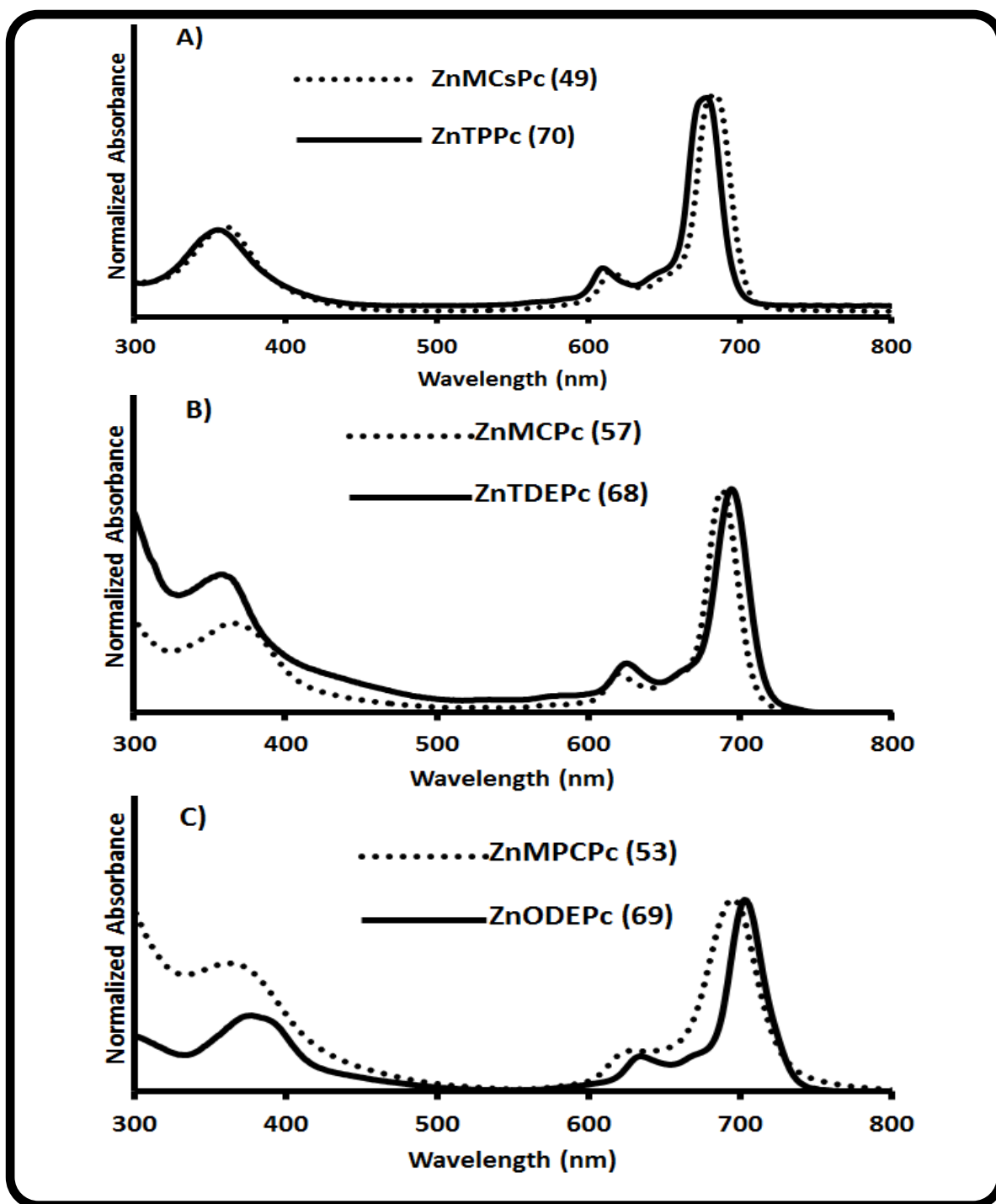
Figure 3.6: Ground state electronic absorption spectra of symmetrical (solid line) versus unsymmetrical (dotted lines) ZnPc derivatives in DMF. Conc ~ 8 × 10⁻⁶ mol.L⁻¹.

The absorption spectra of complex (**70**) tetra-substituted with phenoxy groups was blue shifted compared to the corresponding unsymmetrically substituted complex

(**49**). The red shifting observed can be explained in terms of the electron donating behaviour of the sulfur atom present in the cysteinyl moiety being replaced by one phenoxy group, thus increasing the electron density of the Pc ring. In contrast to the other set of complexes, the absorption spectra of low symmetry complexes (**53** and **57**) were blue shifted compared to their symmetrical counterparts (**69** and **68**). This could have been a result of the electron withdrawing behaviour of the carboxylic acid groups present at the periphery for **53**, and **57**, which reduces the size of the HOMO-LUMO gap.

3.1.3 Fluorescence spectra
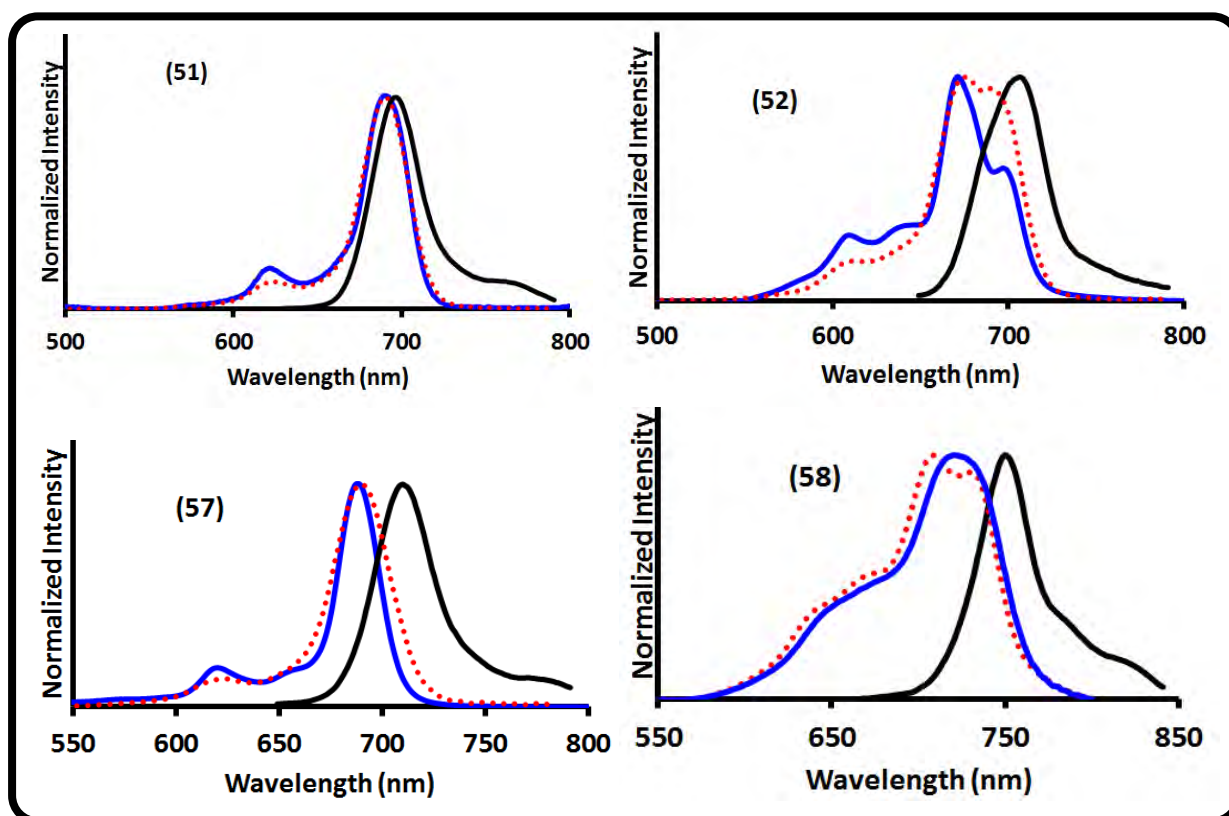
Figure 3.7: Absorption (solid blue line), fluorescence excitation (dotted red line) and emission spectra of (OH)₂GeMCsPc (51), OTiMCsPc (52), ZnMCPc (57) and (ac)₂SnMCPc (58) low symmetric MPc complexes in DMF.

Shown in Fig. 3.7 are the absorption, fluorescence excitation and emission spectra of the various low symmetry Pcs in DMF and the figure serves as an example for the rest of the complexes studied. The fluorescence emission spectra of the $(OH)_2Ge$ (**51**) and Zn (**57**) complexes were mirror images of both the absorption and the excitation spectra, while the excitation spectra was similar to the absorption spectra, typical of monomeric MPc complexes. However, there was a disagreement of the absorption, fluorescence excitation and emission spectra for the OTi (**52**) and $(Ac)_2Sn$ (**58**) complexes and all complexes which showed broadening or split Q bands. The disagreement of the absorption and excitation spectral properties has been documented before (i.e. InPc [371] derivatives). Enhanced splitting of the Q band in the excitation spectra confirms the lack of symmetry in these complexes. Phthalocyanines in general are known to fluoresce with only one main peak which has been assigned as the 0-0 transition in the fluorescence process [387], hence one peak in the emission spectra.

3.2 Synthesis of characterization of nanoparticles and their phthalocyanine conjugates

3.2.1 MPc-GSH capped AuNPs conjugates

3.2.1.1 AuNPs alone

Glutathione capped AuNPs were prepared from the initial TOABr stabilized nanoparticles as explained in the experimental section. Glutathione was selected as the tri-peptide of interest in this work because the availability of a free cysteinyl thiol

group that has a high binding affinity for gold [388]. However, oxidation is a major

problem with GSH solutions because of this free thiol present in the peptide

sequence.

During ligand exchange reactions the GSH solutions, were carefully evacuated to get

rid of excess oxygen and saturated with argon gas to create an inert environment to

prevent oxidation of GSH to oxidized glutathione (GSSG). Glutathione has a

terminal free amino group that can be coupled to a carboxylic acid of a

photosensitizer. Glutathione is also the most abundant thiol containing tri-peptide in

the cytoplasm, serving as a reducing agent in biochemical processes. Glutathione has

been previously employed in situ for targeting and nanoparticles based drug

delivery systems [389].
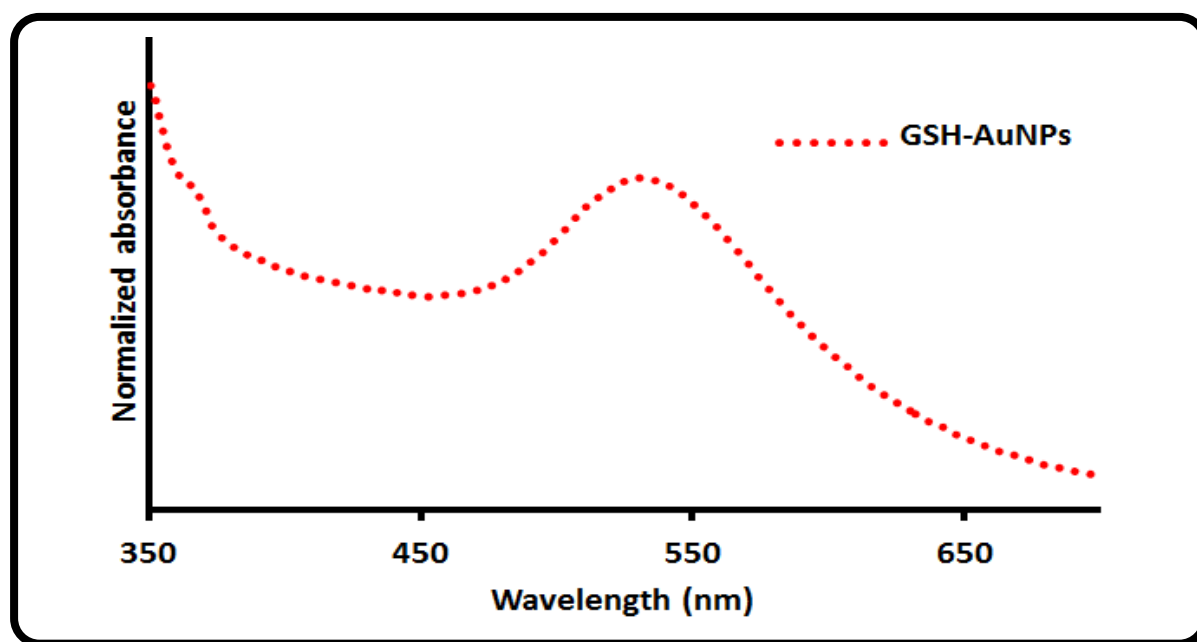
Figure 3.8: Ground state electronic absorption spectra of GSH-AuNPs in water.

Following TOABr ligand exchange with glutathione, the nanoparticles were highly

soluble in aqueous solution, suggesting that a strong interaction between the AuNP

and GSH has occurred. Fig. 3.8 shows UV-vis spectra of GSH-AuNPs with a surface

plasmon resonance band at 533 nm, typical of GSH stabilized AuNPs [390].
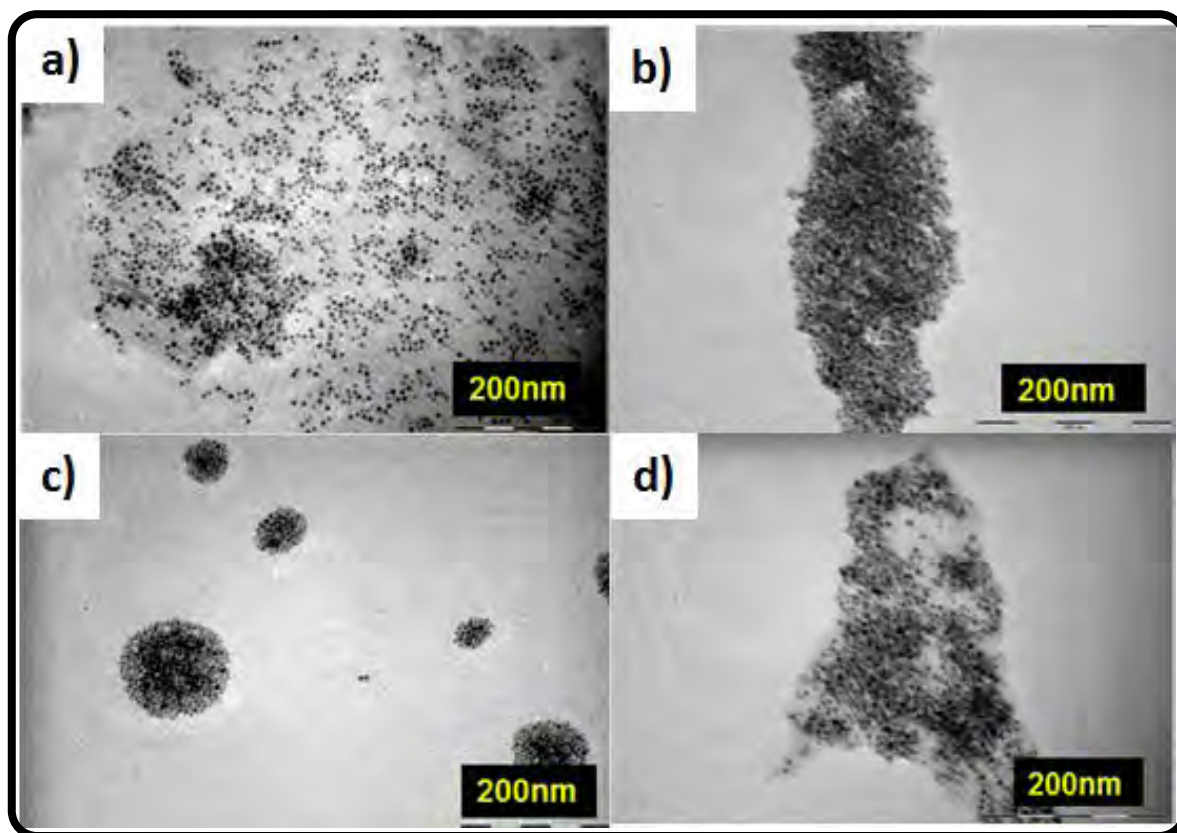
Figure 3.9: Transmission electron microscope (TEM) images of GSH capped AuNPs (a), linked to (ac)$_2$SnMCPc (58) (b), (OH)$_2$GeMCPc (59) (c) and OTiMCPc (60) (d).

The nanoparticles were further characterised by TEM, Fig. 3.9(**a**) and their size was

determined to be 5.2 nm.

Structurally, gold nanoparticles are characterized by a face cantered cubic crystal

structure (fcc) that resembles that of bulk gold as shown in the XRD spectra of GSH-

AuNPs Fig. 3.10, which is typical of AuNPs [391]. The size of the GSH-AuNPs was

estimated using equation 2.1 and also found to be 5.2 nm (as with TEM).

3.2.1.2 Conjugates
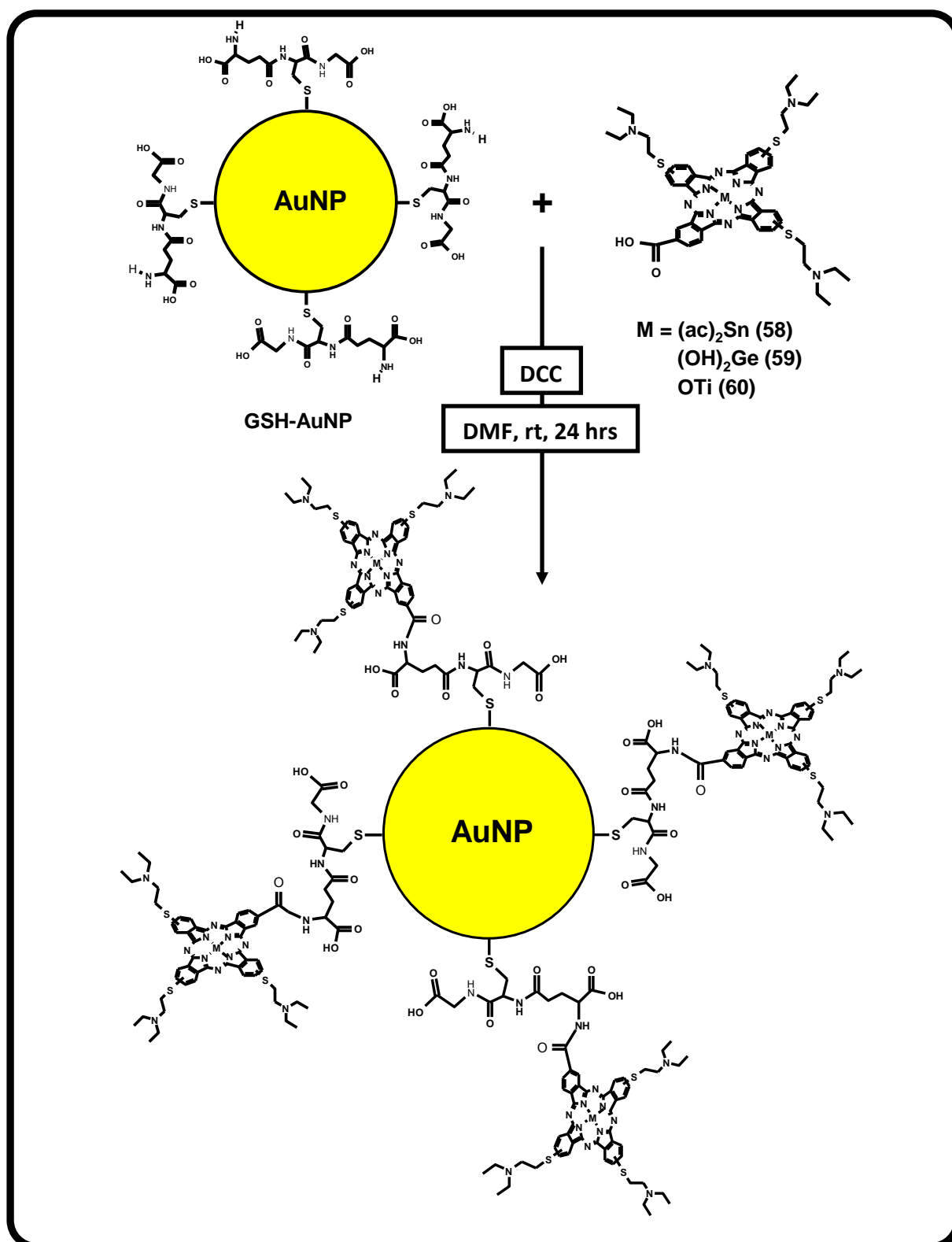
Scheme 3.5: Schematic representation route of coupling glutathione caped gold nanoparticles (GSH-AuNP) to low symmetry monocarboxy MPcs (58, 59 and 60).

Following the synthetic route shown in Scheme 3.5, these nanoparticles were then coupled to the following low symmetry metallophthalocyanines: $(ac)_2SnMCPc$ **(58)**, $(OH)_2GeMCPc$ **(59)** and OTiMCPc **(60).** This resulted in GSH capped AuNPs – low symmetry phthalocyanine conjugates formed via the terminal amine of GSH and the free carboxylic acid of the Pc that was pre-activated with DCC, as mentioned earlier in the experimental section. The conjugates are represented as $(ac)_2SnMCPc$(**58**)-GSH-AuNPs, $(OH)_2GeMCPc$(**59**)-GSH-AuNPs and OTiMCPc(**60**)-GSH-AuNPs respectively. All the low symmetry complexes reported in this work could form conjugates with AuNPs. The monocarboxy complexes (**58-60**) were chosen here as examples. However, the monocysteinyl ring systems (**49-52**) were not chosen since activated carboxylic groups may bind to the amino group of the neighbouring Pc complex.

The TEM images in Fig. 3.9 (a) shows dispersed nano-spherically shaped GSH-AuNPs. A clear indication of agglomeration was observed from the TEM images of the $(ac)_2SnMCPc$(**58**)-GSH-AuNPs (b), $(OH)_2GeMCPc$(**59**)-GSH-AuNPs (c) and OTiMCPc(**60**)-GSH-AuNPs (d) conjugates, suggesting that there is some form of aggregation upon conjugation of these molecules. The $(OH)_2GeMCPc$(**59**)-GSH-AuNPs (c) conjugate is visually different compared to the **58** and **60** NP conjugates, displaying a different form of agglomeration. For the $(OH)_2GeMCPc$(**59**)-GSH-AuNPs (c), Fig. 3.9c, isolated circular islands for the agglomerates were observed.

Fig. 3.10 compares the XRD spectra (parameters are listed in Table 3.2) of the $(ac)_2SnMCPc$(**58**)-GSH-AuNP, $(OH)_2GeMCPc$(**59**)-GSH-AuNP and OTiMCPc(**60**)-

GSH-AuNP conjugates, the unconjugated MPc complexes and the GSH-AuNPs alone.
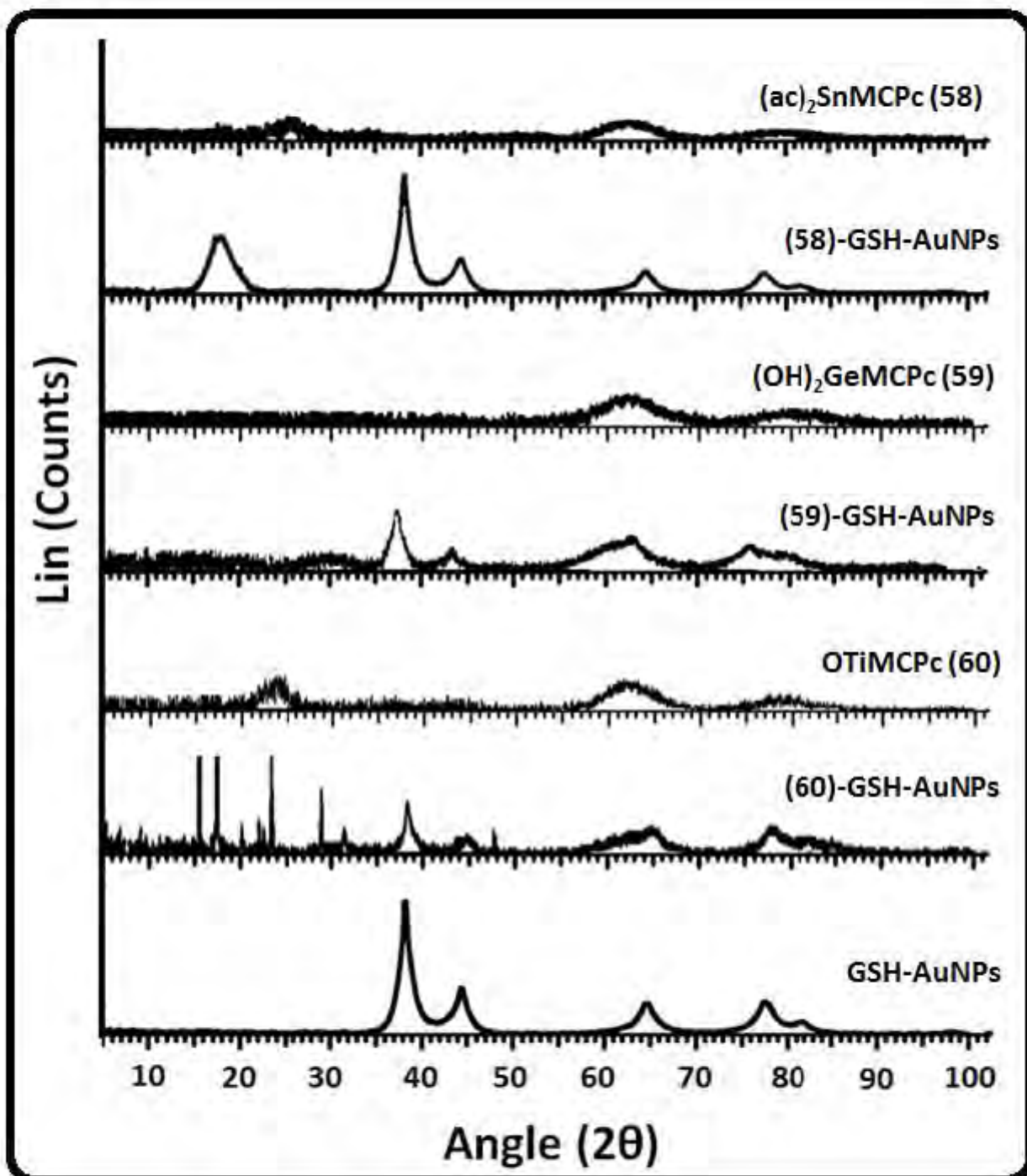
Figure 3.10: XRD spectra of GSH-AuNPs and their MPc conjugates

A broadening of the XRD peaks was observed for the monocarboxy Pcs (MCPc) (**58**, **59** and **60**) suggesting that the complexes are present in an amorphous form as shown in Fig. 3.10. For the $(ac)_2SnMCPc$ (**58**)-GSH-AuNPs and OTiMCPc (**60**)-GSH-AuNPs, the peak near $2\theta = 25°$ for the Pc alone is assigned to the 002 reflection planes of carbon [392]. These observed peaks have been documented previously for other MPc complexes and they are thought to be due to the amorphous nature of phthalocyanines [393].

The XRD spectra of the MPcs-GSH-AuNPs show a number additional peaks corresponding to the GSH-AuNPs when compared to the MPcs alone, suggesting conjugation of the MPc to the nanoparticles. A change in 2θ angles and d-spacings, including the appearance of new peaks in the XRD spectra, Table 3.2, confirms the formation of a new structure [394].

Table 3.2: XRD parameters for the GSH-AuNPs, monocarboxy phthalocyanines (ac)₂SnMCPc(58)-GSH-AuNPs, (OH)₂GeMCPc(59)-GSH-AuNPs and OTiMCPc(60)-GSH-AuNPs and their conjugates with GSH-AuNPs.

Compound	D – spacing and 2Ɵ˚ angles for peaks							
(58)	**d- spacing**	3.48	1.48	1.20				
	2Ɵ˚ angle	25.6	62.9	79.8				
(58)-GSH-AuNPs	**d- spacing**	5.00	2.36	2.04	1.44	1.23	1.18	1.02
	2Ɵ˚ angle	17.7	38.1	44.4	64.5	77.6	81.8	98.4
(59)	**d- spacing**	1.49	1.19					
	2Ɵ˚ angle	62.3	80.8					
(59)-GSH-AuNPs	**d- spacing**	2.36	2.04	1.45	1.23	1.17		
	2Ɵ˚ angle	38.2	44.4	64.3	77.7	82.1		
(60)	**d- spacing**	3.71	1.48	1.19				
	2Ɵ˚ angle	23.9	62.9	80.2				
(60)-GSH-AuNPs	**d- spacing**	5.78	5.13	3.82	3.10	2.36	2.03	1.44	1.23
	2Ɵ˚ angle	15.3	17.3	23.3	28.8	38.2	44.7	64.6	77.8
GSH-AuNPs	**d- spacing**	2.35	2.04	1.44	1.23	1.18	1.02		
	2Ɵ˚ angle	38.2	44.3	64.7	77.7	81.8	98.2		

For all the Pc-GSH-AuNPs conjugates, Fig. 3.10, two peaks appeared corresponding to the GSH-AuNPs at 38.1-38.2˚ and 44.4-44.7˚ (Table 3.2). These broad peaks are typical of GSH-AuNPs. The peak near 65˚ is due to both the GSH-AuNPs and the Pcs. Sharp peaks were observed for the (60)-GSH-AuNPs conjugates, in addition to the GSH-AuNPs peaks suggesting that a crystalline, bulky structure may have been formed. The nanoparticle peaks appear with lower intensity at the 38.2˚ and 44.7˚ for (60)-GSH-AuNPs. Broadening and overshadowing of peaks was also seen for peaks centered at 64.6 and 77.8˚ for (60)-GSH-AuNPs. Less broadening was observed for the (58)-GSH-AuNPs conjugate, compared to the (59)-GSH-AuNPs conjugates. A new broad peak was observed for the former conjugate at 17.7˚ which might be the

shifted peak of complex (**58**). The other six peaks observed at 2θ = 38.1, 44.4, 64.5, 77.6, 81.8 and 98.4° (Table 3.2) corresponds to the GSH-AuNPs peaks.
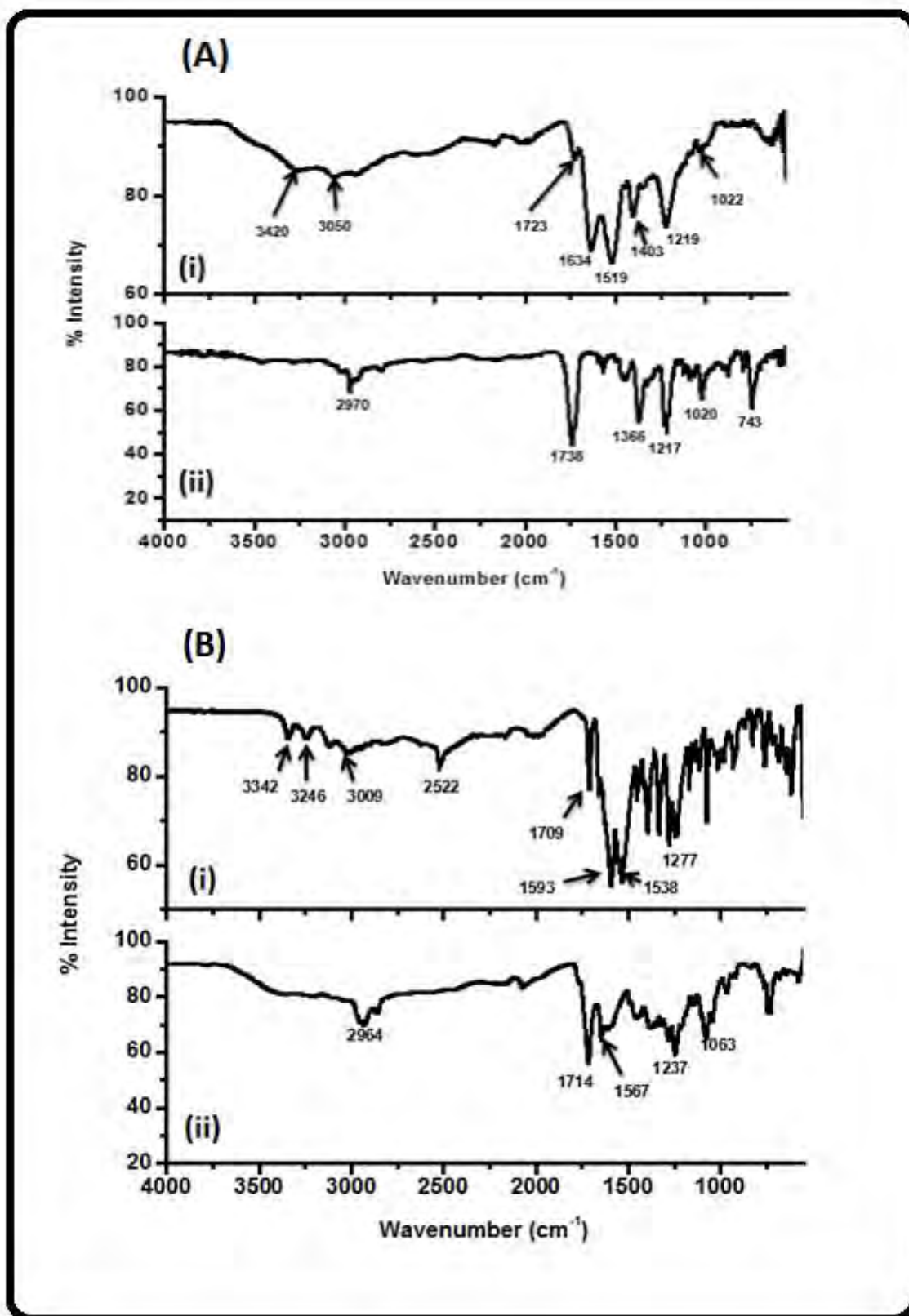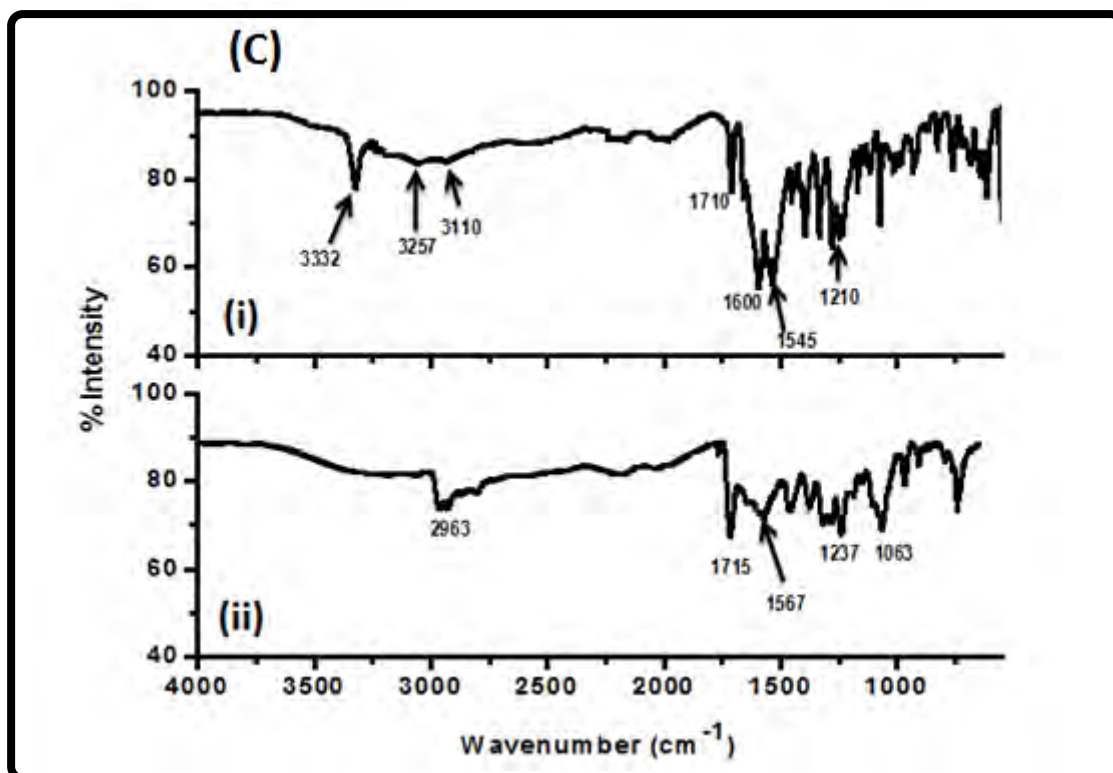
Figure 3.11: Infrared spectra of (ac)₂SnMCPc (A) (58), (OH)₂GeMCPs (B) (59),

OTiMCPc (C) (60) and; linked to GSH-AuNPs (i) and Pc alone (ii).

The FTIR spectra (Fig. 3.11) also served as a qualitative tool to confirm conjugation of

the MPcs to the GSH-AuNPs. The sharp bands observed in all the (i) IR spectra at

3420 cm^{-1} Fig. 3.11A, 3342 cm^{-1} in Fig. 3.11B, and 3332 cm^{-1} Fig. 3.11C are an

indication of the presence of successful amide linkages resulting from the –NH

stretching respectively, confirming the formation of conjugate. Bands resulting from

the C=O stretching in the amide link were also observed as doublets for all the

conjugates. For the (OH)₂GeMCPc-GSH-AuNPs conjugate (Fig. 3.11B, (i)) the C=O

stretching was observed at 1593 and 1538 cm^{-1}, while in the OTiMCPc-GSH-AuNPs

(Fig. 3.11C (i)) conjugate it was at 1600 and 1545 cm^{-1} and the (ac)₂SnMCPc-GSH-

AuNPs (Fig. 3.11A (i)) conjugate showed these bands to be at 1634 and 1519 cm^{-1}.

The peaks below 1500 cm^{-1} are always observed as phthalocyanine fingerprints. The

free carboxylic acid carbonyl (C=O) stretching of the GSH alone was also observed for all the complexes, i.e. at 1709 cm^{-1} for the (OH)$_2$GeMCPc-GSH-AuNPs, at 1710 cm^{-1} for the OTiMCPc-GSH-AuNPs, and at 1723 cm^{-1} for the (ac)$_2$SnMCPc-GSH-AuNPs conjugate. The IR spectra of the Pcs alone all show sharp doublet C-H stretches at 2964 cm^{-1}, Fig. 3.11B (ii), 2963 cm^{-1}, Fig. 3.11C (ii), and 2970 cm^{-1}, Fig. 3.11A (ii). These are due to the aliphatic C-H of the methyl and methylene groups at the peripheral ligands. The carboxylic acid carbonyl (C=O) stretching band was observed at 1714 cm^{-1} for the (OH)$_2$GeMCPc, at 1715 cm^{-1} in the OTiMCPc and at 1738 cm^{-1} for the (ac)$_2$SnMCPc complex, respectively. All other peaks below the region of 1500 cm^{-1}, which were observed in the conjugate, are in the phthalocyanine figure print region.

In the UV/Vis spectra, no drastic changes (Fig. 3.12) were observed in the Q-band maxima for all the MPc complexes before and after the low symmetry phthalocyanine complexes were mixed with the GSH-AuNPs, indicating no discernable interaction. A 1 to 3 nm shift was observed as a result of change in the environment after mixing MPcs with GSH-AuNPs.
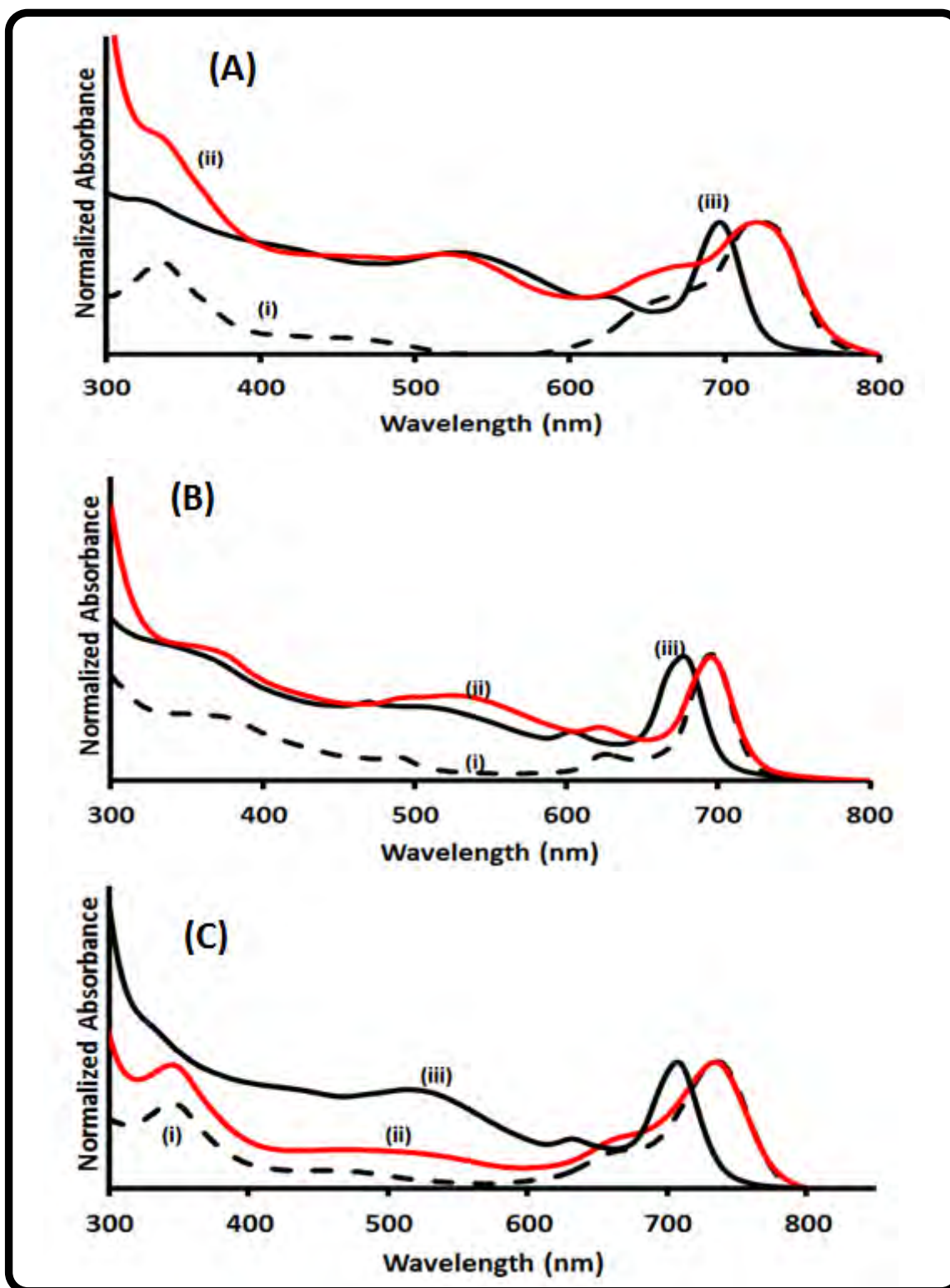
Figure 3.12: Ground state absorption spectra of (ac)₂SnMCPc (A) (58), (OH)₂GeMCPc (B) (59), and OTiMCPc (C) (60); Pc alone (i), mixed with GSH-AuNPs (ii) and linked (iii) in DMF.

A broad absorption band was observed in the region between 450-550 nm, due to the SPR band of AuNPs. Significant blue shifting in the Q band was observed for all the Pc complexes after they were chemically coupled to the GSH-AuNPs. The titanium complex (OTiMCPc-GSH-AuNPs) showed largest spectral separation in the Q band between the conjugate (711 nm) and the Pc alone (734 nm) when linked (Fig. 3.12C, Table 3.3), confirming successful coupling to the nanoparticles.

Table 3.3: Spectral properties of the various MPcs and their conjugates

Complex	Q_{Abs} λ (nm) MPc alone	Q_{Abs} λ (nm) Mixed with GSH-AuNPs	Q_{Abs} λ (nm) Linked to GSH-AuNPs
(ac)$_2$SnMCPc (58)	720	720	702
(OH)$_2$GeMCPc (59)	695	693	680
OTiMCPc (60)	734	733	711

In phthalocyanine chemistry, blue shifting and broadening of the Q band, in most cases, may be explained as a result of the coplanar association of the phthalocyanine rings, progressing from monomers leading to aggregates. However, in the case of these MPc-GSH-AuNPs conjugates, while the Q band is blue shifted, the shape of the Q band is not typical of aggregation. The blue shifting is attributed to the electron withdrawing nature of the carboxylic groups [395, 396] of the GSH from GSH-AuNPs leading to an increase in the highest unoccupied molecular orbital (HOMO) –lowest unoccupied molecular orbital (LUMO) gap of the MPcs. This blue shift in

the Q-band is also seen with the $(ac)_2$SnMCPc-GSH-AuNPs (Fig. 3.12A) and $(OH)_2$GeMCPc-GSH-AuNPs (Fig. 3.2B). Additionally, the blue shifting also shows that the sulphur groups (which result in red shifting in Pcs) are now engaged with AuNPs, serving as a confirmation for successful coupling of the Pc complexes to the nanoparticles.
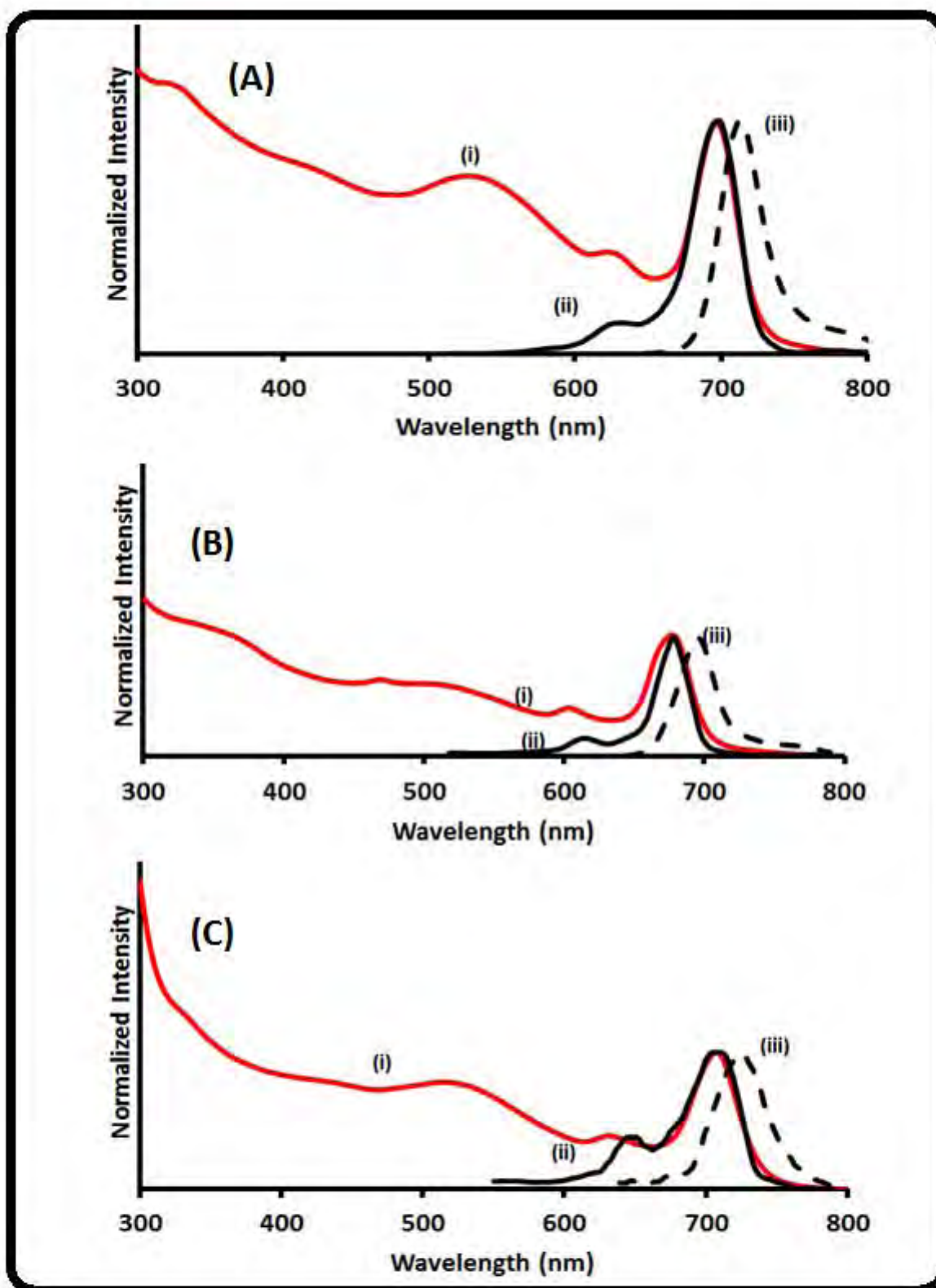
Figure 3.13: Ground state absorption (i), fluorescence excitation (ii) and emission (iii) spectra of (ac)₂SnMCPc-GSH-AuNPs (A), (OH)₂GeMCPc-GSH-AuNPs (B), OTiMCPc-GSH-AuNPs (C) and in DMF

Fig.3.13 shows the absorption, fluorescence excitation and emission spectra of the MPcs-GSH-AuNPs conjugates. The absorption and excitation spectra of all the conjugates were similar (apart from AuNP SPR band near 500 nm) and directly overlapped each other suggesting no changes in symmetry of these molecules upon excitation. The fluorescence emission spectrum of the $(OH)_2GeMCPc$-GSH-AuNPs (Fig. 3.13B) was a mirror image of both the absorption and excitation spectra, typical of non-aggregated Pcs. There was also a good agreement between the fluorescence excitation and absorption spectra of both OTiMCPc-GSH-AuNPs (Fig. 3.13C) and $(ac)_2SnMCPc$-GSH-AuNPs (Fig. 3.13A).

3.2.2 Conjugates of variously shaped of AgNPs with MPcs
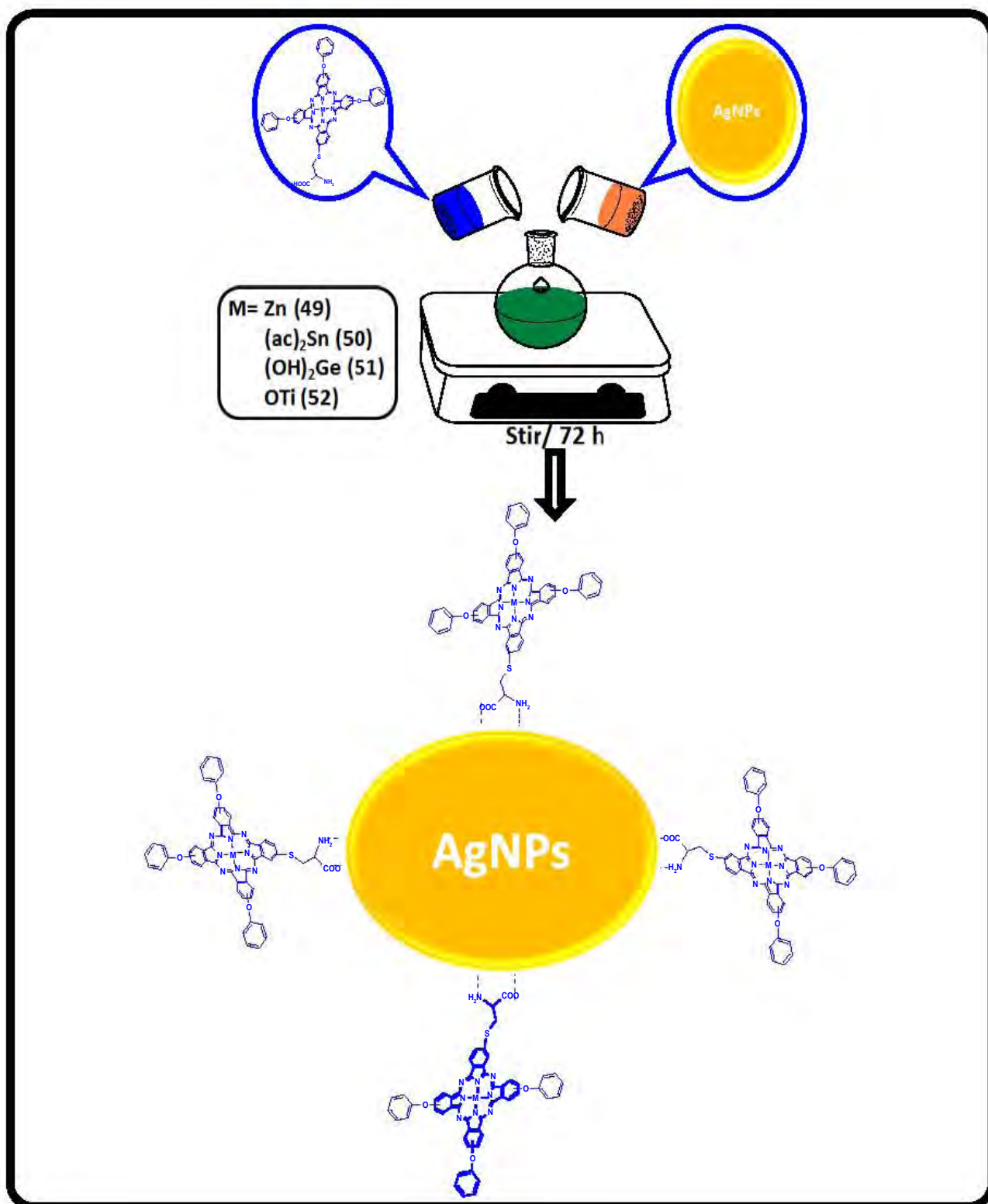
Scheme 3.6: Schematic route for the conjugation of complexes 49, 50, 51 and 52

with the various shapes (spherical, cubic, and triangular) of AgNPs

3.2.2.1 AgNPs alone

The complexes employed in this part of the thesis are those that are substituted with a monocysteinyl group, i.e. ZnMCsPc (**49**), $(OH)_2SnMCsPc$ (**50**), $(OH)_2GeMCsPc$(**51**) and OTiMCsPc (**52**), Scheme 3.6. The monocysteinyl moiety consists of both a carboxylic acid group and an amino group, and the rest of the peripheral positions contain phenoxy groups that allow increased solubility in most common organic solvents. Amino groups have a higher binding affinity for silver, and carboxylic acid groups can also coordinate to the surfaces of the silver nanoparticles, protecting the latter against oxidation [119-127,242]. Thus the use of cysteinyl groups in this work. Various shapes and sizes of AgNPs were synthesized as mentioned in the experimental section. The nanoparticles were characterized by TEM, XRD and UV-Vis spectroscopy.
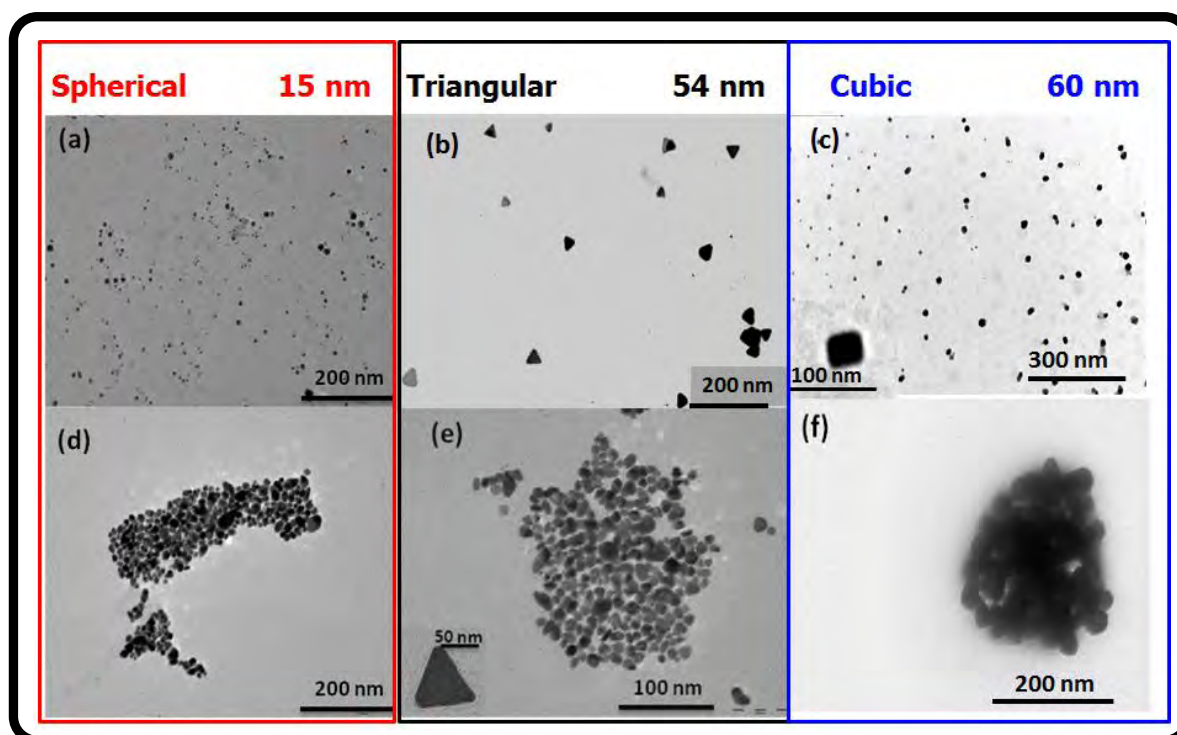
Figure 3.14: Low resolution transmission electron microscope images of spherical citrate capped (a), triangular citrate capped (b) and cubic PVP capped AgNPs. (c), spherical AgNPs + (OH)$_2$SnMCsPc (50) (d), triangular AgNPs + (OH)$_2$SnMCsPc (50) (e), and cubic AgNPs + (OH)$_2$SnMCsPc (50) (f).

The TEM images obtained for the various nanoparticles are shown in Fig. 3.14. Spherical (a), triangular (b) and clustered cubic (c) shapes of AgNPs were observed. The triangular shaped AgNPs were observed to be slightly agglomerated, with the AgNPs stacking to each other. An isolated cubic AgNP is shown in the insert, showing its clear cubic structure. The size distributions of the nanoparticles ranged from 15 nm for the spherical, 54 nm for the triangular and 60 nm for the cubic shaped nanoparticles.
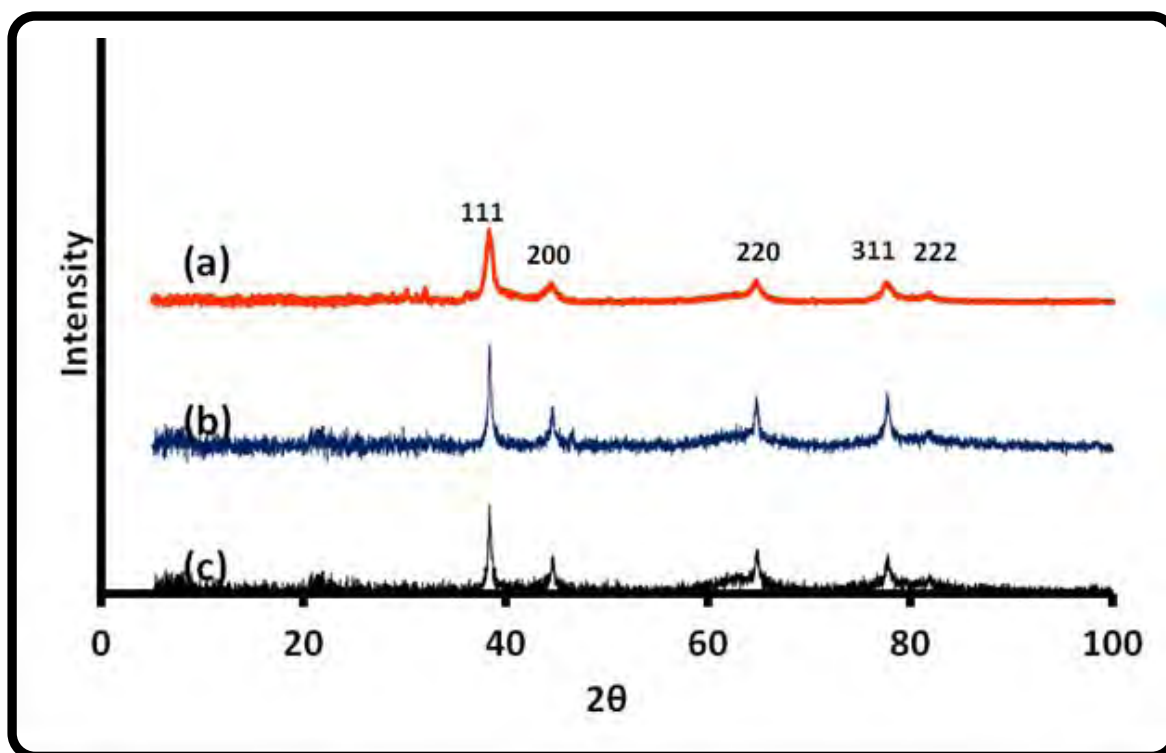
Figure 3.15: X-ray diffraction pattern spectra of spherical (a), triangular (b) and cubic AgNPs (c).

The XRD (Fig. 3.15) revealed peaks to be broader for the spherically shaped nanoparticles (Fig. 3.15a) corresponding to a relatively smaller sized nanoparticles, compared to the triangular (b) and cubic (c) shaped structures that showed narrow peaks, as a result of larger sized nanoparticles. All the nanoparticles exhibited the face centred cubic crystal structure (fcc) of silver.

The ground state electronic UV-Vis spectra of various AgNPs are presented in Fig 3.16. The surface plasmon resonance bands (SPR) of the various AgNPs were observed to be situated at completely different wavelengths. The SPR band of the spherical AgNPs was observed at 412 nm which is typical for these NPs [218, 367].
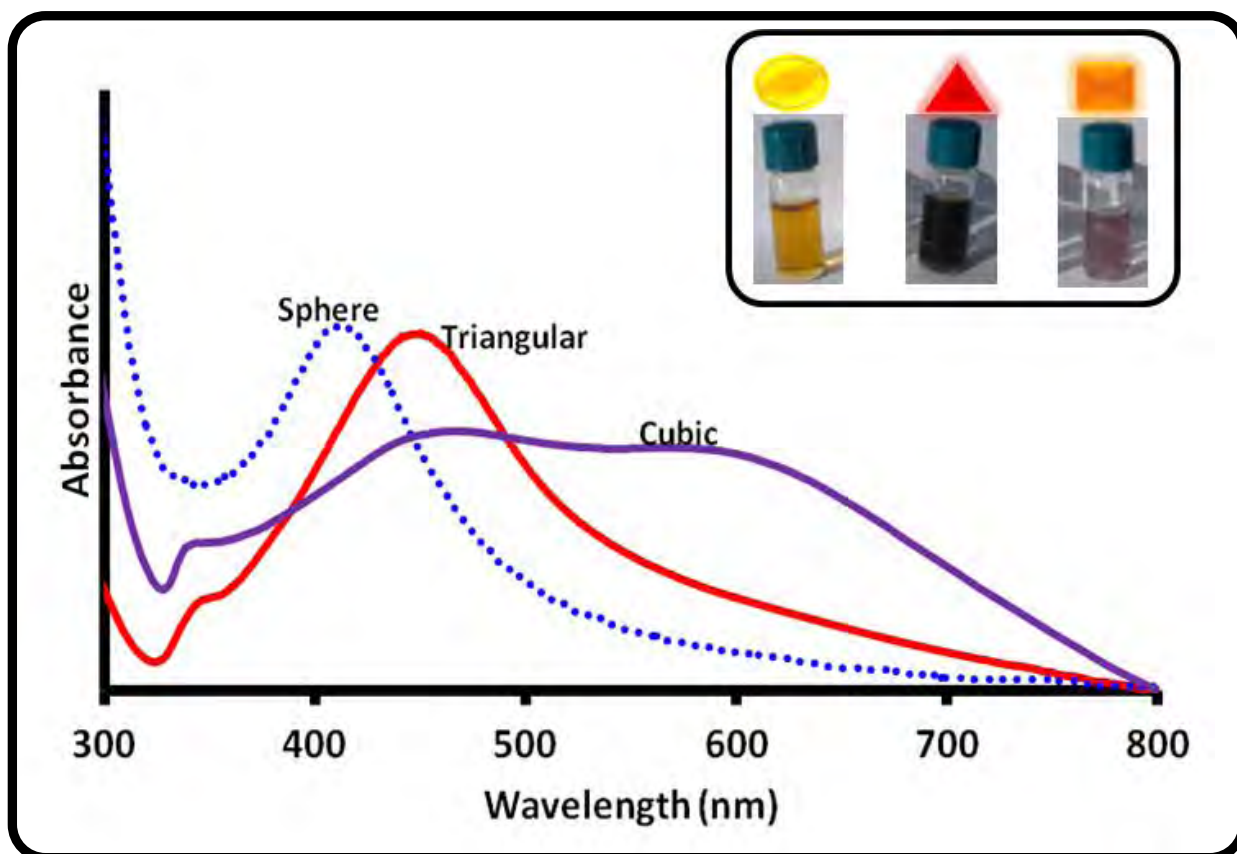
Figure 3.16: Ground state electronic absorption spectra of various AgNPs in DMF. Insert: corresponding digital images.

After etching the spherical AgNPs to form the triangular shaped AgNPs, a significant shift in the SPR band maxima from 412 to 460 nm, accompanied by a change in colour (Fig. 3.16 insert) due to changes in morphology, and apparently an increase in size distribution as judged by the broadening of the SPR band. The cubic structured AgNPs showed a large broadening of the SPR band, with two bands at 460 nm and at 590 nm, respectively.

3.2.2.2 Conjugates

All AgNPs were found to be agglomerated in the presence of phthalocyanines as observed for the (OH)$_2$SnMCsPc (Fig. 3.14 d, e, f), for spherical, triangular and cubic

shaped NPs respectively. The cubic and triangular structured AgNPs were more agglomerated in the presence of phthalocyanines resulting in a difficulty in observing the edges of the AgNPs. Low resolution TEM (the insert Fig. 3.14 (e)) revealed a single triangular shaped AgNP.

Spherical AgNPs

Figs. 3.17 show the ground state UV-vis spectroscopic properties of the various MPc complexes in the presence of spherical AgNPs in DMF.
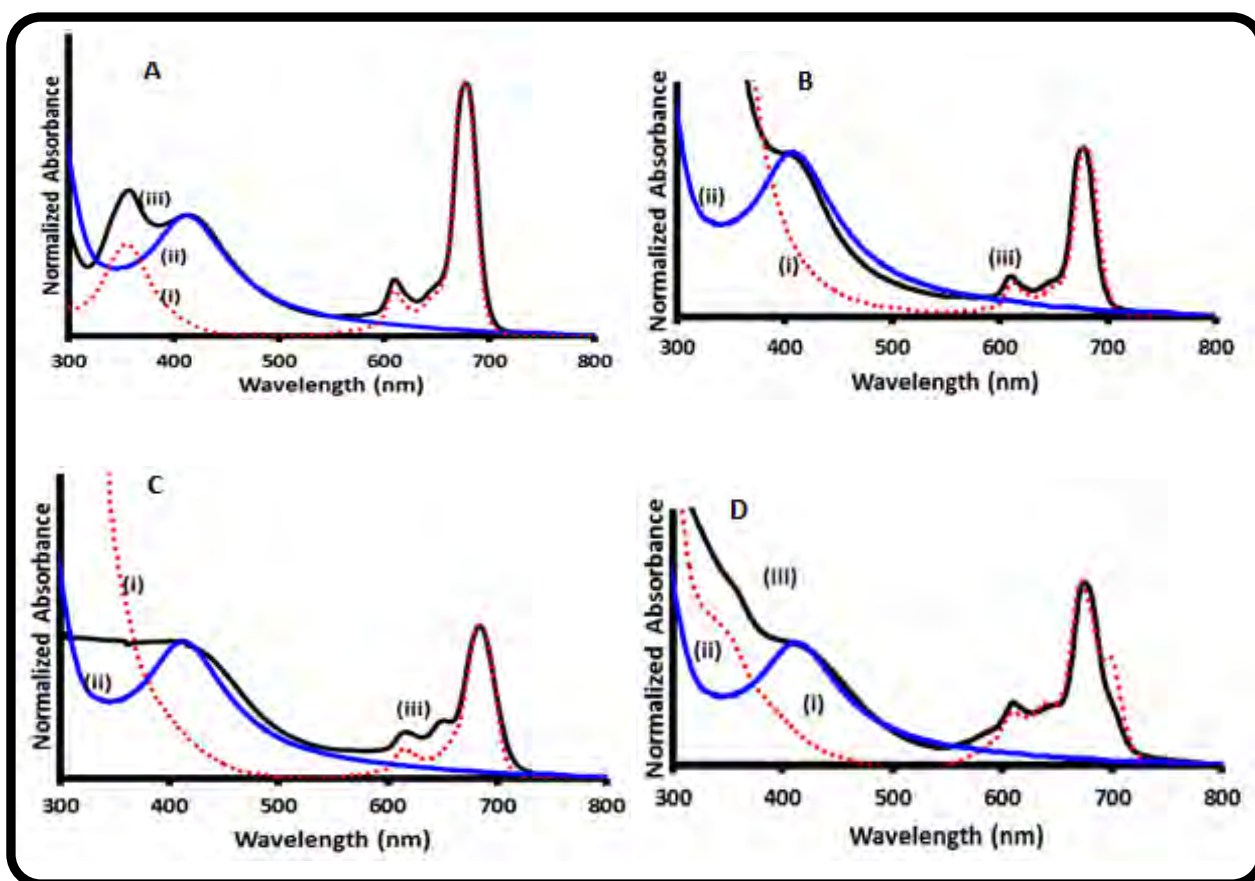
Figure 3.17: Ground state UV-vis spectra of ZnMCsPc (49) (A), (OH)₂SnMCsPc (50) (B), (OH)₂GeMCsPc (51) (C), and OTiMCsPc (52) (D); Pc alone (i), spherical citrate AgNPs alone (ii) and Pcs in the presence spherical AgNPs (iii) in DMF.

No change in the Q-band absorption of the ZnMCsPc (**49**) (Fig. 3.17A) complex was observed after interaction with spherical AgNPs, Table 3.4. An appearance of a new band at the region around 400 nm corresponding to the AgNPs SPR band, close to the B-band, was observed in spectra of the conjugate, suggesting the presence of AgNPs. The OTiMCsPc (**52**) complex (Fig. 3.17D (i)) shows a slight red shifting of the main Q-band (Table 3.4), accompanied by a partial collapse of the band at 696 nm on conjugation to AgNPs. The 696 nm band was attributed to a loss of symmetry for the OTiMCsPc (**52**) above. The disappearance of this band suggests a regain in symmetry due to the attachment of the AgNPs. A small blue shift in the Q-band maxima was observed for the $(OH)_2$SnMCsPc (**50**), in contrast to OTiMCsPc (**52**) that showed a red shift. A blue shift is expected when amino groups are engaged, since their electron donating nature results in a red shift in the spectra. There were no spectral shifts in the presence of AgNPs for the $(OH)_2$GeMCsPc (**51**), however there was broadening in the 600 – 650 nm region. Broadening of the phthalocyanine Q-band absorption in the presence of nanoparticles such as Au, has been attributed the a tight packing of phthalocyanines on the nanoparticle [176]

Table 3.4: Spectral properties of the various MPcs in the presence of various AgNPs

Complex	Q-abs (nm) MPcs alone	Q-abs (nm) Pc + Spheres	Q-abs (nm) Pcs + triangles	Q-abs (nm) Pcs + cubes
ZnMCsPc (49)	678	678	680	680
(OH)$_2$SnMCsPc (50)	680	678	690	680
(OH)$_2$GeMCsPc (51)	691	691	693	691
OTiMCsPc (52)	671	674	680	680

Triangular AgNPs

Fig. 3.18 shows a comparison of the various MPcs in the presence of triangular shaped AgNPs. Red shifting of the Q-band was observed for all the complexes in the presence of triangular shaped AgNPs, Table 3.4. Smaller spectral shifts ~2 nm in the Q-band maxima was observed for the ZnMCsPc (**49**) (Fig. 3.18A) (triangles) and the (OH)$_2$GeMCsPc (**51**) (Fig. 3.18C) in the presence of AgNPs.
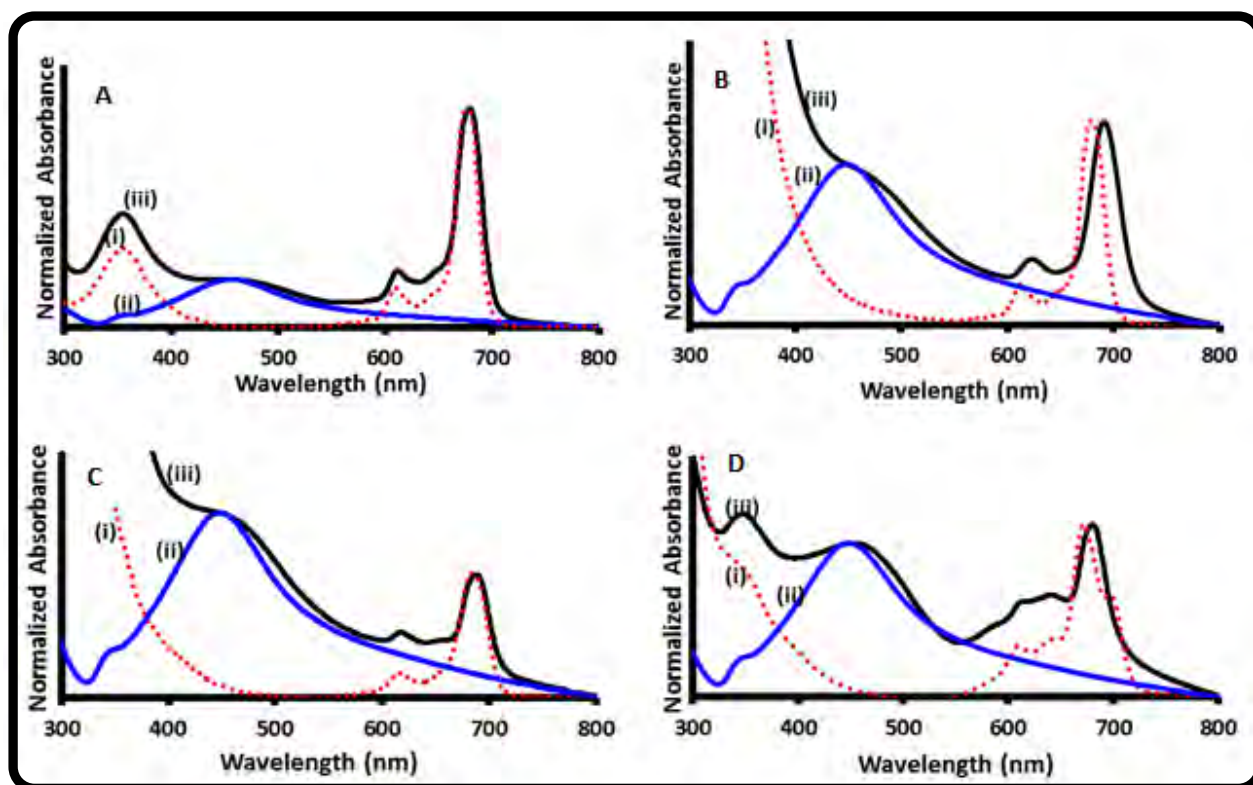
Figure 3.18: Ground state UV-vis spectra of ZnMCsPc (49) (A), (OH)$_2$SnMCsPc (50) (B), (OH)$_2$GeMCsPc (51) (C), and OTiMCsPc (52) (D), alone (i), triangular AgNPs alone (ii) and Pcs in the presence triangular AgNPs (iii) in DMF.

Large and significant spectral red shifting was observed for the OTiMCsPc (**52**) (Fig. 3.18D) and (OH)$_2$SnMCsPc (**50**) (Fig. 3.18B) in the presence of the triangular shaped AgNPs Table 3.4. The broadening observed in the region around 630 nm for the OTiMCsPc (**52**) in the presence of AgNPs is attributed to the tight packing of the Pcs on the NP as described above.
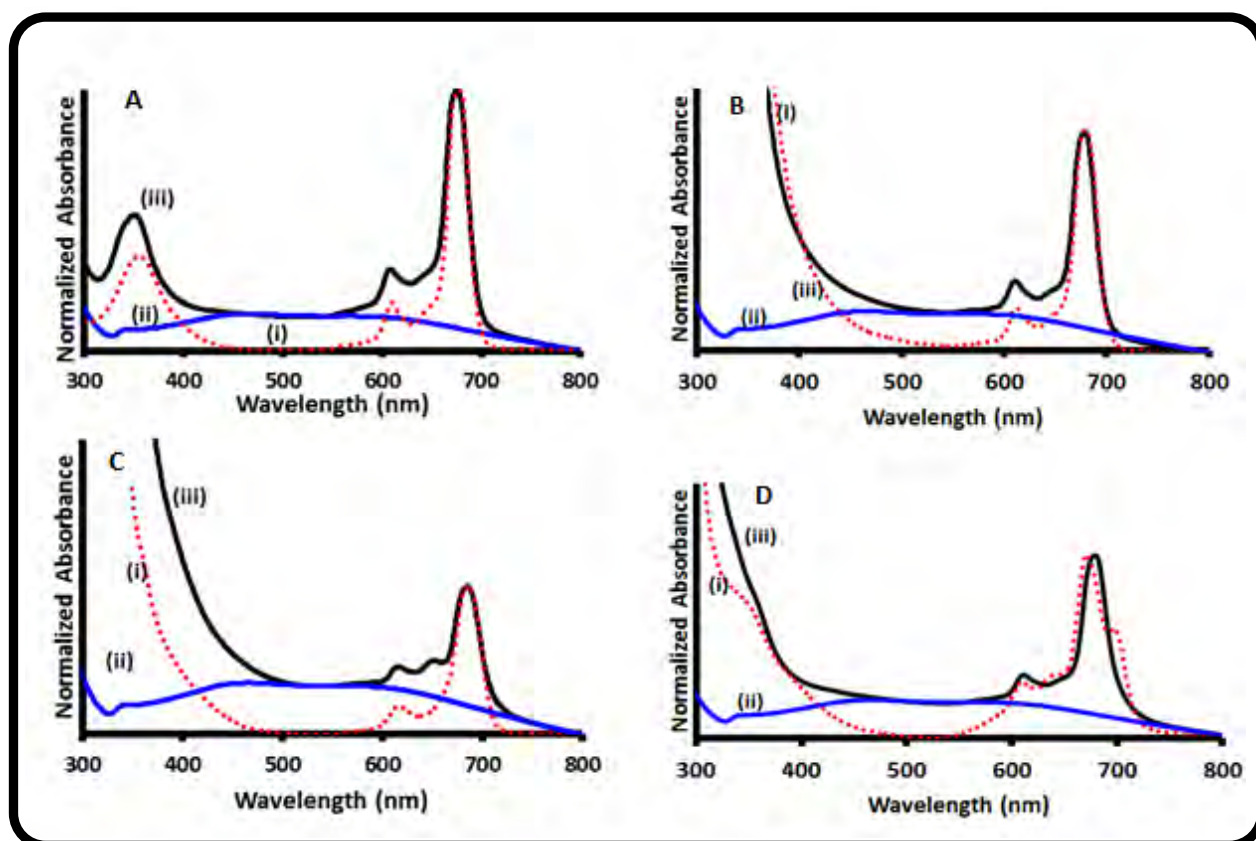
Figure 3.19: Ground state UV-vis spectra of ZnMCsPc (49) (A), (OH)₂SnMCsPc (50) (B), (OH)₂GeMCsPc (51) (C), and OTiMCsPc (52) (D), alone (i), cubic AgNPs alone (ii) and Pcs in the presence cubic AgNPs (iii) in DMF.

Cubic AgNPs

A small red shift was observed in the Q-band for the ZnMCsPc (**49**) (Fig. 3.19A), while no shift was detected for the (OH)₂GeMCsPc (**51**) (Fig. 3.19C) and (OH)₂SnMCsPc (**50**) (Fig. 3.19B) complexes in the presence of the cubic structured AgNPs (Table 3.4). The OTiMCsPc (**52**) (Fig. 3.19D) showed the same behaviour as that for the presence of the spherical NP, with small red shifts accompanied by a disappearance in the shoulder band around 696 nm. All MPcs showed characteristic appearance SPR band corresponding to each shape of AgNPs and changes in absorption spectra suggesting strong interaction of both components in solution.

144

3.2.3 Conjugates of axially ligated SiPc (61) and ZnPc phthalocyanines with spherical AuNPs and AgNPs

Scheme 3.7 shows conjugation of ZnPc and SiPc to MNPs through axial ligation.
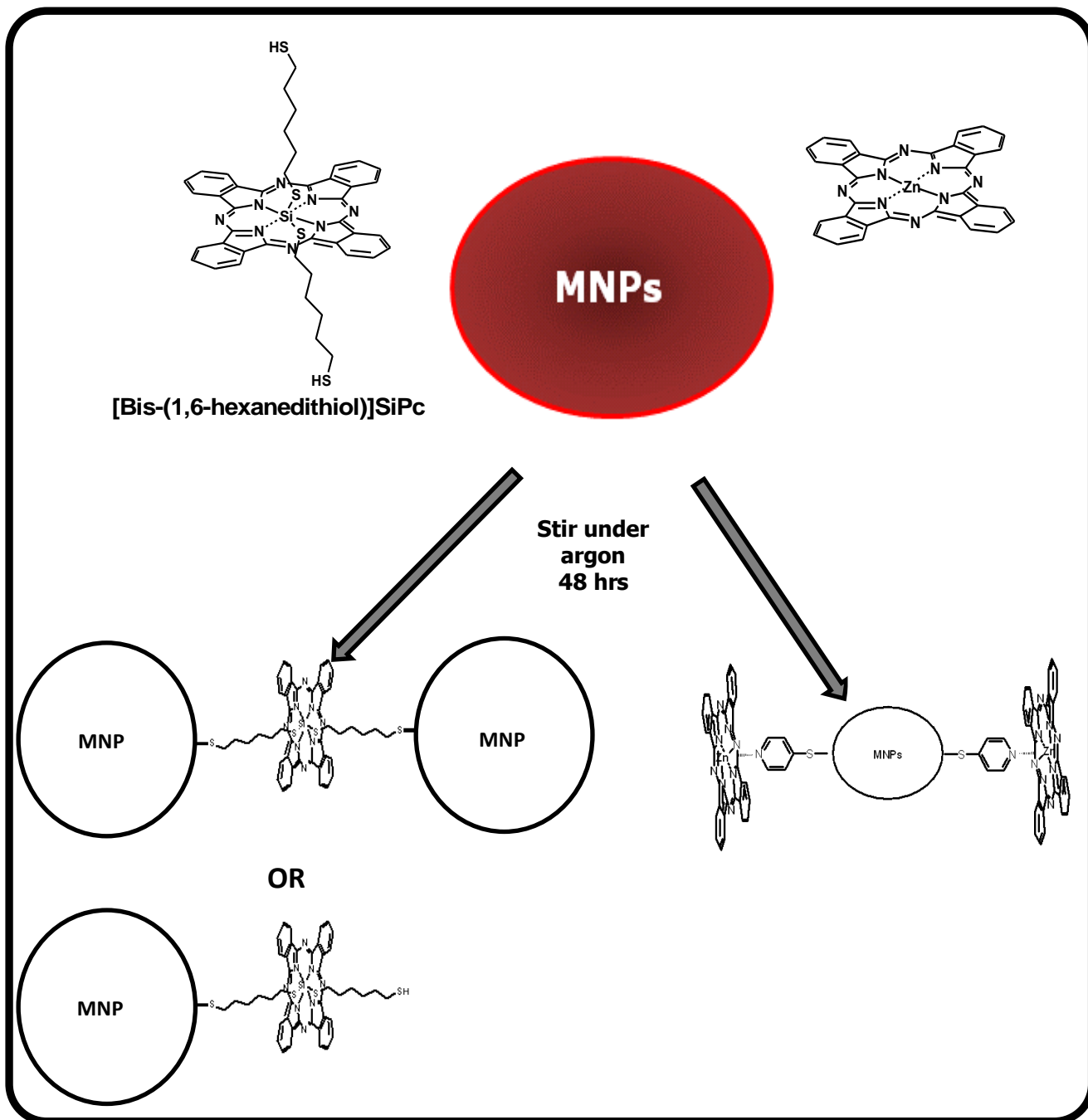
Scheme 3.7: Schematic representation of the conjugation of ZnPc or SiHDTPc (61) with MNPs

3.2.3.1 NPs alone.

Uncapped AgNP or AuNPs stabilized (with TOABr) were synthesised for use in the direct coordination with SiHDTPc (**61**) respectively.

The MNPs were stabilized with 4-mercaptopyridine to allow for further axial coordination to ZnPc. The reaction of zinc complexes with pyridine derivatives via axial ligation is well known [92].
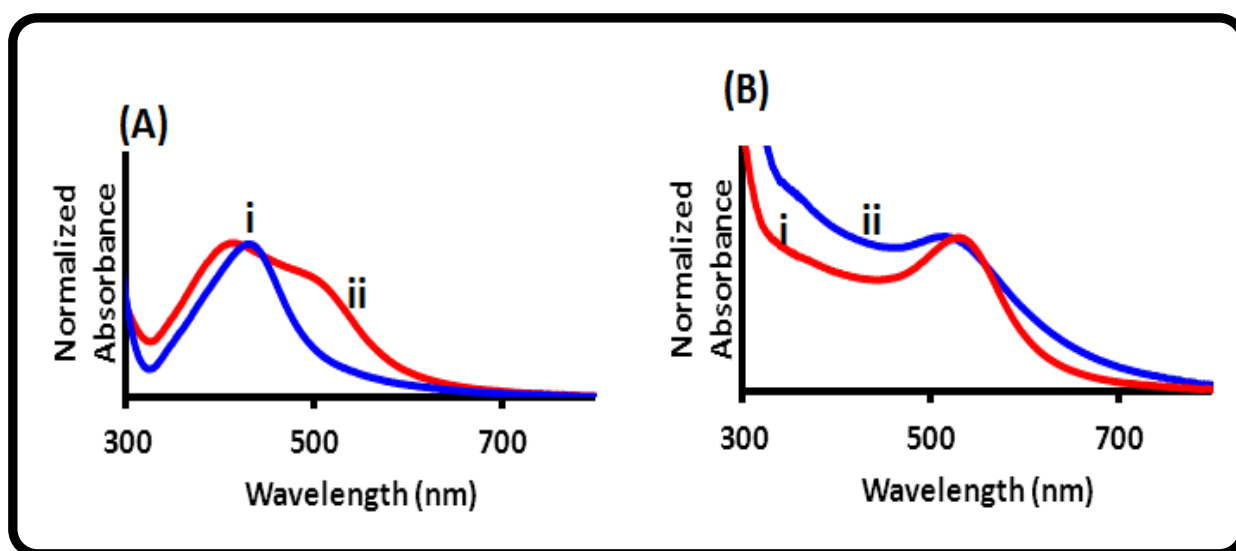
Figure 3.20: UV-vis spectra of (A) (i) uncapped AgNPs and (ii) AgNPs capped with 4-mercaptopyridine and (B) TOABr-AuNPs (i) and 4-mercaptopyridine AuNPs (ii) in DMF.

The surface plasmon resonance (SPR) band was observed at 412 nm for uncapped AgNPs (Fig. 3.20A (i)) and at 516 nm for TOABr stabilized AuNPs (Fig. 3.20B (i)). The SPR peaks, were observed at 412 for 4-mercaptopyrine stabilized AgNPs (Fig. 3.20A (ii)) and at 490 nm for AuNPs (Fig. 3.20B (ii)) capped with 4-mercaptopyridine.
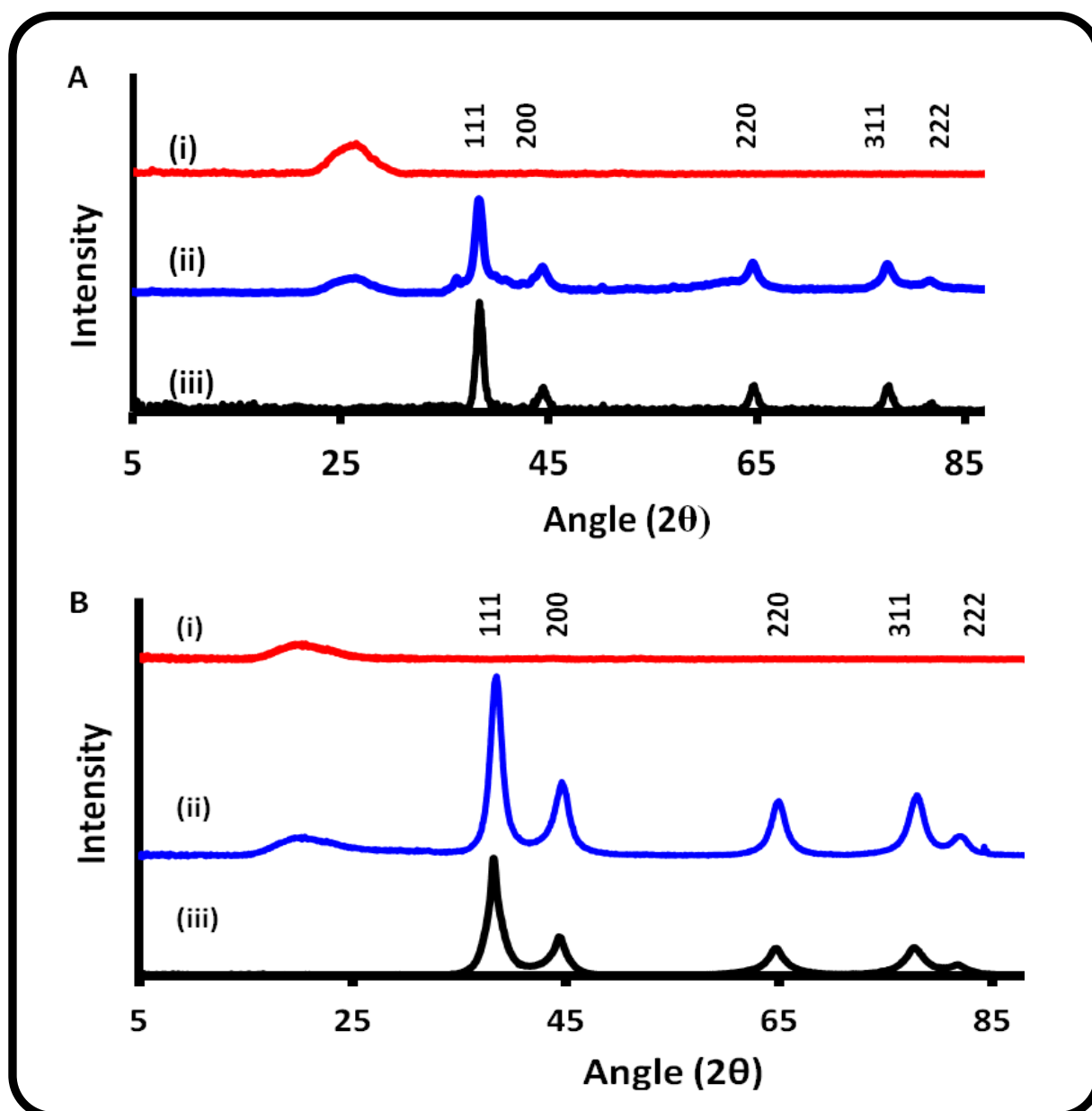
Figure 3.21: X-ray diffraction pattern of (A) ZnPc alone (i),   ZnPc-4MPy-AgNPs (ii), and 4-MPy-AgNPs alone (iii). (B) SiHDTPc alone (i),   SiHDTPc-TOABr-AuNPs, (ii) and TOABr capped AuNPs alone (iii).

Figure 3.21A and B (traces (iii)) shows the X-ray powder diffraction (XRD) pattern of spherical the AuNPs-TOABr and AgNPs-4MPy respectively. Both the AgNPs and AuNPs show a powder diffraction pattern resembling a face centered cubic crystal (fcc), which is typical of gold and silver. The size distribution of the MNPs was

estimated by fitting all the peaks and using the Scherrer equation (equation 2.1). The size was estimated to be 8 nm for the uncapped or 4-mercaptopyridine (4-MPy) functionalized AgNPs (represented as 4-MPy-AgNPs). For TOABr or 4-MPy stabilized AuNPs (the latter represented as 4-MPy-AuNPs), the size was estimated to be 5 nm.

The MNPs were further characterized by TEM (Fig. 3.22A and B (images (i)). The TEM images of the MNPs show well dispersed, spherically shaped 4-MPy-AuNPs (Fig. 3.22A (i)) and 4-MPy-AgNPs (Fig. 3.22B(i)), with the sizes obtained confirming those obtained using XRD. 4-MPy-AuNPs have an average size of ~5 nm, while a size of ~8 nm was obtained for the spherical 4-MPy-AgNPs, smaller than the size 15 nm Fig. 3.14 for citrate capped AgNPs, but with same size as the uncapped AgNPs.
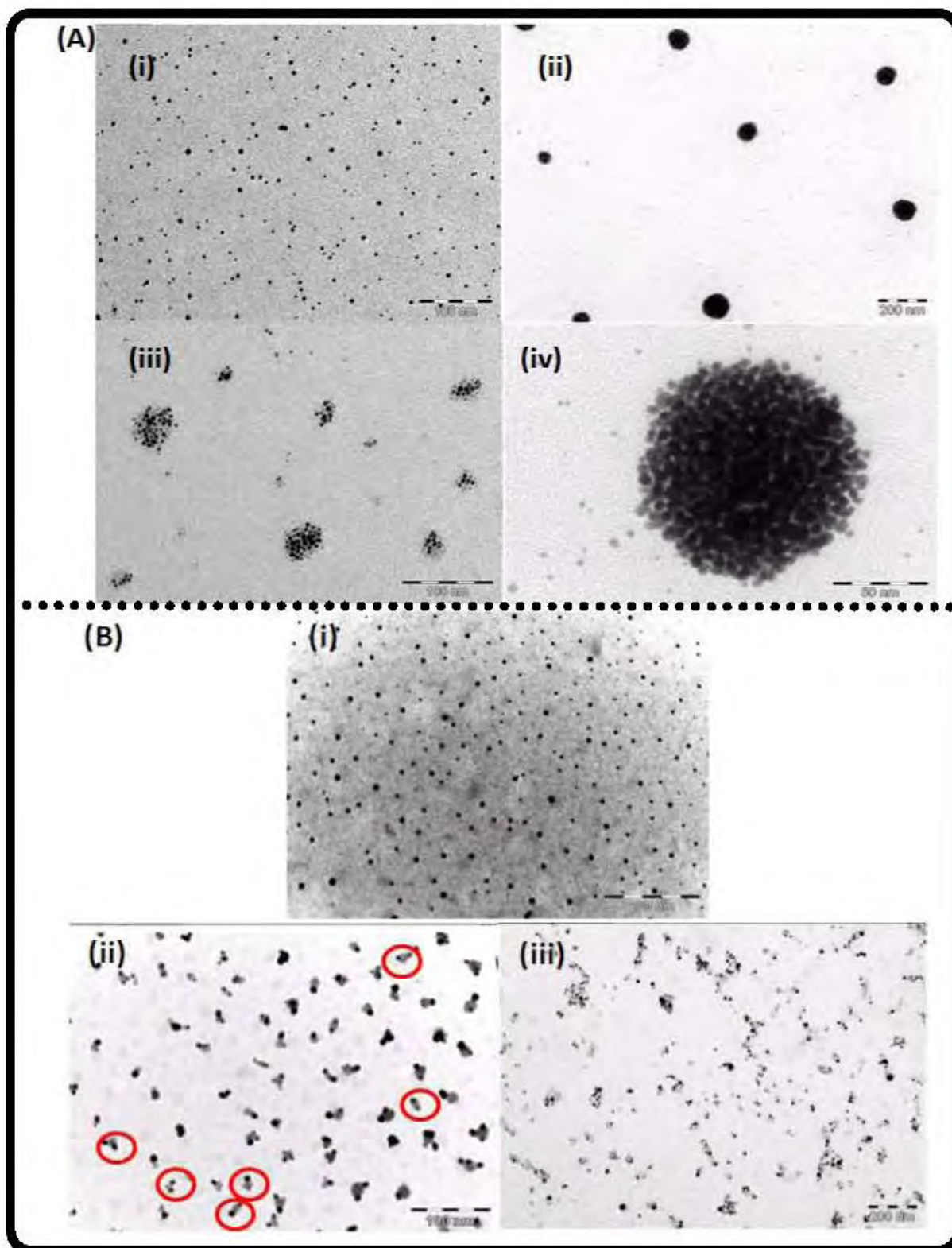
Figure 3.22: Transmission electron microscope (TEM) images of (A) spherical AuNP-4-MPy and (B) spherical AgNP-4-MPy in the absence (i) and presence of MPc (ii – iv). In (A): (ii) = SiHDTPc-AuNPs, (iii) ZnPc-AuNPs while (iv) is the expanded view of (ii). In (B) (ii) =SiHDTPc-AgNPs, (iii) ZnPc-AgNPs.

3.2.3.2. Conjugates

3.2.3.2.1 Synthesis

These MNPs were then conjugated to the MPc complexes following the procedure described in the experimental section. The linking of the SiHDTPc complex to TOABr stabilized AuNPs is achieved by ligand exchange of the loosely bound TOABr, while in the unfunctionalized AgNPs, SiHDTPc acts as the stabilizer without the need for ligand exchange. ZnPc coordinates axially to 4-mercaptopyridine functionalised AuNPs or AuNPs quite easily. The SiHDTPc complex is expected to form a strong sulfur-MNP bond (Scheme 3.7), since gold and silver have high binding affinities for sulphur. Since the SiHDTPc complex has two thiols available for coordination, it may be suggested that both thiol ends are involved during the conjugation as shown in Scheme 3.7. However the smaller size of the phthalocyanine (~ 1 nm) compared to the 5 or 8 nm size of the AuNPs, makes the coordination of two NPs on either side of the Pc unstable. The other possibility is for the free terminal SH groups of the Pcs to link to each other, to form aggregates, but the FT-IR spectra did not show the formation of oxidised S-S bonds (Fig. 3.23). Since the Pc-NP conjugation was prepared without prior isolation of the Au or Ag NPs themselves, the reducing agent, NaBH$_4$, is still present in the solution, keeping any conditions for oxidation at a minimum. There is a third possibility that the Pc has one terminal thiol conjugated to the metal NP, while the other remained as a free SH, Scheme 3.7.

3.2.3.2.2 XRD

The XRD patterns obtained for the conjugates are shown in Fig. 3.21. The XRD pattern of the ZnPc alone (Fig. 3.21A (i)) shows a broad peak centered around ~ 2θ = 25°. SiHDTPc (Fig 3.21B (i)) showed a similar peak at ~ 2θ = 20° which is typical for Pcs [392, 393]. The XRD pattern for both conjugates gave the same face centred cubic structure of AgNPs and AuNPs as well as the broad peaks associated with Pcs at lower 2θ values confirming conjugation. The size of the MNPs was re-estimated and in all cases it was not affected by conjugation.

3.2.3.2.3 TEM

The conjugates were also characterized by TEM as shown in Fig. 3.22. Agglomeration of the nanoparticles into well-ordered islands was observed for the SiHDTPc-AuNP (Fig. 3.22A ii) conjugate.

This cluster of SiHDTPc-AuNPs was magnified at a 50 nm scale (Fig. 3.22A (iv)) and the size of each cluster was estimated to be in the range of ~90-100 nm. Aggregation was also observed in the TEM image of the ZnPc-AuNPs ((Fig. 3.22A (iii)) conjugate, suggesting a very close association of phthalocyanine rings upon conjugation to gold nanoparticles. Aggregation behaviour was also observed when the ZnPc complex was conjugated to AgNPs (Fig. 3.22B (iii)). Aggregation or agglomeration of phthalocyanines has been documented before when the Pcs have been conjugated to MNPs [175, 176 232-239]. The TEM image of the SiHDTPc-AgNPs conjugate (Fig. 3.22B (ii) shows ordered aggregates, confirming perhaps the presence of more than one AgNP coordinated to the MPcs. Once again, the stability of such a structure

comes into question. The features circled in Fig. 3.22B (ii), suggest a V-shaped arrangement of the SiHDTPc when coordinated to AgNPs. Several Pcs could be accommodated in this way and this would address the stability issue in this case. This could also explain the red shifts observed in the Q band of the Pc (discussed below) in the presence of the AgNP since the longitudinal dipole arrangement of both the NP and the Pc would result in a red shift [397].

3.2.3.2.4 FTIR

The MPc-MNP conjugates were further characterized by IR as shown in Fig. 3.23. 1,6-Hexanedithiol (Fig. 3.23A(i)) and SiHDTPc (Fig. 3.23A (ii)) are characterized by the thiol S-H stretching band at ~ 2560 cm^{-1} region. A disappearance of the S-H stretching band in the IR spectra of SiHDTPc-AgNP conjugate (Fig. 3.23A (iii)) is observed, confirming successful conjugation.
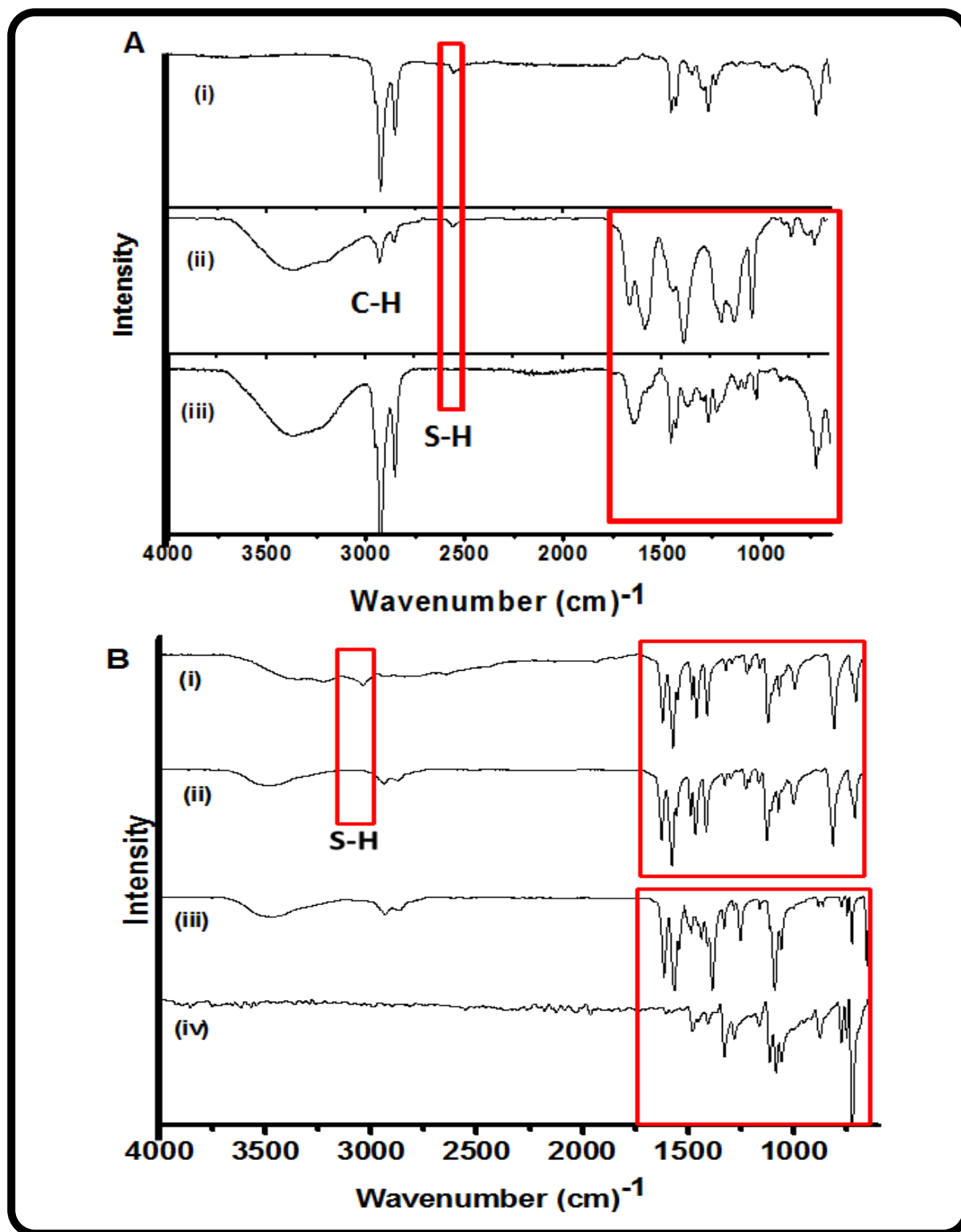
Figure 3.23: Infrared spectra (IR) of (A) 1,6 hexanedithiol (HDT) (i), SiHDTPc (61) alone (ii) and SiHDTPc-AgNPs (iii). (B) 4-mercaptopyridine (4-MPy) alone (i), 4-MPy-AgNPs alone (ii), ZnPc-AgNPs (iii) and ZnPc alone (iv).

A disappearance of the S-H signal of 4-mercaptopyridine (Fig. 3.23B (i)) was observed in the IR spectra of the AgNPs, suggesting formation of 4-mercaptopyridine stabilized AgNPs. There were no changes in the peaks associated with 4-mercaptopyridine in the aromatic fingerprint region. An increase in peak density, accompanied by changes in symmetry of the aromatic signals was observed in the IR spectra of the ZnPc-AgNP conjugate, suggesting successful conjugate formation, Fig. 3.23B(iii). The IR spectra of the MPcs-AuNP (spectra not shown) showed a similar behaviour, also confirming formation of MPc-AuNP conjugates.

3.2.3.2.5 UV-Vis spectra

The spectral properties of the MPcs and their axially ligated MNP conjugates are presented in Table 3.5.

Table 3.5: Spectral properties of the various complexes axially ligated to MNPs in DMF

Complex	$\lambda_{abs \text{ (nm)}}$	$\lambda_{emi \text{ (nm)}}$	$\lambda_{exci(nm)}$	Δstokes (nm)
ZnPc	670	676	671	5
ZnPc-AgNPs	673	680	673	7
ZnPc-AuNPs	671	682	671	11
SiHDTPc (61)	676	683	676	7
SiHDTPc-AgNPs	683	691	682	9
SiHDTPc-AuNPs	682	688	682	6
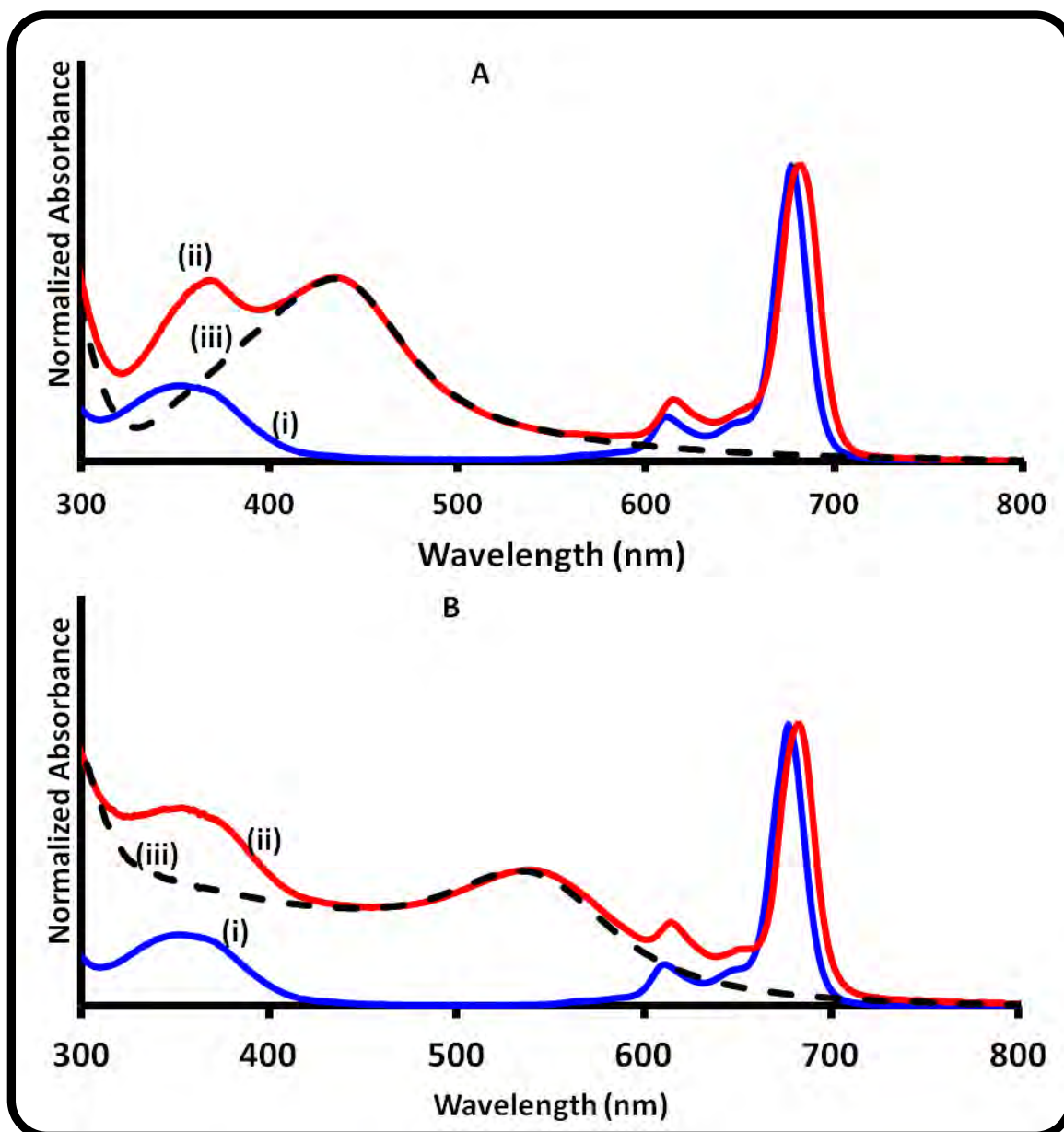
Figure 3.24: UV-Vis spectra of SiHDTPc in the presence of (A) uncapped AgNPs and (B) TOABr coated AuNPs. (i) SiHDTPc alone, (ii) SiHDTPc with MNPs and (iii) MNPs alone in DMF.

Red shifting of the Q-band absorption (Table 3.5) accompanied by the appearance of new bands (due to the SPR bands of the NPs) was observed for SiHDTPc in the presence uncapped AgNPs (Fig. 3.24A) and TOABr coated AuNPs (Fig. 3.24B). Red shifting can be associated with the longitudinal dipole arrangement of both the NP and the Pc as discussed above [397].
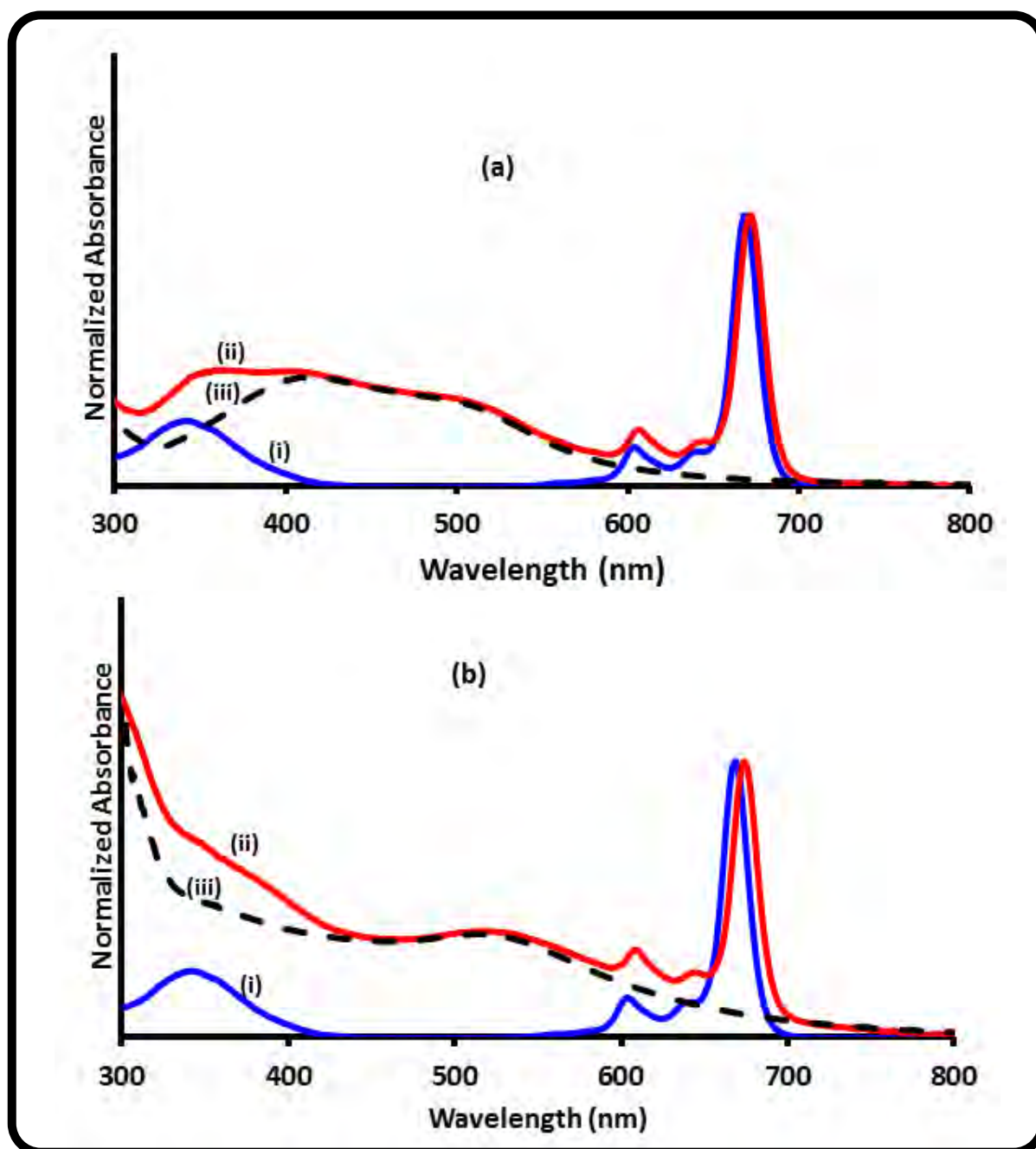
Figure 3.25: UV-Vis spectra of ZnPc (i) alone, and in the presence of (a) 4-MPy-AgNPs (ii) and (b) 4-MPy-AuNPs (ii). Traces (iii) spectra of 4-MPy-AgNPs (a) and 4-MPy-AuNPs (b).

Red shifting was also observed with the ZnPc-MNPs conjugates as shown above in Fig.3.25, Table 3.5, though a smaller scale compared to complex **61**. Negligible changes observed for the AuNPs-ZnPc conjugate.
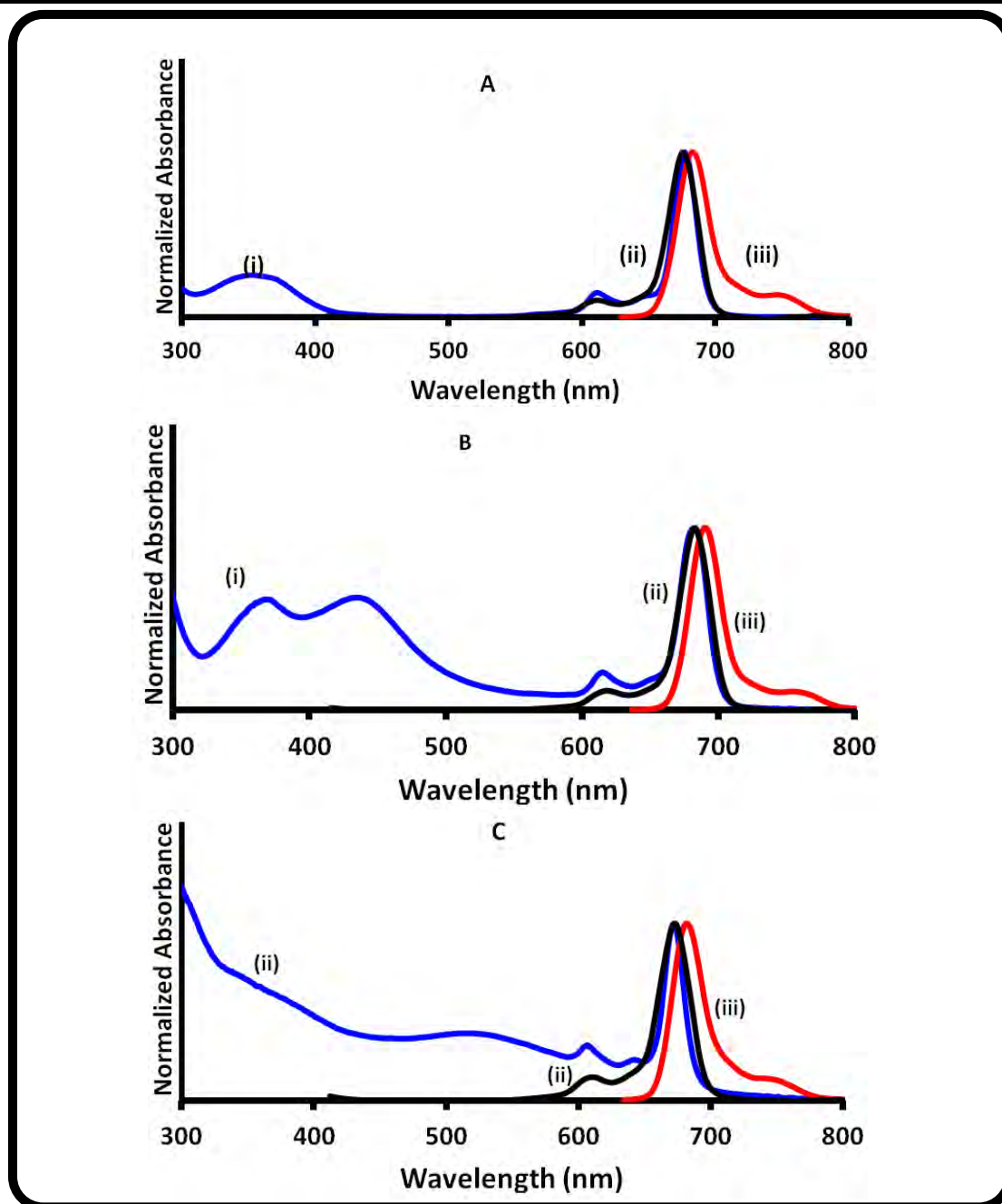
Figure 3.26: Absorption (blue line, i), excitation (black line, ii) and fluorescence emission (red line, iii) and spectra of (A) SiHDTPc alone, (B) SiHDTPc-AgNPs and (C) ZnPc –AuNPs in DMF.

The absorbance, fluorescence excitation and emission spectra for SiHDTPc alone are shown in Fig. 3.26A. The excitation spectra were in agreement with absorption spectra and both were mirror images of the emission spectra suggesting no changes

in the molecule when excited with light. Fig. 3.26B show the fluorescence spectral behaviour of the SiHDTPc conjugated to bare AgNPs, Fig. 3.26C, and that of the ZnPc conjugated to 4-MPy-AuNPs as examples. The SPR bands are not seen upon excitation and no additional broadening of the spectra in the region around ~500 nm is observed, since the AgNPs and AuNPs do not fluoresce. The Stokes' shifts for the all the complexes and their corresponding conjugates were observed in the range of 6 to 11 nm (Table 3.5), which is typical for MPc complexes.

3.2.4 Conjugates of MPcs to Quantum dot core shells (QDs)
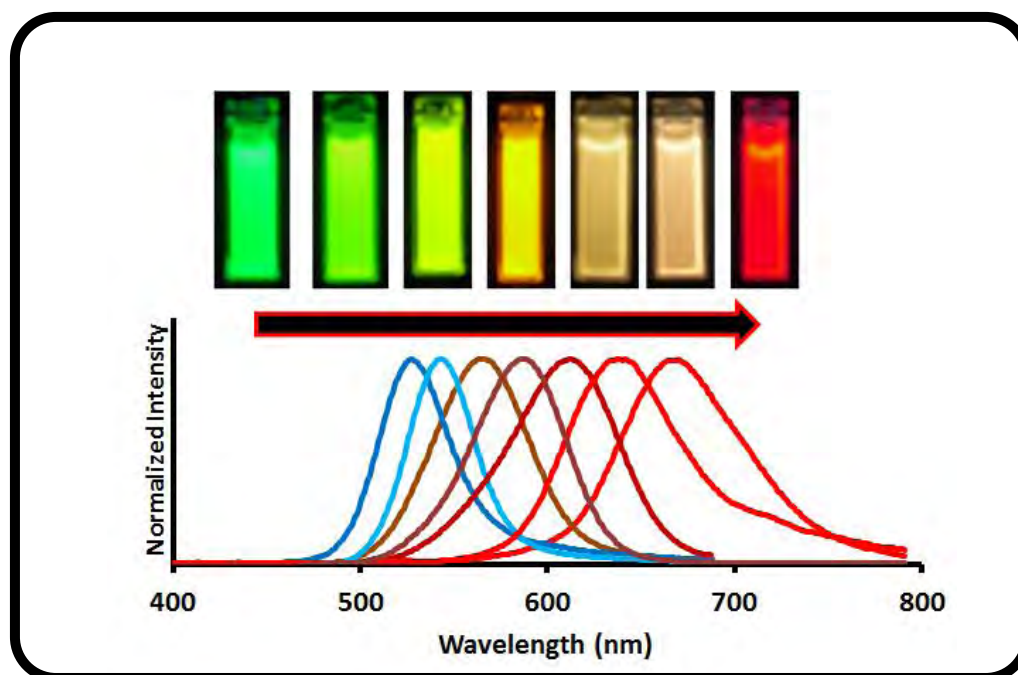
Figure 3.27: Photoluminescence spectra of CdTe-TGA quantum dots at various growth times. Insert = changes in the quantum dots colour with time.

The MPc complexes used in this section are: ZnMCsPc (**49**), ZnMPCPc (**53**), (ac)$_2$SnMCPc (**58**), (OH)$_2$MCPc (**59**) and OTiMCPc (**60**) representing all the ring systems as examples.

3.2.4.1 QDs alone

The CdTe QD coresused were synthesiszed in aqueous media using thioglycolic acid as a stabilizing thiol (Scheme 3.8). As is typical of QDs, the absorption and emission spectra are shifted to the red with an increase in size, Fig. 3.27. Digital images were also taken during the period of growth (Fig. 3.27, insert) showing changes in colour from blue to red as a result of an increase in QD size.
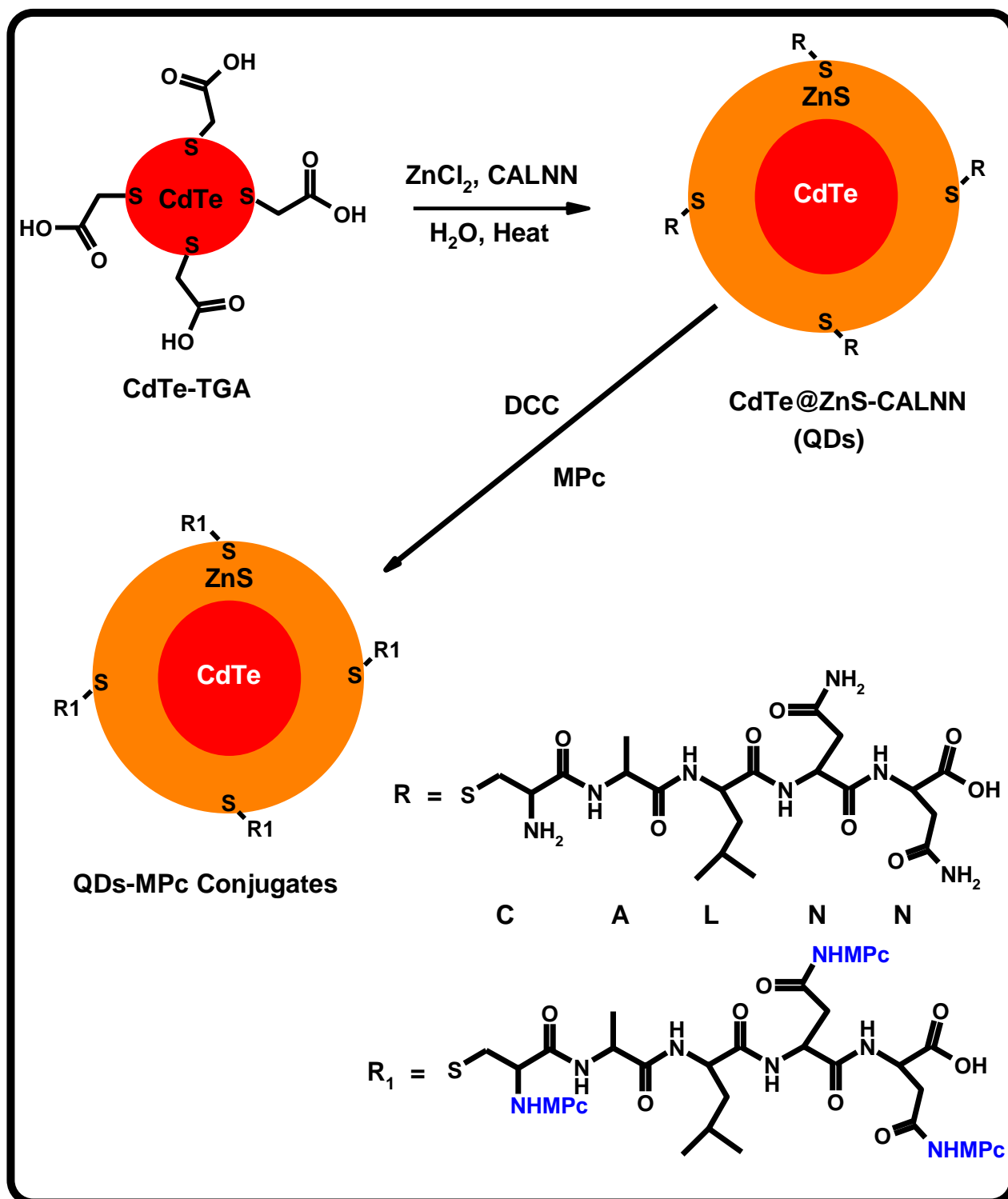
Scheme 3.8: Synthesis of CdTe@ZnS-CALNN coreshell quantum dots and QDs-MPc conjugates respectively. Inset – the structure of CALNN used.

Two sizes of CdTe-TGA QDs with emission maxima at 607 (CdTe-TGA QDs1 (3.2 nm)) and 645 nm (CdTe-TGA QDs2 (3.7 nm)) were precipitated, dried and further characterized in the preparation of the coreshells (CdTe@ZnS-CALNN QDs). The

latter (Scheme 3.8) were obtained by reacting the CdTe-TGA QDs in aqueous NaOH solution (pH 10), in the presence of $ZnCl_2$ and CALNN as discussed in the experimental section. CALNN was used both as source of sulfur and a stabilizing agent. The CdTe@ZnS-CALNN QDs were further characterized using UV-Vis, XRD, IR and XPS. In this work the coreshells will be represented by CdTe@ZnS-CALNN QDs1 (made from CdTe QDs 3.2 nm in size) and CdTe@ZnS-CALNN QDs2 (made from CdTe QDs 3.7 nm in size).
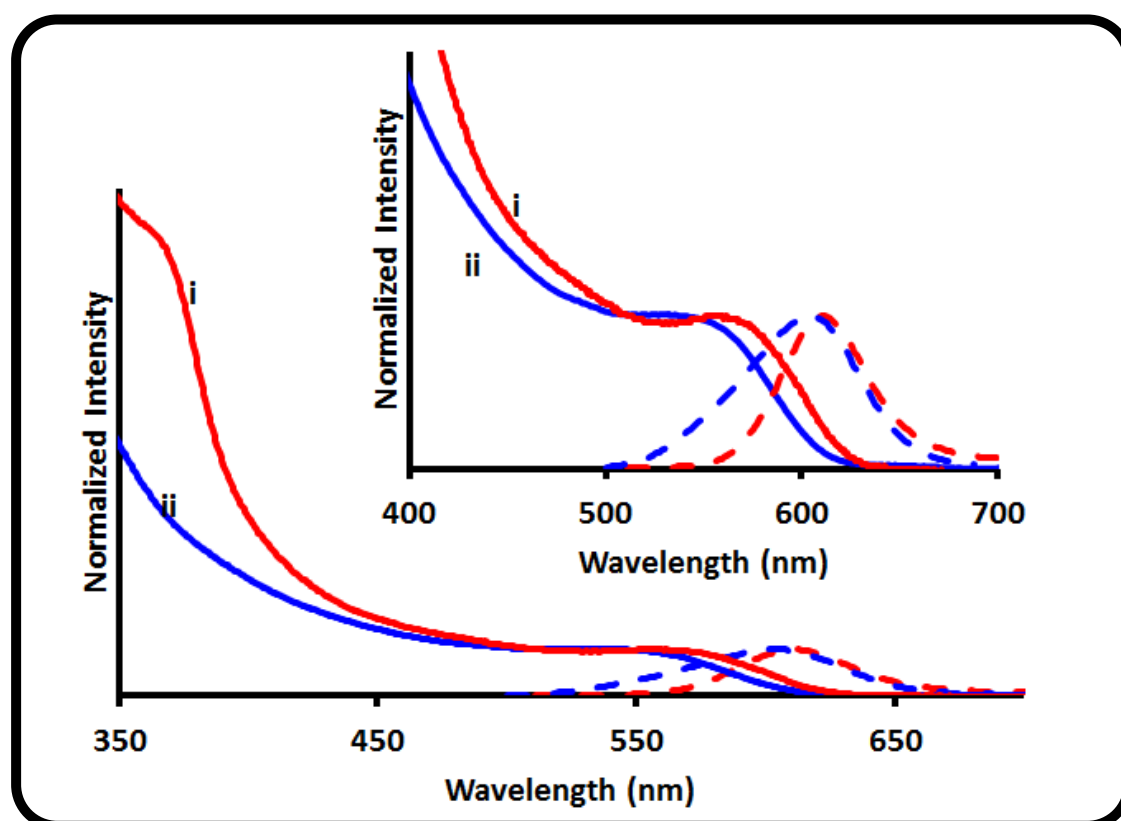
Figure 3.28: Ground state electronic absorption and fluorescence emission spectra (dotted line) of CdTe@ZnS-CALNN QDs1 (3.9 nm) (i) and CdTe-TGA QDs 1 (3.2 nm) (ii) in water, pH 7.4. Inset = expansion of the 400 to 700 nm region.

The UV-visible spectra of CdTe-TGA and its core-shell counterpart (CdTe@ZnS-CALNN QDs1) are presented in Fig. 3.28. Red shifting of spectra and a new

absorption band around 370 nm were observed in the UV-vis spectra of CdTe@ZnS-CALNN QDs1. This red shift in the spectra is a result of nanoparticle growth, which is seen more clearly in the expanded absorbance and fluorescence emission spectra as given by the insert in Fig. 3.28. Similar spectral behaviour was observed with CdTe@ZnS-CALNN QDs2.
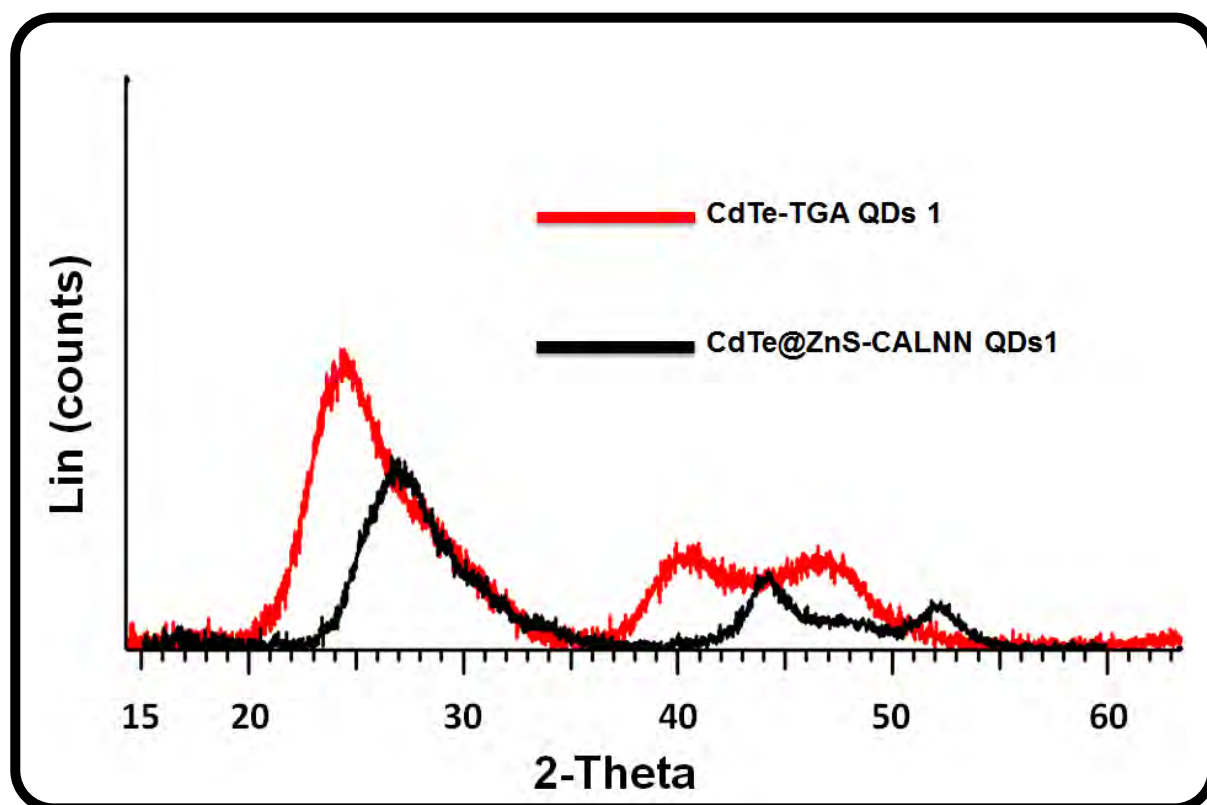
Figure 3.29: X-ray diffraction pattern of CdTe@ZnS-CALNN QDs1 (black) and CdTe-TGA QDs 1 (red).

The XRD spectra for CdTe@ZnS-CALNN QDs1 and its core (CdTe-TGA QDs) are presented in Fig. 3.29. The crystalline structure derived from the diffraction patterns of the powdered QD sample suggests a cubic zinc-blende phase (sphalerite) which is also known to be favoured with bulk CdTe [398, 399]. The XRD was employed to determine the size of the core-shell QDs and the CdTe@ZnS-CALNN QDs1. The size

was determined to be 3.9 nm and 4.4 nm for CdTe@ZnS-CALNN QDs2 indicating an

increase in size upon coreshell formation from 3.2 and 3.7 nm for the core CdTe-TGA

QDs1 and CdTe-TGA QDs2, respectively. A relatively large shift to higher 2θ

values was also observed for the coreshell compared to the core QD alone (Fig. 3.29).

Changes in peak positions suggest changes in crystal structure that might have

resulted upon coreshell formation.
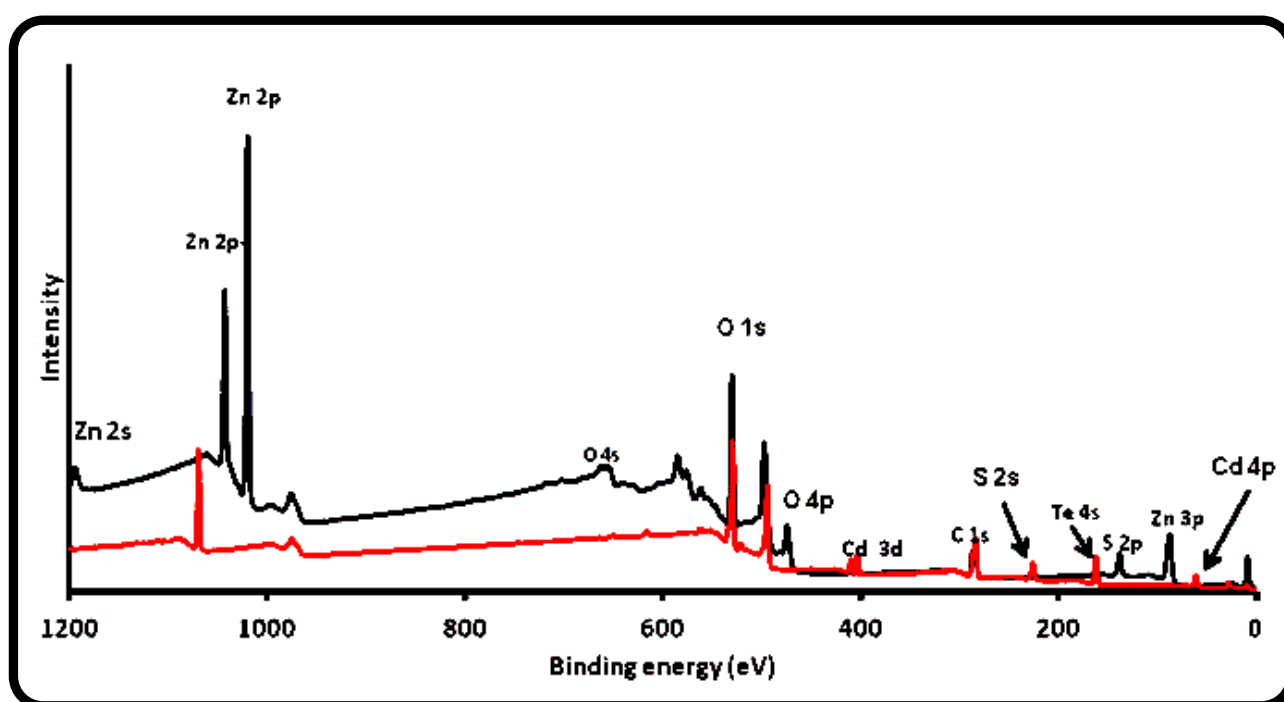
Figure 3.30: X-ray photoelectron spectra of CdTe@ZnS-CALNN QDs1 (black) and CdTe-TGA QDs1 (red).

The XPS spectra of the QD core and coreshells are presented in Fig. 3.30. The CdTe-

TGA QDs core is characterized by a split Cd 3d binding energy peak at 405 and 412

eV [364], and Te 4s peak at 165 eV, a clear indication of the presence of CdTe. A

disappearance of the Cd and Te peaks was observed with the spectra for the

coreshell QDs, which serves as solid evidence for the formation of CdTe@ZnS

coreshell. The Zn 2p peaks were observed in the coreshell spectra, further serving as

a proof of its formation. All other peaks are attributed to the Auger peaks or stabilizers used in the quantum dots synthesis.

3.2.4.2 Conjugates

Following the synthetic route shown in Scheme 3.8, these QDs (CdTe@ZnS-CALNN QDs1 and CdTe@ZnS-CALNN QDs2), were coupled to low symmetry metallophthalocyanines: ZnMCsPc (**49**), ZnMPCPc (**53**), (ac)$_2$SnMCPc (**58**) (OH)$_2$GeMCPc (**59**), OTiMCPc (**60**). The conjugates were formed by coupling the amine groups of CALNN with the free carboxylic acid on the Pcs that were pre-activated with DCC as mentioned in the experimental section. The linked conjugates are represented as ZnMCsPc(**49**)-QD-linked, (ac)$_2$SnMCPc(**58**)-QD-linked, (OH)$_2$GeMCPc(**59**)-QD-linked, OTiMCPc(**60**)-QD-linked, and ZnMPCPc(**53**)-QD-linked. However, the formation of Pc-Pc dimer during activation of complex **49** cannot be ruled out. The mixed conjugates (in the absence of covalent bond formation) are represented as ZnMCsPc(**49**)-QD-mixed, (ac)$_2$SnMCPc(**58**)-QD-mixed, (OH)$_2$GeMCPc(**59**)-QD-mixed, OTiMCPc(**60**)-QD-mixed, and ZnMPCPc(**53**)-QD-mixed, where QD represents CdTe@ZnS-CALNN QDs1 or CdTe@ZnS-CALNN QDs2.

The UV-visible spectra of ZnMCsPc (**49**) alone, linked and mixed to CdTe@ZnS-CALNN QDs1 is presented in Fig. 3.31A. Broadening, together with the presence of a blue shifted peak (attributed to aggregation) in the region around 620 nm was observed for the mixture of **49** with QD (without a chemical bond). As stated already, aggregation arises as a result of the co-planar association of the

phthalocyanine rings. However, in this case the aggregation tendencies might be influenced by the presence of the QDs, probably resulting in some salting out effect. Aggregation of phthalocyanines in the presence of quantum dots in aqueous media has been reported before [269]. There were no bands due to aggregation or salting out observed for the linked complex (for ZnMCsPc (**49**)), Fig. 3.31A. The absorption band near 400 nm is observed in both the mixed and linked conjugates which correspond to the absorption of the QDs.
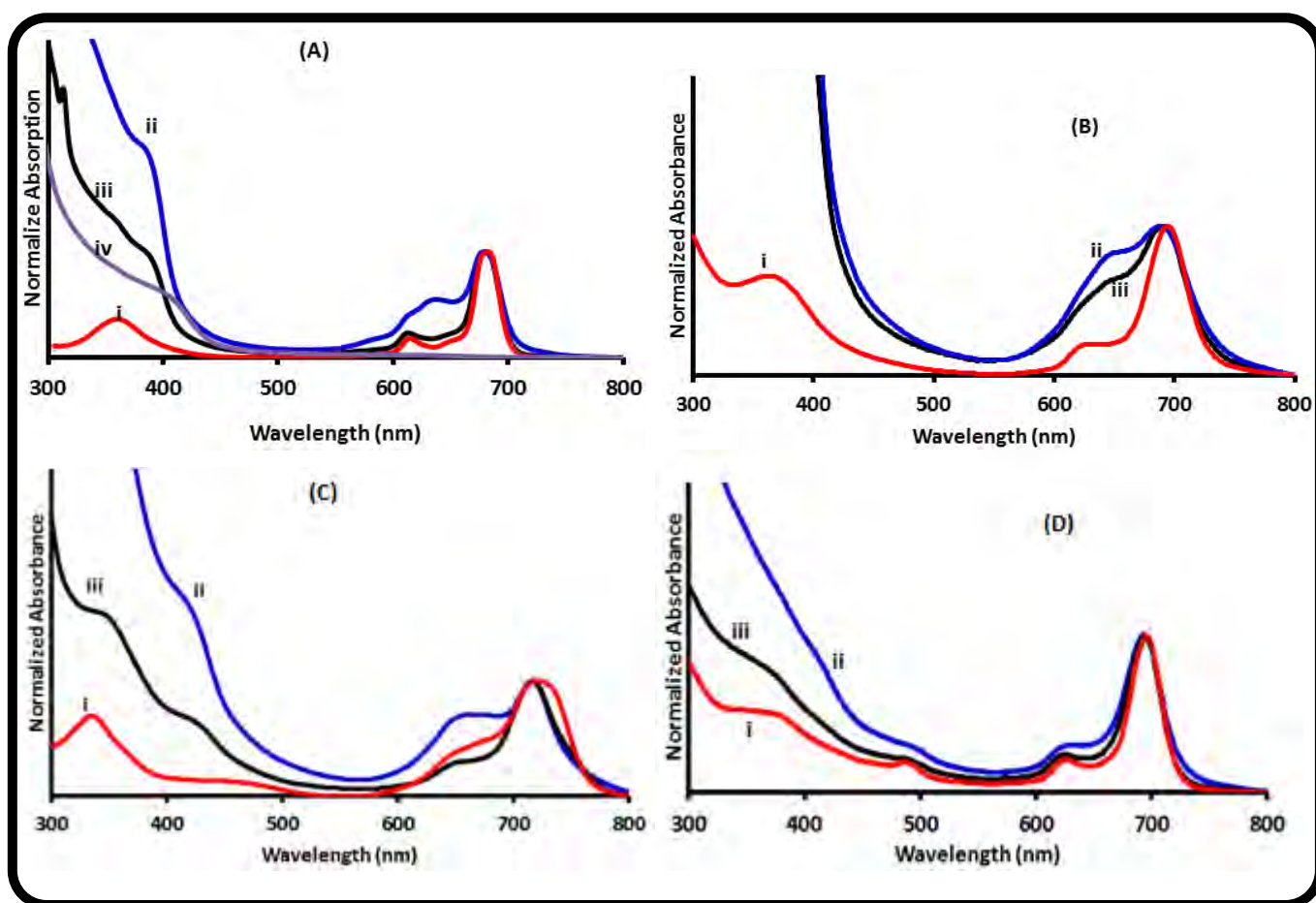
Figure 3.31: UV-Visible spectra of (A) ZnMCsPc (49), (B) ZnMPCPc (53), (C) (ac)₂SnMCPc (58) and (D) (OH)₂GeMCPc (59).   (i)   alone, (ii) mixed with CdTe@ZnS-CALNN QDs1 or (iii) linked to CdTe@ZnS-CALNN QDs1. (iv) in (A) is for and CdTe@ZnS-CALNN QDs1 alone. Solvent: DMSO:water (8:2).

Absorption bands due to aggregates or salting out were also observed for the ZnMPCPc(**53**)-QDs-mixed, Fig. 3.31B and (ac)₂SnMCPc(**58**)-QDs-mixed, Fig. 3.31C. The band due to aggregation was less evident for (OH)₂GeMCPc(**59**)-QDs-mixed, Fig. 3.31D.
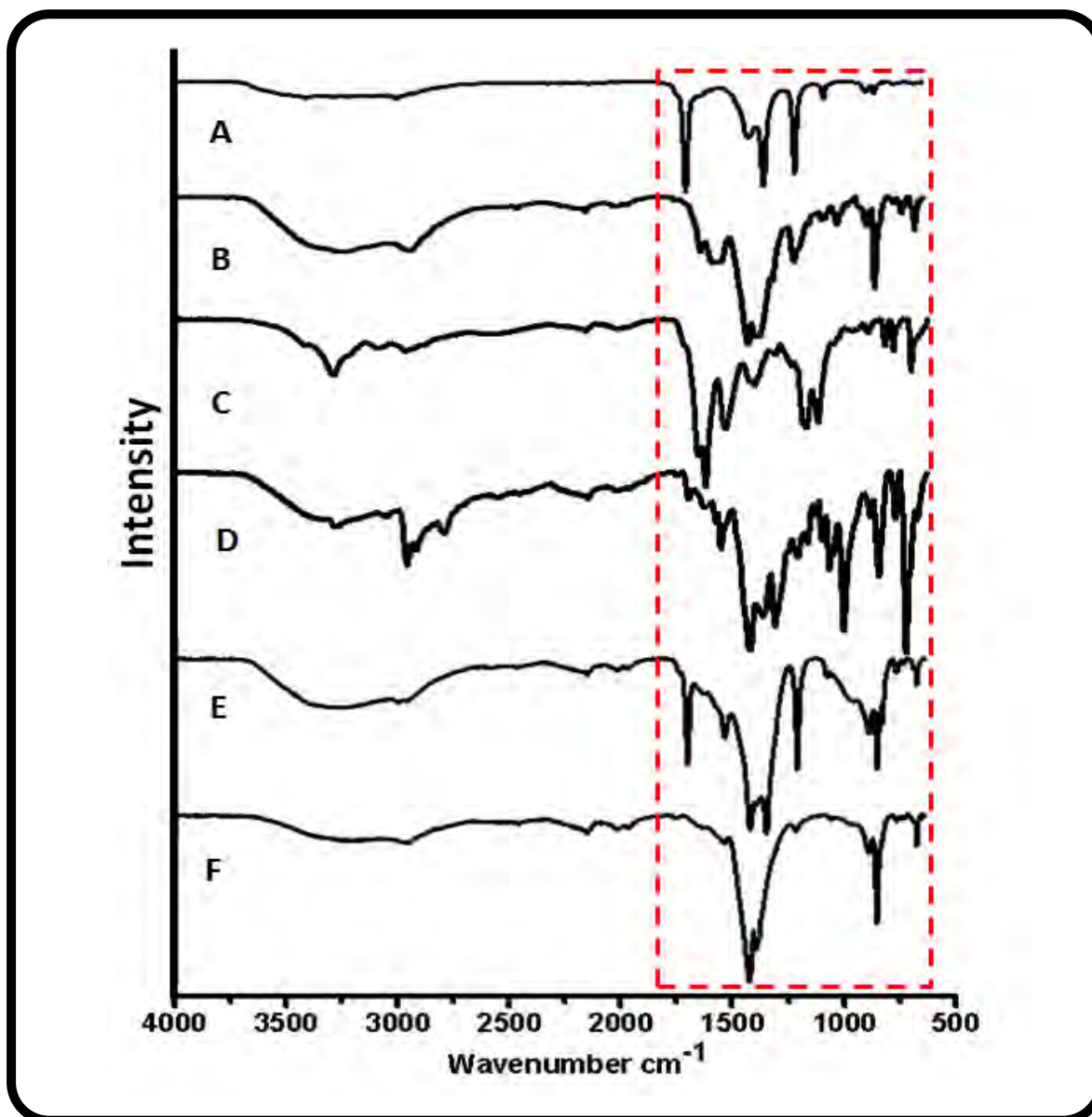
Figure 3.32: Infrared spectra of the ZnMCsPc (49)(A), ZnMPCPc (53)(B), (OH)₂GeMCPc (59)(C), (ac)₂SnMCPc (58)(D) and OTiMCPc (60)(E) linked to CdTe@ZnS-CALNN QDs1 and CdTe@ZnS-CALNN QDs1 alone (F).

Changes in the infrared spectra of the quantum dots (Fig. 3.32) upon conjugation to the low symmetry phthalocyanines was observed for all the complexes suggesting conjugation. The peptide backbone on CALNN contains a number of amide linkages, Scheme 3.8. An increase in peak intensity in the amide carbonyl regions (~1600-1700 cm^{-1}) was observed for all the complexes, which may have resulted from the additional amide bonds due to coordination between phthalocyanine and quantum dots. Peaks corresponding to the QDs were observed in all the Pc's IR spectra.
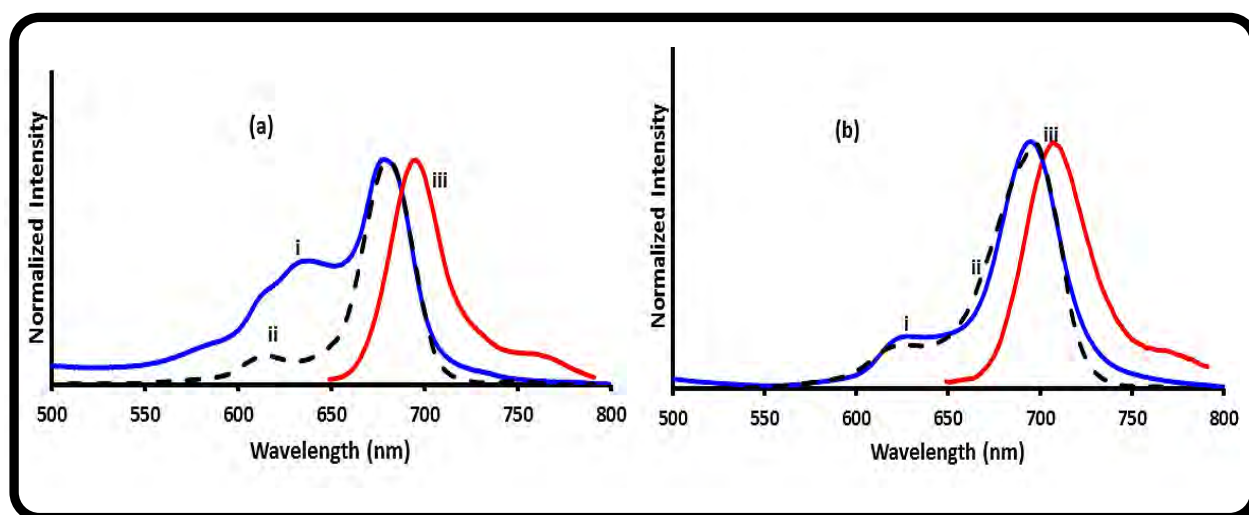
Figure 3.33: UV-Visible absorption (i), fluorescence excitation (ii) and emission (iii) spectra of ZnMCsPc mixed with CdTe@ZnS-CALNN QDs1 (a) and ZnMPCPc linked to CdTe@ZnS-CALNN QDs1 (b) in 8:2 DMSO: water.

The fluorescence spectra of the ZnMCsPc QDs mixed and ZnMPCPc QDs linked are presented in Fig. 3.33. The broadening of absorption spectra due to aggregation or salting out is diminished in the excitation and emission spectra of the mixed QDs:Pc systems, Fig. 3.33. It has been documented that aggregates do not fluoresce which

serves as confirmation that the observed broadening and blue shifting of spectra for the mixed complex was due to aggregation.

3.3 Preparation and characterization of MPc supported polymer fibers

This section discusses the preparation and characterization of physisorbed Pc/Polystyrene and Pc-AgNPs/Polystyrene polymer fibers, for use in the antimicrobial inhibition of bacteria which is discussed later in this thesis. The choice of the polystyrene polymer in this work was due to the ease with which electrospinning may be carried out to form cotton like fiber mats together with its physical and chemical stability. Polystyrene (PS) has extensive aromatic system that can interact with the aromatic system of phthalocyanines through of π-π interactions.

Part 1: The phthalocyanines which were employed for these studies were unsubstituted ZnPc, ZnMCsPc (**49**), ZnMPCPc (**53**), (ac)$_2$SnMCPc (**58**), (OH)$_2$GeMCPc (**59**), OTiMCPc (**60**), and ZnTPCPc (**71**) complexes, which were chosen as representatives of each ring system for the Pcs. The complexes were electrospun into polystyrene polymer fibers and their antimicrobial properties tested and compared.

Part 2: In another set of experiments the unsymmetrical zinc Pc complexes (ZnMCsPc(**49**), ZnMPCPc (**53**), and ZnMCPc (**57**)) and their symmetric counterparts (ZnTPPc(**70**), ZnODEPc (**69**) and ZnTDEPc (**68**)) were electrospun alone and in the presence of AgNPs for bacterial growth inhibition. Only the ZnPc derivatives were used, to expand on the known PACT activity of unsubstituted ZnPc. Both sets have

symmetrical and unsymmetrical Pcs in order to evaluate the effects of the lack of symmetry of Pc on PACT.

3.3.1 Interaction of MPcs with polystyrene

The MPc complexes were mixed with polystyrene and electrospun into nanofibers as explained in the experimental section. Scanning electron microscope images of the various MPc complexes alone or incorporated into polystyrene, show highly branched cylindrical network of nanofibers, Fig. 3.34.
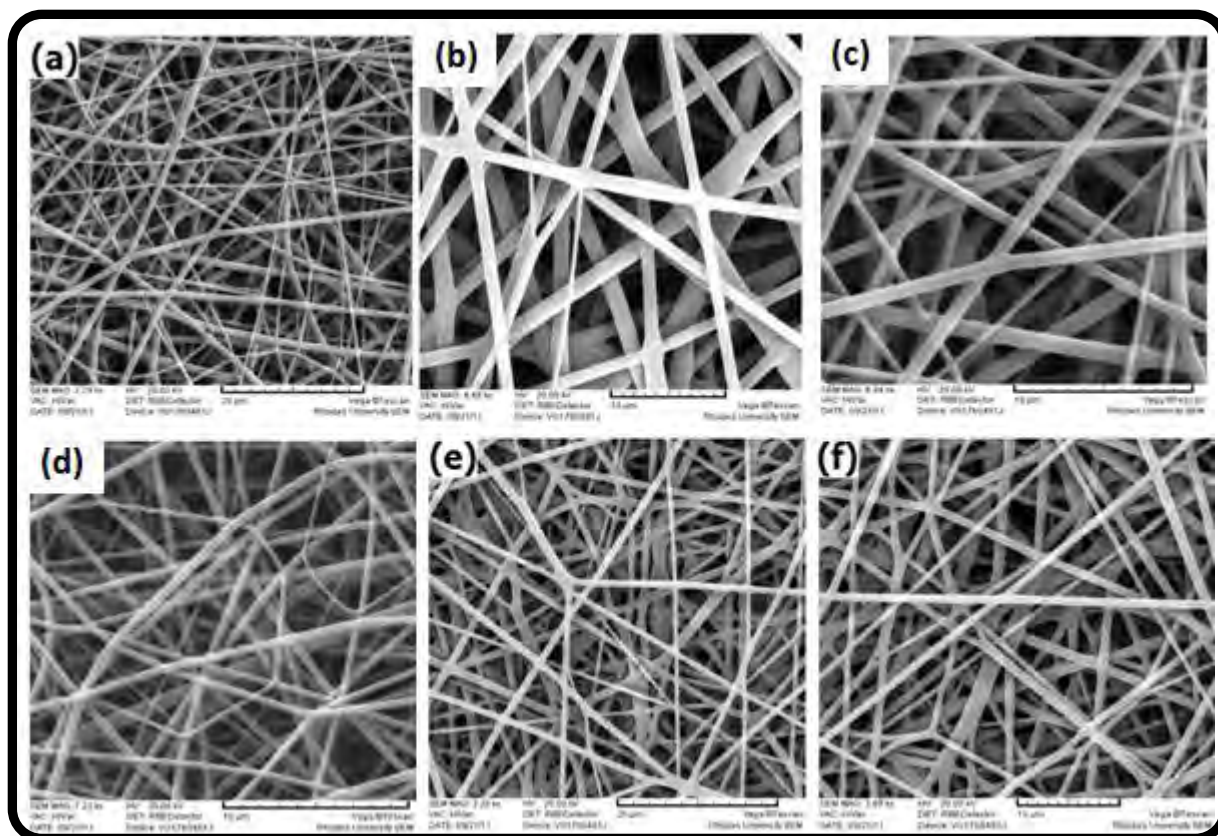
Figure 3.34: Scanning electron microscopic (SEM) images polystyrene electrospun fiber alone (a), (ac)$_2$SnMCPc (58):PS (b), (OH)$_2$GeMCPc (59):PS (c), OTiMCPc (60):PS (d), ZnMCsPc (49):PS (e) and ZnMPCPc (53):PS (f). Scale = 10 μm.

The fiber diameter ranged from 240 ± 45 nm to 390 ± 30 nm, Table 3.6. The polystyrene fibers alone gave the smallest fiber diameter with an average size of 240 ± 45 nm, which is within the range of previously reported average diameters for polystyrene [302-304].

Table 3.6: Spectral, microscopic and photochemical properties of the low symmetry MPc complexes in solution (DMF) and in the fiber matrix

Sample	λ_Q/nm (solution)	λ_Q/nm (solid)	Average diameter (nm)
$(OH)_2$GeMCPc (**59**)	695	692	275 ±30
OTiMCPc (**60**)	734	728	315 ±30
$(ac)_2$SnMCPc (**58**)	720	716	370 ±30
ZnMCsPc (**49**)	678	680	260 ±30
ZnMPCPc (**53**)[a]	695 (683)	684 (680)	390 ±30
ZnPc	670	668	305 ±35
Polystyrene	-	-	240 ±45

[a]Numbers in brackets are for the symmetrical ZnTPCPc(**71**)

An increase in fiber diameter was obtained in the presence of phthalocyanines. The ZnMPCPc(**53**)-PS composite gave the highest average fiber diameter of 390 ± 30 nm compared to all the other complexes, followed by $(ac)_2$SnMCPc(**58**) with the average diameter of 370 ± 30 nm, respectively, Table 3.6. The solutions properties such as viscosity, conductivity and surface tension may affect the fiber formation, hence the diameter of the fibers. The nature and the conductivities of MPc complexes may have a large effect on the electrospinning process. Differences in the nature of the central metal atom, inter-planar distances between the molecules and differences in

stacking arrangements of the molecules all affect conductivity in phthalocyanines [302-304], hence the fiber diameter.
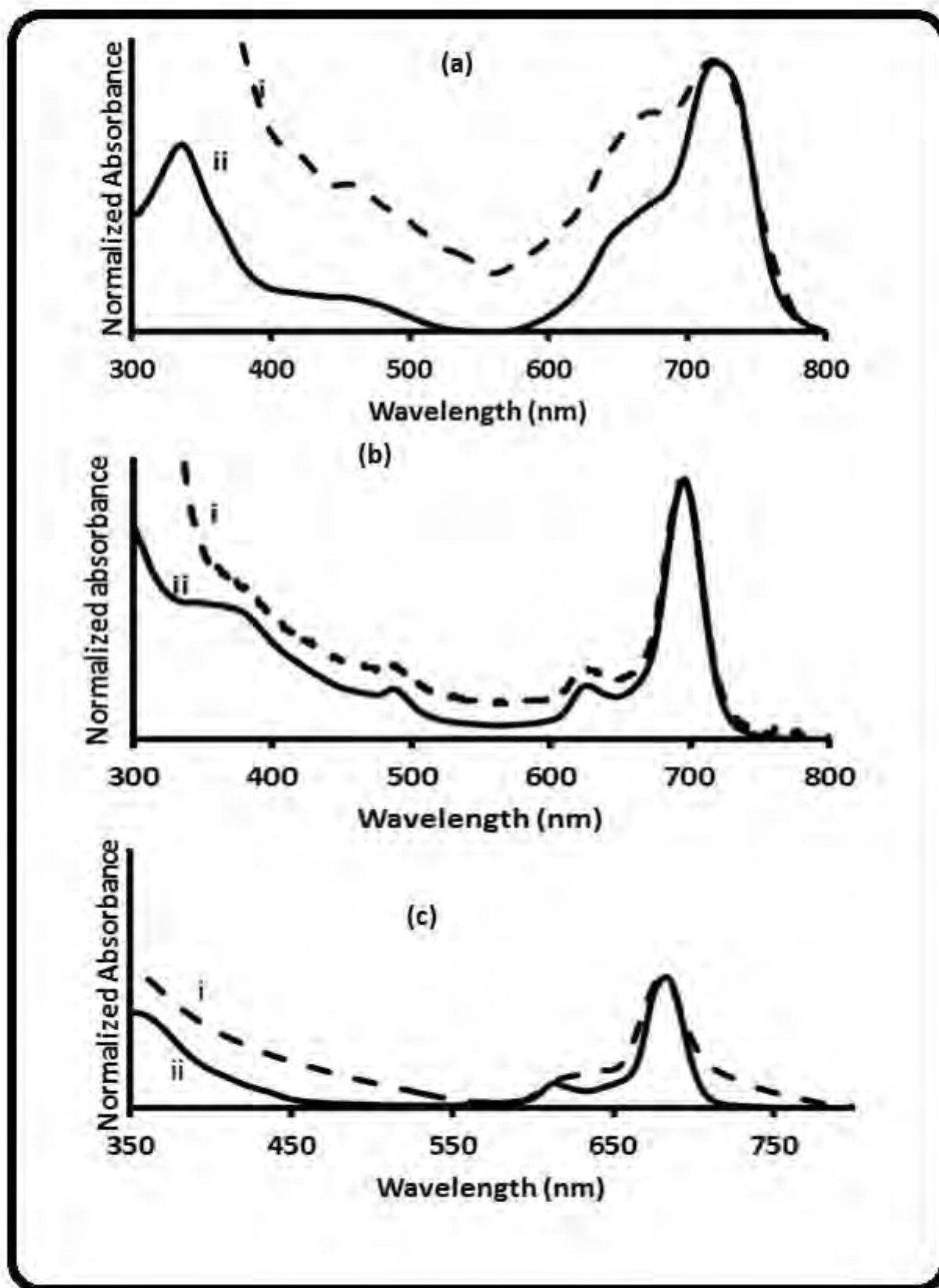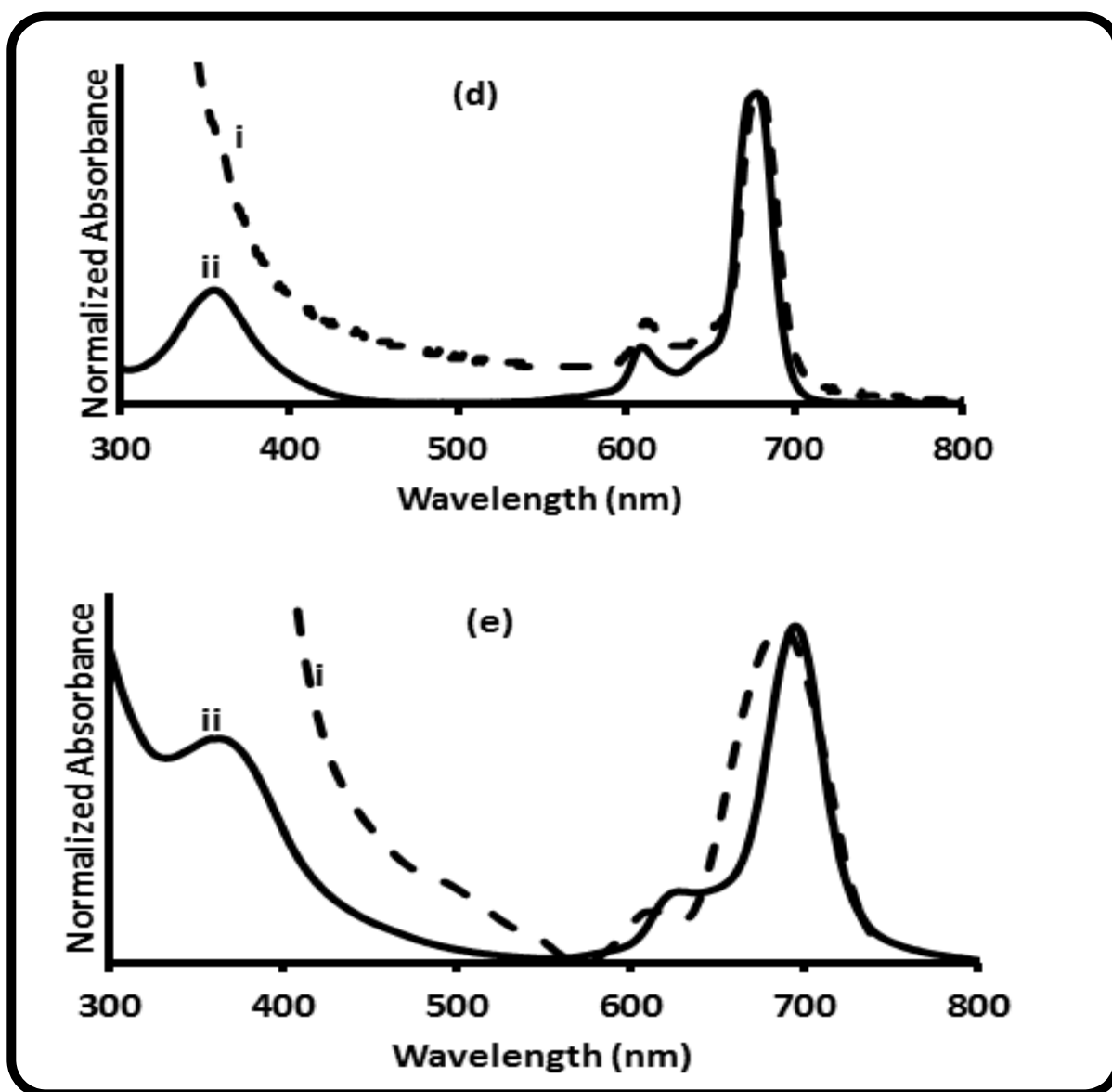
Figure 3.35: Ground state electronic absorption spectra of (a) (ac)₂SnMCPc (58), (b) (OH)₂GeMCPc (59), (c) OTiMCPc (60), (d) ZnMCsPc (49) and (e) ZnMPCPc (53), in (i) (polymer fiber) and in solution (DMF) (ii).

The UV-visible absorption spectra of the complexes in solution and in the polymer support are shown in Fig. 3.35. Blue shifts in the Q band spectra were observed for ZnMPCPc(**53**), (ac)₂SnMCPc(**58**), (OH)₂GeMCPc(**59**) and OTiMCPc(**60**) on the fiber

(spectra(i) in Fig. 3.35). The blue shifting in the spectra of these complexes, which contain sulfur bridges, suggests that there is an interaction between the fiber and the S groups, since the sulfur groups are known to result in red shifting in Pc Q band. (ac)$_2$SnMCPc(**58**), Fig. 3.35a, showed a clear split in the Q band with the high energy band being attributed to the aggregate and the low energy band to the monomer. Aggregation of phthalocyanines in general is expected in the solid state due to the close proximity of Pc-Pc rings, which results in very strong $\pi - \pi$ interations. The (OH)$_2$GeMCPc(**59**) (Fig. 3.35b) and ZnMCsPc(**49**) (Fig. 3.35d) complexes did not show extensive broadening of the Q band on the polymer fiber.

The observed behaviour and differences in the spectral properties could also be explained in terms of molecular exciton theory. This theory is usually used to rationalize the differences between the optical spectra in the liquid phase and those in the solid state [400-402].

These differences in spectra for phthalocyanines in the solid state and solution have been reported by other workers [403]. Aggregation in the solid state however does not favour generation of singlet oxygen.
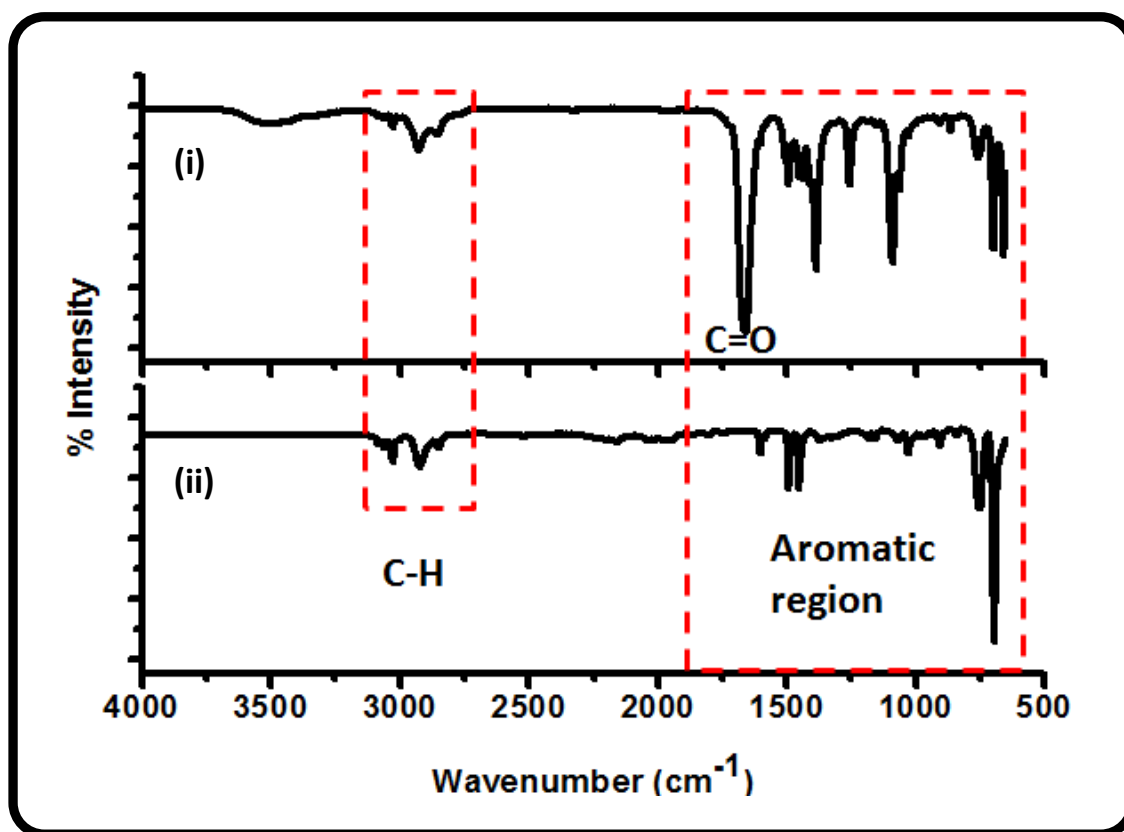
Figure 3.36: Infrared spectra of (ac)₂SnMCPc(58)/PS (i) and polystyrene fiber alone (ii).

The IR spectra of the polystyrene fiber shows the characteristic signals in the aromatic finger print region which are due to the styrene subunits (Fig. 3.36(ii)). The aromatic C=C bands from the styrene ring are observed at the region of ~1470-1600 cm^{-1}. An increase in the intensity of aromatic signals in the 1470 to 1600 cm^{-1} was observed in the IR spectra of MPc-PS composite (using (ac)₂SnMCPc (**58**) as an example) suggesting additional aromatic rings contributed by the Pc ring (Fig. 3.36 (i)). The intense carbonyl C=O stretching band around ~ 1650 cm^{-1} was observed for all the complexes, and is due to the carboxylic acid groups of the phthalocyanine complexes, serving as a further confirmation of the presence of Pc in the polymer fiber.

3.3.2 Interaction of low symmetry and symmetrical Pcs with polystyrene in the presence of spherical AgNPs

This part compares the unsymmetrically substituted zinc Pc complexes (ZnMCsPc **(49),** ZnMPCPc **(53)**, and ZnMCPc **(57)**) and their symmetrical counterparts (ZnTPPc **(70),** ZnODEPc **(69)** and ZnTDEPc **(68)).**

The complexes were first allowed to react with 4-mercaptopyridine capped AgNPs as explained in the experimental section for the unsubstituted ZnPc. 4-Mercaptopyridine capped AgNPs were selected because of their ease of coordination to Zn via axial ligation. The reaction of the pyridine derivatives with ZnPc and its analogues is known [92, 404]. After coordination to AgNPs, the complexes alone and in the presence of the NPs, were mixed with polystyrene and allowed to dissolve under stirring for 24 h. After this time, a homogenous mixture was obtained and electrospun into fibers as described in the experimental section.

Table 3.7: Spectral data and fiber diameters of the low symmetry MPc complexes in solution (DMF) and in the fiber matrix

Sample	λ_Q/nm (solution)	λ_Q/nm (fiber)	Average diameter (nm) ($\pm$30)
ZnMCsPc (**49**)	678	676	260
+ AgNPs	681	677	180
ZnMPCPc (**53**)	695	691	380
+ AgNPs	692	691	265
ZnMCPc (**57**)	688	685	200
+AgNPs	686	684	120
ZnTPPc (**70**)	673	670	350
+AgNPs	675	672	160
ZnODEPc (**69**)	704	699	360
AgNPs	701	698	150
ZnTDEPc (**68**)	695	693	310
+AgNPs	691	690	175
Polystyrene	-	-	242
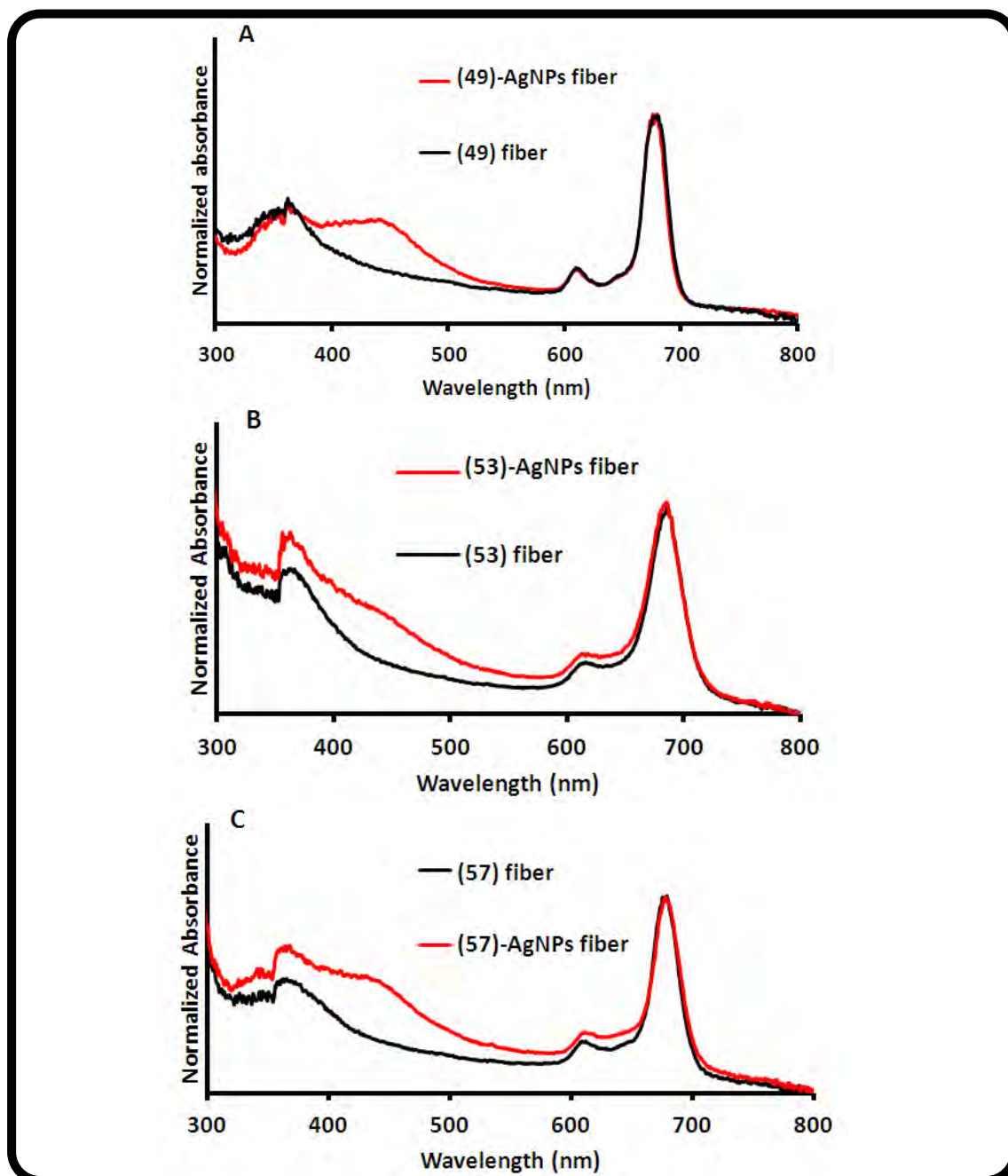
Figure 3.37: Ground state electronic absorption spectra of the low symmetry ZnPc derivatives alone (black line) and in the presence of AgNPs (red line), in fiber matrix

The Q band absorption of the complexes alone and in the presence of AgNPs were observed at about the same wavelengths when electrospun into fiber, Fig. 3.37, and are listed in Table 3.7, though the Q band absorption maxima of the complexes were broad in the fiber compared to that when the Pc is in solution.

The complexes and their conjugates in the fiber were also characterised by transmission electron microscopy (TEM), with which two geometric properties of the fibers were assessed: the fiber diameter (Table 3.7) and fiber morphology (Fig. 3.38). The average diameters of the electrospun fibers of polymer alone and when functionalized with Pcs or Pcs-AgNPs were determined using Cell^D software from Olympus.
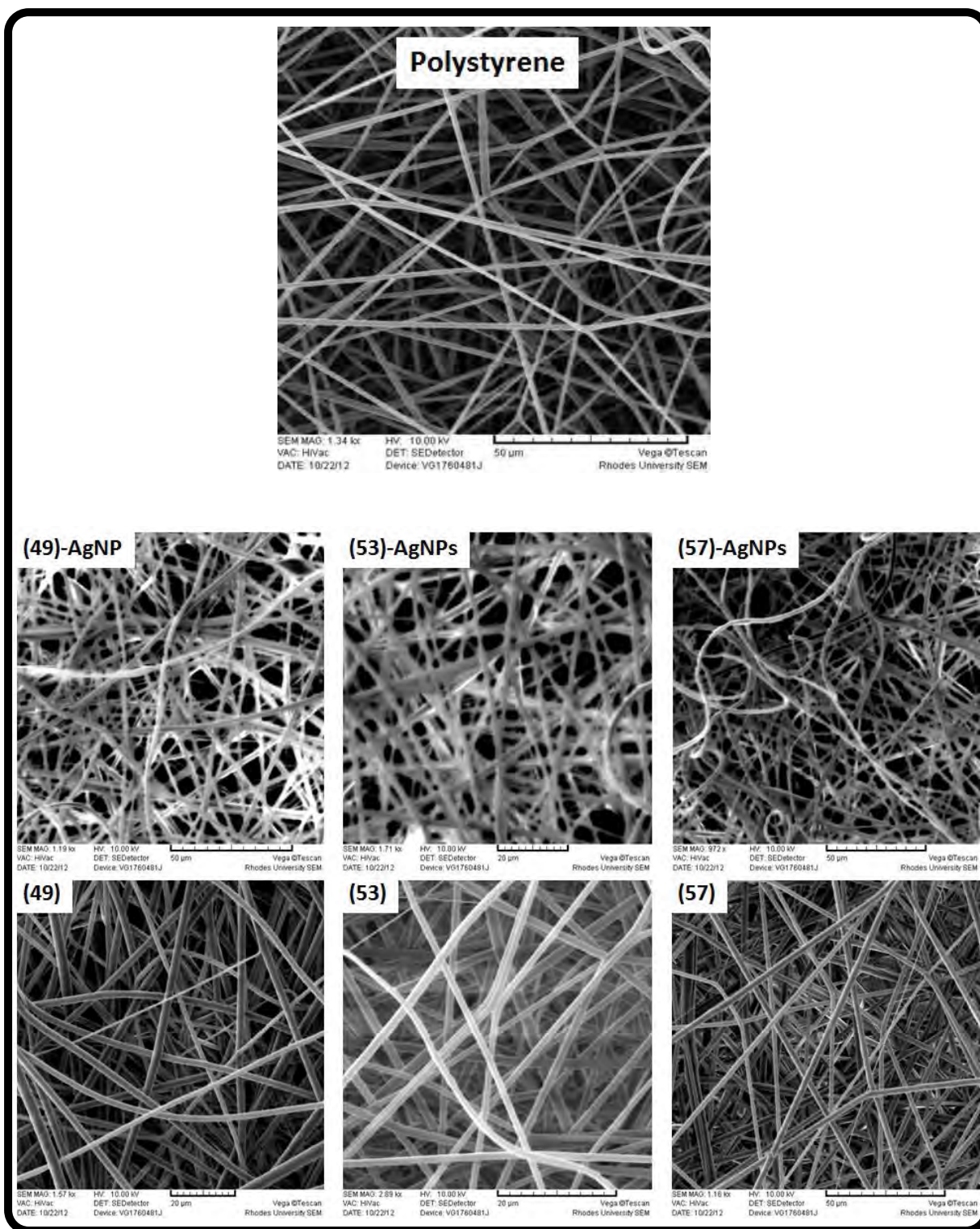
Figure 3.38: Scanning electron microscope images of polystyrene alone and in the presence of the low symmetry Pcs alone (49, 53 and 57) and Pcs-AgNPs conjugates

Fig. 3.38 shows the highly branched cylindrical network of nanofibers. Smaller average fiber diameters were obtained for these complexes in the presence of AgNPs

compared to the Pc alone Table 3.7, this may be due to an increase in conductivity of the solution during electrospinning in the presence of AgNPs, that resulted to smaller fiber diameters. The fiber diameters were in the range of 200 to 380 nm for the MPc/PS alone, and ranged between 120 to 260 nm when in the presence of AgNPs. The fiber surface was rough in the presence of AgNPs compared to when the fibers were electrospun with the Pcs alone.

The fiber diameter of the polystyrene alone was found to be 242 nm. This fiber diameter was thinner than that obtained (3.52-4.09 µm) by Pai C.-L. *et al*. [405], using DMF alone as an electrospinning solvent, instead of THF:DMF solvent mixture used in this work. This is expected because a higher concentration of polymer ~30%, was used in their case, while the polymer concentration of ~25% used in this work is slightly lower. This observation is consistent with the theory which predicts that the fiber diameter depends allometrically on solution viscosity [300-308].

3.4 Summary

Novel low symmetrically substituted phthalocyanine complexes of zinc, tin, germanium and titanium have been successfully synthesized. The complexes were successfully characterised with various techniques, confirming their relative purity.

The UV-vis spectroscopic (in DMF) characterization of novel low-symmetry complexes were discussed in detail and metal size dependant red shifting of the spectra were observed. The complexes were successfully conjugated to various nanoparticles (AuNPs, AgNPs and QDs), and their conjugates were successfully characterized.

Complexes showed blue shifts in the absorption spectra when conjugated to GSH-AuNPs compared to when studied alone. Aggregation was observed for some complexes in the presence of QDs.

All complexes and their MNP conjugates presented in this chapter gave spectroscopic data indicating high purity and behaved in accordance with the predicted structures.

The complexes were successfully electrospun into a PS fiber matrix to be used for the inhibition of bacterial growth

CHAPTER 4

Photophysical and photochemical

properties

4.1 Photophysical properties of the phthalocyanines

The photophysical and photochemical parameters of all the novel compounds synthesized in this thesis are presented in Table 4.1

Table 4.1: Photophysical and photochemical parameters of the various novel MPc complexes studied in this thesis in DMF.

Compound	Φ_F	Φ_T	τ_F(ns) (±0.05)	τ_T (µs)	Φ_Δ
ZnMCsPc (49)	0.16	0.61	2.55	135	0.57
(OH)₂SnMCsPc (50)	0.20	0.66	3.10	174	0.58
(OH)₂GeMCsPc (51)	0.23	0.70	3.90	268	0.67
OTiMCsPc (52)	0.25	0.68	3.50	285	0.63
ZnMPCPc (53)	0.07	0.68	2.18	160	0.64
(OH)₂SnMPCPc (54)	0.15	0.68	2.88	180	0.61
(OH)₂GeMPCPc (55)	0.10	0.74	1.84	250	0.69
OTiMPCPc (56)	0.13	0.65	2.81	110	0.54
ZnMCPc (57)	0.19	0.64	2.60	122	0.55
(ac)₂SnMCPc (58)	0.14	0.65	2.35	64	0.52
(OH)₂GeMCPc (59)	0.09	0.70	1.61	70	0.66
OTiMCPc (60)	0.11	0.63	1.84	57	0.54
SiHDTPc(61)	0.34	0.48	6.12	136	0.44

183

4.1.1 Fluorescence quantum yields (Φ_F) and lifetimes (τ_F)

Fluorescence lifetimes were obtained from the photoluminescence decay curves as shown in Fig. 4.1 ((OH)$_2$GeMCsPc(**51**) as an example).
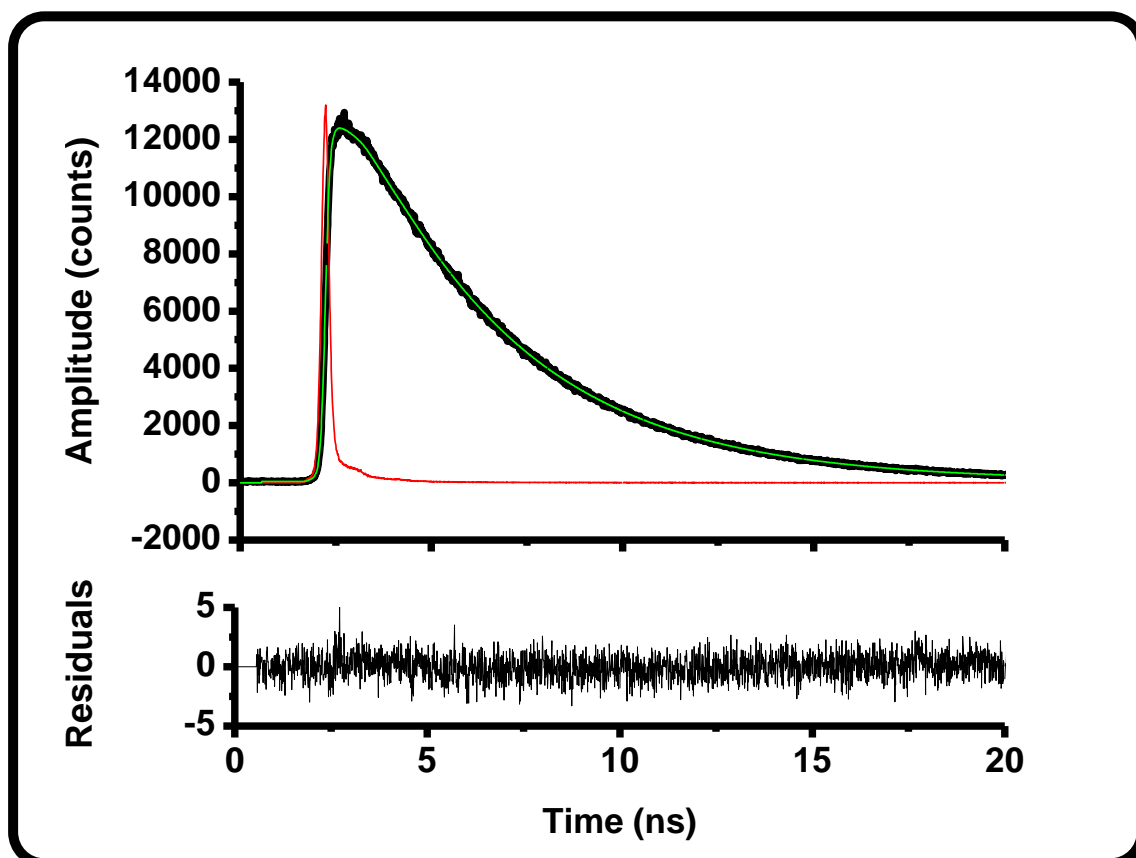
Figure 4.1: Photoluminescence decay curve of complex (51) in DMF.

All the complexes showed mono-exponential luminescence decays, Table 4.1, suggesting that only one fluorescing species was present in solution, thus confirming the relative purity of these complexes.

With exception of **49**, the fluorescence lifetimes (Table 4.1) were higher for the complexes substituted with three phenoxy groups (**50-52**) compared to their

corresponding counterparts substituted with six (**53-56**) and three (**57-60**) 2-diethylaminoethylthiol groups.

The fluorescence quantum yields (Φ_F) were determined by comparative methods [146, 147] using the Φ_F of a known Pc as a standard. In this work ZnPc in DMSO has been used (Φ_F) = 0.20 [148]. The Φ_F was calculated according to Equation 4.1 (same as equation 1.2)

$$\Phi_F = \Phi_F^{std} \frac{F.A_{std}.n^2}{F_{std}.A.n_{std}^2}$$

4.1

where F and F_{Std} are the areas under the fluorescence curves of the MPc derivatives and the used standard used. A and A_{Std} are the absorbances of the sample and reference at the excitation wavelength, and n and n_{Std} are the refractive indices of solvents used for the sample and standard, respectively.

High fluorescence quantum yields were obtained for complexes **50-52,** with complex **52** giving the highest yield at 0.25. In terms of the heavy atom effect, it would be expected that the Sn complexes would give the lower values of Φ_F and τ_F for every set of complexes. This is observed for complexes **50-52,** but not with **53-56** or **57-60**, suggesting that the effect of the substitution is more important than the central metal.

The fluorescence quantum yields and lifetimes were within the range reported for MPcs in general [99-117].

4.1.2 Triplet quantum yields (Φ_T) and lifetimes (τ_T)

The triplet state properties can be explained by the ability of a photosensitizer to be efficiently excited, and undergo a spin forbidden transition (intersystem crossing) from its excited singlet state to the triplet state.

The triplet quantum yields (Φ_T), Table 4.1, were determined using laser flash photolysis (set up shown on the experimental section (Chapter 2)). A typical triplet decay curve is shown in Fig. 4.2.

The triplet quantum yields (Φ_T) were determined using comparative method [162], using unsubstituted ZnPc in DMF Φ_T^{std} = 0.68 [360] and DMSO Φ_T^{std}= 0.65 [361] as a standard, DMSO was used as standard for Pc-QD experiments even though a DMSO:water (8:2) ratio was employed for the experiments and the amount of water was trivially small compared to the DMSO. Triplet quantum yields were calculated using Equation 4.2 (same as Equation 1.3)

$$\Phi_T = \Phi_T^{std} \frac{\Delta A_T . \varepsilon_T^{std}}{\Delta A_T^{std} . \varepsilon_T}$$
                                                                                                4.2

where ΔA_T and ΔA_T^{std} are the changes in triplet state absorbance of a Pc molecule and the standard respectively. ε_T and ε_T^{std} are the triplet state molar extinction coefficients for the Pc molecule and the standard, respectively. Φ_T^{std} is the triplet quantum yield of the standard.

Deoxygenation is important in carrying out accurate determination of the triplet state parameters, since the triplet states of MPcs is known to be quenched by oxygen [406]. In the presence of oxygen, a drastic decrease of the triplet state lifetimes was

observed (data not shown), such behaviour is well known [406]. High triplet

quantum yields ranging from 0.48 to 0.74 (Table 4.1) were obtained for the

complexes in DMF. The germanium Pc complexes (**51, 55** and **59**) gave the highest

triplet state quantum yields of 0.70, 0.74 and 0.70 compared to all the other

complexes. High triplet quantum yields have been reported for germanium

complexes [407, 408]. Based on heavy atom effect, the largest central metals would be

expected to give the highest Φ_T in all sets, but this is not the case as shown in Table

4.1.
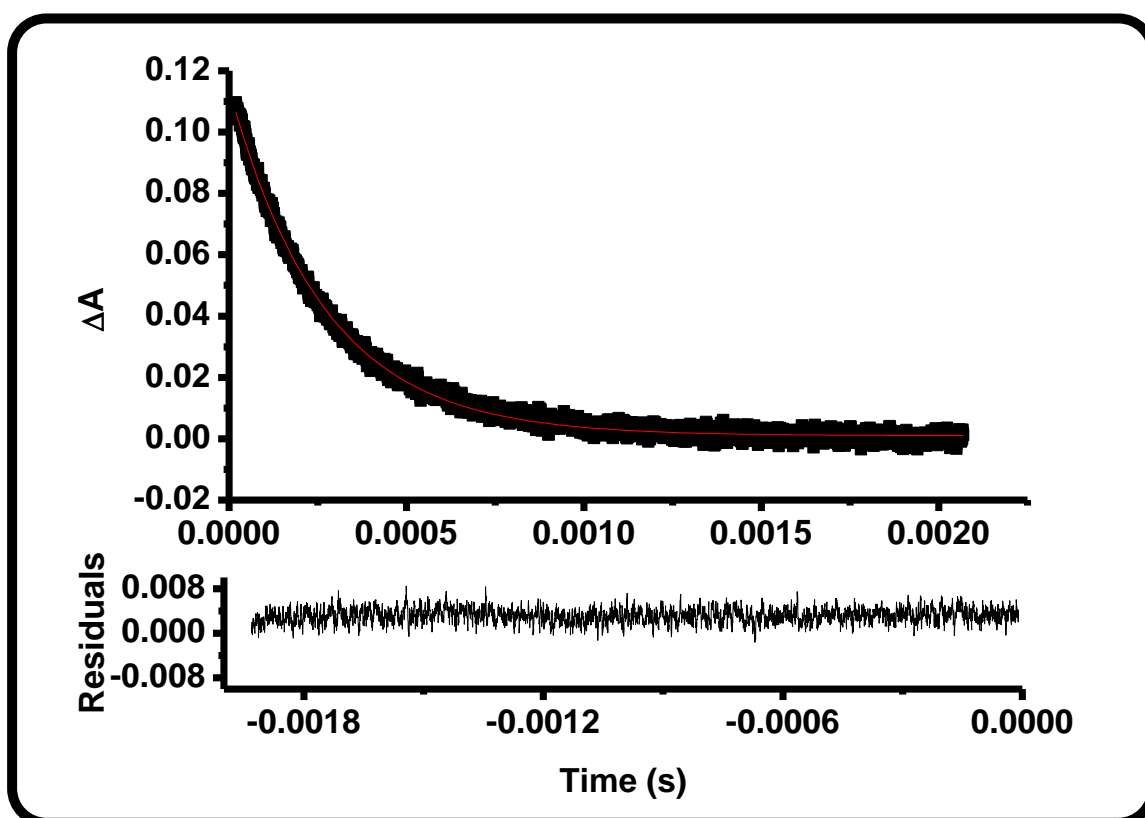
Figure 4.2: Triplet state decay curve of complex 51 in DMF

The triplet lifetimes were determined from the triplet decay curves (Fig. 4.2). The

triplet decay curve of complex (**51**) obeyed the first order kinetics, which is typical of

MPc complexes. This was the case for all complexes except when the Pcs were conjugated to the NPs. The monocysteinyl titanium complex **52** gave the highest triplet lifetime of 285 μs followed by the germanium Pc complex **51,** with a lifetime value of 268 μs. Complex **60** gave the lowest lifetime at 57 μs among all the complexes studied. All the (MCPc) complexes gave low triplet lifetime values, though their triplet quantum yields were comparable to the rest of the complexes.
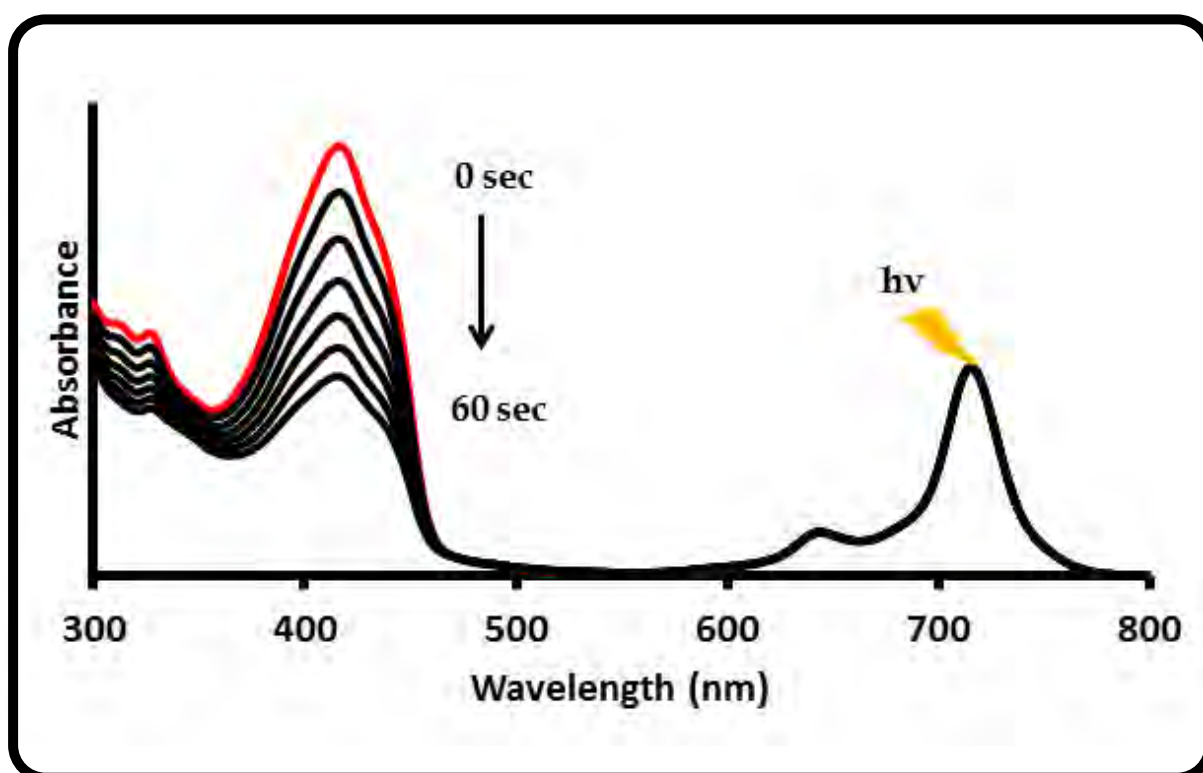
Figure 4.3: Typical spectra observed during the generation of DPBF as a singlet oxygen scavenger for complex 55 in DMF.

Fig. 4.3 shows the photodegradation of the DPBF (from 0 to 60 sec) used as a quencher during the singlet oxygen determination for complex **55** (as an example). The stability of the photosensitizer in the presence of a quencher is of great importance during the singlet oxygen determination as observed for complex **55**, which showed no changes in the Q-band absorption during irradiation with visible

light. The singlet oxygen quantum yields strongly depend on the triplet quantum yields and lifetimes. The singlet oxygen quantum yields (Φ_Δ) of the phthalocyanines were calculated using a comparative method based on Equation 4.3 (same as Equation 1.6), using ZnPc in DMF, $\Phi_\Delta^{std} = 0.56$ [362] as a standard.

$$\Phi_\Delta = \Phi_\Delta^{Std} \cdot \frac{R I_{abs}^{Std}}{R^{Std} I_{abs}} \qquad \qquad 4.3$$

where Φ_Δ^{Std} is the singlet oxygen quantum yield the standard, R and R^{Std} are the singlet oxygen quencher photobleaching rates in the presence of the respective MPcs under investigation and of the standard respectively. I_{abs} and I_{abs}^{Std} are the rates of light absorption by the MPcs and the standard, respectively. Relatively high singlet oxygen generation was observed for the long lived complexes (**51** and **55**) in DMF corresponding to high triplet quantum yield obtained for the GePc derivatives. The lower singlet oxygen production taking place with complex **58** and **60** may be associated to its short lived triplet state lifetime behaviour. All the germanium complexes (**51**, **55** and **59**) gave the best triplet and singlet oxygen quantum yields compared to their counterparts. The SiHDTPc (**61**) complex gave the lowest singlet oxygen quantum yield compared to the low symmetry complexes. The high singlet oxygen generation obtained for the complexes serves as a selective tool in photodynamic therapy applications.

4.2 Photophysicochemical properties of MPcs in the presence of nanoparticles

4.2.1 Photophysicochemical properties of MCPc-GSH-AuNPs conjugates, complexes 58-60 used as examples for peripherally linked GSH-AuNPs

The Φ_T, Φ_Δ, Φ_F, τ_T, and τ_F were studied for all these complexes in order to understand the effect of AuNPs on the photophysicochemical behaviour.

The photophysicochemical properties of complex **58-60** in the presence of GSH-AuNPs are presented in Table 4.2.

Table 4.2: Fluorescence and photophysical parameters of (59), (60) and (58) mixed and linked to GSH capped AuNPs in DMF

Complex	Φ_T	Φ_Δ	Φ_F	τ_T (µs)	Fluorescence lifetimes τ_F (ns)				τ_0 (ns)
					τ_{F1}	amplitude	τ_{F2}	amplitude	
(58)	0.65	0.52	0.14	64	2.35	1			12.88
(58) mixed	0.66	0.60	0.02	61	1.50	0.79	0.84	0.31	87.00[a]
(58) linked	0.67	0.64	>0.01	80	1.70	0.96	0.74	0.04	153.0[a]
(59)	0.70	0.66	0.09	70	1.61	1			16.72
(59) mixed	0.72	0.68	>0.01	110	1.10	0.85	0.64	0.15	35.50[a]
(59) linked	0.75	0.70	>0.01	130	1.0	0.90	0.53	0.10	220.0[a]
(60)	0.63	0.54	0.11	57	1.84	1			16.79
(60) mixed	0.64	0.57	0.03	62	1.20	0.80	0.93	0.20	58.50[a]
(60) linked	0.65	0.61	>0.01	95	1.40	0.95	0.80	0.05	174.0[a]

[a]Average lifetime used

Fig. 4.4 shows the time-resolved fluorescence decay curve of $(ac)_2SnMCPc$ (**58**) and $(ac)_2SnMCPc$-GSH-AuNPs in DMF, indicating a bi-exponential decay. All the Pcs shows only one lifetime Tables 4.1 and 4.2; however the conjugates show two lifetimes, Table 4.2. The existence of two components in the fluorescence decay curves obtained for the Pcs in the presence AuNPs with GSH as capping agent or other capping agents has been reported [230].
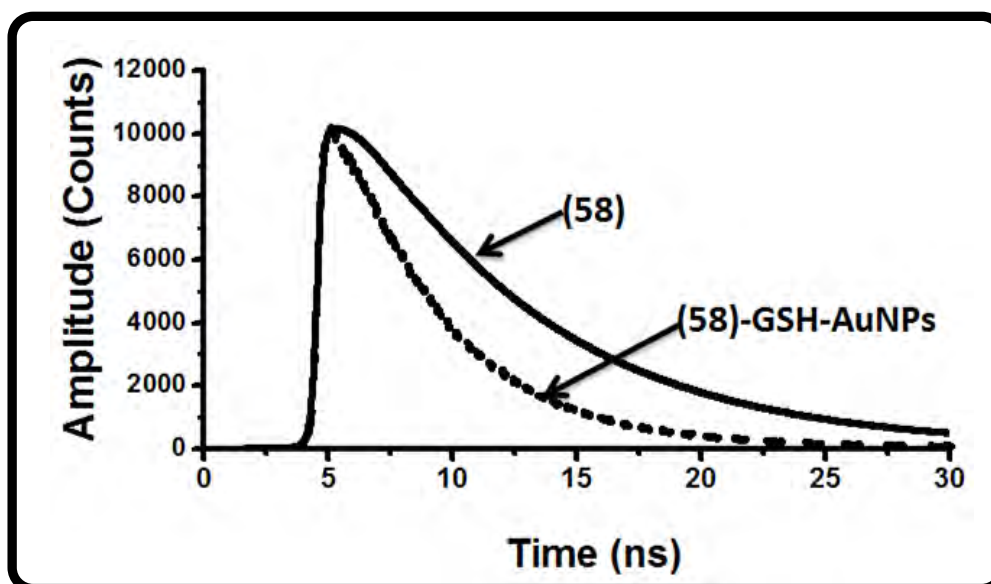
Figure 4.4: Photoluminescence decay curve of complex 58 alone (solid line) and linked to GSH-AuNPs (dotted line).

The fluorescence lifetimes of the free Pc is decreased for both the conjugates and the mixed GSH-AuNPs/MPc (without a chemical bond). The decrease in lifetime suggests energy transfer takes place from the excited singlet state of the Pc macrocycle to the GSH-AuNPs, as reported before [176, 230].

Two lifetimes may be due to different orientation and packing of Pc molecules on the AuNPs surfaces. The quenching of lifetimes may be explained using fluorescence radiative lifetimes (τ_0), which measure the lifetime of the molecule in the absence of the non-radiative processes. This lifetime is directly connected to absorption coefficients and excited state lifetimes, and can be calculated from the measurement of fluorescence quantum yields and lifetimes using Equation 4.4 [409].

$$\tau_0 = \frac{\tau_F}{\phi_F}$$ 4.4

The τ_0 values were found to be higher than that for the measured fluorescence lifetimes (Table 4.2). The large τ_0 values compared to τ_F are not surprising because non-radiative processes cause faster fluorescence decay. The larger τ_0 values have been reported before for similar studies [234, 410], where MPc-AuNPs conjugates were found to have a higher τ_0 as compared to MPc alone. The radiative lifetime in the presence of AuNPs can either increase or decrease depending on the molecular dipole and the distance between the fluorophore and the metal. According to the studies done previously by Lakowicz [411, 412], the radiative rate will increase when the oscillating dipole is not in line with the reflected field [411, 412]. Therefore the observed increase in τ_0 when the MPcs were attached to the gold surface could suggest an uncorrelated field.

The fluorescence quantum yields of the conjugates (MPcs-GSH-AuNPs linked) are compared to the MPcs alone, and to those of the MPcs mixed with GSH-AuNPs (with no linking agent). Lower fluorescence quantum yields (<0.01) and lifetimes were observed for all the linked complexes. The drastic decrease of the fluorescence quantum yields after conjugation is caused by the fluorescence quenching ability of the gold nanoparticles. Intersystem crossing due to heavy atom effect of Au will also result in decrease of fluorescence quantum yields. It has been documented that gold nanoparticles quench fluorescence [176]. The fluorescence quantum yields decreased for the mixed compared to the MPcs alone due to the reasons given above for the linked.

There was an insignificant increase in Φ_T for all the mixed GSH-AuNPs/MPc complexes (without a chemical bond), Table 4.2. A slight improvement in triplet

192

yields was observed for the chemically linked MPc-GSH-AuNPs compared to the MPc alone, suggesting that the GSH-AuNPs encourages intersystem crossing to the triplet state. The triplet state lifetimes (τ_T) of the free MPc complexes are low, ranging from 57 to 70 μs and all show increase in the presence of GSH-AuNPs (mixed or linked), with the largest increase observed with the (OH)$_2$GeMCPc(**59**). The increase of the τ_T with increase in Φ_T is not expected but could reflect the protection of Pc by AuNPs. The (OH)$_2$GeMCPc-GSH-AuNP conjugate gave the highest singlet oxygen quantum yield (0.70) triplet quantum yield (0.75) and lifetime (130 μs). As stated above, the high singlet and triplet quantum yields are typical for most germanium phthalocyanine complexes.

4.2.2 SiHDTPc (61) and unsubstituted ZnPc axially linked to AgNPs (spherical) and AuNPs
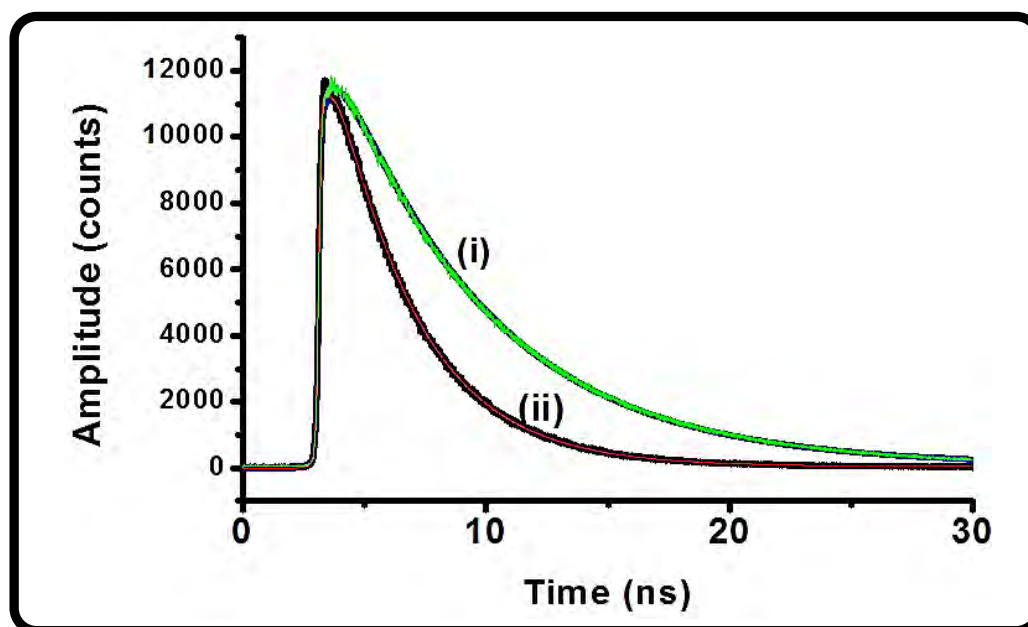
Figure 4.5: Photoluminescence decay curves of SiHDTPc (61) (i) and SiHDTPc-AuNPs (ii) in DMF.

The summary of the photophysical and photochemical parameters of **61** and ZnPc and their MNP conjugates are presented in Table 4.3. The fluorescence lifetimes were determined from the exponential fitting of the fluorescence decay curves (Fig. 4.5). The SiHDTPc alone gave high fluorescence quantum yield and lifetime, 0.34 and 6.12 ns, respectively, compared to the ZnPc alone, Table 4.3.

Table 4.3: Photophysicochemical properties of the ZnPc and 61 complex and their conjugates in DMF

Complex	Φ_T	$\tau_{T\ (\mu s)}$	Φ_Δ	Φ_F	$\tau_{F\ (ns)}$ (±0.02)
ZnPc	0.58 0.58 [413]	330 330 [413]	0.56 0.58 [413]	0.17 0.17 [413]	3.14 -
ZnPc-4MPy-AgNPs	0.64	250	0.63	0.08	2.74
ZnPc-4MPy-AuNPs	0.61	198	0.58	0.03	2.51
SiHDTPc (61)	0.48	136	0.44	0.34	6.12
[a]SiHDTPc-AgNps	0.51	110	0.50	0.21	4.41
[a]SiHDTPc-AuNps	0.55	90	0.53	0.19	3.37

[a] TOABr replaced by SiHDTPc during ligand exchange

The determination of the ZnPc photophysical parameters is repeated here, but the values were found to be similar to those reported in literature [145, 413]. A decrease in fluorescence quantum yield and lifetime values was observed in the presence of AuNPs and AgNPs for all conjugates. As stated above, AuNPs quench fluorescence [176]. The ZnPc-MNP conjugate showed poor fluorescence behaviour in general,

when compared to the corresponding SiHDTPc-MNP conjugates (Table 4.3). This is due to the heavy atom effect of the Zn central metal in the ZnPc-MNP system.

The ZnPc complex gave higher triplet quantum yields and lifetime values compared to the SiHDTPc alone. The high triplet quantum yields are expected for the former due to the heavy atom effect. A decrease in the triplet lifetimes was observed with a concomitant improvement in the triplet state quantum yields for both complexes in the presence of the MNPs. The ZnPc-AuNPs conjugate gave the highest triplet quantum yield of 0.64 when compared to ZnPc and complex **61**.

The SiHDTPc (**61**) complex gave the lowest singlet oxygen quantum yield of 0.44. However, a significant improvement in the singlet oxygen quantum yield was observed for this complex in the presence of MNPs, with the ZnPc-AuNPs conjugate giving the highest singlet oxygen quantum yield (0.63). The improvement in the triplet and singlet oxygen quantum yield of the complexes might be due to the heavy metal effect afforded by the silver and gold nanoparticles, which enhances intersystem crossing to triplet state, thus resulting in increase in triplet and singlet oxygen quantum yield.

4.2.3 Singlet oxygen generation of Pcs in the presence of differently shaped AgNPs in solution.

These complexes (**49-52**) contain a cysteinyl group for attachment to AgNPs through both the amino and the carboxylate groups. The aim was to use the conjugates for PACT hence only singlet oxygen quantum yields were determined.
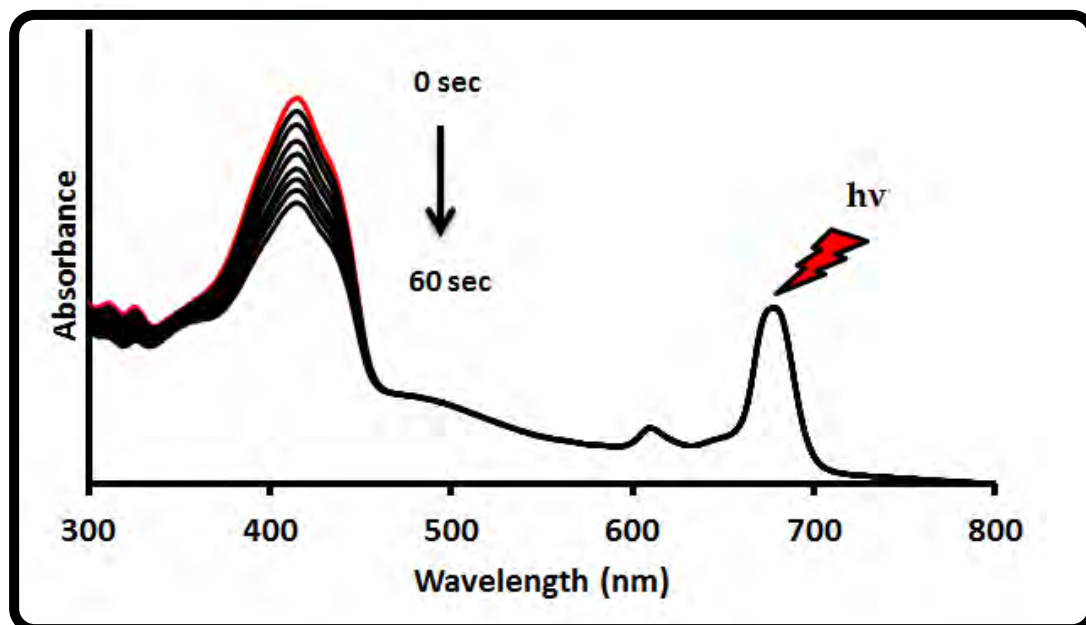
Figure 4.6: Photodegradation of DPBF, following illumination of ZnMCsPc (49) in the presence of triangular shaped AgNPs

The photochemical behaviour of the various MPc complexes alone and in the presence of AgNPs was investigated in DMF. The ability of a photosensitizer to be excited and be able to undergo intersystem crossing to the triplet state and generate singlet oxygen is a requisite for its application in photodynamic related experiments. All Pcs were evaluated for singlet oxygen production when alone, and in the presence of each AgNPs. The singlet oxygen quantum yields are presented in Table 4.4. The spectra show the photodegradation of DPBF in the presence of ZnMCsPc(**49**) and triangular AgNPs as an example, are presented in Fig. 4.6.

Table 4.4: Spectral and photochemical properties of various MPcs in DMF

Complex	Φ_Δ (MPcs)	Φ_Δ Pcs+Sphere	Φ_Δ Pcs+Triangle	Φ_Δ Pcs+Cubic
ZnMCsPc (49)	0.57	0.58	0.61	0.60
SnMCsPc (50)	0.58	0.60	0.59	0.62
(OH)₂GeMCsPc (51)	0.67	0.69	0.70	0.70
OTiMCsPc (52)	0.63	0.65	0.68	0.66

All the complexes gave reasonable singlet oxygen quantum yields in DMF before their interaction with various AgNPs, Table 4.4. The $(OH)_2$GeMCsPc shows the highest singlet oxygen quantum yield of 0.67 which is typical of germanium complexes in solution, followed by the OTiMCsPc with quantum yield of 0.63. The ZnMCsPc and SnMCsPc have similar singlet oxygen quantum yields (0.57 and 0.58 respectively). An improvement in singlet oxygen quantum yields was observed in the presence of all the AgNPs, suggesting an enhanced intersystem crossing to the triplet state as was observed for the AuNPs conjugates studied above. Heavy metals encourages intersystem crossing to the triplet state which enhances singlet oxygen production. The larger size NPs (square and triangles) showed the best improvement in singlet oxygen production compared to the spherically shaped AgNPs, with OTiMCsPc showing the best improvement from 0.63 to 0.68 in the presence of triangular shaped AgNPs.

4.2.4 Singlet oxygen of MPcs alone and in the presence of spherical AgNPs in the fiber matrix

Fig. 4.7 shows the degradation of ADMA following irradiation with light for singlet oxygen quantification.
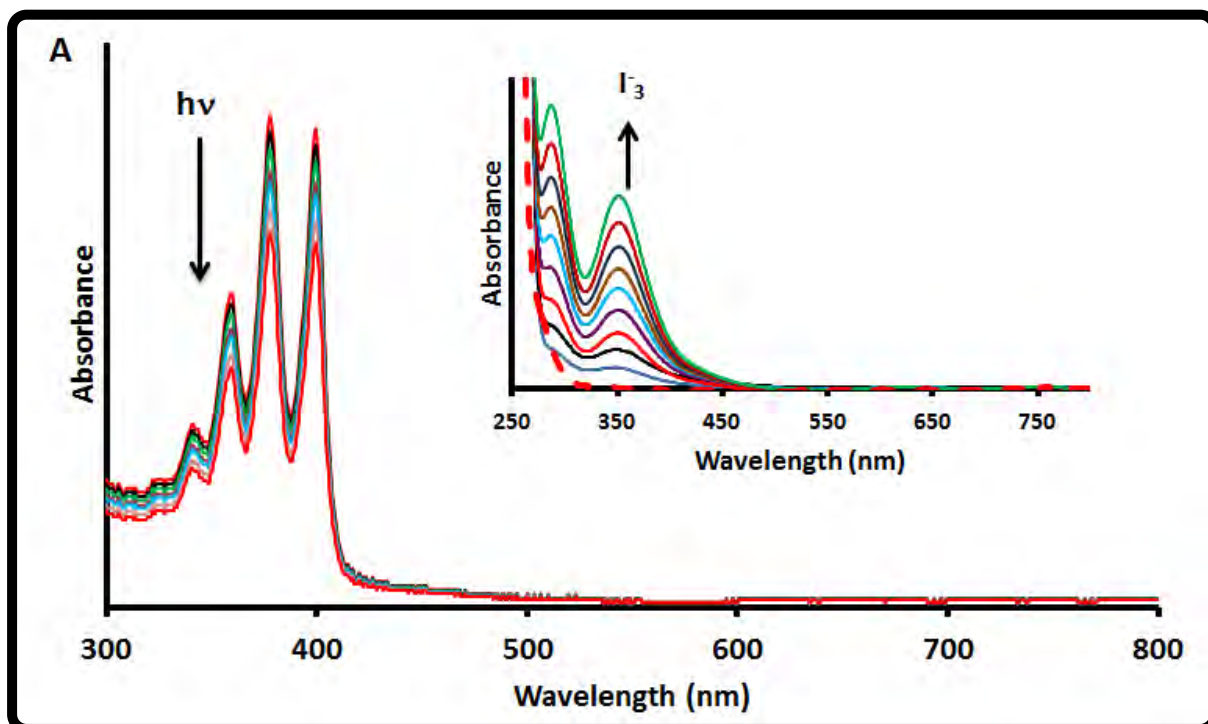
Figure 4.7: Photodegradation of ADMA in the presence of ZnMCsPc (49):PS fiber. Insert: Photo-oxidative generation of triiodide in the presence ZnMCsPc (49):PS in aqueous media.

The singlet oxygen quantum yields (Φ_Δ) were determined by monitoring the photo-degradation of ADMA (in aqueous solution for the fiber matrix (Fig. 4.7)) using ZnMCsPc (**49**) complex as an example. Complimentary to the degradation of ADMA, the polymer composite consisting of the MPcs alone or in the presence of AgNPs was used for the generation of triiodide (I_3^-) (from iodide (I^-)) in the presence

of light as observed in Fig. 4.7 (insert), serving as a clear proof that singlet oxygen is produced by the fiber, as the I_3^- absorption band increases with time [414]. There was no absorption in the region between 600-800 nm (Fig. 4.7) where the main absorption band of the phthalocyanine is located, suggesting no leakage of phthalocyanines from the fiber to the solution in aqueous media. This is expected since the phthalocyanines reported in this work are not water soluble. The lack of leaching in water is important for real life biological applications of the fibers in aqueous media. This is also true for this work, where these systems are to be used for photodynamic antimicrobial chemotherapy. Higher singlet oxygen quantum yields were obtained for the complexes and their AgNPs conjugates in solution compared to fiber matrix (Table 4.5). The decrease in the values of singlet oxygen (Φ_Δ) in the solid state might due to aggregation in some cases. Aggregation in the solid state has been shown not to favour singlet oxygen generation [300-307]. The Φ_Δ values for the fibers are estimates due to the errors introduced by light scattering (discussed in Chapter 2). The $(OH)_2GeMCPc$ (**59**) complex gave the highest Φ_Δ value of 0.66 and 0.46, both in solution and in the fiber matrix. In the fiber, ZnMCsPc (**49**) gave the second highest value of Φ_Δ = 0.42. Higher Φ_Δ values for the ZnMCsPc (**49**) and the $(OH)_2GeMCPc$ (**59**) complexes in fiber may have been a result of the marginal aggregation behaviour of these complexes in the solid state, as it was discussed in Chapter 3.

Table 4.5: Photochemical properties of various MPcs and MPcs-AgNPs (4-MPy) in solution and in the fiber matrix

Sample	Φ_Δ (DMF)	Φ_Δ (Fiber)
ZnMCsPc (**49**) + 4-MPy-AgNPs	0.57 0.59	0.42 0.43
ZnMPCPc (**53**) + 4-MPy-AgNPs	0.64 0.66	0.28 0.31
ZnMCPc (**57**) + 4-MPy-AgNPs	0.55 0.59	0.22 0.29
ZnTPPc (**70**) + 4-MPy-AgNPs	0.51 0.56	0.11 0.16
ZnODEPc (**69**) +4-MPy-AgNPs	0.60 0.62	0.15 0.18
ZnTDEPc (**68**) + 4-MPy-AgNPs	0.64 0.69	0.17 0.22
(ac)$_2$SnMCPc (**58**)	0.52	0.30
(OH)$_2$GeMCPc (**59**)	0.66	0.46
OTiMCPc (**60**)	0.54	0.31
ZnTPCPc (**71**)	0.45	0.12
ZnPc	0.56	0.14
Polystyrene	-	-

Of the unsymmetrical Pc complexes, ZnMCPc (**57**) gave the lowest singlet oxygen value (0.22) in the fiber matrix. An improvement in singlet oxygen generation was observed for all the ZnPc complexes studied in the presence of AgNPs. The higher singlet oxygen production in the presence of AgNPs is due to the heavy metal effect of silver that favours intersystem crossing to the triplet state. Singlet oxygen production in the fiber matrix was observed to be higher for the unsymmetrical ZnPcs (**57**, **53** and **49**) compared to their corresponding symmetrical (**68**, **69** and **70**) counterparts, Table 4.5. These observations confirm literature reports which state

that Φ_Δ values are lower for symmetrical derivatives compared to their unsymmetrical counterparts [178]. The singlet oxygen quantum yield production of low symmetry phthalocyanines and their AgNPs conjugates in the solid stage (fiber) are reported for the first time in this thesis. Symmetrically substituted ZnTPPc (**70**), ZnTPCPc (**71**) and unsubstituted ZnPc showed the lowest Φ_Δ values of all complexes, both in solution and when embedded in the fiber, Table 4.5.

4.2.5 Photophysical properties of low symmetry Pcs in the presence of QDs

This section presents the fluorescence and energy transfer behaviour taking place between various low symmetry phthalocyanines (**49**, **53**, **58**, **59** and **60,** as examples from each ring system) and quantum dot core shell (CdTe@ZnS-CALNN QDs1) NPs. The triplet state behaviour of these systems is also discussed.

4.2.5.1 Fluorescence quantum yields and lifetimes

Table 4.6 shows the fluorescence quantum yield and lifetime values for the quantum dot core-shell phthalocyanine conjugates.

Table4.6: Fluorescence parameters of the low symmetry phthalocyanines in the presence of CdTe@ZnS-CALNN QDs1 (represented as QDs1) and CdTe@ZnS-CALNN QDs2 (represented as QDs 2) in 8:2 DMSO: water.

Complex	QDs 1[a] (3.9 nm)				QDs2[a] (4.4 nm)			
	$\Phi_{F(QD)}$ λ_{exc} = 500 nm	$\tau_{1\,(ns)}$ ± 0.15	$\tau_{2(ns)}$ ± 0.17	$\tau_{3(ns)}$ ± 0.05	$\Phi_{F(QD)}$ λ_{exc} = 500 nm	$\tau_{1(ns)}$ ± 0.11	$\tau_{2(ns)}$ ± 0.10	$\tau_{3(ns)}$ ± 0.09
CdTe TGA QDs	0.48	43.24 (0.55)	13.45 (0.31)	0.34 (0.14	0.35	32.01 (0.47)	17.34 (0.28)	0.70 (0.15)
CdTe@ZnS-CALNN QDs	0.74	86.03 (0.62)	32.33 (0.24)	12.47 (0.16)	0.56	45.10 (0.51)	15.52 (0.33)	5.63 (0.16)
(49) QD-mixed	0.35	44.5 (0.50)	17.16 (0.32)	2.13 (0.18)	0.20	18.60 (0.42)	8.38 (0.32)	0.42 (0.26)
(49) QD-linked	0.22	23.80 (0.63)	9.22 (0.21)	0.34 (0.16)	0.15	13.72 (0.66)	3.46 (0.21)	0.65 (0.13)
(53) QD-mixed	0.36	46.42 (0.58)	21.11 (0.31)	3.76 (0.11)	0.27	26.33 (0.51)	10.23 (0.22)	0.32 (0.27)
(53) QD-linked	0.20	21.61 (0.48)	5.30 (0.39)	0.23 (0.13)	0.15	12.93 (0.47)	4.25 (0.31)	0.21 (0.22)
(58) QD-mixed	0.29	40.32 (0.55)	14.30 (0.34)	2.15 (0.11)	0.23	24.9 (0.71)	2.4 (0.12)	0.36 (0.17)
(58) QD-linked	0.28	32.65 (0.46)	8.22 (0.38)	1.20 (0.18)	0.18	15.24 (0.61)	3.16 (0.23)	0.80 (0.16)
(59) QD-mixed	0.38	35.11 (0.71)	4.28 (0.15)	0.90 (0.14)	0.22	23.82 (0.42)	2.56 (0.24)	0.70 (0.34)
(59) QD-linked	0.29	25.16 (0.63)	3.73 (0.31)	0.50 (0.06)	0.15	15.10 (0.50)	2.3 (0.26)	0.43 (0.24)
(60) QD-mixed	0.29	34.90 (0.61)	10.12 (0.32)	0.25 (0.07)	0.18	20.82 (0.60)	5.27 (0.26)	0.61 (0.14)
(60) QD-linked	0.24	28.0 (0.57)	1.30 (0.31)	0.26 (0.12)	0.17	16.6 (0.51)	1.0 (0.42)	0.11 (0.07)

[a]abundances for fluorescence lifetimes are shown in brackets.

Fluorescence quantum yields were determined using Equation 4.1. The fluorescence quantum yields (Φ_F) of the coreshell alone were found to be 0.74 for CdTe@ZnS-CALNN QDs1 and 0.56 for CdTe@ZnS-CALNN QDs2, Table 4.6. These values are relatively higher than their core counterparts which gave Φ_F = 0.48 for CdTe-TGA

QDs1 and 0.35 CdTe-TGA QDs2. Φ_F values have been found to increase with the size of the QDs, depending on the nature of the capping agent [264].

The fluorescence lifetimes for the coreshell were found to be τ_1 = 86.03 ns, τ_2= 32.33 ns and τ_3 = 12.47 ns for the CdTe@ZnS-CALNN QDs1 and 45.10 ns, 15.52 ns, 5.63 ns, respectively for CdTe@ZnS-CALNN QDs2, Table 4.6.

The fluorescence lifetimes decreased for linked and mixed QD-Pc conjugates for both CdTe@ZnS-CALNN QDs1 and CdTe@ZnS-CALNN QDs2 compared to the QD alone, perhaps due to energy transfer discussed below. The fluorescence quantum yields value also decreased for QDs (CdTe@ZnS-CALNN) mixed or linked to Pcs, compared to the quantum dots alone suggesting quenching of fluorescence by the MPc complexes (Table 4.6). The (OH)$_2$GeMCPc (**59**) CdTe@ZnS-CALNN QDs1-mixed gave the highest quantum yield value (0.38) followed by the ZnMPCPc (**53**) CdTe@ZnS-CALNN QDs1-mixed (Φ_F = 0.36, Table 4.6). Higher fluorescence quantum yields and lifetimes of QDs were observed for all the MPc QDs-mixed samples compared to when they were linked, though as stated in the experimental section in Chapter 2, comparison between the mixed and linked conjugates must be treated with caution since the amounts of QDs may be different.

4.2.5.2 Förster Resonance Energy Transfer between QDs and MPcs

Förster resonance energy transfer (FRET) is the non-radiative transfer of energy from a donor chromophore to an acceptor chromophore (or fluorophore if it is fluorescent in nature).

Quantum dot coreshells were designed such that an efficient overlap between the fluorescence emission spectra of the donor (QDs) and the absorption spectra of the acceptor (MPcs) was achieved (Fig. 4.8).
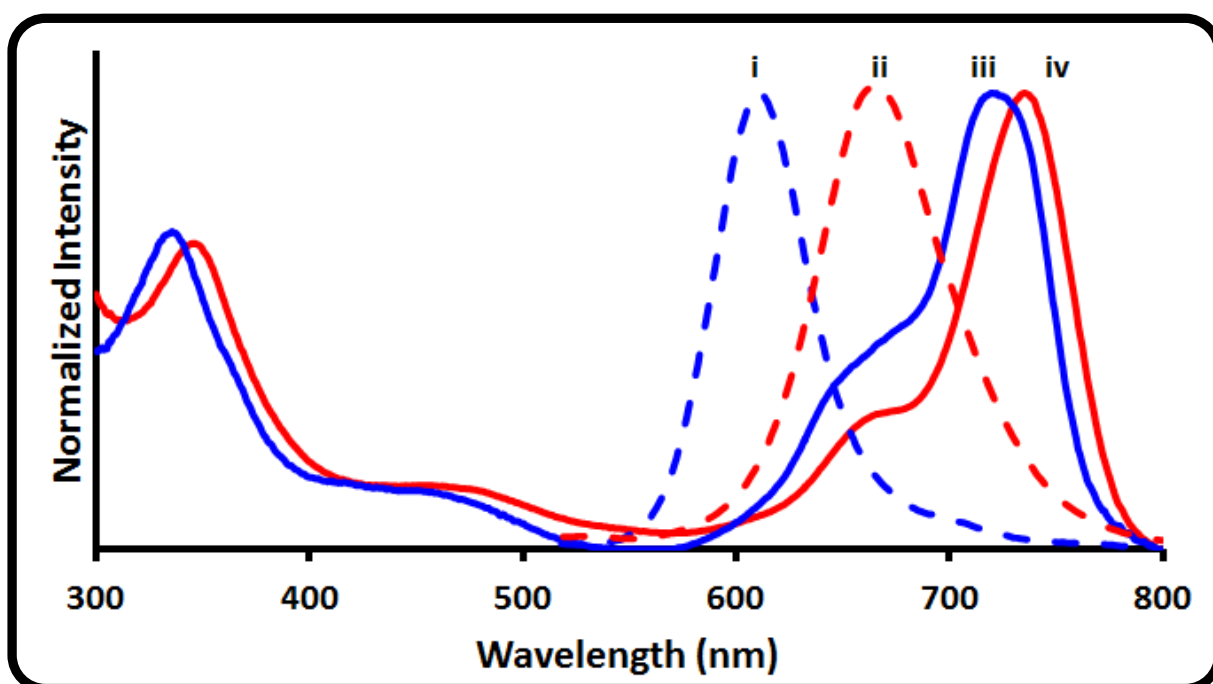
Figure 4.8: Emission spectra of CdTe@ZnS-CALNN QDs1 (i), CdTe@ZnS-CALNN QDs 2 (ii) overlapped with the ground state UV-Visible spectra of (ac)$_2$SnMCPc (iii), OTiMCPc (iv). Solvent = 8:2 DMSO: water.

Growing larger particle size quantum dots have some disadvantages such as low photoluminescence properties. These properties are, however, significantly improved on formation of coreshells. Due to the red shifted nature of the emission spectrum, there will be higher overlap between the CdTe@ZnS-CALNN QDs2 emission and the MPc absorption, Fig. 4.8.

Table 4.7: FRET parameters of the low symmetry phthalocyanines in the presence of the presence of CdTe@ZnS-CALNN QDs1 (represented as QDs1) and CdTe@ZnS-CALNN QDs2 (represented as QDs 2) in 8:2 DMSO:water

Complex	QD 1 (3.9 nm)				QD 2 (4.4 nm)			
	J $(\times 10^{-13})$ (cm^6)	R_0 (Å)	r (Å)	Eff	J $(\times 10^{-13})$ (cm^6)	R_0 (Å)	r (Å)	Eff
(49) QD-mixed	2.74	54.78	53.69	0.53	1.04	68.51	61.34	0.66
(49) QD-linked	2.21	56.90	49.40	0.70	0.77	61.20	51.41	0.74
(53) QD-mixed	3.49	30.69	30.49	0.51	1.61	59.21	57.65	0.54
(53) QD-linked	2.56	30.69	26.00	0.73	1.28	59.33	49.40	0.75
(58) QD-mixed	2.10	24.57	22.80	0.61	1.42	57.87	56.72	0.53
(58) QD-linked	2.46	28.84	21.67	0.85	1.74	55.76	48.79	0.69
(59) QD-mixed	3.11	32.41	32.63	0.49	0.95	62.10	62.10	0.50
(59) QD-linked	3.32	27.14	23.57	0.70	0.81	59.70	49.71	0.75
(60) QD-mixed	2.71	28.10	26.08	0.61	1.01	60.14	56.60	0.59
(60) QD-linked	2.18	27.3	22.53	0.76	0.92	59.21	51.00	0.71

The overlap integrals (J) were estimated by integration of the spectra in Fig. 4.8 from 400 to 800 nm and the J values are reported in Table 4.7. Relatively high J values of the order of 10^{-13} were obtained for all the complexes, compared to typical values of the order 10^{-14} cm^6 [279] for porphyrin-based structures.

A decrease in the fluorescence emission intensity of QDs was observed upon excitation of the CdTe@ZnS-CALNN QDs1 or CdTe@ZnS-CALNN QDs2 at 500 nm, where QDs absorb and the MPcs show negligible absorbance, Fig 4.9.
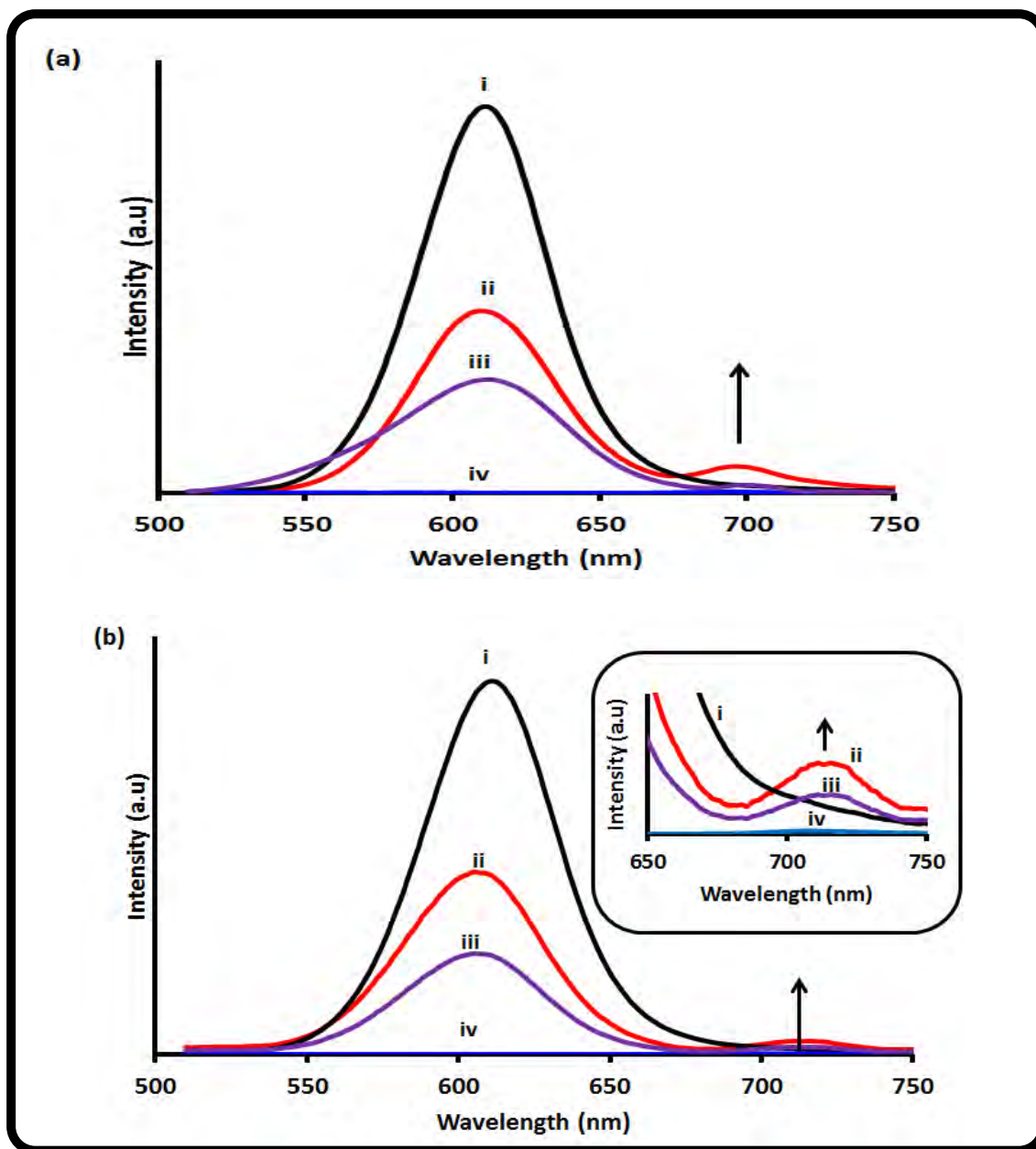
Figure 4.9: Fluorescence spectra of CdTe@ZnS-CALNN QDs1 in the presence of ZnMCsPc (49) (a) and ZnMPCPc (53) (b). QDs 1 alone (i), mixed with (ii), linked to QDs (iii) and MPc alone (iv) in 8:2 DMSO: water. Inset = expanded 700 nm area for b.

Upon excitation of the mixture containing the CdTe@ZnS-CALNN QDs1 and ZnMCsPc ((**49**), Fig. 4.9a) and ZnMPCPc ((**53**), Fig. 4.9b), an emergence of fluorescence peak at ~702 nm and ~710 respectively was observed. This suggests that energy transfer occurs from the QDs to the MPc complexes. A drastic decrease in fluorescence intensity of QDs was observed for the linked counterparts, compared to when they were mixed. There was no significant fluorescence observed for MPcs when excited at ~500 nm in the absence of QDs, which serves as a proof that the observed fluorescence of the MPcs that emerges in the presence of QDs is due to the fluorescence induced by QDs to the MPc complexes (Fig. 4.9). A small increase in fluorescence emission intensity of Pcs in the presence of QDs has also been observed before [415]. There is a clear stimulated emission of the phthalocyanine confirms energy transfer from the QDs to the Pc (Fig. 4.9).

The values of Förster distance, R_0 (Å) which is the critical distance between the donor (QDs) and the acceptor (MPc) molecules for which efficiency of energy transfer is 50% [282] as well as center-to-center separation distance between donor and acceptor (r, Å), values are shown in Table 4.7. With the exception of $(OH)_2GeMCPc$ (**59**) QDs1-mixed, all r values were below the critical distance (R_0) at which energy transfer is 50% which will allow good interaction of the donor and acceptor thereby allowing energy transfer to occur readily with a high efficiency.

The $(ac)_2SnMCPc$ (**58**) QDs1-linked and TiMCPc QDs1-linked exhibit the lowest r values of 21.67 and 22.53 Å, respectively, indicating a very close proximity of these MPc complexes to the donor (QDs) and thus resulting in high energy transfer (Eff) values, Table 4.7.

FRET efficiencies (Eff) were determined experimentally from the fluorescence quantum yields of the donor in the absence ($\Phi_{F(QD)}$)and presence ($\Phi_{F(QD)}^{Mix}$) of the acceptor using Equation 4.5 (same as Equation 1.10) [280, 281]:

$$\text{Eff} = 1 - \frac{(\Phi_{F(QD)}^{Mix})}{(\Phi_{F(QD)})} \qquad\qquad 4.5$$

There are many factors reported, and still under debate, that influence photoluminescence decrease other than FRET [415-417], thus the values presented here are estimates. The FRET efficiency values were relatively high for the linked complexes compared to their mixed counterparts, suggesting that linking of the MPc complexes is of great importance for energy transfer efficiencies due to the short distances compared to mixed conjugates. This also serves to confirm that the MPc complexes are indeed covalently linked to the quantum dots, thus they display improved energy transfer properties compared to their mixed counterparts.

4.2.5.3 Triplet state behaviour and parameters
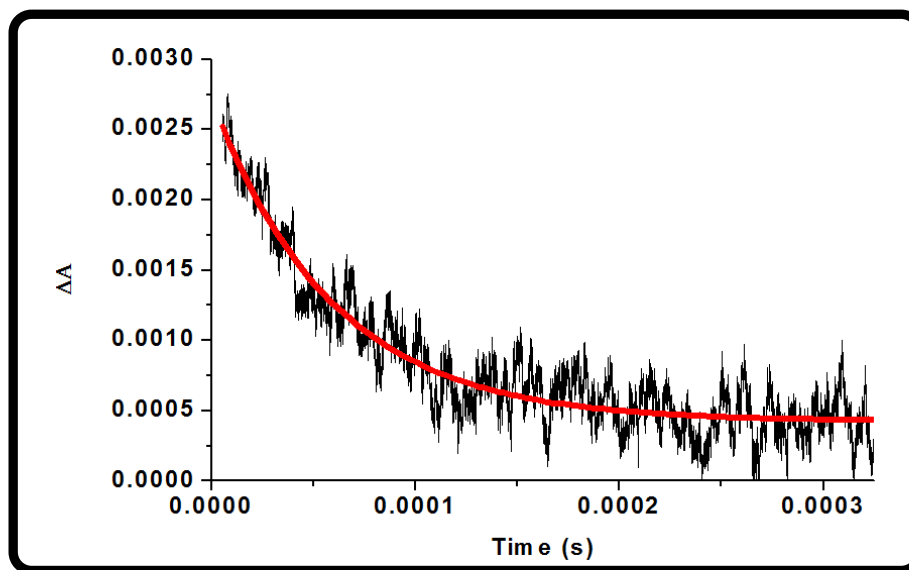
Figure 4.10: Triplet decay curve of (ac)$_2$SnMCPc linked to QDs in 8:2 DMSO:water

CdTe@ZnS-CALNN QDs1 was employed to study the triplet state behaviour for both covalently linked and mixed MPc complexes.

Fig. 4.10 shows the triplet decay curve of (ac)$_2$SnMCPc (**58**) QDs-linked in DMSO:water as an example. The triplet decay curves for all complexes in the presence of QDs obeyed the second order kinetics. This is typical for MPc complexes at high concentrations (>1×10^{-5} M) [418] due to the triplet–triplet recombination.

Table 4.8: Triplet state parameters of the low symmetry phthalocyanine complexes in the absence and in the presence of CdTe@ZnS-CALNN QDs1 in 8:2 DMSO: water.

Complex	Φ_T	τ (μs)
(49)	0.61	132
(49) QD-mixed	0.66	210
(49) QD-linked	0.71	240
(53)	0.67	140
(53) QD-mixed	0.70	217
(53) QD-linked	0.71	226
(58)	0.64	64
(58) QD-mixed	0.66	98
(58) QD-linked	0.68	117
(59)	0.69	75
(59) QD-mixed	0.71	111
(59) QD-linked	0.74	123
(60)	0.61	60
(60) QD-mixed	0.65	100
(60) QD-linked	0.67	115

An improvement in triplet quantum yields and lifetimes was observed for both the MPcs when mixed and linked to quantum dots, Table 4.8. High triplet quantum yields (ranging from 0.65 to 0.74) and long triplet lifetimes ranging from 100 to 240 μs (Table 4.8) were observed for the linked and mixed complexes, suggesting enhancement of intersystem crossing in the presence of QDs as compared to the MPcs alone. The $(OH)_2$GeMCPc (**59**) QDs-linked gave the highest triplet quantum yield value (0.74); however the complex that gave the highest triplet quantum yield did not show the shortest lifetime as expected. There is an increase in the triplet lifetimes for both the mixed and linked complexes in the presence of QDs as was the case with triplet quantum yields. This behaviour has been reported before [264]. The

longest lifetimes were obtained for the Zn complexes with the ZnMCsPc (**49**) QDs-linked with a lifetime of 240 μs. The long lifetimes are surprising, but could reflect the shielding (from environmental effects) of the phthalocyanines by QDs.

4.3 Summary

The photophysical and photochemical properties of the various low symmetry Pcs reported in this thesis were fully investigated. The studies show that various Pcs give different photophysicochemical behaviour as a function of the central metal ion and the nature of the peripheral substituents. All the germanium complexes showed best triplet and singlet oxygen quantum yield behaviour compared to all the complexes studied. A consistent improvement of the triplet and singlet oxygen quantum yields was generally observed when the complexes were conjugated to MNPs, which makes these molecules applicable in real life for PACT.

CHAPTER 5

Photodynamic antimicrobial chemotherapy (PACT) studies

5.1 Photo-inhibition of *Staphylococcus Aureus (S. Aureus)* using Pcs alone

In this section the unsymmetrical complexes ZnMCsPc (**49**), ZnMPCPc (**53**), (ac)$_2$SnMCPc (**58**), (OH)$_2$GeMCPc (**59**) and OTiMCPc (**60**), are studied and compared to the symmetrical ZnTPCPc (**71**), and unsubstituted ZnPc, as examples, in solution and when supported in a fiber matrix, for photo-inhibition of *S. Aureus.* Table 5.1 summarizes the singlet oxygen values obtained for the Pcs used in this chapter, in solution and in a fiber matrix.

As stated above, the mechanism and the science behind photodynamic antimicrobial chemotherapy (PACT) is in its infancy, but it seems to follow the same mechanistic principles as PDT, and therefore involves singlet oxygen. It is known that singlet oxygen reacts with intercellular molecules (peptides, DNA and proteins etc.) leading to oxidative damage of the cell wall and cell membrane which cause cell death [321, 322]. Literature reports show that gram-negative bacteria are drug resistant, compared to their gram positive counterparts [331-338]. The resistance of gram-negative bacteria to the photo-inhibition by sensitizers has been ascribed to the presence of a highly organized outer membrane on the bacteria, which hinders the interaction of the photosensitizer with the cytoplasmic membrane and intercepts the photogenerated reactive species [419, 420].

A series of low symmetry phthalocyanines presented in this study show photo-activity in the presence of light hence their PACT is investigated.

Table 5.1: Singlet oxygen behaviour of various Pcs in DMF and in fiber matrices

Sample	Φ_Δ (DMF)	Φ_Δ (Fiber)
ZnMCsPc (**49**)	0.57	0.42
+ AgNPs spheres	0.59	0.43
+ AgNPs triangles	0.61	a
+ AgNPs cubes	0.60	a
SnMCsPc(**50**)	0.58	a
+ AgNPs spheres	0.60	a
+ AgNPs triangles	0.59	a
+ AgNPs cubes	0.62	a
(OH)$_2$GeMCsPc (**51**)	0.67	a
+ AgNPs spheres	0.69	a
+ AgNPs triangles	0.70	a
+ AgNPs cubes	0.70	a
OTiMCsPc (**52**)	0.63	a
+ AgNPs spheres	0.65	a
+ AgNPs triangles	0.68	a
+ AgNPs cubes	0.66	a
ZnMPCPc (**53**)	0.64	0.28
+ AgNPs spherical	0.66	0.31
ZnMCPc (**57**)	0.55	0.22
+AgNPs spherical	0.59	0.29
(ac)$_2$SnMCPc (**58**)	0.52	0.30
(OH)$_2$GeMCPc (**59**)	0.66	0.46
OTiMCPc (**60**)	0.54	0.31
SiHDTPc (**61**)	0.44	a
+AgNPs spherical	0.50	a
+AuNPs	0.53	a
ZnTDEPc (**68**)	0.64	0.17
+AgNPs	0.69	0.22
ZnODEPc (**69**)	0.60	0.15
AgNPs spherical	0.62	0.18
ZnTPPc (**70**)	0.51	0.11
+AgNPs spherical	0.56	0.16
ZnTPCPc (**71**)	0.45	0.12
ZnPc	0.56	0.14
+AgNPs spherical	0.63	a
+AuNPs	0.58	a

[a]Not used in fiber, hence Φ_Δ values when in fiber were not determined
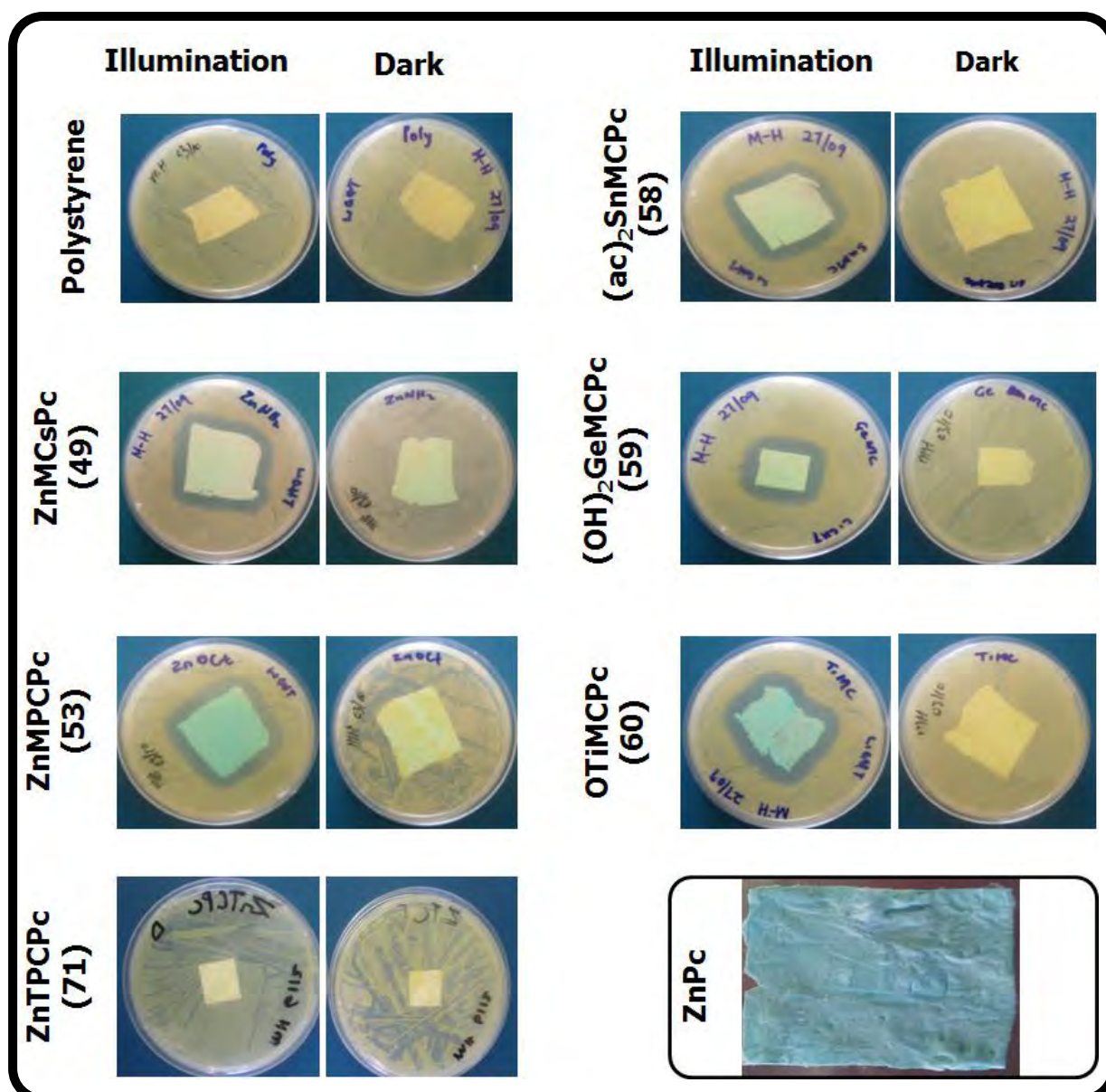
Figure 5.1: Digital images of the antimicrobial inhibition of *S. Aureus* using phthalocyanine modified fibers, studies in the dark and under illumination with visible light. Unmodified polystyrene alone employed as a control. The figure also shows PS/ZnPc fiber before use in agar plate for bacterial growth.

The photodynamic responses of the complexes were investigated in the fiber matrix. Fig. 5.1 shows digital images of the nutrient agar plates containing *S. aureus* in contact with the electrospun fibers. The Pcs embedded in the fiber are blue in colour in the absence of bacteria (in nutrient broth or as a separate fiber, Fig. 5.1, for ZnPc).

The bacteria were observed to grow on or around the fiber resulting in the blue colour of the Pcs on the fiber disappearing. The samples irradiated with light in the presence of bacteria showed growth inhibition as compared to those that were kept in the dark. This is judged by the clearing around the fiber and the restoration of the blue colour of the fiber.

A pair of plates containing a nutrient agar with polymer fiber in the absence of bacteria was used as a control both in the dark and under illumination with light. The colour of the Pc modified fiber remained blue both under illumination and in the dark. The nutrient agar was prepared in aqueous media and Pcs are insoluble in aqueous media, thus there was no possibility for leaching or migration of the phthalocyanine from the fiber matrix to the nutrient agar.

The polystyrene fiber alone did not show any bacterial inhibition, both in the dark and under illumination with light. This lack of growth of the bacteria around the polymer fiber modified with photosensitizers (Fig. 5.1) was obtained for all unsymmetrical MPc complexes as a result of bacterial growth inhibition. This serves as evidence that the monocarboxy phthalocyanine complexes generate reactive oxygen species that prevent bacterial growth.

The symmetrical ZnTPCPc (**71**) (Φ_Δ=0.12, Fig. 5.1) and ZnPc (Φ_Δ=0.14) complexes showed no activity towards bacterial inactivation, most likely due to the low singlet oxygen quantum yield values obtained for them alone, Table 5.1, compared to the values ranging from 0.22 to 0.46 for the other complexes in the absence of AgNPs. Thus, even though unsubstituted ZnPc embedded in electrospun fiber was reported

to show inactivation of *Escherichia coli* [307], its low singlet oxygen quantum yield resulted in zero activity for the more drug resistant *S. Aureus.* This confirms the importance of reasonably large values of singlet oxygen quantum yields for successful bacterial inactivation. The lack of activity of the symmetrical ZnTPCPc (**71**), shows the importance of unsymmetrical substitution, which results in increased singlet oxygen quantum yield values as reported before [178].

The photo-inhibition studies were also carried out for all the complexes in solution as described in Chapter 2, and the results are presented as graphs Fig. 5.2. The minimum inhibitory concentration (MIC) required to inhibit 50% bacterial growth was used as a reference to determine the effectiveness of these promising antimicrobial photosensitizers towards the inactivation of *S. aureus*.

In this thesis, control experiments were also undertaken to determine the effects of DMF on the various bacteria studied. It has been reported that DMF is not harmful to *S. aureus* but only when low amounts of the solvent are used [421]. At 50% DMF, without the AgNPs or Pcs, a minimal reduction in bacterial growth was observed showing that DMF also causes bacterial growth inhibition, thus effects of DMF were corrected for all the data sets shown.
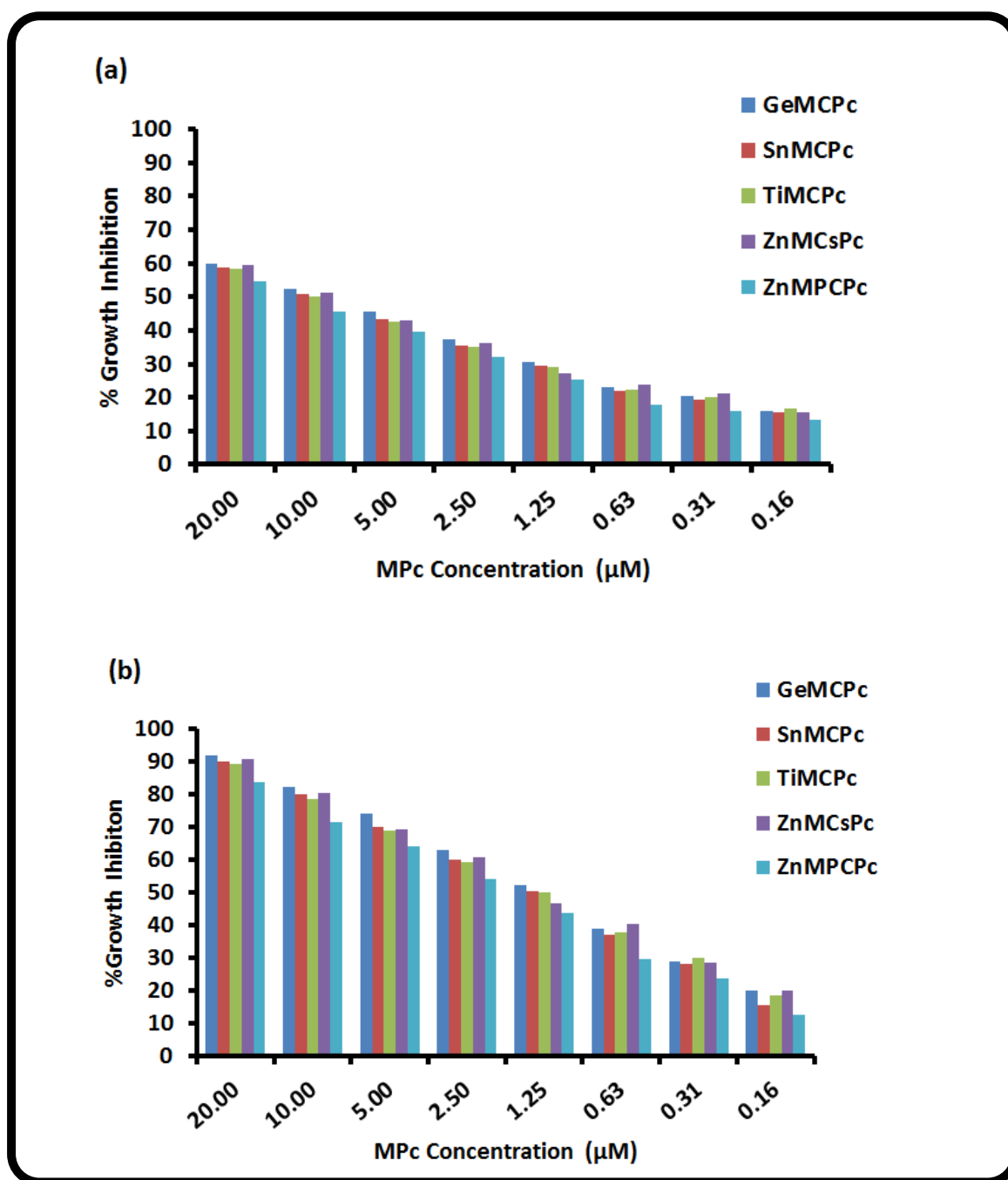
Figure 5.2: Antimicrobial activity of the MPc complexes in liquid broth solution, in the dark (a) and under illumination with visible light (b), against *S. Aureus*.

A minimum concentration of ~10 μM at which approximately ~50% bacterial inhibition was obtained for all the MPc samples when kept in the dark, Fig. 5.2 (a) was necessary. A significant improvement in bacterial inhibition was obtained for the samples illuminated with light (Fig. 5.2(b)) giving ~50% bacterial inhibition at a

much lower concentration of ~1.25 μM. This suggested that the singlet oxygen produced by irradiation in the Q band region had a strong contribution to the photo-inhibition of bacteria.

Thus phthalocyanines show dark toxicity which is also important since it has been reported that *S. aureus* infected burn wounds in guinea pigs were treated with porphyrins without the need for illumination [422]. Dark toxicity of the phthalocyanines is known [423].

5.2. Effect of low symmetry versus symmetrical Pcs on bacterial growth inhibition in solution

In order to study the effects of the ring systems and symmetry, unsymmetrical complexes (**49, 53, 57**) were studied and compared to their corresponding symmetrical complexes (**70, 69, 68**). Table 5.1 shows the singlet oxygen quantum yield of the complexes since Φ_Δ values are important for PACT.

Fig. 5.3 compares the antimicrobial behaviour of complex **53** and **69** alone and in the presence of AgNPs against *B. Subtilis* in solution.
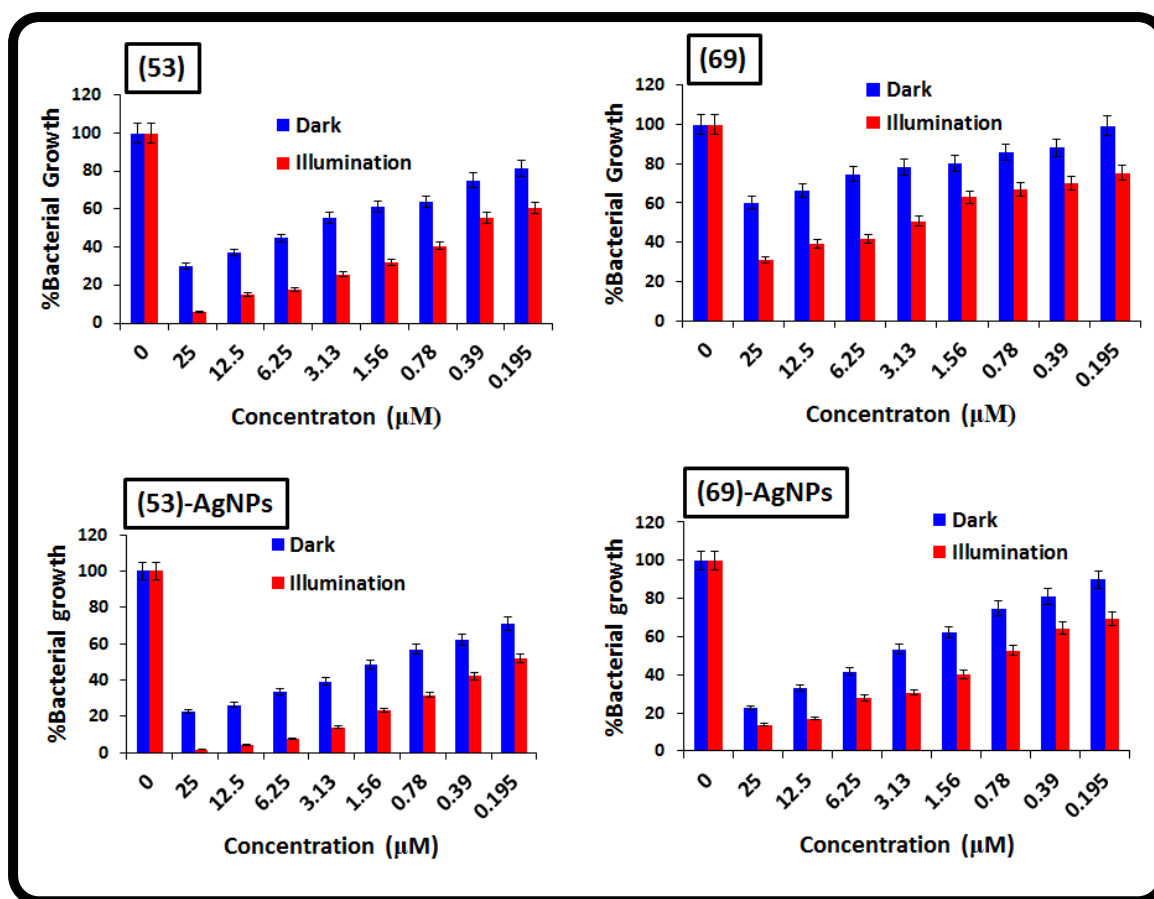
Figure 5.3: Antimicrobial behaviour of ZnMPCPc (53) and ZnODEPc (69) alone and in the presence of AgNPs, against *B. Subtilis* in liquid broth solution.

The antimicrobial growth inhibition of *Bacillus Subtilis* is investigated, since there are fewer reports on the gram positive (*B. Subtilis*) antimicrobial behaviour of Pcs compared to gram negative bacteria (*S. Aureus*). The antimicrobial properties of low symmetrically substituted ZnPc derivatives (**49**, **53** and **57**) and their symmetrical counterparts (**70**, **69** and **68**) alone and when conjugated to AgNPs, in solution are compared in Fig. 5.3.

Higher antimicrobial activities were observed for the unsymmetrical complex (**53**) compared to the symmetrical (**69**) counterpart. An increase in bacterial inhibition is observed as the concentration of the photosensitizer increases, both in the dark and under illumination. This behaviour suggests that the complexes have antimicrobial

activity even in the absence of light as stated above this is also an advantage. The best antimicrobial behaviour is observed for these complexes under illumination with light, due to the presence of singlet oxygen. A high improvement in antimicrobial growth inhibition was observed in the presence of AgNPs, due to high Φ_Δ values in the presence of AgNPs, Table 5.1.

Fig. 5.4 compares the antimicrobial behaviour of the various Pcs alone or in the
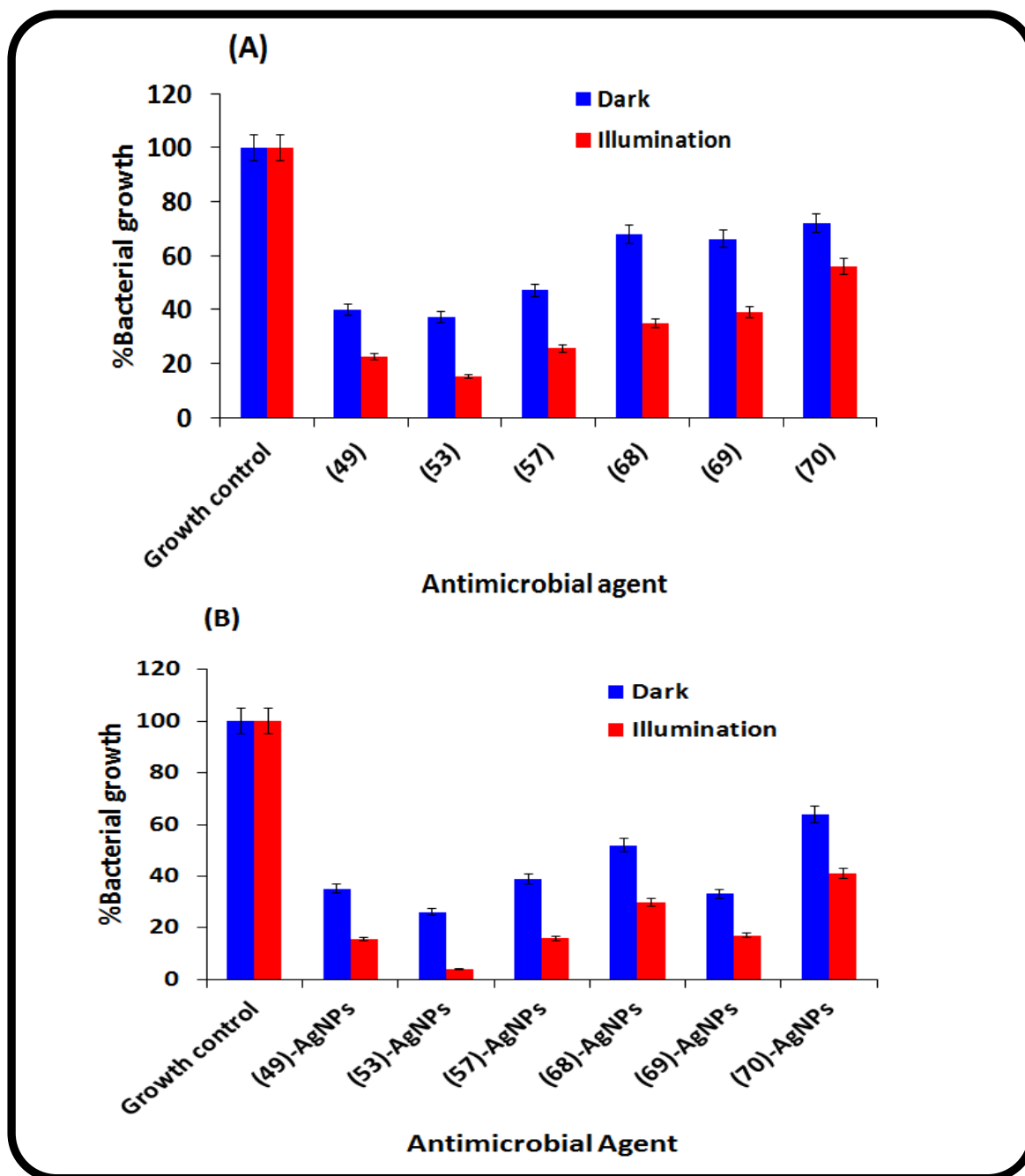
presence of AgNPs

Figure 5.4: Bar graphs showing antimicrobial activities of all the low symmetry (49, 53, and 57) ZnPcs and symmetrical (70, 69 and 68) complexes alone (A) and in the presence of AgNPs (B) against *B. Subtilis*, in liquid broth solution, concentration of Pc =12.5 μM.

In general, the low symmetry complexes (**49, 53, 57**) show higher antimicrobial behaviour compared to their symmetrical (**70, 69, 68**) counterparts, both in the dark and under illumination and in the presence of AgNPs, Fig. 5.4. Complex **53** gave the best antimicrobial inhibition compared to all complexes tested in the absence or presence of AgNPs, followed by the monocysteinyl ZnPc (**49**), both alone and in the presence of AgNPs. Complex **69** showed better bacterial inhibition in the presence of AgNPs compared to all the symmetrical Pcs.

The antimicrobial behaviour against *B. subtilis* of the low symmetry phthalocyanine in the fiber matrix is presented in Fig. 5.5. Positive antimicrobial inhibition of the bacterial strain is observed for all the complexes, as judged by the clearing of bacteria on the surface and on the edges of the fiber for all the plates under illumination. The clearing of the bacteria at the fiber edge was more pronounced in the presence of AgNPs under illumination, suggesting improved bacterial inhibition. The colour of the bacterial growth colonies appears as white, and as discussed above, the growth of bacteria on the surface of the fiber resulted in complete masking of the MPc blue colour. The plates with the MPcs-AgNP conjugates shows some bacterial inhibition even in the dark as judged by the restoration of the blue colour of the fiber, suggesting that there might be diffusion of Ag ions from the fiber.
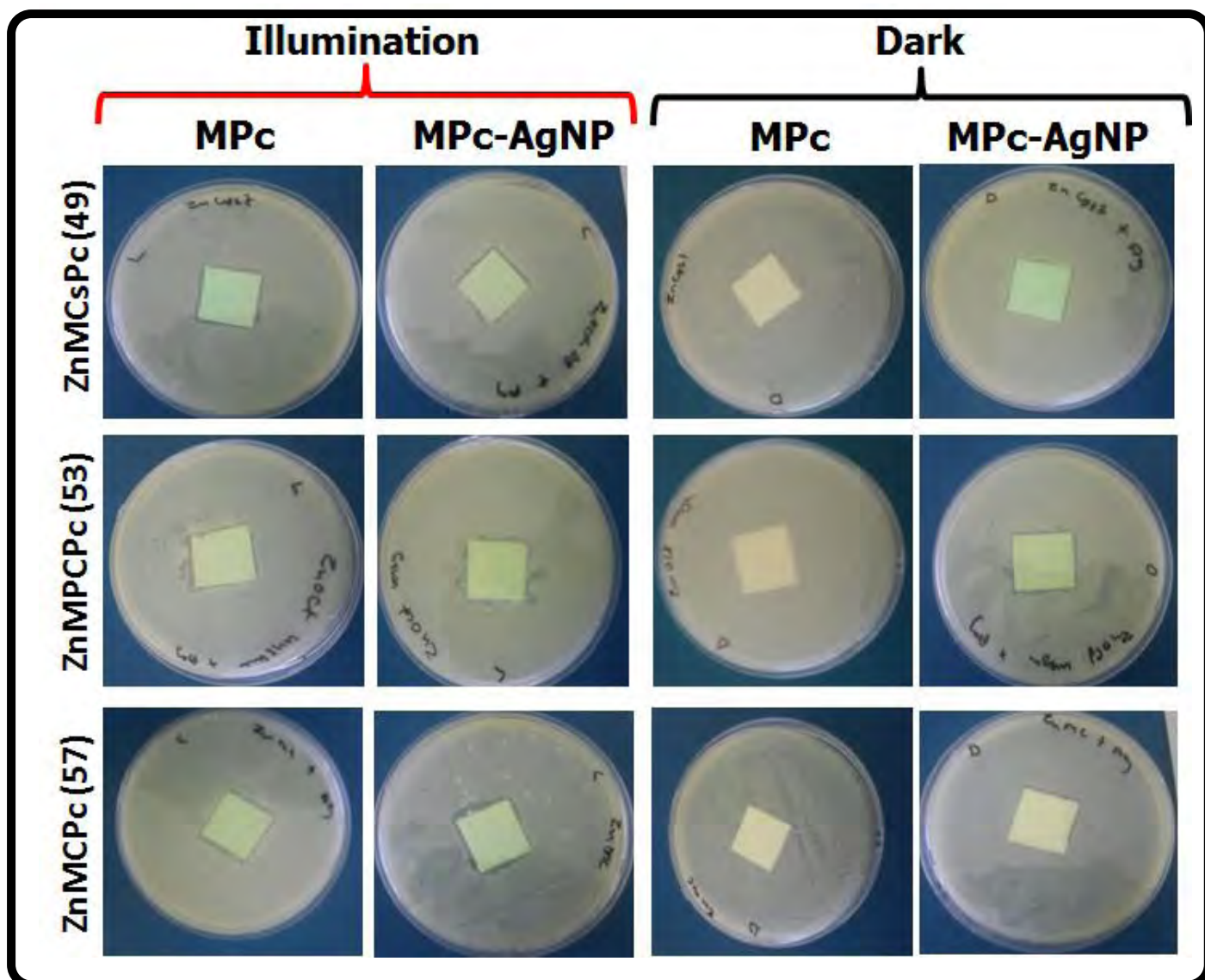
Figure 5.5: Digital images of the antimicrobial inhibition test using the low symmetry ZnPc derivatives modified fibers alone and in the presence of AgNPs, studies in the dark and under illumination with visible light, against *B. Subtilis*.
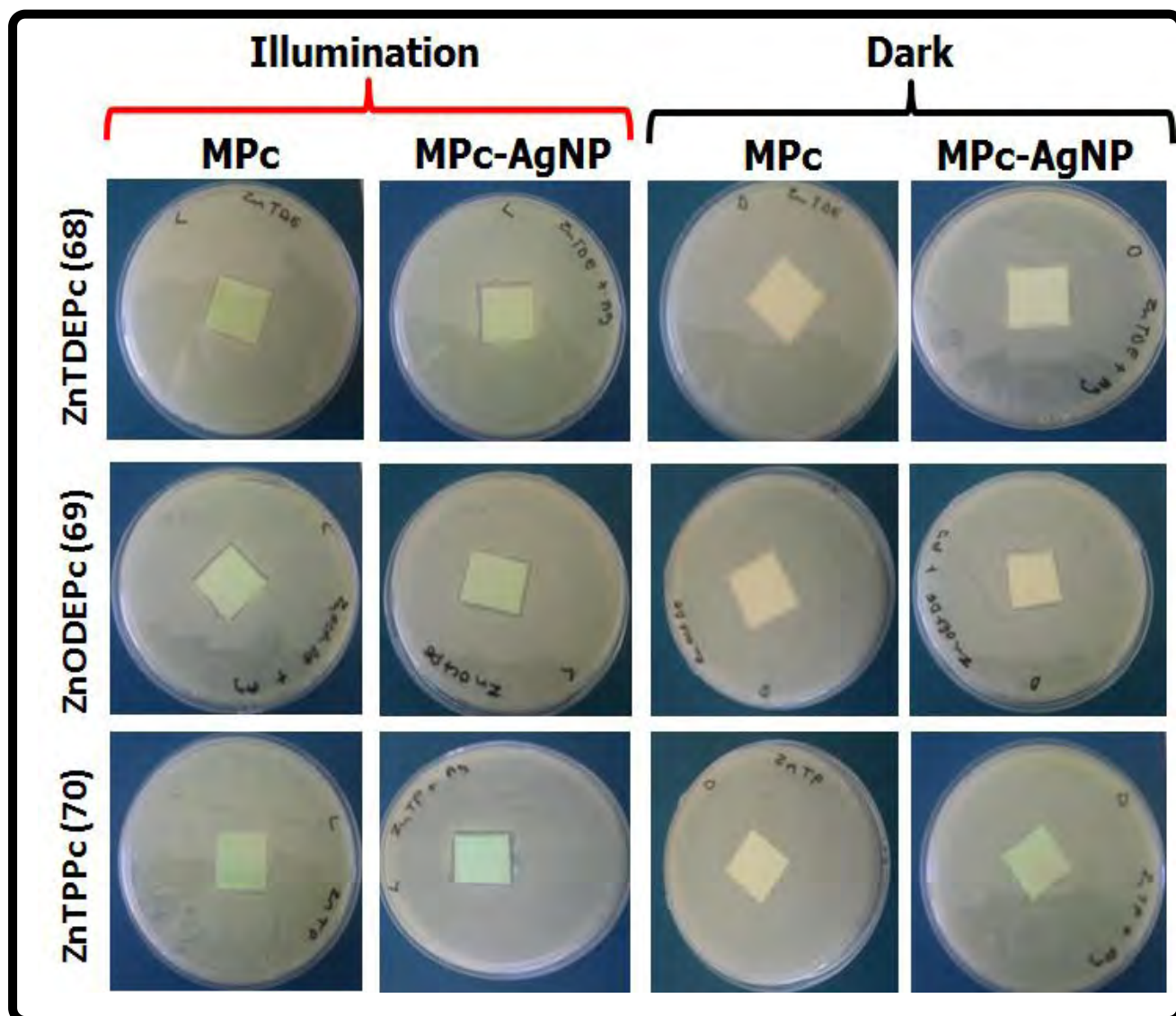
Figure 5.6: Digital images of the antimicrobial inhibition test using symmetrical ZnPc derivatives modified fibers alone and in the presence of AgNPs, studies in the dark and under illumination with visible light, against *B. Subtilis.*

Fig. 5.6   shows the antimicrobial activities of the corresponding symmetrically substituted ZnPc derivatives in the fiber matrix. The colour of the fiber is also used here to explain the bacterial activities of the MPcs in the dark and under illumination. Clearing of the fiber (returning to a blue colour) was observed for all the complexes under illumination with light, due to bacterial growth inhibition.

5.3 Effect of shape of the AgNPs in the AgNP-Pc conjugates on the antimicrobial inhibition of *S. Aureus*

The antimicrobial behaviour of complex **49-52** is studied in the presence of various shapes of AgNPs in solution.
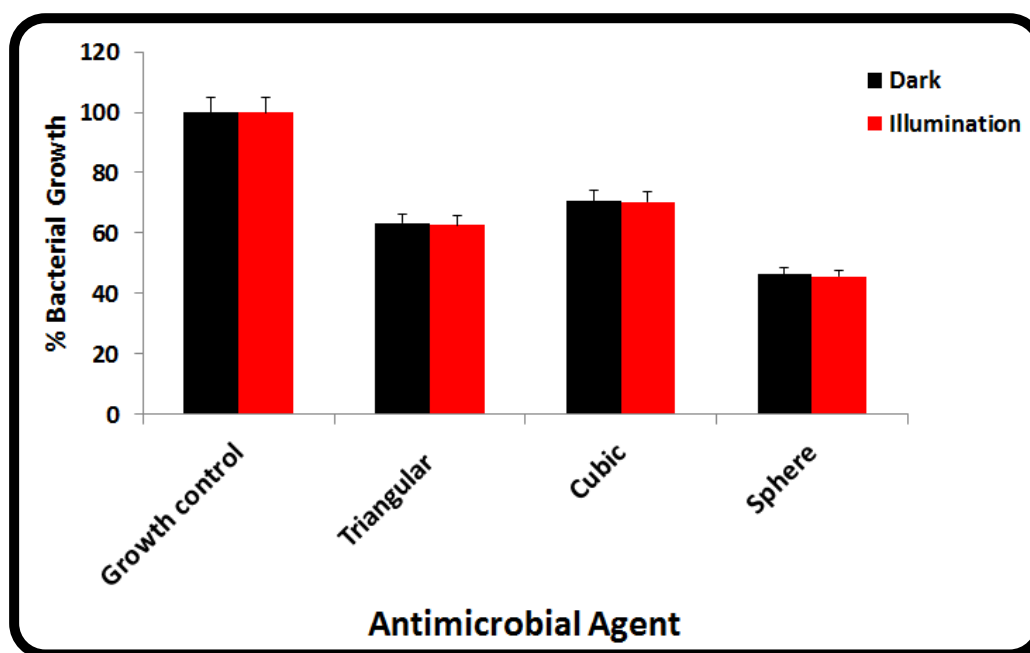
Figure 5.7: Bar graph representation of antimicrobial activities of various AgNPs shapes toward *S. aureus* in the dark and illuminated with visible light, in liquid broth solution.

The antimicrobial activities of various AgNPs were tested without photosensitizers both in the presence of the light and in the dark. Fig. 5.7 shows a bar graph representation of various AgNPs against *S. Aureus.* Antimicrobial action of the differently shaped AgNPs appear not to be affected or enhanced either in the dark or under illumination with light as expected. Lower bacterial growths (~45%) were obtained with the spherically shaped AgNPs, followed by the triangular shaped AgNPs, suggesting higher bacterial inhibition. The spherical AgNPs have a higher

surface area due to its smaller (15 nm) size, compared to the triangular (size 54 nm) and cubic (60 nm) NPs. The antibacterial activities of variously shaped AgNPs in different media, with a variety of sizes compared to the NPs presented in this study, have been reported before [218]. The effect of shape and size of the AgNPs towards antibacterial growth is still not well understood. The cubic AgNPs in this work (Fig. 5.7) showed the lowest antibacterial action against *S. aureus*.

From the geometry point of view it is not possible to have the same size in different shapes. Different shapes of AgNPs will inevitably give different surface areas. Hence it is hard to compare AgNPs with different shapes in terms of activity towards bacteria even if they had the same size due to different shapes and as a result different active surface areas.
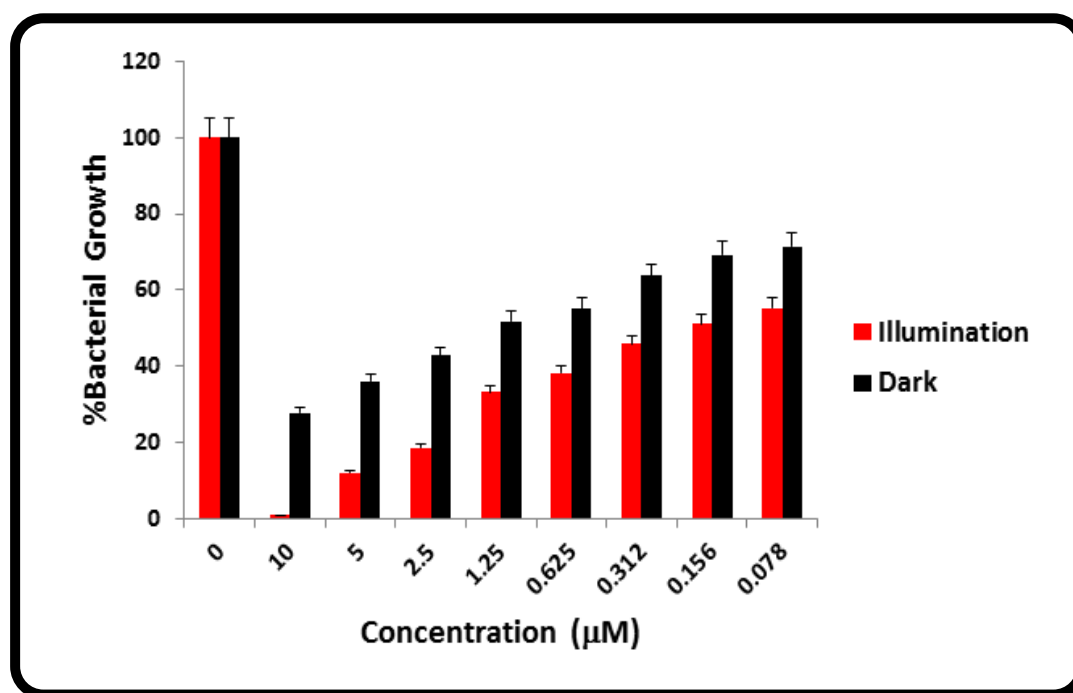
Figure 5.8: Antimicrobial activities of (OH)$_2$GeMCsPc (51) + spherical AgNPs towards *S. Aureus*, in the dark and under illumination with light, in liquid broth solution.

To improve the antimicrobial activities of various AgNPs, experiments were carried out in the presence of various MPc photosensitizers as described in the experimental section. Fig.5.8 shows a bar graph representing a serial two fold dilution of the $(OH)_2GeMCsPc$ (**51**) complex (as an example) in the presence of spherically shaped AgNPs. An increase in antibacterial activity, both in the dark and under illumination, is observed as the concentration was increased two fold. As expected greater antibacterial activity was observed under illumination.
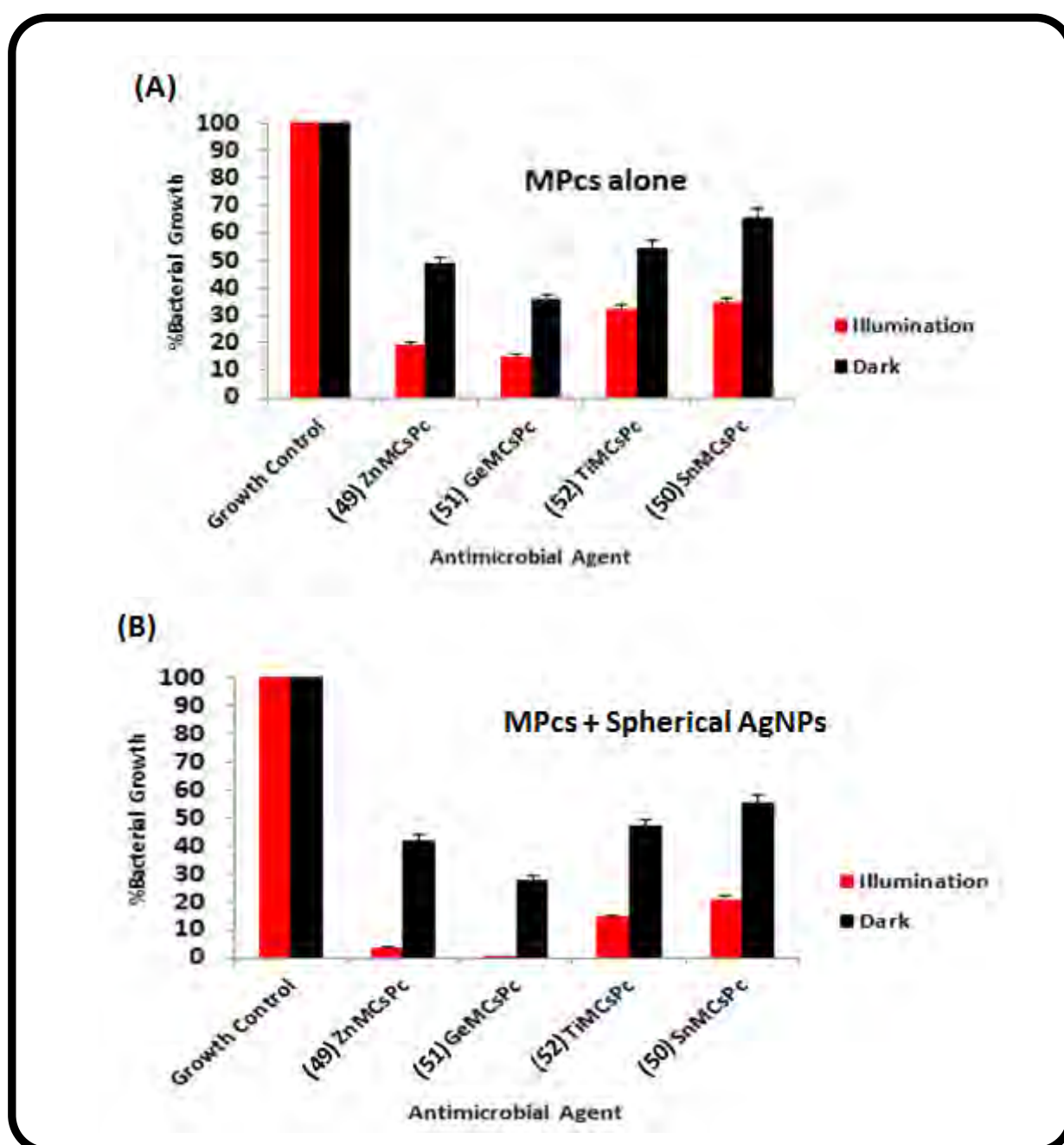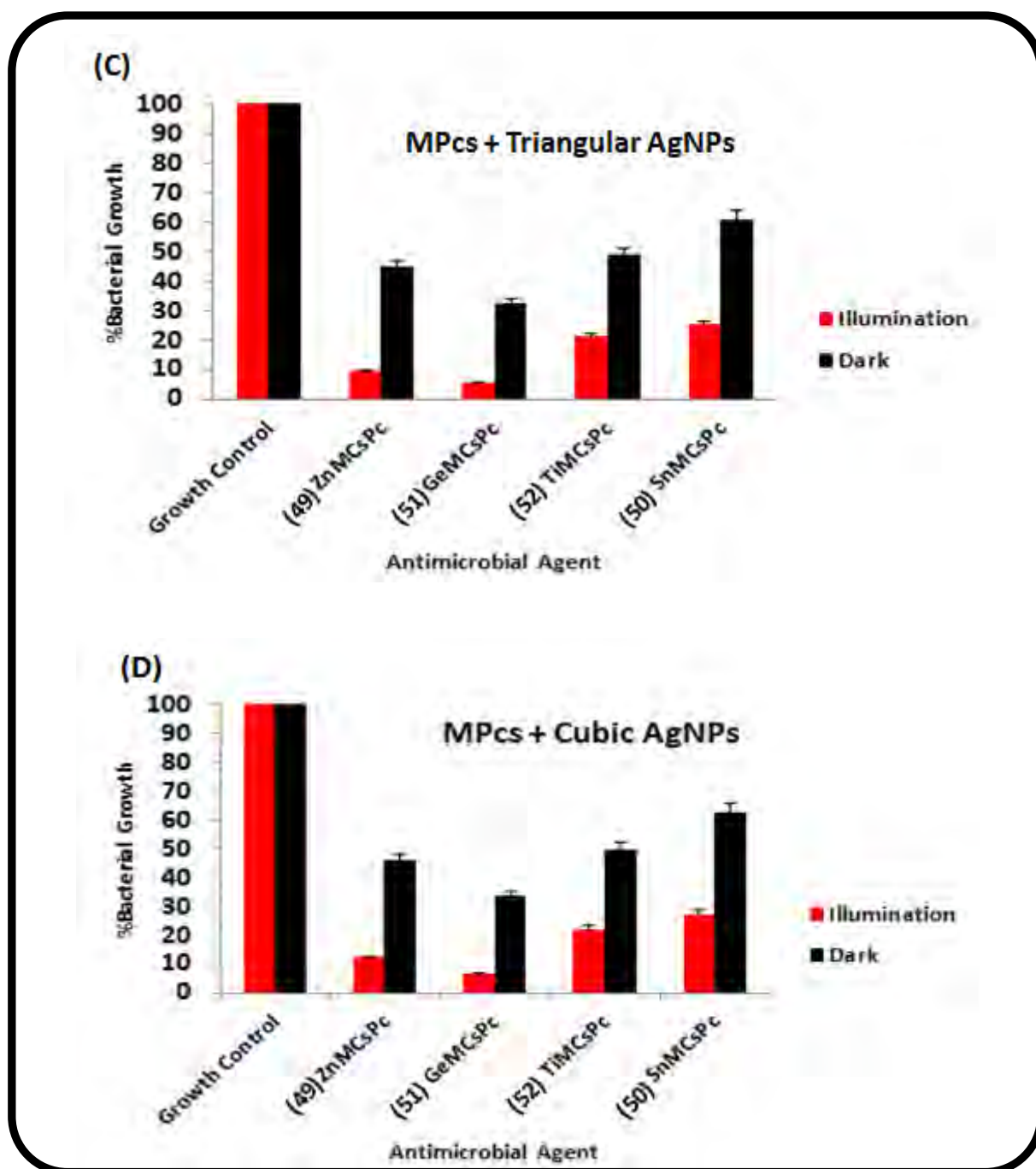
Figure 5.9 : Antimicrobial activities towards *s. aureus* of various MPcs alone (A) and in the presence of various AgNPs (B-D), under illumination with light and in the dark. Concentration of Pc = 10 μM

The antimicrobial activities of various MPcs were first investigated alone (Fig. 5.9(A)) and the in the presence of various AgNPs, Fig. 5.9 B-D. The $(OH)_2GeMCsPc$ (**51**) gave the highest antibacterial activity compared to all the other complexes, both

under illumination and in the dark. The best antimicrobial activity of complex (**51**) can be associated to its high singlet oxygen production in solution, Table 5.1. Fig. 5.9 presents bar graphs showing the antimicrobial activities of the various combinations of AgNPs with phthalocyanines. Higher antimicrobial activity was observed for the spherical AgNPs in the presence of various MPcs (Fig. 5.9 (B)) compared to the other shapes and to the MPcs alone as was the case for AgNPs alone. Thus spherical AgNPs seem to have the best activity. The OTiMCsPc and (OH)$_2$SnMCsPc showed lower antibacterial activity when studied alone (Fig. 5.9A), however an improvement is achieved in the presence of all various shaped AgNPs. Under irradiation, all complexes showed improved antibacterial activity due to the presence of singlet oxygen, hence PACT.

5.4 Comparative study of *B. Subtilis* and *S. Aureus* using ZnPc and SiHDTPc (61) in the presence of spherical AuNPs and AgNPs

The bacterial inhibition behaviour against *Bacillus Subtilis* and *Staphylococcus Aureus* of unsubstituted ZnPc and axially ligated SiHDTPc are compared, when alone and in the presence of gold and silver nanoparticles. The antimicrobial activities of the photosensitizers in the absence of nanoparticles is presented in Fig. 5.10.

These complexes were chosen due to their axial coordination to AgNPs and AuNPs as opposed to peripheral coordination using sulfur groups.
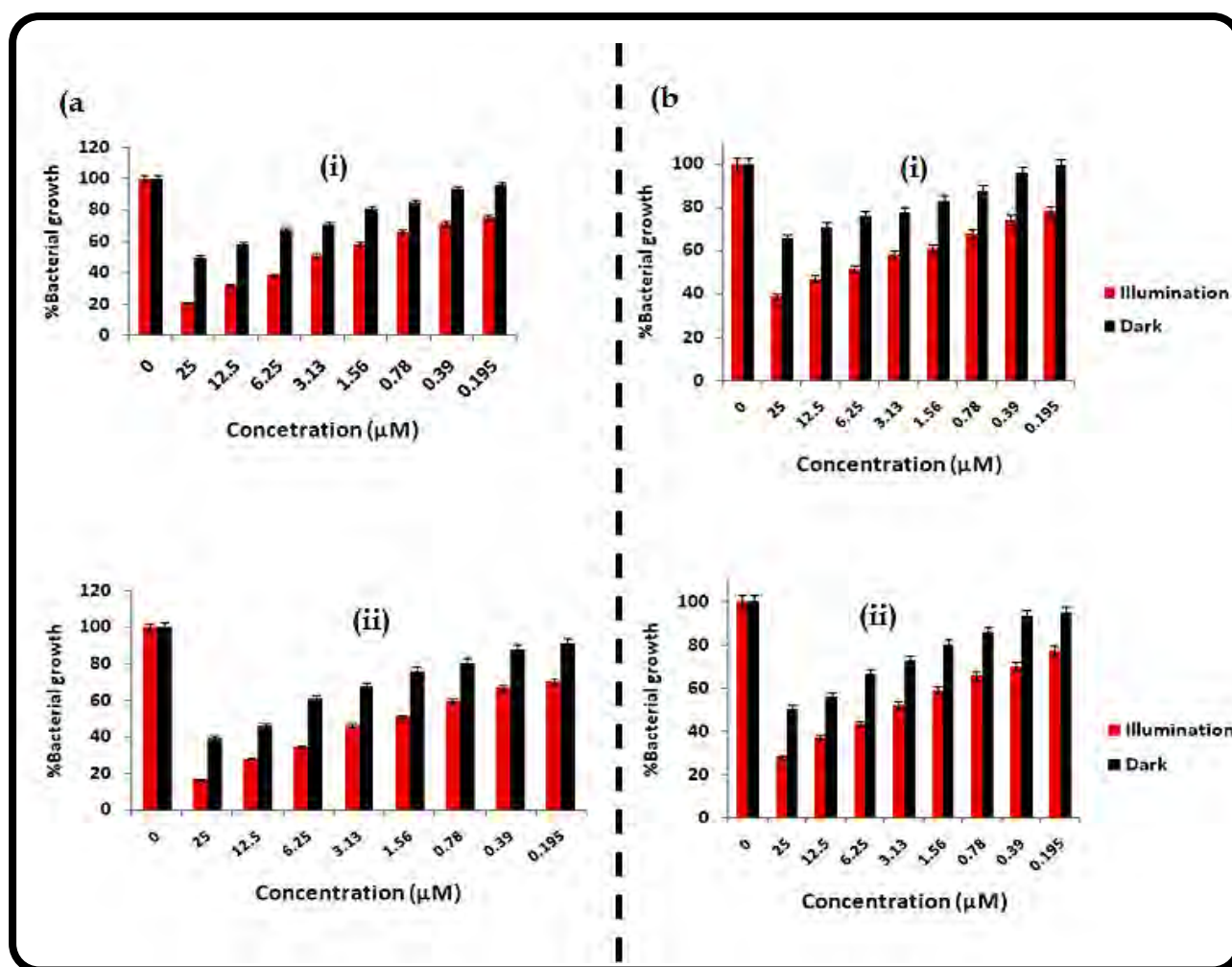
Figure 5.10: Bar graph representing the antimicrobial activities of SiHDTPc (a) and ZnPc (b), against *S. Aureus* (i) and against *B. Subtilis* (ii) in liquid broth solution.

The SiHDTPc (**61**) gave better bacterial inhibition for both *B. subtilis* and *S. aureus* compared to the ZnPc alone, which may be due to the dithiol axial ligands, since thiols have been reported to be lipophilic [424]. This may have resulted in the enhanced uptake of the SiHDTPc by the bacteria compared to the corresponding ZnPc. Based on singlet oxygen quantum yields obtained in solution, Table 5.1, ZnPc would be expected to perform better. The antimicrobial inhibition was found to be best with the gram positive *B. subtilis* compared to gram negative *S. aureus* for both MPcs. As documented before [331-338], the antimicrobial behaviour of

phthalocyanines has been shown to be best on gram positive compared to gram negative bacteria. The concentration to which 50% bacterial inhibition was achieved was found to be 3.13 μM for the SiHDTPc against both bacteria (*S. Aureus* and *B. Subtilis*) and 6.25 μM for the ZnPc under illumination with light. The antibacterial activities of AgNPs and AuNPs were tested without photosensitizers both in the presence of light and in the dark. There were no changes in the bacterial growth levels in the dark as compared to light as also observed in Fig. 5.7 for AgNPs. Fig. 5.11 shows the antimicrobial activities of SiHDTPc in the presence of AgNPs and AuNPs. Enhanced bacterial inhibition was observed for the SiHDTPc in the presence of both AgNPs and AuNPs under illumination when comparing Figs. 5.10 and 5.11. The enhanced photochemical activity of the conjugates is related to the increase in singlet oxygen generation in the presence of MNPs, Table 5.1.
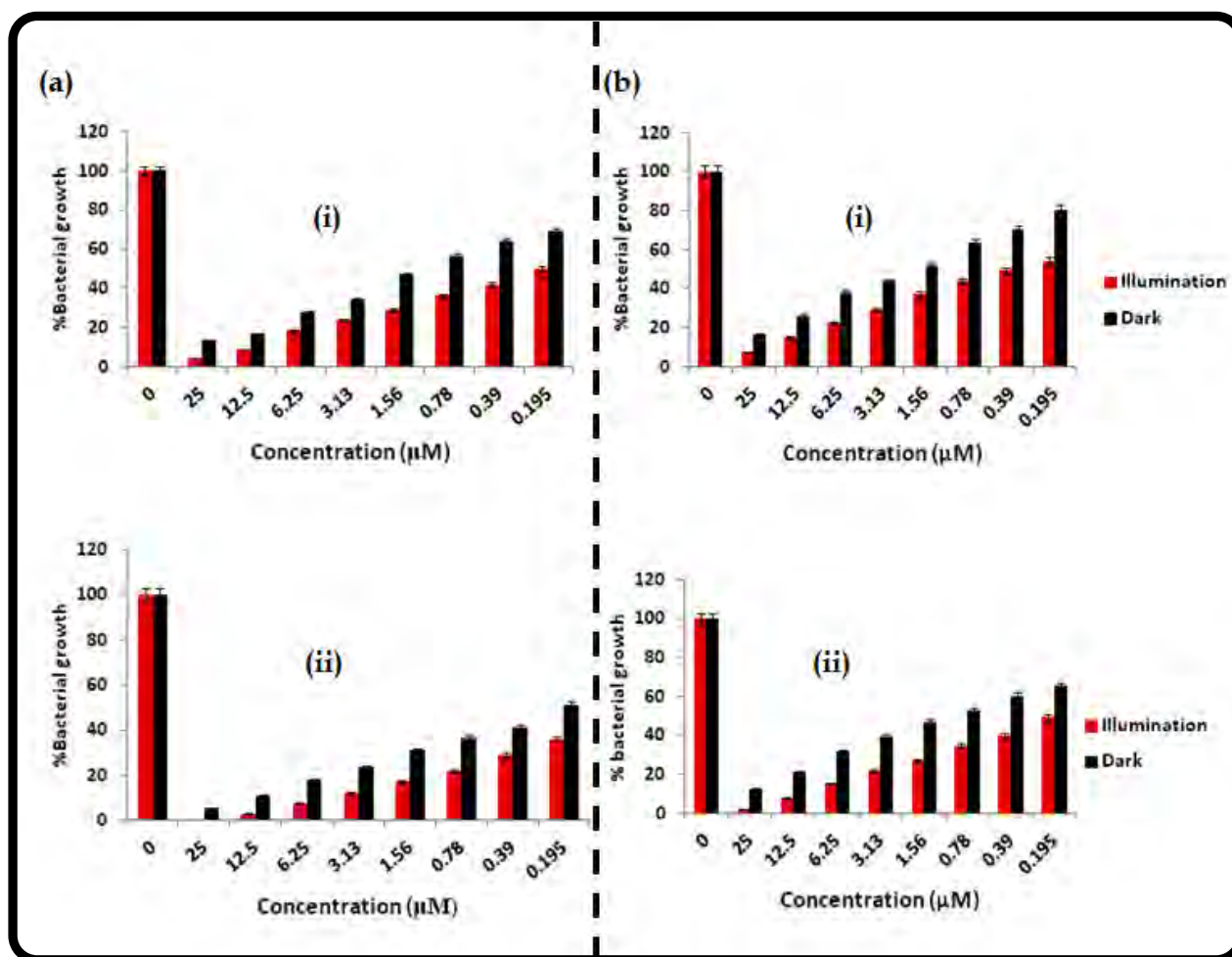
Figure 5.11: Bar graph representing the antimicrobial activities of SiHDTPc in the presence of AuNPs (i) and AgNPs (ii), against *B. Subtilis* (a) and against *S. Aureus* (b) in liquid broth solution.

Again, higher antimicrobial (Fig. 5.11) inhibitions were observed against the gram positive *B. subtilis* in the presence of Pc-MNPs conjugates compared to *S. aureus*. The SiHDTPc showed greater antimicrobial activity when linked to AgNPs as compared to the AuNP conjugate. 0% bacterial growth was achieved for the SiHDTPc-AgNPs against *B. subtilis* at 25 μM under illumination with light. The minimum inhibitory concentration required to inhibit the growth of 50% of organisms (MIC_{50}) was found

to be at < 0.195 μM for the SiHDTPc-AgNP conjugate for both the bacteria under illumination.

Fig. 5.12 shows a summary of the antimicrobial activities of both the ZnPc and SiHDTPc in the presence of AuNPs and AgNPs. The results show that good antimicrobial activities were obtained for all Pc-MNP combinations against *B. subtilis* compared to *S. aureus* both under illumination with light and in the dark. The best bacterial growth inhibition was achieved for SiHDTPc and ZnPc in the presence of AgNPs. This may have been due to the dual contribution of bacterial growth inhibition by the AgNPs and the singlet oxygen generation by the MPcs. For SiHDTPc, its enhanced uptake by the bacteria as discussed above could also contribute to greater bacterial growth inhibition.
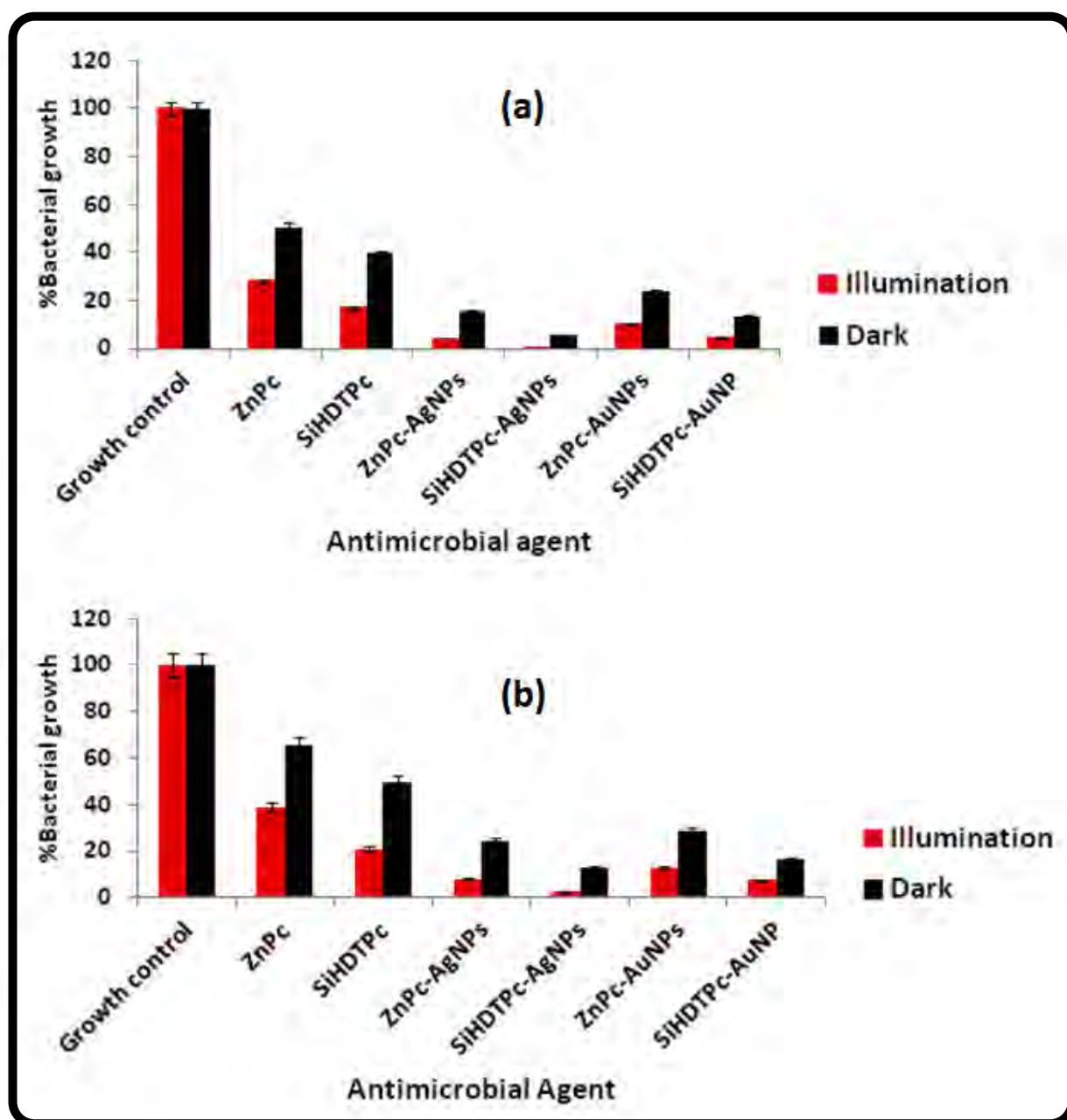
Figure 5.12: Bar graphs displaying a summary of the antimicrobial activities of various MPcs and their MNPs conjugates against *B. Subtilis* **(a) and against** *S. Aureus* **(b), in liquid broth solution.**
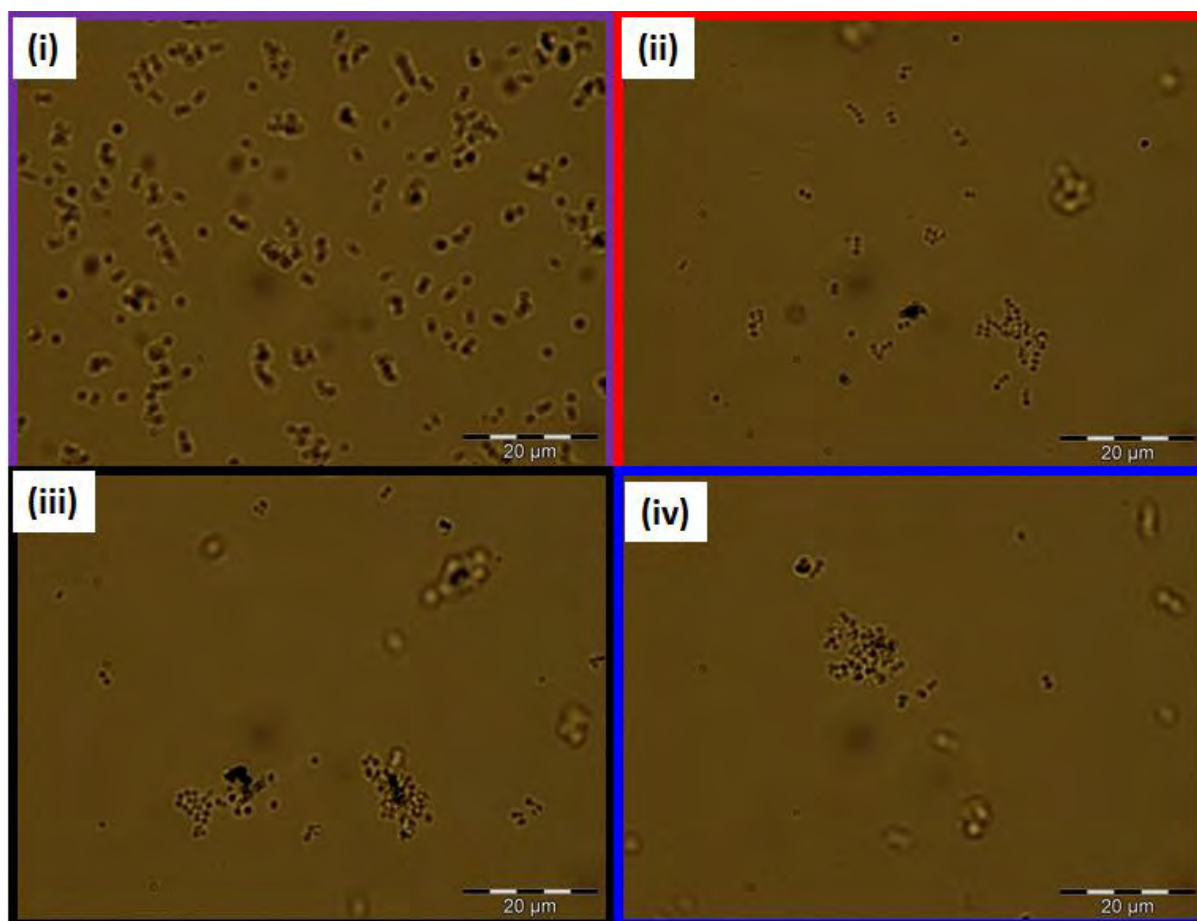
Figure 5.13: Microscopic images of *S. Aureus* **(i), in the presence of SiHDTPc (ii), SiHDTPc-AuNPs (iii), and in the presence of SiHDTPc-AgNPs**

The microscopic images of SiHDTPc against the gram negative *S. aureus* in the presence of MNPs are shown Fig. 5.13. Fig 5.13(i) shows the bacteria without treatment with antimicrobial agents. The *S. aureus* bacteria are characterised by their spherical shape, as observed in Fig. 5.13(i). A decrease in bacterial population density accompanied by shrinking in size and change in shape was observed in the presence of the antimicrobial agents. Clustering into groups together with a decrease in density of bacteria was observed in the presence of both Pc-MNP conjugates suggesting unfavourable conditions for the bacteria to grow.

5.4: Summary

Various MPc complexes have been successfully studied in solution and in the fiber matrix, either alone or in the presence of MNPs. Enhancement of antimicrobial activities are observed when the MPc complexes are conjugated to AgNPs. With the results presented in this chapter, the phthalocyanine complexes studied show potential industrial application for antimicrobial photo-inhibition of *Bacillus Subtilis* and *Staphylococcus Aureus*.

CHAPTER 6

Binding of SiPc to Metallothionein

The SiPc (**61**) complex was further studied for binding to metallothionein protein, due to the presence of free SH groups on its axial ligand positions, that can covalently couple to the protein via S-S crosslinking.

6.1 Brief description of metallothionein (MT) Protein

Coupling of macrocyclic compounds (such as metallophthalocyanines, MPc) to the MT protein will improve the optical and chemical properties that may be very useful in medical applications and drug delivery. In this work, the attempted conjugation of the protein with axially ligated thiol silicon phthalocyanine (**61**) is investigated. To date no reports have been documented on MT protein binding other ligands (i.e. macrocyclic compounds) either than metals.

Fig. 6.1 shows the structure of the two main domains (beta and alpha) of the metallothionein protein with its corresponding amino acid sequence.
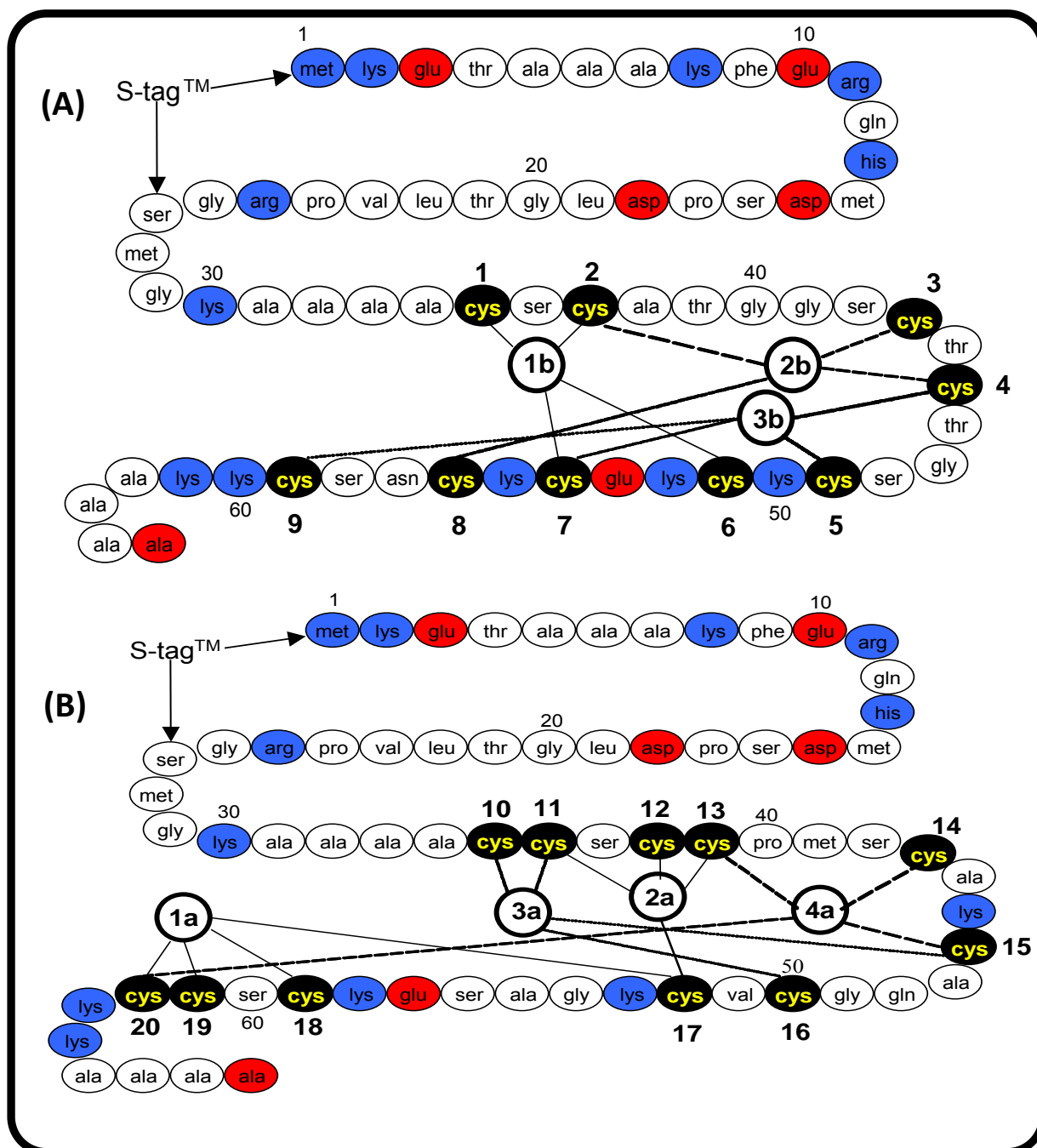
Figure 6.1: Structure of the Beta (A) and Alpha (B) domain of metallothionein protein used in this work.

Metallothionein (MT) is a small cysteine rich protein that consists of a ~ 60 amino acid sequence of which 20 amino acids are mainly cysteine [425-432], Fig. 6.1. MT is ubiquitous in nature, but most abundant in the liver and kidney of mammals [425-

432]. The protein consists of two main domains, the alpha (α) and the beta (β) domain, that are separated by a short peptide linker of a ~ 2-3 amino acid sequence [426-429].

The beta domain consists of 9 cysteinyl thiols in its sequence, while the alpha domain consist of 11 cysteinyl thiols leading to a total of 20 cysteinyl amino acids in the full beta-alpha MT protein [425-432]. Since the first characterisation done by Vallee and co-workers in 1957 [433], MT has been extensively studied, though its main role in the body is not known. However previous reports have shown that the MT protein has the ability to coordinate metals from groups 11 and 12 via its cysteine thiols [434-436]. Since then, many reports have shown that MT binds to a series of metals in vivo and in vitro, this includes metals such Ag^+, Au^+, Co^{2+}, As^{3+} ,Cu^+, Hg^{2+}, Cd^{2+}, Fe^{2+}, Bi^{3+}, $Pb^{2+}$and Zn^{2+} [425-436]. Metallation studies of MT involve the binding of metals either to the apo-MT or the substitution of the metallated-MT (holo) with a metal that possesses a stronger binding constant [425-436]. The demetallation of metallated-MT uses either a chelator or an electrophile to displace the metals [425-433]. Previous reports have also shown that MT lacks aromatic amino acids (i.e. tyrosine, phenylalanine and tryptophan) in its sequence, which results in poor optical properties in the visible region, and absorption is observed only in the region between 230-300 nm (where the protein backbone absorbs) allowing for monitoring of metal or ligand binding to the protein [431].

Metal coordination in mammalian MTs have been reported to be via the cysteinyl thiols [426-434]. Coupling of complex **61** will be via its free axially ligated terminal

thiols to the free cysteine of the protein leading to the formation of chemically bonded disulphide bridges.

6.2 Experimental

6.2.1 Preparation of the metallothionein protein

The metallothionein protein was prepared according to the previously reported experimental procedure by Ngu and Stillman [431]. Briefly, recombinant human metallothionein (MT) was expressed in BL21 (DE3) *Escherichia coli* cells that were transformed using a pP-1 plasmid which contains an N-terminal S-tag as previously described [437]. The purity of the protein used in this study and its binding studies to the Pc complex were monitored using Electro Spray Ionization Mass spectrometry (ESI-MS). Before the binding studies, the protein was purified and demetallated by elution through a Sephadex G25 column using a 20 mM ammonium formate buffer at pH 2.7 (Fisher). Elution was monitored by UV-visible absorption spectroscopy at the characteristic metal-free (apo) MT wavelengths of 200 to 300 nm. Fractions that contained metal-free MT were collected and the purity checked using ESI-MS. The apo-MT protein concentrations were determined from the extinction coefficients of 40,000 L. mol^{-1} cm^{-1} at 220 nm.

6.2.2 Equipments

UV-visible spectra were recorded on a Varian 500 UV-Vis/NIR spectrophotometer.
Mass spectral data for the analysis of the MT protein was obtained using a
Micromass LCT mass spectrometer in the positive ion mode. The mass spectrometer
was operated using the parameters: 3500.0 V capillary voltage, 50.0 V sample cone
voltage, 15.0 V extraction cone, acquisition scan time of 4 s, and the inter scan delay
time of 0.1 s. The ESI-MS data were processed and deconvoluted using the MaxEnt I
software (Micromass). ESI-MS measurements were obtained using a wide scan range
(200-3000 m/z) and MS mass calculations were integrated from a minimum of 10
scans. Magnetic circular dichroism (MCD) spectra were recorded with a JASCO
J–725 spectrodichrometer equipped with a JASCO electromagnet producing
magnetic fields of up to 1.09 T (tesla) with both parallel and antiparallel fields.

6.3 Results and discussions

The cadmium MT is cleaved off at lower pH by protonating the thiol of the cysteine
to prepare free thiol binding sites which would then be accessible to the SiPc
complex (**61**). Size exclusion chromatography was employed to get rid of the free
cadmium in the solution of the pure apo-MT protein. Oxidation is a major problem
with MT solutions because of the large number of free cysteinyl thiol present in the
protein sequence. The cysteinyl thiols of the metal-free protein were kept in their
reduced state by carefully evacuating the samples to get rid of excess oxygen and the
samples were saturated with argon gas such that the protein was contained within a

sealed, inert environment to prevent intra-molecular disulphide bond formation amongst the cysteinyl moieties of the protein.

ESI-MS was employed as a monitoring tool in this study since it uses soft ionization, which does not generally fragment proteins or disrupt the cysteinyl thiol binding site. An additional advantage of using ESI-MS includes the ability to (i) directly inject dilute solutions of protein of low concentration (~6μM), (ii) monitor reactions in real-time to obtain time and temperature dependent mass spectra, (iii) identify different species by their unique mass-to-charge ratios and (iv) observe the effect of ligand or metal binding to the protein through changes in the charge states [431]. Thus, using this technique, it was possible to monitor the phthalocyanine binding reactions and identify intermediate species with different masses, and at the same time to determine the structural changes that occur to the protein itself that are induced by the binding of the phthalocyanine complex. The ESI-MS data can then be linked to the data obtained using UV-vis and magnetic circular dichroism MCD spectroscopy.
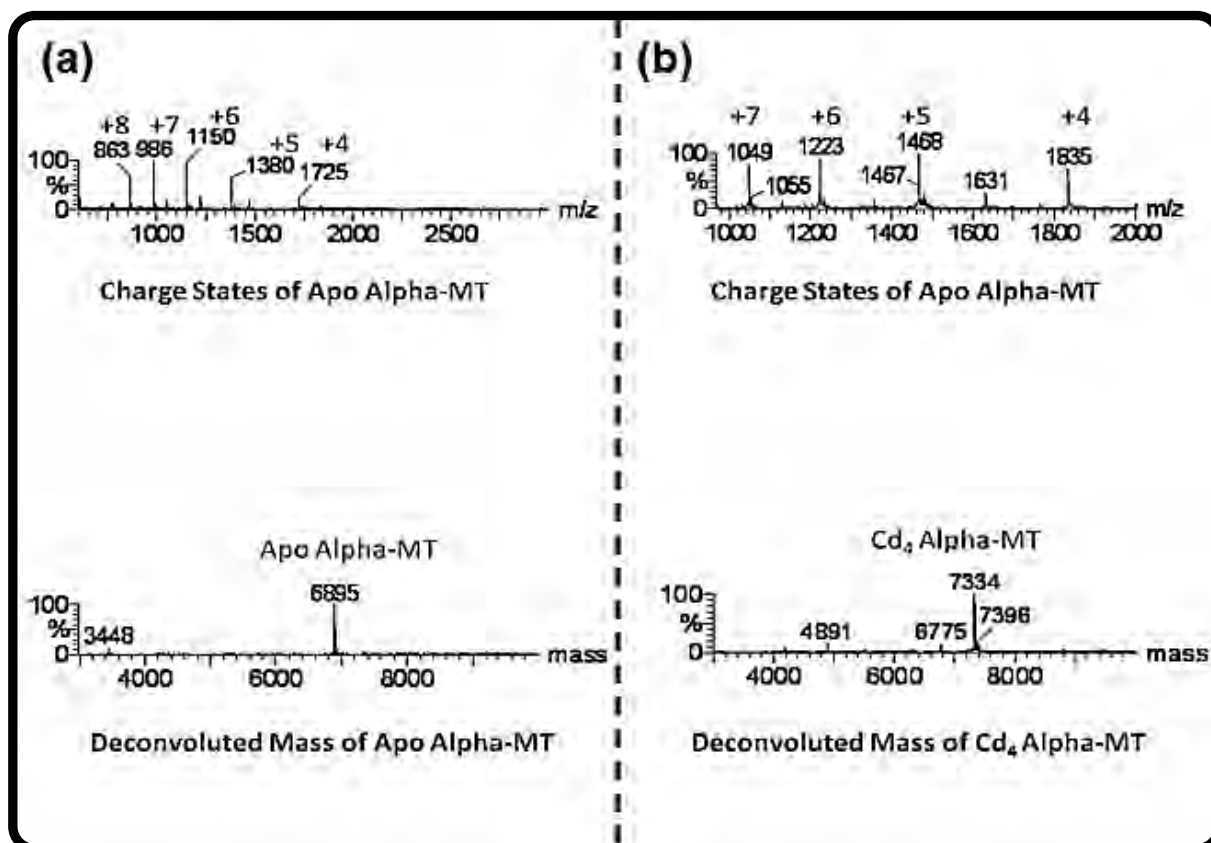
Figure 6.2: The ESI-MS of apo alpha-MT (a) and Cd₄-alpha MT (b), showing various charge states (m/z) and corresponding deconvoluted mass.

Fig. 6.2 shows the ESI-MS spectra (including the charge states) recorded for the metal-free apo alpha-MT domain (a) and the cadmium 4 alpha MT (b). Metallothioneins generally exhibit an ESI mass spectrum with a series of charge states of measurable intensity (Fig. 6.2) depending on the metallation status and the pH of the measurement [425-436]. The observed charge states result from protonation of basic amino acids present in the alpha domain of the MT sequence in the form of adducts. The ESI mass spectra of the metal free apo-MT and that of cadmium 4 MT domain shown in Figs. (6.2a and b) indicate the presence of a single species (i.e. only one protein species present in the solution). The measured masses perfectly correspond to the calculated masses with the Cd₄-alpha MT, showing

masses corresponding to 7334 Da and, after demetallation, the apo alpha protein with a mass corresponding to 6895 Da. The amino acid sequence of the alpha domain corresponding to the observed molecular weight is GSMGKAAAACCSCCPMSCAK CAQGCVCKGA SEKCSCCKKA AAA and for the N-terminus S-tag is MKETAAAKFE RQHMDSPDLG TLVPRGS. The S-tag was not cleaved off from the protein used in this work to maintain the stability of the protein in the presence of the phthalocyanine complex (**61**). Only 11 cysteinyl amino acids residues are present in the protein sequence and the S-tag does not consist of any of the cysteinyl thiol in its sequence, therefore it is not involved during the coupling.

Conjugative coupling of complex (**61**) to the MT protein was achieved by titrating stoichiometric amounts of the Pc to a metal free alpha MT protein. MT (25 μM) solution at low pH (~2.6), was allowed to react with 90 μM Pc in the presence of reduced glutathione (GSH). Changes in the charge states of the metal free protein were observed as the SiPc (**61**) complex was allowed to react with the protein (Fig. 6.3a). GSH was employed to remove any free oxygen from the solution and a peak resulting from the oxidation of GSH (308 Da) to GSSG (615 Da) was observed on the mass spectra.
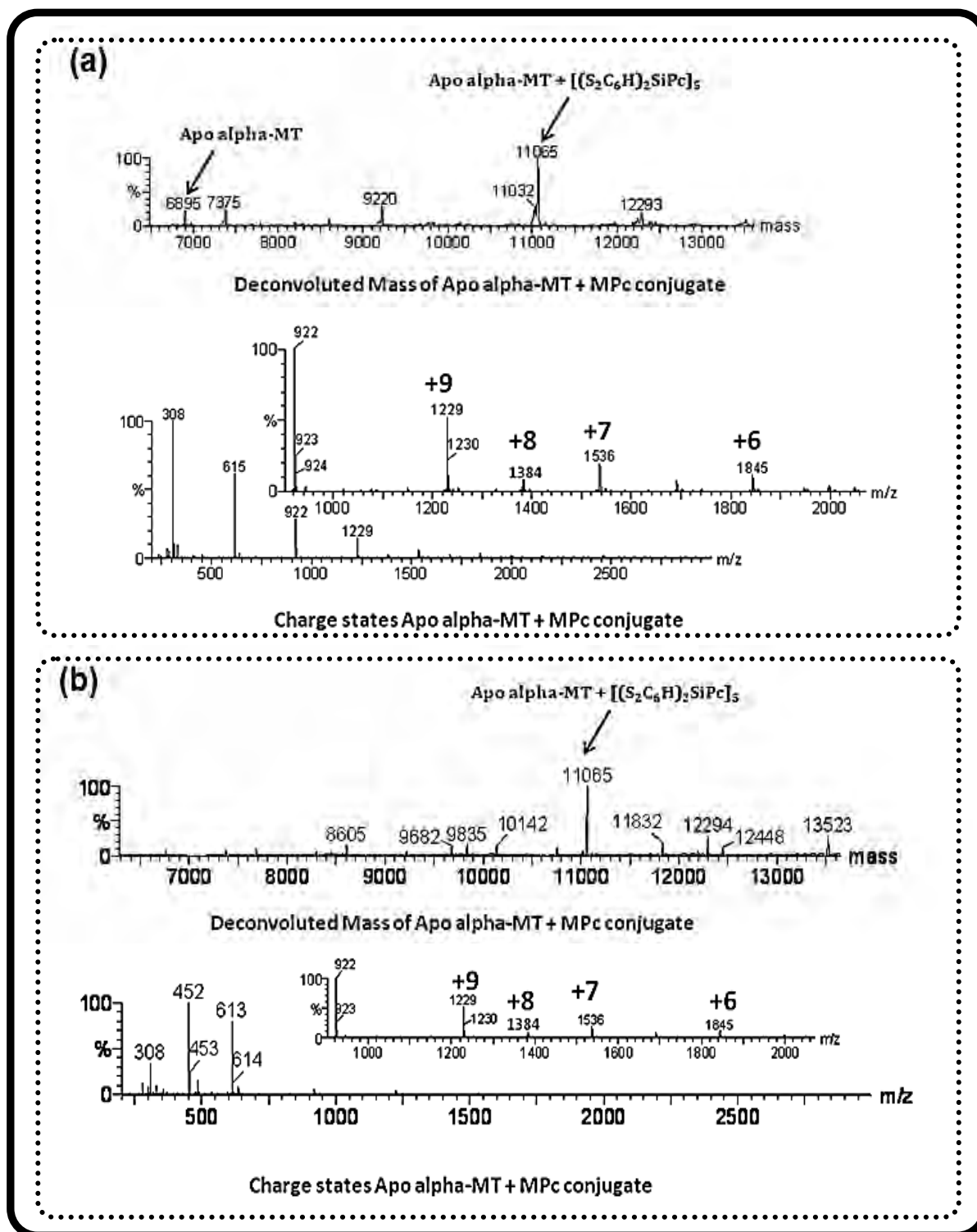
Figure 6.3: The ESI-MS of [bis-(1,6-hexanedithiol)]SiPc + apo alpha-MT conjugate for reaction ratio of 25 µM MT protein: 90 µM Pc at pH 2.6 (a) and after the concentration of the Pc was increased to 120 µM and the pH of the reaction was raised to pH 6 with influx of oxygen (b).

The deconvoluted ESI-MS of the reaction content (Fig. 6.3a) shows the presence of two species, the apo alpha protein (6895 Da) which is the main species. Though the mass of the apo protein is observed after deconvolution, there were no charge states corresponding to the mass of the protein which might have been as a result of the overshadowing of the peaks for the mass charges in both species. All the mass charge states observed deconvoluted to the mass corresponding to the main species of a 5 silicon ring-apha MT protein conjugate.

When the pH of the solution was raised from pH 2.6 to pH 6 and the concentration of the silicon phthalocyanine was increased to 120 μM (Fig. 6.3b), a clear disappearance of the apo protein species was observed suggesting complete consumption of the protein to form the product (Apo alpha-MT + $[(S_2C_6H)_2SiPc]_5$). The relative abundance of the GSSG formation from GSH was increased, and that of the reduced GSH showed a decrease, suggesting an influx of oxygen during the titration. The observed behaviour suggests that the oxidation of GSH to GSSG plays a vital role in the SiPc-alpha MT coupling. When the SiPc was employed without the GSH oxidation, the ESI-MS showed only the apo protein species to be present, even after a period of 24 hours of reaction, suggesting no coupling was taking place between the protein and the SiPc complex (results not shown). Similar studies were also carried out with GSH alone in the absence of the SiPc, and the ESI-MS results also showed no coupling between the protein and GSH in the absence of the phthalocyanine complex. It is very important to note that only 10 cysteinyl residues are involved in the coupling, meanwhile the alpha domain of the protein consists of 11 cysteines. The deconvoluted mass suggest that each silicon phthalocyanine

complex is cross linked via both of its free thiol axial ligands to two cysteinyl thiols (to form 5-SiPc ring-protein conjugate). Since MT is known for its ability to coordinate various metals through the cysteinyl thiols, several metallation studies using copper, mercury, silver and cadmium were undertaken to trace one of the free cysteinyl thiols that was not involved in the Pc-protein binding. ESI-MS showed no additional masses that were due to coordination of any of the metals employed; this might be due to the bulkier nature or the steric effect brought about by the bound phthalocyanine complex, thus hindering the free unbound cysteinyl thiol of the protein.
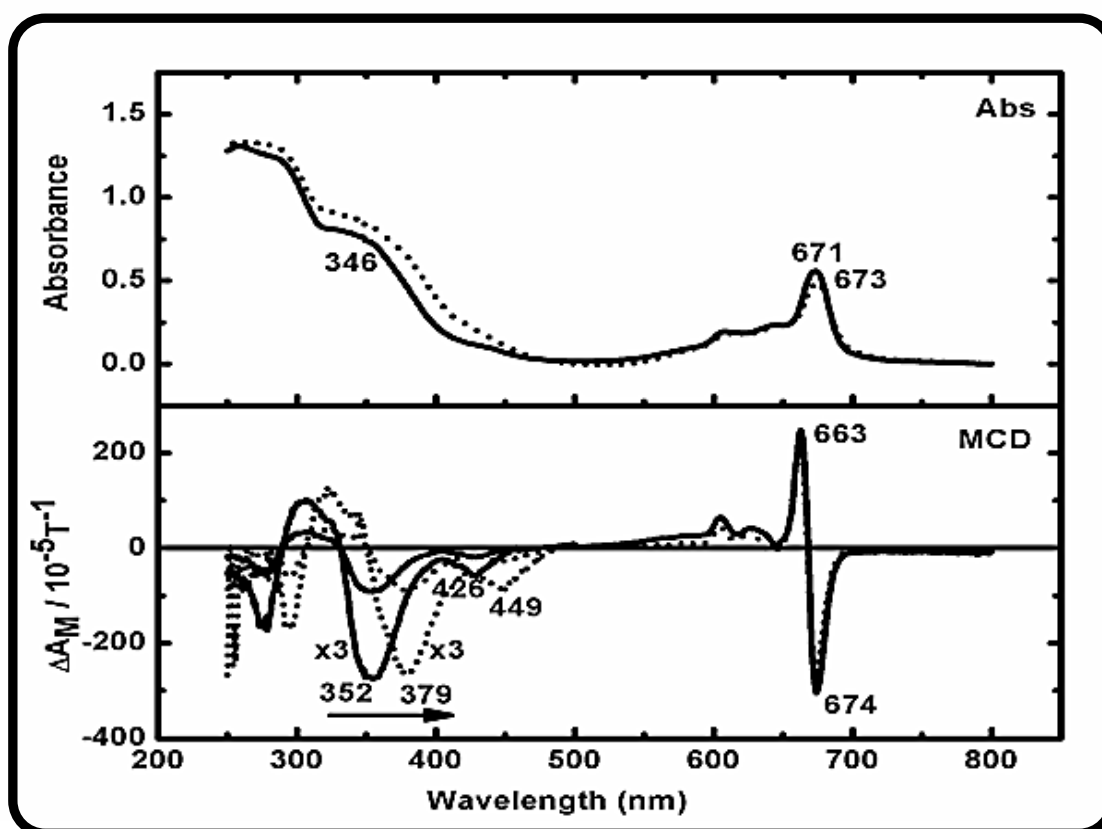
Figure 6.4: The UV-vis and magnetic circular dichroism spectra of [bis-(1,6-hexanedithiol)]SiPc in 1:5 DMF:H₂O ratio, before conjucation (solid black) and after (doted black) conjugation with MT.

In addition to the ESI-MS studies undertaken in this work, magnetic circular dichroism and UV-vis spectra of the pure (five molecules of SiPc attached to the MT protein) 5-SiPc(**61**)-protein conjugate were measured to confirm the MS results. Fig.6.4 shows the UV-vis (top) and MCD (bottom) of the 5-SiPc-protein conjugate. There were no significant changes in the UV-vis spectra of the SiPc alone (solid line) compared to the 5-SiPc-protein conjugate (dotted line). A 2 nm shift of the Q-band maxima from 671 nm of SiPc alone to 673 nm SiPc-protein conjugate was observed. Connection of the SiPc complex (**61**) to the protein is via the free thiol axial ligands. The derivative-shaped signals observed in the MCD spectrum in the Q-band region of both the SiPc complex (**61**) and the 5-SiPc-protein conjugate closely resemble the Faraday *A* terms as observed for other high symmetry phthalocyanine complexes [438-440]. A significant 27 nm shift, from 352 nm of the SiPc alone before coupling to 379 nm after coupling to the protein, is observed in the Soret band region. The observed shifting is unusual in phthalocyanines, however a positive deviation suggests changes in the electronic system of the complex that may be resulting from stretching of the axial ligands of the silicon complex upon coupling to the protein.

6.4: Summary

Complex (61) was successfully coupled to the alpha domain of metallothionein protein. The ESI-MS data obtain suggests that five SiPc complexes coupled to the ten cysteinyl thiols of the protein. Metal probes for the eleventh free thiol not involved during the coupling were not successful as a result of steric effect of the

phthalocyanine rings. Significant shifts in the MCD spectra of the SiPc-protein

conjugate was observed, suggesting coupling.

CHAPTER 7

General conclusions

7.1 Conclusions

The synthesis and separation of novel, low symmetrically substituted phthalocyanine complexes of Zn, Sn, Ge and Ti has been successfully achieved. The complexes were successfully characterized by various techniques that confirmed their relative purity. Red shifting of absorption spectra was seen with complexes containing a large number of sulfur atoms due to its electron donating ability. Metal dependent red shifting of the absorption spectra was observed for the complexes. The synthesis and characterisation of various AgNPs, QDs and AuNPs showing interesting spectral and chemical properties with different sizes and shapes achieved.

The MPc complexes were successfully conjugated to quantum dots (QDs), silver nanoparticles (AgNPs) and to gold nanoparticles (AuNPs). All conjugates were successfully characterized with various instrumental techniques and displayed properties corresponding to their unique predicted structures. The UV-vis spectral properties of all the conjugates reported in this thesis were discussed in detail. Conjugation of the phthalocyanine complexes to GSH-AuNPs resulted in blue shifting of the Q-band absorption spectra, confirming successful linking. Appearance of peaks both nanoparticle and phthalocyanines in the XRD spectra together with changes in the angle and d-spacing confirmed a new crystal form which further confirmed conjugation.

For the QD conjugates, some MPc complexes showed aggregation when they were mixed to quantum dots and aggregation was found to be less when they were chemically linked. An increase in energy transfer from the quantum dots to the MPc

complexes was observed when they were covalently linked to the quantum dots as compared to when they were mixed.

The photophysical and photochemical behaviour of the complexes and their metal nanoparticles conjugates were investigated and compared.

Low fluorescence and higher triplet quantum yields were achieved for the complexes in the presence of MNPs. Enhanced singlet oxygen generation was however achieved for all these complexes in the presence of MNPs.

In general, all complexes gave good triplet state and singlet oxygen production. A decrease in singlet oxygen production was observed when the complexes were electrospun into a fiber matrix; however an improvement was observed in the presence of AgNPs.

The complexes and their MNP conjugates were successfully tested for their antimicrobial activity against gram positive *B. Subtilis* and gram negative *S. Aureus* bacteria, when alone and when supported in fiber. Higher bacterial inhibition were achieved in the presence of AgNPs. The antimicrobial behaviour of low symmetry phthalocyanines supported in a fiber matrix is reported for the first time in this thesis.

The germanium complexes gave the highest singlet oxygen production both alone and in the presence of MNPs. The antimicrobial activities of various MPcs can be expressed in increasing order based on the central metal as Sn<Ti< Zn<Ge. The low symmetrically substituted ZnPc derivative showed the best antimicrobial behaviour when they were compared to their symmetrical counterparts.

7.2 Future Prospects

The low symmetry phthalocyanines presented in this thesis showed potential in the industrial applications of antimicrobial photo-inhibition of *Bacillus Subtilis* and *Staphylococcus aureus*. These systems can be engineered for use in many medical equipment as well as for wound dressing. However, in future it would be interesting to see if these systems are optimized further e.g. introducing ligands at the periphery of phthalocyanines that are already in clinical trials (used as antibiotics) or as antimicrobial agents.

References

1. R. P. Linstead, Br. Ass. Adv. Sci. Rep. (1933) 465.

2. A. von Braun, J. Tscherniac, Ber. Deut. Chem. Ges., 40 (1907) 2709.

3. L.R. Milgrom, InThe colours of life: An introduction to the chemistry of porphyrins and related compounds, Oxford University Press, (1997).

4. H. de Diesbach, E. von der Weid, Helv. Chim. Acta, 10 (1927) 886.

5. R.P. Linstead, J. Chem. Soc., (1934) 1016.

6. P. Gregory, J. Porphyr.Phthalocya.,3 (1999) 468.

7. N.B. McKeown, Chem. Ind., (1999) 92.

8. A. G. Dandridge, H.A.E. Drescher, J. Thomas, Dyes British Patent,322(1929)169.

9. J. M. Robertson, J. Chem. Soc., (1936) 1195.

10. J. M. Robertson, J. Chem. Soc., (1935) 615.

11. C.C. Leznoff, A.B.P. Lever (Eds.), Phthalocyanines: Properties and Applications, vols. 3, VCH Publishers, New York, 1989

12. M. Calvete, G.Y. Yang, M. Hanack, Synth. Met. 141 (2004) 231.

13. M. Kandaz, S.L.J. Michel, B.M. Hoffman, J Porphyr. Phthalocya. 7 (2003) 700.

14. P. Tau, T. Nyokong, Polyhedron 25 (2006) 1802.

15. J. J. Simon, H.J. Andre, Molecular Semiconductors, Springer, Berlin, 1985.

16. C.C. Leznoff, In Phthalocyanines: Properties and Applications, eds. C.C. Leznoff, A.B.P. Lever, VCH publishers, New York, Vol. 1(1989)1, Chp. 1.

17. M.J. Stillman, T. Nyokong, In Phthalocyanines: Properties and Applications, eds. C.C. Leznoff, A.B.P. Lever, VCH publishers, New York, Vol. 1 (1989) 133

18. M. K. Friedel, B.F. Hoskins, R.L. Martin, S.A. Mason, J. Chem. Soc., Chem. Commun., (1970) 400.

19. Y. Zhang, X. Zhang, Z. Liu, H. Xu, J. Jiang, Vib. Spectrosc.,40(2006) 289.

20. P. N. Day, Z.Q. Wang, R. Pachter, J. Mol. Struct. (Theochem), 455 (1998) 33.

21. K. M. Kadish, R. Guilard, K.M. Smith,the porphyrin handbook, Eds.,phthalocyanines: synthesis vol 11 (1998) 63

REFERENCES

22. P. Gregory in High Technology Applications of Organic Colorants, Plenum Press, New York, 1991.

23. W. Li , A. Yu , D. C. Higgins , B. G. Llanos , Z. Chen, J. Am. Chem. Soc., 132 (2010) 17056

24. K. Hanabusa and H. Sharai in Phthalocyanines: Properties and Applications, eds. A.P.B. Lever and C.C. Leznoff, VHC Publishers, New York, 1993, Vol.2.

25. R.K. Sen, J. Zagal and E. Yerger, Inorg. Chem., 16 (1977) 3379.

26. H. Kasuga in Phthalocyanine: Properties and Applications, Eds. A.P.B. Lever and C.C. Leznoff, VCH Publishers, New York, 1996, Vol.4.

27. D. Schlettwein, M. Kaneko, A. Yamada, D. Wohrle and N. 1. Jaeger, J. Phys. Chem.95 (1991) 1748.

28. T. Yoshida, M. Tochimoto, D. Schlettwein, D. Wöhrle, T. Sugiura, H. Minoura, Chem. Mater. 11 (1999) 2657.

29. D. Worhle and D. Meissener, Adv. Mater., 3 (1991) 129.

30. D. Worhle, L. Kreienhoop, D. Schlettwein in Phthalocyanine: Properties and Applications, eds. A.P.B. Lever and C.C. Leznoff, VCH Publishers, New York, 1996, Vol.4.

31. A.B.P. Lever, M.R. Hempstead, C.C. Leznoff, W. Lui, M. Melnik, W.A. Nevin and P. Seymour, Pure Appl. Chem., 58 (1986) 1467.

32. D.K.P. Ng, Y.-O. Yeung, W.K. Chan and S.-C. Yu, Tet. Lett.,38 (1997) 6701.

33. J. Simon and P. Bassoul, Phthalocyanine: Properties and Applications, Leznoff, C.C., Lever, A.B.P., Eds. V.H.S. Publishers: New York, 1989.

34. J. Limson and T. Nyokong, Electroanalysis, 9 (1997) 255.

35. A.W. Snow and W.R. Barger in Phthalocyanines: Properties and Applications eds. A.P.B. Lever and C.C. Leznoff, VCH Publishers, New York, 1989, Vol.1.

36. I. A Akinbulu, T. Nyokong, ElectrochimicaActa 55 (2009) 37

37. M. Thamae and T. Nyokong, J. Electroanal. Chem., 470 (1999) 126.

38. N. Toshina and T. Tominaga, Bull. Chem. Soc. Jpn., 69 (1996) 2111.

REFERENCES

39. M.M. Nicholson in Phthalocyanine: Properties and Applications, eds. A.P.B. Lever, C.C. Leznoff, VCH Publishers, New York, 1993. Vol. 3.

40. G.C.S. Collins and D.J. Schiffrin, J. Electroanal. Chem., 139 (1982) 335.

41. M.K. Emmelius, G. Pawlowski, H. Vollman, Angew. Chem. 28 (1989) 1445.

42. S. Nalwa and J.A. Shirk in Phthalocyanine: Properties and Applications, eds. A.P.B. Lever and C.C. Leznoff, VCH Publishers, New York, 1993, Vol. 4.

43. B. Simic-Glavaski in Phthalocyanine: Properties and Applications, eds. A.P.B. Lever and C.C. Leznoff, VCH Publishers, New York, 1993, Vol.3.

44. N.B. McKeown, In Phthalocyanine Materials: Synthesis, Structure and Function. Chemistry of Solid State Materials, Cambridge University Press, New York, (1998).

45. M. S. Wesley, E. V. Johan, M. A. Cynthia, Adv. Drug Deliv. Rev., 56 (2004) 53.

46. M. W. Cecilia, H. S. Taroh, X. Liang-yan, H. G. Nahida, L. O. Nancy, Cancer Lett.,179 (2002) 43.

47. I.J. MacDonald, T. Dougherty, J. Porphyr. Phthalocya., 5 (2001) 105.

48. R. Bonnett, In Chemical Aspects of Photodynamic Therapy, Gordon and Breach Science Publishers, Amsterdam, (2000).

49. C. M. Allen, W. M. Sharman, J. E. Van Lier, J. Porphyr. Phthalocya. 5 (2001) 161

50. Md. K. Nazeeruddin, M. Humphry-Baker, M. Grätzel, D. Wöhrle, G. Schnurpfeil, G. Schneider, A. Hirth, N. Trombach, J. Porphyr. Phthalocya.,3(1999) 230.

51. G. Jori, C. Fabris, M. Soncin, S. Ferro, O. Coppellotti, D. Dei, L. Fantetti, G. Chiti and G. Roncucci, Lasers Surg. Med., 38 (2006), 468

52. Steven Parker ,J Laser Dent 17 (2009) 131.

53. M.S. Rodríguez-Morgade, G. de la Torre, T. Torres, in: K.M. Kadish, K.M. Smith, R. Guilard (Eds.), The Porphyrin Handbook, vol. 15, Academic Press, New York, 2003 (Chapter 99).

54. C.C. Leznoff, C.R. McArthur, Y. Qin, Can. J. Chem. 71 (1995) 1319.

55. S.V. Kudrevich, H. Ali, J.E. van Lier, J. Chem. Soc. Perkin Trans. 1 (1994) 2767.

56. M. Geyer, F. Plenzig, J. Rauschnabel, M. Hanack, B. del Rey, A. Sastre, T. Torres, Synthesis (1996) 1139.

57. T. Torres**,** J. Porphyr. Phthalocya. 4 (2000) 325

58. S. Dabak, A. Gul, O. Bekaroglu, Chem. Ber. 127 (1994) 2009.

59. A.Weitemeyer, H. Kliesch, D. Wöhrle, J. Org. Chem. 60 (1995) 4900.

60. N. Kobayashi, R Kondo, S Nakajima, T. J. Osa, Am. Chem. Soc. 112 (1990) 9640.

61. A. Sastre, B. delRey, T. Torres. J. Org. Chem. 61 (1996) 8591.

62. A. Sastre, T. Torres, M. Hanack, Tetrahedron Lett. 36 (1995), 8501.

63. A. Weitemeyer, H. Kliesch, D. Wohrle, J. Org. Chem. 60 (1995) 4900.

64. T. W. Hall, S. Greenberg, C. R. McArthur, B. Khouw, C. C. Leznoff, New J. Chem. 6 (1982) 653.

65. S. S. Erdem, I. V. Nesterova, S. A. Soper, R. P. Hammer, J. Org. Chem. 73 (2008) 5003.

66. C.C. Leznoff, T.W. Hall, Tetrahedron Lett. 23 (1982) 3023.

67. C.C. Leznoff, P. Snirskaya, B. Khouw, R.L. Cerny, P. Seymour, A.B.P. Lever, J. Org.Chem. 56 (1991) 82.

68. J. Mack, N. Kobayashi, Chem. ReV, 111 (2011) 281

69. F. Dumoulin, M. Durmuş, V. Ahsen, T. Nyokong, Coord. Chem. Rev. 254 (2010) 2792.

70. N. B. McKeown in: The Porphyrin Handbook, Eds. K.M. Kadish, K.M. Smith, R. Guilard, Academic Press, New York, Vol. 15 (1999), p 61-116, , 1999.

71. C.C. Leznoff, In Phthalocyanines: Properties and Applications, eds. C.C. Leznoff, A.B.P. Lever, VCH publishers, New York, Vol. 1 (1989) (Chapter 1) p 1-54.

72. V. N. Nemykin, E. A. Lukyanets, ARKIVOC 2010 (i) 136

73. J. Britton, E. Antunes, T. NyokongJ. Photochem. Photobiol. A. Chem. 210 (2010) 1.

74. S. D'Souza, E. Antunes, C. Litwinski, T. Nyokong, J. Photochem. Photobiol A: Chem. 220 (2011) 11

75. S. D'Souza, E. Antunes, T. Nyokong, Inorg. Chim. Acta 367 (2011) 173

76. M. Thomas, A.M. Klibanov, Proc. Natl. Acad. Sci. U. S. A. 100 (2003) 9138.

REFERENCES

77. A. Synak, M. Gil, J. A. Organero, F. Sanchez, M. Iglesias, A. Douhal, J. Phys.

Chem. C 113 (2009) 19199

78. V.J. Mohanraj ,Y. Chen, Trop. J. Pharmaceut. Research, 5 (2006) 561.

79. W. Chidawanyika, T. Nyokong, Carbon 48 (2010) 2831

80. W. Chidawanyika, C. Litwinski, E.Antunes, T. Nyokong, J. Photochem.

Photobiol. A: Chem 212 (2010) 27.

81. K. T. de Oliveira, F. F. de Assis, A. O. Ribeiro, C. R. Neri, A. U. Fernandes, M. S.

Baptista, N. P. Lopes, O. A. Serra, Y. IamamotoJ. Org. Chem. 74 (2009) 7962.

82. D.A. Li, M.A. Ratner, T.J. Marks, J. Am. Chem. Soc. 110 (1988) 1707.

83. I. Rosenthal, Photochem. Photobiol. 53 (1991) 859.

84. T.J. Dougherty, Photochem. Photobiol. 58 (1993) 895.

85. M.J. Cook, R. Hersans, J. McMurdo, D.A. Russell, J. Mater. Chem. 6 (1996) 149.

86. M.-E. Ragoussi, J.-J. Cid, J.-H. Yum, G. de la Torre, D. Di Censo, M.Gratzel, M.

K. Nazeeruddin, and T. Torres Angew. Chem. Int. Ed. 51 (2012) 4375

87. H. Kliesch, A. Weitemeyer, S. Muller, D.Wohrle, Liebigs Ann. 7 (1995) 1269.

88. J. Morgan, H. Lottman, C.C. Abbou, D.K. Chopin, Photochem. Photobiol. 60

(1994) 486.

89. A.B.P Lever, Adv. Inorg. Chem. Radiochem., 7 (1965) 27

90. M.D. Maree, T. Nyokong J. Porphyr. Phthalocya. 5 (2001) 555.

91. M.D. Maree, Nyokong T. J. Photochem. Photobiol A: Chem 142 (2001) 39.

92. A.O. Ogunsipe, T. Nyokong, J. Mol. Struct. 689 (2004) 89

93. J. Metz, O. Schneider, M. Hanack, Inorg. Chem., 23 (1984) 1065

94. P.C. Kreuger, M.E Kenney, J. Org. Chem., 28 (1963) 3379

95. R. Rafaeloff, F.J Kohl, P.C. Kreuger, M.E. Kenney, J. Inorg. Nucl.Chem., 28

(1965) 899

96. R.D. Joyner, M.E. Kenney, Inorg. Chem., 1 (1962) 236

97. J. He, H.E. Larkin, Y.S. Li, B.D. Rihter, S.I.A. Zaidi, M.A.J. Rodgers, H.

Mukhtar, M.E. Kenney, N.L. Oleinick, Photochem. Photobiol., 65 (1997) 581

98. W. Chidawanyika, T. Nyokong. J. Photochem. Photobiol. A: Chem. 206 (2009)

169

REFERENCES

99. Y. Arslanoglu, T. Nyokong, Polyhedron 30 (2011) 2733

100. M. Kimura, H. Nomoto, N. Masaki, S. Mori, Angew. Chem. Int. Ed. 51 (2012) 4371

101. M.-E. Ragoussi, J.-J. Cid, J.-H. Yum, G. de la Torre, D. Di Censo, M. Gratzel, M. K. Nazeeruddin, T. Torres, Angew. Chem. Int. Ed. 51 (2012) 4375

102. P. Matlaba, T. Nyokong , Polyhedron 21 (2002) 2463

103. J. Chen, N. Chen, J. Huang , J. Wang, M. Huang, Inorg. Chem. Commu. 9 (2006) 313

104. F. Silvestri, M. García-Iglesias, J.-H Yum, P. Vázquez, M. V. Martínez-Díaza, M. Grätzel, M. K. Nazeeruddinand T. Torres, J. Porphyr. Phthalocya. 13 (2009) 369

105. T. Mugadza, T. Nyokong. Polyhedron 30 (2011) 1820

106. S. Forteath, E. Antunes, W. Chidawanyika, T. Nyokong, J. Lumin. 132 (2012) 2318

107.N. Nombona, E. Antunes, T. Nyokong, Dyes Pig. 86 (2010) 68.

108.N. Nombona, W. Chidawanyika, T. Nyokong, J. Mol. Struc. 1012 (2012) 31.

109.N. Nombona W. Chidawanyika, T. Nyokong, Polyhedron 30 (2011) 654

110. H. Kliesch, A. Weitemeyer, S. Muller, D. Wöhrle, Liebigs Ann. (1995) 1269

111.A. Hirth, A. K. Sobbi, D. Wöhrle,J. Porphyr. Phthalocya., 1 (1997) 275

112.N. Nombona, E. Antunes, C. Litwinski, T. Nyokong, Dalton Trans. 40 (2011) (1884) 11876.

113. I. Chambrier, M. J. Cook, D. A. Russell, Synthesis (1995) 1283

114. E. Sariola, A. Kotiaho, N. V. Tkachenko, H. Lemmetyinen, A. Efimov, J. Porphyr. Phthalocya. 7 (2003) 610

115. B.K. Mandal, A.K. Sinha, M. Kamath, J. Polym. Sci. A: Polym. Chem., 34 (1996) 643

116. Z. Bıyıklıoglu, D. Cakır , Spectrochim. Acta Part A: Mol. Biomol. Spectroscopy 98 (2012) 178

117. Y.-J. Zhu, J.-D. Huang, X.-J. Jiang, J.-C. Sun, Inorg. Chem. Commun. 9 (2006) 473

REFERENCES

118. X.-J. Jiang, P.-C. Lo, Y.-M. Tsang, S.-L. Yeung, W.-P. Fong, D. K. P. Ng, Chem. Eur. J. 16 (2010) 4777

119. M. Brust, M. Walker, D. Bethell, D.J. Schiffrin, R. Whyman, J. Chem Soc Chem. Commun. 7 (1994) 801

120. C.S. Weisbecker, M.V. Merritt, G.M. Whitesides, Langmuir. 12 (1996) 3763

121. A.C. Templeton, M.J. Hostetler, C.T. Kraft, R.W. Murray, J. Am. Chem. Soc. 120 (1998) 1906

122. K.S. Mayya, V. Patil, M. Sastry Langmuir 13 (1997) 3944

123. Y. Tan, Y. Li, D. Zhu, Langmuir 18 (2002) 3392

124. J. Liu, S. Mendoza, E. Roman, J. Am. Chem. Soc. 121(1999) 4304

125. D. Li, Q. He, J. Li, Adv. Colloid Interface Sci. 149 (2009) 28

126. P.R. Selvakannan, S. Mandal, R. Pasricha, Chem. Commun. 13 (2002) 1334

127. T. Pradeep, S. Mitra, A.S. Nair, R. Mukhopadhyay, J. Phys. Chem. B 108 (2004) 7012

128. T. Nyokong, Z. Gasyna, M.J. Stillman, Inorg. Chem., 26 (1987) 548.

129. E.A. Ough, Z. Gasyna, M.J. Stillman, Inorg. Chem., 30 (1991) 2301.

130. T.H. Huang, K.E. Reickhoff, E.M. Voight, J. Chem. Phys., 77 (1982) 3424.

131. E. M. Maya, A. W. Snow, J. S. Shirk, R. G. S. Pong, S. R. Flom and G. L. Roberts ,J. Mater. Chem., 13 (2003) 1603

132. K. Nakai, J. Usami, N. Kobayashi, J. Porphyr. Phthalocya. 11 (2007) 222.

133. R. D. George, A.W. Snow, J. S. Shirk, W. R. Barger, J. Porphyr., Phthalocya., 2 (1998) 1

134. K. Kameyama, A. Satake, Y. Kobuke Tetrahedron Lett. 45 (2004) 7617

135. A.C.H. Ng, X. Li, D.K.P. Ng, Macromolecules 32 (1999) 5292.

136. W. Chidawanyika, E. Antunes, T. Nyokong, J. Photochem. and Photobiol. A: Chem. 195 (2008) 183.

137. O.T.E. Sielcken, M.M. van Tilborg, M.F.M. Rocks, R. Hendricks, W. Drenth, R.J.M. Nolte, J. Am. Chem. Soc., 109 (1987) 4261.

138. M. Kasha, Radiat. Res., 20 (1960) 55.

139. Z. Gasyna, N. Kobayashi, M.J. Stillman, J. Chem. Soc., Dalton Trans., (1989) 2397.

REFERENCES

140. D.R. Arnold, N.C. Baird, J.R. Bolton, J.C.D. Brand, P.W.M. Jacobs, P. de Mayo, W.R. Ware, Photochem. An Introduction, Academic Press, New York, (1974).

141. M. Durmus, T. Nyokong, Photochem. Photobiol. Sci. 6 (2007) 659

142. V. Chauke, M. Durmus¸ T. Nyokong, J. Photochem. Photobiol. A: Chem. 192 (2007) 179

143. R. A. Mayers, Encyclopedia of analytical chemistry: Applications, Theory, and instrumentation 2000, Vol. 12, John Wiley & Sons Ltd, UK.

144. A. Ogunsipe, T. Nyokong, J. Photochem. Photobiol. A: Chem., 173 (2005) 211.

145. K. Ishii, N. Kobayashi, In The Porphyrin Handbook, eds., K.M. Kadish, K.M. Smith, R. Guilard, Elsevier Sc., USA, Vol. 16 (2003) 1, Chp.102.

146. J. Fu, X.Y. Li, D.K.P. Ng, C. Wu, Langmuir 18 (2002) 3843.

147. S. Fery-Forgues, D. Lavabre, J. Chem. Ed. 76 (1999) 1260.

148. A. Ogunsipe, J. Y. Chen, T. Nyokong, New. J. Chem. 28 (2004) 822

149. T.W.J. Gadella Jr, R.M. Clegg, T.M. Jovin, Biomaging 2 (1994) 139.

150. X.F. Wang, T. Uchida, S. Minami, Appl. Spectrosc. 3 (1989) 840.

151. H.C. Gerritsen, R. Sanders, A. Draaijer, Proc. SPIE 2329 (1994) 260.

152. X.F. Wang, T. Uchida, M. Maeshima, S. Minami, Appl. Spectrosc. 45 (1991) 560.

153. A.D. Scully, A.J. MacRobert, S. Botchway, P. O'Neill, A.W. Parker, R.B. Ostler, D. Phillips, J. Fluoresc. 6 (1996) 119.

154. G.J. Brakenhoff, M. Müller, R.I. Ghauharali, K. Visscher, Proc. SPIE 2412 (1995) 115.

155. A.G. Ryder, S. Power, T.J. Glynn, J.J. Morrison, Proc. SPIE 4529 (2001) 102.

156. S.E. Maree, D. Phillips, T. Nyokong, J. Porphyr. Phthalocya. 6 (2002) 17.

157. J.C. Swarts, M.D. Maree, J. Porphyr. Phthalocya. 11 (2007) 613.

158. A.P. de Silva, H.Q.N. Gunaratne, T. Gunnlaugsson, A.J.M. Huxley, C.P. McCoy, J.T. Rademacher, T.E. Rice, Chem. Rev., 97 (1997) 1515.

159. S.J. Strickler, R.A. Berg, J. Phys. Chem. 37 (1962) 814.

160. R. Zugle, C. Litwinski, T. Nyokong,Polyhedron 30 (2011) 1612

REFERENCES

161. J. Turro, In Modern Molecular Photochemistry, The Benjamin Cummings Publishing Co., Inc., New York (1978).

162. P. Kubát, J. Mosinger, J. Photochem. Photobiol. A: Chem. 96 (1996) 93.

163. R. A Keller, S. G Hadley, J. Chem. Phys. 42 (1965) 2382

164. S.M. Bishop, A. Beeby, H. Meunier, A.W. Parker, M.S.C. Foley, D. Phillips, J. Chem. Soc., Faraday Trans., 92 (1996) 2689.

165. M. Grimm, E. Eybl, M. Grabenwoger, H. Spreitzer,W. Jager, G. Grimm, P. Bock, M.M. Muller, E. Wolner, Surg., 111 (1992) 74.

166. J.R. Darwent, P. Douglas, A. Harriman, G. Porter, M.C. Richoux, Coord. Chem. Rev., 44 (1982) 83.

167. K. Kasuga, M. Tsutsui, Coord. Chem. Rev., 32 (1980) 67.

168. A. A. Frimer, The Spectrum, 13 (2000) 9.

169. M. Niedre, M. S. Patteerson, B. C. Wilson, Photochem. Photobiol., 75 (2003) 382

170. C. S. Foote, SPIE Institute Series, 6 (1990) 115

171. F. Wilkinson, W. P. Helman and A. B. Ross, J. Phys. Ref. Data., 22 (1993) 113

172. I. B. C. Matheson, Photochem. Photobiol., 29 (1979) 875

173. M. Jirsa, M. Jirsa Jr, P. Kubat, S. lekarsky, 96 (1995) 1

174. C. S. Foote, In singlet oxygen (eds H. H. Wasserman and R. W. Murray) Academic Press, New York, San Francisco, London, 1979, 139

175. M. E. Wieder, D. C. Hone, M. J. Cook, M. M. Handsley, J. Gavrilovic, D. A. Russell, Photochem. Photobiol. Sci., 5 (2006) 727

176. A. Kotiaho, R. Lahtinen, A. Efimov, H.-K. Metsberg, E. Sariola, H. Lehtivuori, N. V. Tkachenko, H. Lemmetyinen J. Phys. Chem. C, 114 (2010) 165

177. A. Sholto, B. Ehrenberg, Photochem. Photobiol. Sci., 7 (2008) 344

178. A. Weitemeyer, H. Kleish, U. Michelsen, A. Hirtb, D. Wöhrle, in Photodynamic tumor therapy: 2nd and 3rd generation photosensitizers, J. G. Moser (Ed.) Harwood Academic Publishers, The Netherlands, Chpt. 2, 1998

179. P. Alivisatos, Nat. Biotechnol. 22 (2004) 47

180. C. A. Mirkin, Inorg. Chem. 39 (2000) 2258

181. S.J. Park, T.A. Taton, Science (Washington, DC) 295 (2002)1503.

REFERENCES

182. C.A. Mirkin, R. Letsinger, R. Mucic, J. Storhoff, Nature (London) 382 (1996) 607.

183. D. Astruc, F. Lu, J.R. Aranzaes, Ang. wandte Chemie Int. Ed., 44 (2005) 7852

184. O. Lopez-Acevedo, K. A. Kacprzak, J. Akola, Nature Chemistry, 2 (2010) 329

185. J. H. Fendler. Chem. Mater., 13 (2001) 3196

186. E. Ozbay, Science 311 (2006) 189

187. S. A. Maier, M. L. Brongersma, P. G. Kik, Adv. Mater., 13 (2001) 1501

188. P. V. Kamat, J. Phys. Chem. B, 106 (2002) 7729

189. C. B. Murray, S. Sun, H. Doyle, MRS Bulletin, 26 (2001) 985

190. S. Nie, S. R. Emory, Science 275 (1997) 1102

191. L. A. Dick, A. D. McFarland, C. L. Haynes, J. Phys. Chem. B, 106 (2001) 853

192. J. F. Li, Y. F. Huang, Y. Ding, Nature, 464 (2010) 392

193. N. R. Panyala, E. M. Pena-Mendez, J. Have, J. Appl. Bio. Med., 7 (2009) 75

194. D. A. Giljohann, D. S. Seferos, L. Daniel, Ang. wandte Chem. Int. Ed., 49 (2010) 3280

195. C. L. Brown, G. Bushell, M. W. Whitehouse, Gold Bulletin, 40 (2007) 245

196. D. Gust, T.A. Moore, A.L. Moore, Acc. Chem. Res. 26 (1993) 198

197. P.K. Sudeep, B.I. Ipe, K.G. Thomas, M.V. Geoge, S. Barazzouk, S. Hotchandani, P.V. Kamat, Nano let 2 (2002) 29

198. J.-F. Eckert, J.-F. Nicoud, J.-F. Nierengarten, S.-G. Liu, L. Echegoyen, N. Armaroli, F. Barigelletti, L. Ouali, V.Krasnikov, G. Hadziioannou, J. Am. Chem. Soc. 122 (2000) 7467

199. M. Faraday, Philos. Trans. R. Soc. London, 147 (1857) 145

200. P. P. Edwards, R. L. Johnston and C. N. R. Rao, in Metal clusters in Chemistry, Eds. P. Braunstein, G. Oro and P. R. Raithby, Wiley-VCH,1998

201. A. I. Kirkland, P. P. Edwards, D. A. Jefferson and D. G. Duff, Annu. Rep. Prog. Chem., Sect. C, Phys. Chem., 84 (1988) 247.

202. M. Haruta, J. Nanopart. Res. 5 (2003) 3

203. H. H. Lee, K. S. Chou, K. C. Huang, Nanotech. 16 (2005) 2436

204. P. Ghosh, G. Han, M. De, C. K. Kim, V. M. Rotello, Adv. Drug Delivery Rev. 60 (2008) 1307

REFERENCES

205. M. C. Daniel, D. Astruc Chem. Rev. 104 (2004) 293

206. K. Chung, Tiny is Beautiful: Translating Nano into Practical, New York Times Feb. 22 (2004)

207. K. Marubayashi, S. Takizawa, T. Kawakusu, T. Arai, H. Sasai Org. Lett. 5 (2003) 4409

208. H. Gu, P. L. Ho, E. Tong, L. Wang, B. Xu Nano Lett. 3 (2003) 1261

209. N. Rosi, C. S. Thaxton, C. A. Mirkin, Angew. Chem Int. Ed. 43 (2004) 5500

210. M. Zayats, S. P. Pogorelova, A. B. Kharitonov, O. Lioubashevski Chem. Eur. J. 9 (2003) 6108

211. T. Hasobe, H. Imahori, P. V. Kamat, S. Fukuzumi J. Am. Chem. Soc. 125 (2003) 14962.

212. F. Kim, J. H. Song, P. Yang, J. Am. Chem. Soc. 124 (2002) 14317.

213. Q. Zhang, N. Li, J. Goeb, Z. Lu, Y. Yin, J. Am. Chem. Soc. 133 (2011) 18931

214. C. J. Murphy, T. K. Sau, A. M. Gole, C. J. Orendorff. J. L. Gou, S. E. Hunyadi, T. Li, J. Phys. Chem. B, 109 (2005) 13857

215. S.K. Ghosh, T. Pal, Chem. Rev. 107 (2007) 4797.

216. A. Willets, R.P. Duyne, Annu. Rev. Phys. Chem. 58 (2007) 267.

217. M. Tsuji, S. Gomi, Y. Maeda, M. Matsunaga, S. Hikino, K. Uto, T. Tsuji, H. Kawazumi, Langmuir. 28 (2012) 8845

218. A. A. Ashkarran, M. Ghavami, H. Aghaverdi, P. Stroeve, M. Mahmoudi, Chem. Res. Toxicol 25(2012) 1231

219. J. Turkevich, P. C. Stevenson, J. Hiller Discuss. Faraday Soc. 11 (1951) 55

220. J. Turkevich, Gold Bull. 18 (1985) 86

221. G. Frens, Nature Phy. Sci. 20 (1971) 241

222. L. M. L. Marzàn, Materials Today 7 (2004) 26

223. A. C. Templeton, W. P. Wuelfing, R. W. Murray, Acc. Chem. Res. 33 (2000) 27

224. H. Imahori, M Arimura, T. Hanada, Y. Nishimura, I. Yamazaki, Y. Sakata, S. J Fukuzumi, J. Am. Chem. Soc. 123(2001) 335.

225. H. Sun, A. M. Scharff-Poulsen, H. Gu, K. Almdal, Chem. Mat. 18 (2006) 3381.

REFERENCES

226. Y. Cheng, A. C. Samia, J. Li, M. E. Kenney, A. Resnick, C. Burda, Langmuir 26 (2010) 2248.

227. S. E. A. Gratton, P. A. Ropp, P. D. Pohlhaus, J. C. Luft, V. J. Madden, M. E. Napier, J. M. DeSimone, Proc. Natl. Acad. Sci. USA. 105 (2008) 11613.

228. J. Panyam, V. Labhasetwar, Pharmaceut. Res. 20 (2003) 212.

229. L. W. Zhang, N. A. Monteiro-Riviere, Toxicol. Sci. 110 (2009)138.

230. I. H. El-Sayed, X.H. Huang, M.A. El-Sayed. Nano Lett. 5 (2005) 829

231. D.C. Hone, P.I. Walker, R. Evans-Gowing, S. FitzGerald, A. Beeby, I. Chambrier, M. J. Cook, D. A. Russell, Langmuir 18 (2002)2985.

232. V. P. Chauke, Y. Arslanoglu, T. Nyokong, J. Photochem. Photobiol. A: Chem. 221 (2011) 38

233. V. P. Chauke, E. Antunes, W. Chidawanyika, T. Nyokong, J. Mol.Cat. A: Chemical 335 (2011) 121

234. T. P. Mthethwa , Y. Arslanoglu , E. Antunes , T. Nyokong, Polyhedron 38 (2012) 169

235. S. Forteath, E. Antunes, W. Chidawanyika, T. Nyokong, Polyhedron 34 (2012) 114

236. S. Moeno, E. Antunes, T. Nyokong, J. Photochem. Photobiol. A: Chem. 222 (2011) 343

237. S. Tombe, W. Chidawanyika , E. Antunes , G. Priniotakis, P.Westbroek, T. Nyokong, J. Photochem. Photobiol. A: Chem. 240 (2012) 50

238. N. Nombona, E. Antunes, W. Chidawanyika, P. Kleyi, Z. Tshentu, T. Nyokong, J. Photochem. Photobiol. A: Chem. 233 (2012) 24

239. D. Pissuwan , T. Niidome, M. B. Cortie, J. Controlled Release 149 (2011) 65

240. M. Camerin , M. Magaraggia , M. Soncin , G. Jori , M. Moreno , I.Chambrier , M. J. Cook , D. A. Russell, Eur. J. Cancer 4 6 (2 0 1 0) 1 9 1 0

241. N. Nombona, E. Antunes, C. Litwinski, T. Nyokong, Dalton Trans. 40 (2011) (1884) 11876.

242. K. S. Lokesh, V. Narayanan, S. Sampath, Microchim. Acta. 167 (2009) 97

243. E. Zenkevich, A. Shulga, F. Cichos, E. Petrov, T. Blaudeck, C. von Borczyskowski, J. Phys. Chem. B 109 (2005) 8679

244. M.J. Bruchez, M. Moronne, P. Gin, S. Weiss, A. P. Alivisatos, Science 281 (1998) 2013.

245. I. L. Medintz, H.T. Uyeda, E.R. Goldman, H. Mattoussi, Nat. Mater. 4 (2005) 435.

246. X. Michalet, F.F. Pinaud, L.A. Bentolila, J.M. Tsay, S. Doose, J.J. Li, G. Sundaresan, A.M. Wu, S.S. Gambhir, S. Weiss, Science 307 (2005) 538.

247. H. Peng, L. Zhang, T.H.M. Kjallman, C. Soeller, J. Travas-Sejdik, J. Am. Chem. Soc. 129 (2007) 3048.

248. J. Ma, J.-Y. Chen, Y. Zhang, P.-N. Wang, J. Guo, W.-L. Yang, C.-C. Wang, J. Phys. Chem. B 111 (2007) 12012.

249. D.A. Gaul, W.S. Rees Jr., Adv. Mater.12 (2000) 935.

250. C.M. Niemeyer, Angew. Chem. Int. Ed. Engl. 40 (2001) 4128

251. V.I. Klimov, Los Alamos Science, 28 (2003) 214.

252. W. Schroter, In Handbook of semiconductor technology, Electronic structure and properties of semiconductors, Wiley VCH, Weinheim, (2000).

253. A.P. Alivisatos, Science, 271 (1996) 933.

254. M. Bruchez Jr., M. Moronne, P. Gin, S. Weiss, A.P. Alivisatos, Science, 281 (1998) 2013.

255. M. A. El-Sayed, Acc. Chem. Res., 37 (2004) 326.

256. B. O. Dabbousi, J. Rodriguez-Viejo, F. V. Mikulec, J. R. Heine, H. Mattoussi, R. Ober, K. F. Jensen and M. G. Bawendi, J. Phys. Chem. B, 101 (1997) 9463

257. A.P. Alivisatos, J. Phys.Chem., 100 (1996) 13226

258. A.J. Sutherland, Curr. Opin. Solid State Mater. Sci., 6 (2002) 365.

259. S. Moeno, T. Nyokong, J. Photochem. Photobiol. A: Chem. 201 (2009) 228

260. S. Moeno, E. Antunes, T. Nyokong, J. Photochem. Photobiol. A: Chem. 218 (2011) 101

261. S. Moeno, T. Nyokong, J. Photochem. Photobiol. A: Chem. 215 (2010) 196

262. S. Moeno, E. Antunes, S. Khene, C. Litwinski, T. Nyokong, Dalton Trans., 39 (2010) 3460

263. S. Khene, T. Nyokong, Microchem. Journal 99 (2011) 478

264. M. Idowu, J. –Y. Chen, T. Nyokong, New J. Chem., 32 (2008) 290.

REFERENCES

265. M. Idowu, T. Nyokong, J. Luminescence., 129 (2009) 356.

266. W. Chidawanyika, C. Litwinski, E. Antunes, T. Nyokong, J. Photochem. Photobiol A. Chem., 212 (2010) 27.

267. S. Dayal, Y. Lou, A. C. S. Samia, J. C. Berlin, M. E. Kenney, C. Burda, J. Am. Chem. Soc., 128 (2006) 13974.

268. S. Dayal, C. Burda, Photochem. Photobiol. Sci., 7 (2008) 605.

269. M. Idowu, T. Nyokong, Spectrochimi. Acta Part A 75 (2010) 411

270. M. Idowu, T. Nyokong, Polyhedron 28 (2009) 891

271. A. Eychmüller, A. L. Rogach, Pure Appl. Chem., 72 (2000) 179.

272. A.L. Rogach, L. Katsikas, A. Kornowski, D. Su, A. Eychmüller, H. Weller, Ber. Bunsenges. Phys. Chem., 101 (1997) 1668.

273. N.N. Mamedova, N. A. Kotov, A. L. Rogach, J. Studer Nano Lett., 1 (2001) 281.

274. N. Gaponik, D. V. Talapin, A. L. Rogach, K. Hoppe, E. V. Shevchenko, A. Kornowski, A. Eychmüller, H. Weller, J. Phys. Chem. B, 106 (2002) 7177.

275. J.R. Lakowicz, Principles of Fluorescence Spectroscopy, 3rd ed. Springer, New York, (2006).

276. P. Kaláb,J. Soderholm,Methods 51 (2010) 220

277. D. Stepensky,Biochem. Biophys. Res. Commun. 359 (2007) 752.

278. A. Periasamy, In Molecular Imaging: FRET Microscopy and Spectroscopy, ed. N.R. Day, Oxford University Press, New York, (2005).

279. J.S. Hsiao, B.P. Krueger, R.W. Wagner, T.E. Johnson, J.K. Delaney, D.C. Mauzerall, G.R. Fleming, J.S. Lindsey, D.F. Bocian, R.J. Donohoe, J. Am. Chem. Soc., 118 (1996) 11181

280. J.R Lakowicz in: Principles of Fluorescence Spectroscopy, 2nd ed., Kluwer Academic/Plenum Publishers, New York, 1999.

281. C. Deng, J. Li, W. Ma, Talanta 82 (2010) 771.

282. T. Förster, Discuss. Faraday Soc., 27 (1959) 7.

283. H. Du, R. A. Fuh, J. Li, L. A. Cockan, J. S. Lindsey, Photochem. Photobiol.,68 (1998) 141.

284. D. Li, Y. N. Xia, Adv. Mater, 16 (2004) 1151

285. A. Frenot, I. S. Chronakis, Curr. Opin. Colloid interface Sci., 8 (2003) 64

286. A. Koski, K. Yim S. Shivkumar, Mater. Lett., 58 (2004) 493

287. B. Carlberg, M. Z. Axell, U. Nannmark, J. Liu, H. G. Kuhn, Biomed. Mater., 4 (2009) 045004

288. B. Decostere, N. Daels, S. De Vrieze, P. Dejans, T. Van Camp, W. Audenaert, J. Hogie, P. Westbroek, K. De Clerck, S.W.H. Van Hulle, Desalination 249 (2009) 942

289. N. Daels, S. De Vrieze, B. Decostere, P. Dejans, A. Dumoulin, K. De Clerck, P. Westbroek, S.W.H. Van Hulle, Desalination 257 (2010) 170

290. D. V. Sander, N. Daels, K. Lambert. Text. Res. J. 82 (2012) 37

291. R. Neppalli, Eur. Polym. .J 46 (2010) 968

292. M.M. Bergshoef, G.J. Vancso, Adv. Mater. 11 (1999) 1362

293. S. Honarbakhsh, B. Pourdeyhimi, J. Mater. Sci. 46 (2011) 2874.

294. S. Agarwal, Polymer 49 (2008) 5603

295. L. Van der Schueren, Eur. Polym. J. 47 (2011) 1256

296. C. Xu, F. Xu, B. Wang, T. Lu., J. Nanomater. 201 (2011) 834

297. Y.C. Ahn, Curr. Appl. Phys. 6 (2006) 1030

298. S. Ramakrishna, K. Fujihara, W.E. Teo, T.C. Lim, Z. Ma An introduction to electrospinning and nanofibres. World Scientific Publishing, Singapore (2005)

299. B. D. Schoenmaker , L. Van der Schueren , R. Zugle , A. Goethals , P. Westbroek , P. Kiekens , T. Nyokong , K. De Clerck, J. Mater. Sci., in press

300. R. Zugle, T. Nyokong, J. Mol. Cat. A: Chem. (2012) in press

301. R. Zugle, T. Nyokong, J. Mol. Cat. A: Chem. 358 (2012) 49

302. R. Zugle, E. Antunes, S. Khene, T. Nyokong, Polyhedron 33 (2012) 74

303. R. Zugle, C. Litwinski, N. Torto, T. Nyokong New J. Chem., 35 (2011) 1588

304. R. Zugle, T. Nyokong, J. Appl. Polym. Sci. (2012) In Press

305. R. Zugle, T. Nyokong, J. Macromol. Sc., Part A: Pure and Applied Chemistry 49 (2012) 279

306. S. Tang, C. Shao, Y. Li, R. Mu, J. Phys. Chem. Solids, 68 (2007) 2337

307. J. Mosinger, K. Lang, P. Kubát, J. Sýkora, M. Hof, L. Píštil, B. Mosinger Jr., J. Fluorec., 19 (2009) 709

308. S.-L. Cheng, X.-J. Huang, Z.-K. Xu, Cellulose, 18 (2011) 1295

309. Z. Guo, B. Chen, J. Mu, M. Zhang, P. Zhang, Z. Zhang, J. wang, X. Zhang, Y. Sun, C. Shao, Y. Liu, J. Hazard. Mater., (2012) 219

310. M. Karaskova, J. Rakusan, O. Jirsak, P. Jilek, Nancon 2010, Olomouc, Czech Republic, EU.

311. G. Jori, S.B Brown,.Photochem. Photobiol. Sci 3(2004)403.

312. O. Tunger, G Dinc, B. Ozbakkaloglu, C. Atman, U. Algun, Int. J. Antimicrob. Agents 15 (2000) 131.

313. M.R. Hamblin, T. Hasan, Photochem. Photobiol. Sci. 3 (2004) 436.

314. B.A Cunha, Crit. Care Clin. 14 (1998) 309.

315. M. Wainwright, J. Antimicrob. Chemother. 42 (1998) 13.

316. Z. Malik, J. Hanania, Y. Nitzan, J. Photochem. Photobiol. B Biol. 5 (1990) 281.

317. O. Raab, Biol. 39 (1900) 524

318. P.W. Taylor, P.D. Stapleton, J.P. Luzio, Drug Discovery Today 7 (2002) 1086.

319. K.D. Winckler, J. Photochem. Photobiol. B Biol. 86 (2007) 43.

320. A.P. Castano, T.N. Demidova, M.R. Hamblin, Photodiagn. Photodyn. Ther., 1 (2004) 279

321. T. Maisch, C. Bosl, R.M. Szeimies, N. Lehn, C. Abels, Antimicrob. Agents Chemother., 49 (2005) 1542

322. P.H. Makela, M. Hovi, H. Saxén, M. Valtonen, H. Valtonen, Immunol. Lett., 19 (1988) 217

323. A. Pfitzner, B.W. Sigusch, V. Albrecht, E. Glockmann. J. Periodontol. 75 (2004) 1343.

324. S. Dutta, D. Ray, B.K. Kolli, K.P. Chang. Antimicrob. Agents Chemother. 49 (2005) 4474.

325. A.S. Garcez, M.S. Ribeiro, G.P. Tegos, S.C. Nunez, A.O. Jorge, M.R. Hamblin. Lasers Surg. Med. 39 (2007) 59.

326. G. Jori, Environ. Toxicol. Oncol. 25 (2006) 505.

327. H.J. A. Tappeiner, Munch. Med. Wochenschr. 50 (1903) 2041.

328. M. Wainwright, D. A. Phoenix, S. L. Laycock, D. R. A. Wareing, P. A. Wright, FEMS Microbiol. Lett. 160 (1998) 177.

329. G. S. Anderson, W. H. H. Gunter, R. Searle, Photochem. Photobiol. 64 (1996) 683.

330. H. C. Neyndorff, L. D. Barel, F. Turafo, G. J. Levy, Transfusion 30 (1990) 485.

331. I. Scalise, E. N. Durantini, Bioorg. Med. Chem. 13 (2005) 3037

332. B. Cosimelli, G. Roncucci, D. Dei, L. Fantetti, F. Ferroni, M. Ricci, D. Spinelli, Tetrahedron 59 (2003) 10025

333. J. Chen, Z. Chen, Y. Zheng, S. Zhou, J. Wang, N. Chen, J. Huang, F. Y. Huang, J. Porphyr. Phthalocya. 15 (2011) 294

334. A. Minnock , D. I. Vernon , J. Schofield , J. Griffiths , J. H. Parish , S. B. Brown,J. Photochem. Photobiol. B: Biol. 32 (1996) 159

335. A. Minnock, D. I. Vernon, J Schofield, J. Griffiths, J.H. Parish, S B. Brown, antimicrob. agents and chemother., (2000) 522

336. V. Mantareva , I. Angelov , V. Kussovski , R. Dimitrov , L. Lapok , D. Wöhrle, Eur. J. Med. Chem. 46 (2011) 4430

337. V. Mantareva, V. Kussovski, I. Angelov, D. Wöhrle, R. Dimitrov, E. Popova, S. Dimitrov, Photochem. Photobiol. Sci. 10 (2011) 91.

338. V. Mantareva ,V. Kussovski, I. Angelov, E. Borisova, L. Avramov, G. Schnurpfeild, D. Wohrle, Bioorg. Med. Chem. 15 (2007) 4829

339. R. Brayner, R. Ferrari-Iliou, N. Brivois, S. Djediat, M. Benedetti, F. Fiévet, Nano Lett. 6 (2006) 866.

340. A. Simon-Deckers, S. Loo, M. Mayne-L'hermite, N. Herlin-Boime, N. Menguy, C. Reynaud, B. Gouget, M. Carrie re: Environ. Sci. Technol. 43 (2009) 8423.

341. A.J. Huh, Y.J. Kwon   J. Control. Release 156 (2011) 128

342. G.M. Whitesides, Small 1 (2005) 172

343. Y. Xia. Nat. Mater. 7 (2008) 758

344. Q. Li, S. Mahendra, D.Y. Lyon, L. Brunet, M.V. Liga, D. Li, Water Res 42 (2008) 4591.

345. W.B. Hu, C. Peng, W.J. Luo, M. Lv, X.M. Li, D. Li, ACS Nano 4 (2010) 4317.

346. I. Banerjee, D. Mondal, J. Martin, R.S. Kane. Langmuir 26 (2010) 17369.

347. K. Chaloupka, Y. Malam, A.M. Seifalian. Trends Biotechnol. 28 (2010) 580.

REFERENCES

348. Z. Huang, X. Zheng, D. Yan, G. Yin, X. Liao, Y. Kang, Langmuir 24 (2008) 4140.

349. V.K. Sharma, R.A. Yngard, Y. Lin, Adv. Colloid Interface Sci. 145 (2009) 83.

350. G.A. Martínez-Castañón, N. Niño-Martínez, F. Martínez-Gutierrez, J.R. Martínez- Mendoza, F. Ruiz, J. Nanopart. Res. 10 (2008) 1343.

351. Y.H. Lv, H. Liu, Z. Wang, L.J. Hao, J. Liu, Y.M. Wang, G.J. Du, D. Liu, J. Zhan, J.Y. Wang, Polym. Adv. Technol. 19 (2008) 1455.

352. W. K. Son, J. H Youk. T. S. Lee, W. H Park, Macromol. Rapid Commun. 25 (2004) 1632.

353. Q. L Feng, J. Wu, G. Q. Chen. F. Z. Cui, T. N. Kim, J. O. Kim, J. Biomed. Mater. Res. 52 (2000) 662.

354. J. L. Clement, P. S. Jarrett, Met.-Based Drugs 1 (1994) 467.

355. Y. Jin, X. Zhao: Cytotoxicity of photoactive nanoparticles. In Safety of Nanoparticles: From Manufacturing to Medical Applications. Edited by Webster T. Springer Science + Business Media, LLC, 233 Spring St.:New York, NY 10013 (2008) 19.

356. A. Nirmala Grace, K. Pandian, Colloids Surf., A 297 (2007) 63.

357. B. Saha, J. Bhattacharya, A. Mukherjee, A. Ghosh, C. Santra, A. Dasgupta, P. Karmakar, Nanoscale Res. Lett. 2 (2007) 614.

358. J. Banerjee, R.T. Narendira Kannan, Dig. J. Nanomat. Biostruct. 6 (2011) 961.

359. D.D. Perrin, W.L.F. Armarego, in Purification of Laboratory Chemicals, 2nd Ed., Pergamon Press, Oxford, (1989).

360. J. Kossanyi, D. Chachraroui, Int. J. Photoenergy, 2 (2000) 9

361. T. H. Tran-Thi, C. Desforge, C. Thiec, J. Phys. Chem., 93 (1989) 1226

362. W. Spiller, H. Kliesch, D. Worhle, S. Hackbarth, B. Röder, G. Schnurpfeil, J. Porphyr. Phthalocya. 2 (1998) 145

363. A. L. Rogach, L. Katsikas, A. Kornowsiki, D. Su, A. Eychmuller, H. Weller, Phys. Chem. 100 (1996) 1772

364. Y-F Liu , J-S Yu, J. Colloid Interface Sci. 351 (2010) 1

365. S. Sapra and D. D. Sarma, Pramana 65 (2005) 565

REFERENCES

366. Z. Zhang, J. Jia, Y. Lai, Y. Ma, J. Weng, L. Sun, Bioorgan. Med. Chem. 18 (2010) 5528

367. D. Jana, G. De, J. Mater. Chem.21 (2011) 6072-6078

368. R.D. George, A.W. Snow, J. Heterocyclic Chem. 32 (1995) 495-498.

369. J.G. Young, W. Onyebuagu, J. Org. Chem. 55 (1990) 2155-2159.

370. D. Wöhrle, M. Eskes, K. Shigehara, A. Yamada, Synthesis (1993) 194-196.

371. M. Durmus, T. Nyokong, Tetrahedron 63 (2007) 1385.

372. L. Zhang, J. Huang, L. Ren, M. Bai, L. Wu, B. Zhai, X. Zhou, Bioorg. Med. Chem. 16 (2008) 303.

373. Z.A. Bayir, Dyes Pig. 65 (2005) 235.

374. S.V. Kudrevich, M.G. Galpern, J.E. van Lier, Synthesis 8 (1994) 779

375. M. Idowu, T. Nyokong, Polyhedron 28 (2009) 416

376. Y. Li, T. M. Pritchett, J. Huang, M. Ke, P. Shao, W. SunJ. Phys. Chem. A 112 (2008)7200

377. W.W. Yu, L. Qu, W. Guo, X. Peng, Chem. Mater. 15 (2003) 2854

378. R. M. Silverstein, G. C. Bassler and T. C. Morrill, Spectrometric Identification of Organic Compounds, 4th edn, John Wiley andSons, New York, 1981

379. S. Gaspard, P. Maillard, Tetrahedron 43 (1987) 1083

380. A.Y. Tolbin, V.E. Pushkarev, G.F. Nikitin, L.G. Tomilova, Tetrahedron Lett. 69 (2009) 4848

381. N. Kobayashi, A. Muranaka, K. Ishii. Inorg. Chem. 39 (2000) 2256

382. T. Nyokong, H. Isago, J. Phthalocya. Porphyr.8 (2004) 1083

383. T. Nyokong in Functional Phthalocyanine Molecular Materials, Structure and Bonding (J. Jiang J. Ed.) Springer, New York, Vol. 135, (2010).

384. I. Chambrier, M.J. Cook, P.T. Wood. Chem Commun, (2000) 2133-2134

385. N. Kobayashi, O. Toshie, M. Sato, N. Shin-ichiro, Inorg. Chem. 32 (1993) 1803

REFERENCES

386. N. Kobayashi, T. Ishizaki, K. Ishii, H. Konami,J. Am. Chem. Soc. 121 (1999) 9096

387. W. Freyer, S. Müller, K.J. Teuchner, J. Photochem. Photobiol. A: Chem. 163 (2004) 231

388. A. Meister, M. E. Anderson, Annu. Rev. Biochem. 52(1983) 711.

389. R. Hong, G. Han, J. M. Fernandez, B. J. Kim, N. S. Forbes, V. M. Rotello, J. Am. Chem. Soc. 128(2006)1078.

390. M. Zheng, X. Huang, J. Am. Chem. Soc. 126 (2004) 12047

391. V. C Verma, S. K Singh, R. Solanki, S. Prakash.Nanoscale Res Lett 6 (2011) 16

392. A. W. Snow, J. R. Griffith, N. P. Marullo, Macromolecules, 17 (1984) 1614

393. S. Sensthilarasu, Y.B. Hahn, S.-H. Lee, J. Appl. Phys. 102 (2007) 043512

394. Z.-L. Yang, H.- Chen, L. Cao, H.-Y Li, M. Wang, Mater. Scie. Eng. B 106 (2004) 73

395. D. Schlettwein, K. Hesse, N.E. Gruhn, A.P. Lee, K.W. Nebesny, N.R. Armstrong, J. Phys. Chem. B 105 (2001) 4791.

396. K. Sakamoto, E. Ohno, Prog. Org. Coat. 31 (1997) 139.

397. S. Vukovic, S. Corni, B. Mennucci J. Phys. Chem. C 113 (2009)121

398. O. Adegoke T. Nyokong, J Fluoresc 22 (2012)1513

399. A. L. Rogach, L. Katsikas, A. Kornowski, D. Su, A. Eychmuller, H. Weller, B. Bunsen-Ges. Phys. Chem., 100 (1996) 1772

400. N. Kobayashi, in: C. C. Leznoff, A. B. P. Lever (Eds.), Phathalocyanines—Properties and Applications, vol. 2, VCH Publishers Inc., New York, 1993, p. 97

401. K. Lang, J. Mosinger, D. M. Wagnerova, Coord. Chem. Rev., 248 (2004) 321

402. L. Alagna, A. Capobianchi, M. P. Casaletto, G. Mattogna, A. M. Paoletti, G. Pennesi, G. Rossi, J. Mater. Chem. 11 (2001) 1928

403. N. Peltekis, B. N. Holland, S. Krishnamurty, I. T. McGovern, N. R. J. Poolton, S. Patel, C. McGuiness, J. Am. Chem. Soc., 132 (2008) 13008

404. Z. Wang, A.-M. Nygård, M. J. Cook, D. A. Russell, Langmuir 20 (2004) 5850

405. C. L. Pai, M. C. Boyce, G. C. Rutledge, Macromolecules 42 (2009) 2102

406. A. Grofcsik, P. Baranyai, I. Bitter, V. Csokai, M. Kubinyi, K. Szegletes, J. Tatai, T. Vidoczy, J. Mol. Struct. 704 (2004) 11

407. M. Idowu, T. Nyokong, J. Photochem. Photobiol. A: Chemistry 204 (2009) 63

408. M. Idowu, T. Nyokong, J. Photochem. Photobiol. A: Chemistry 197 (2008) 273

409. C. D. Geddes, J. R. Lakowicz, Topics in Fluorescence Spectroscopy, Springer, New York, 2005.

410. Y. Kaneko, Y. Nishimura, N. Takane, T. Arai, H. Sakuragi, N. Kobayashi, D. Matsunaga, C. Pac and K. Tokumaru, J. Photochem. Photobiol. A, 106 (1997) 177

411. J. R. Lakowicz, Ana. Biochem., 298 (2001) 1

412. J. R. Lakowicz, Ana. Biochem., 337 (2005) 171

413. J. Cerny, M. Karaskova, J. Rakusan, S. Nespurek, J. Photochem. Photobiol. A: Chemistry 210 (2010) 82

414. S. Dayal, C. Burda, J. Am. Chem. Soc. 129 (2007) 7977

415. C. L. Takanishi, E. A. Bykova, W. Cheng, J. Zheng, brain research 1091 (2006) 132

REFERENCES

416. T. Blaudeck, E. I. Zenkevich, F. Cichos, C. von Borczyskowski, J. Phys. Chem. C, 112 (2008) 20251

417. D. Kowerko, J. Schuster, N. Amecke, M. Abdel-Mottaleb, R. Dobrawa, F. Würthner, C. von Borczyskowski, Phys. Chem. Chem. Phys, 12 (2010) 4112

418. M.G. Debacker, O. Deleplanque, B.V. Vlierberge, F. X. Sauvage, Laser Chemistry 8 (1988) 1

419. Y. Nitzan, H. Ashkenazi,. Curr. Microbiol. 42 (2001) 408

420. M. Salmon-Divon,Y. Nitzan, Z. Malik,. Photochem. Photobiol. Sci. 3 (2004) 423

421. A. L. Barry, R.A. Lasner, Antimicrob. Agents Chemother. 9 (1976) 549

422. A. Orenstein , D. Klein, J. Kopolovic, E. Winkler, Z. Malik, N. Keller, Y. FEMS Immunol. Med. Microbiol. 19 (1997) 307

423. S. Ghammamy, M. Azimi, S. Sedaghat Scientific Res. Essays 7 (2012) 3751

424. P. Domenico, R.J. Salo, S.G. Novick, P. ESchoch, K. Van Horn, B.A. Cunha, Antimicrob Agents Chemother 41 (1997) 1697

425. J. H. R. Kagi, M Nordberg, Metallothionein, 1st ed.; Birkhauser: Boston, Vol. 1(1978)

426. A. Krezel, W. Maret, J. Am. Chem. Soc. 192 (2007) 10911.

427. M. J. Stillman,C. F. Shaw,K. T. Suzuki, Metallothioneins, 1st ed.; VCH Publishers: New York, 1992.

428. J. H. R. Kagi, Y. Kojima, Metallothionein II, 1st ed.; Birkhauser: Boston, Vol. 2 (1985).

429. K. T. Suzuki, N. Imura, M. Kimura, Metallothionein III, 1st ed.; Birkhauser: Boston, Vol. 3 (199).

REFERENCES

430. C. A. Blindauer, N. C. Polfer, S. E. Keiper, M. D. Harrison, N. J. Robinson, P. R. R. Langridge-Smith, P. J. Sadler, J. Am. Chem. Soc. 125 (2003) 3226.

431. T. T. Ngu, M. J. Stillman, J. Am. Chem. Soc. 128 (2006) 12473.

432. M. Dabrio, G. Van Vyncht, G. Bordin, A. R. Rodriguez, Anal. Chim. Acta 435 (2001) 319.

433. M. Margoshes, B. L. Vallee, J. Am. Chem. Soc. 79 (1957) 4813.

434. G. Jiang, Z. Gong, X.-F Li, W. R Cullen, X. C. Le, Chem. Res. Toxicol. 16 (2003) 873.

435. M. E Merrifield, T.T. Ngu, , Stillman M. J., Biochem. Biophys. Res. Commun. 324 (2004) 127.

436. M. Toyama, M. Yamashita, N. Hirayama, Y. Murooka, J. Biochem. (Tokyo) 132 (2002) 217.

437. M. E. Merrifield, Z. Huang, P. Kille, M. J. Stillman, J. Inorg.Biochem. 88 (2002) 153

438. J. Mack, M. J. Stillman. J. Am. Chem. Soc. 116 (1994) 1292.

439. S.P. Keizer, J. Mack, B.A. Bench, Gorun S. M, and Stillman M. J, J. AM. CHEM. SOC. 125 (2003) 7067.

440. J. Mack, M. J. Stillman, J. Phys. Chem. 95 (1995) 7935.